STRATEGIES FOR IMPROVING THE DETERMINATION OF DISPLACEMENTS OF SEA SURFACE TEMPERATURE PATTERNS USING CONSECUTIVE AVHRR THERMAL IMAGES

XUE-QUN LU

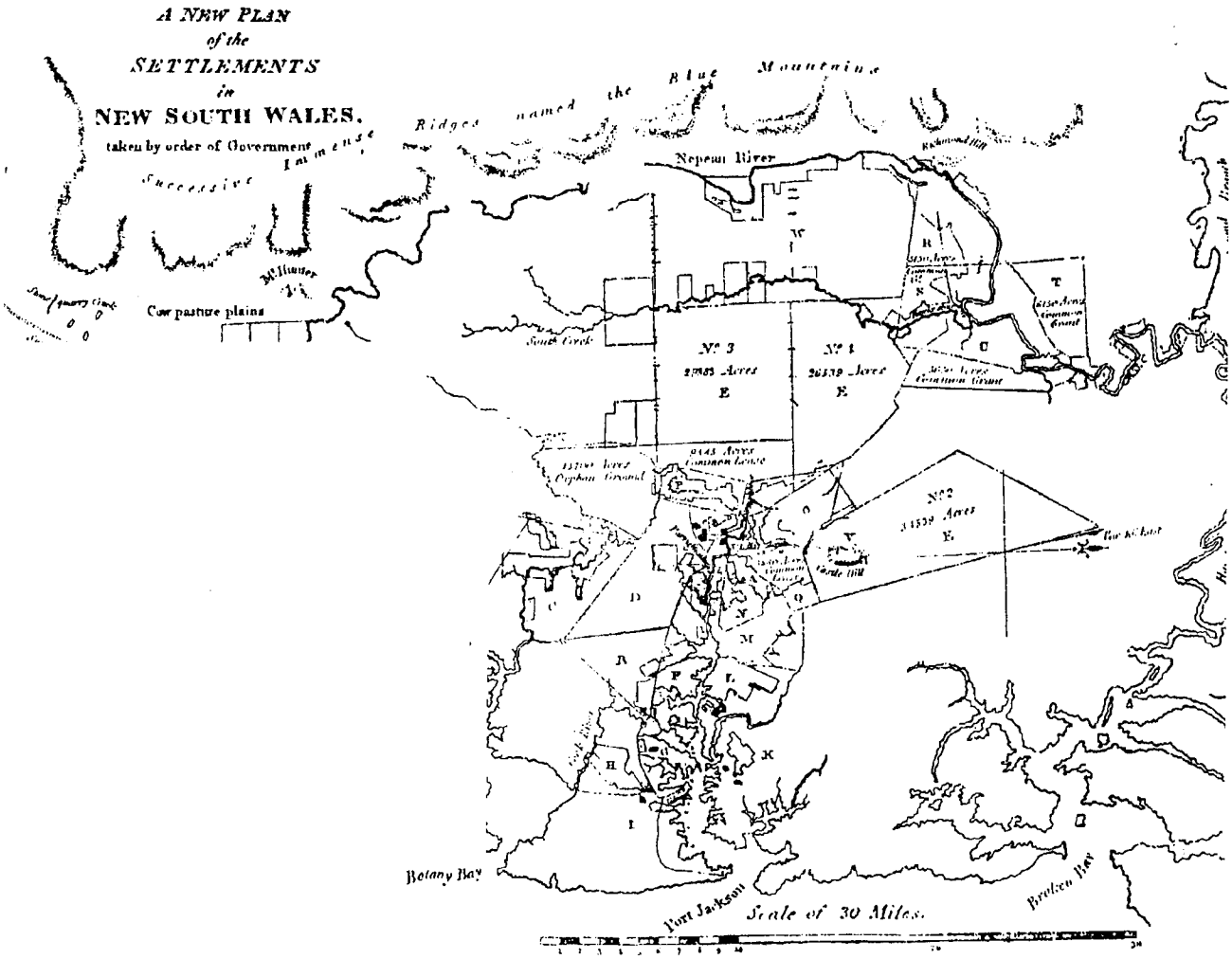

UNISURV S-59, 2000

Reports from

SCHOOL OF GEOMATIC ENGINEERING

THE UNIVERSITY OF NEW SOUTH WALES SYDNEY NSW 2052 AUSTRALIA

UNISURV REPORT S-59, 2000

STRATEGIES FOR IMPROVING THE DETERMINATION OF DISPLACEMENTS OF SEA SURFACE TEMPERATURE PATTERNS USING CONSECUTIVE AVHRR THERMAL IMAGES

XUE-QUN LU

Received: November 2000
Accepted: November 2000

SCHOOL OF GEOMATIC ENGINEERING
UNIVERSITY OF NEW SOUTH WALES
UNSW SYDNEY NSW 2052
AUSTRALIA

UNISURV REPORTS

Series Editor: Dr. J. M. Rüeger

National Library of Australia

Card No. and ISBN 0 - 7334 - 1721 - 3

Foreword

Since the 1970's a range of increasingly sophisticated satellite remote sensing systems have become available for monitoring the earth's atmosphere, oceans and land surfaces. One of these, the Advanced Very High Resolution Radiometer was first launched by NOAA in 1978 on board TIROS-N as part of their Polar Orbiting Environmental Satellites (POES) program. Since then a further 14 AVHRR sensor systems have been launched, and four are currently operational. AVHRR has sensors that record in the visible, infrared and thermal infrared spectral ranges, with a resolution element size of approximately 1 kilometre, and a return period of 12 hours between the descending and ascending orbital paths, at an altitude of 833 km. It is this range of wavelengths and better than daily return period that has made the data useful for a range of applications. These include deriving sea surface temperatures, ocean colour, vegetation indices (NDVI), atmospheric aerosols over oceans, monitoring volcanic eruptions and volcanic ash clouds, and monitoring cloud patterns.

The work that Frank Lu undertook for his PhD examined the sea surface temperatures (SST) derived from AVHRR thermal infrared image data as a means of determining sea surface velocity (SSV). At any instant the spatial distribution of sea surface temperatures have unique patterns. As currents caused by temperature differences and surface winds move the ocean surface, the shape, distribution and location of these patterns are changed. If the movements of the same points, on these moving and distorting patterns, can be tracked, then the spatial distribution of sea surface velocity, or the sea surface displacement field, can be estimated. The difficulty is caused by the up to 12 hours time difference between successive images, and thus the ability to locate the same points in each pattern. Methods used to date relied on the determination of the maximum correlation between successive SST images using a fixed, non-rotating template for image processing. This approach can result in a large number of errors, particularly when there is a significant time difference between images. The contribution made by Lu's work was to develop a processing method that integrated the contextual relation of the displacement field with the correlation method, and allowed for a flexible processing template to resolve the deformation of the SST pattern. His

research also saw the development of a partially cloud contaminated pixel detection algorithm, based on the Förstner operator.

Lu's research was somewhat unique in the School of Geomatic Engineering, as only limited ocean related remote sensing research has been previously undertaken, most notably on sediment load and chlorophyll distribution in near coastal waters. His research though, has close links to other image processing work in the School particularly edge detection in photogrammetry for automated road tracing and also image matching for automated DEM production, and to a lesser extent with image deconvolution of SPOT data using point spread functions, and to research into radar speckle filtering and segmentation for better classification of forest images and other classification procedures. Some remote sensing image processing research is also undertaken in the School of Geography (UNSW), which is associated to the School of Geomatic Engineering through the Centre for Remote Sensing and GIS. Internationally a significant amount of research is being undertaken for ocean monitoring, using a wide range of remote sensing tools from visible to microwave systems, and Lu's work forms a part of these ongoing studies.

Bruce Forster

November 2000

Abstract

The reliability and accuracy of the determination of the sea surface displacement field from consecutive sea surface temperature (SST) images using maximum cross-correlation (MCC) method with non-rotate fixed-shape template, are affected by a number of factors, and result in a large number of erroneous estimates. The research described in this thesis investigates uncertainty in the determination of displacement of SST patterns due to the correlation function form, and the error in the correlation function computed using a non-rotate fixed-shape template due to the unresolved rotational motion and deformation. Based on the understanding of the factors which affect the displacement determination, a comprehensive algorithm based on a relaxation labelling technique and joined-patch least squares matching (JPLSM) technique was developed. Besides these, a partially cloud contaminated pixels detection algorithm, based on the Förstner operator, was developed to minimise the effect of cloud contamination.

The investigation shows that the correlation function was frequently of multi-peak and elongated distribution, due to the high auto-correlation of the SST patterns in the along-isothermal direction, and this distribution form of the correlation function introduces an uncertainty in the displacement determination. The unresolved rotational motion and the deformation of SST patterns further distorts the correlation function, and thus, results in erroneous estimates.

To resolve the uncertainty due to the multi-peak and elongated distribution of the cross-correlation function, additional information is required. The proposed relaxation labelling approach integrates the contextual relation of the displacement field with the correlation measure. The experimental results show that the proposed relaxation approach resolves well the uncertainty, and significantly improves the reliability and robustness of the determination.

The proposed JPLSM refinement approach, integrates the patches of the entire grid as a single flexible template. The strength of the inter-patch and intra-patch constraints are controlled according to the condition of the features contained in the templates. The use of the joined flexible template resolves the deformation of the SST patterns and overcomes the over-smoothness due to the trade-off in template size selection, therefore, significantly improving the accuracy of the determination. The experimental results also show that, by controlling the strength of the constraints according to the feature condition, the integration of the contextual information and the minimisation of the effect due to the imperfection of the constraints can be well balanced. The study further discussed the inherent relation between the least squares matching method and the inversion method, and the error caused by using the large elementary unit and the necessity of the use of the iterative process with large to small elementary unit in the JPLSM approach.

The partially cloud contaminated pixel detection algorithm based on the Förstner operator, that is proposed in this thesis, detects the partial-cloudy pixels based on the strength of the gradient, consistency of gradient orientation, and the intensity difference between the candidate pixels and the average of the neighbouring pixels. The experimental results show that the algorithm can effectively detect the point-type cloudy pixels.

Table of Contents

List of Tables

List of Figures

Acknowledgments

This thesis could not have been completed without the help and support of my supervisor Professor Bruce Forster. He has given me advice on various aspects this thesis, and carefully read the thesis and made valuable comments. His suggestions and advices have been very helpful.

A very special thankyou must be extended to Professor Bruce Forster for his warm friendship and encouragement. As I have been studied for this Ph.D. as a private overseas student, and this research was not financially supported, I encountered financial difficulty and a number of other personal difficulties. He has seen me through depression when the things were not going well, and his door was always open when I need help. He gave me the opportunity to work for him as a research assistant on a number of substantial research projects in the field of urban monitoring with remotely sensed data and in the field of radar (SAR) image processing. This not only financially supported the research described in this thesis, but has also further extended the range of my knowledge and my capabilities.

Chapter 1

Introduction

1.1 General

The ocean currents are one of most basic dynamic phenomenon of oceans, and they carry an enormous amount of dynamic and thermal energy. Thus, the precise information on current field at various depths has significant importance to numerous modern ocean-related industries and applied sciences, such as, meteorology, shipping, fishing, ocean engineering, ocean pollution monitoring and ocean geology.

However, unlike the atmosphere, for which environmental observations are performed routinely by a global synoptic satellite and on-land station monitoring system, the inhospitable conditions of the oceans and the prohibitively high costs prevented the establishment of a long-term large-scale routine observations with a sufficient spatial-temporal density based on these sea-borne observational techniques. The advent of modern observation technologies since the 1970's, especially space technology, have opened up the possibility of investigating the ocean on a global scale with an integrated composite systems of satellites, buoys, moorings, drifters and ship based observations. The remote sensing of the ocean surface brought novel information on surface temperature and colour, surface topography, surface roughness, sea ice and wind stress. These information were gradually assimilated into oceanographic research and have become important components in ocean studies.

Two types of satellite remotely sensed observations are currently available for the ocean circulation estimation. The first is high resolution satellite imagery. It can image either thermal infrared sea surface temperature (SST) pattern or ocean surface colour. Sea surface temperature patterns or water colour patterns are used as tracers. Under the assumption that the SST or the water colour pattern advects passively along with the sea surface current, the displacement of homologous features of SST or colour pattern on a

sequence of images can be used to estimate the sea surface velocity field. To date, considerable research, to identify the surface movements in the boundary current zones, has been reported.

The other (perhaps the most attractive) satellite technique for large scale ocean circulation determination is the sea surface topography measurements from satellite radar altimetry. Under the geostrophic approximation, the altimetric along-satellite-subtrack sea surface height (the vertical distance between the surface to geoid) can be used to calculate the cross-track sea surface velocity component.

Besides these two satellite remote sensing techniques, radar interferometer techniques have a great potential for sea surface current determination. By determining the difference in phase of the return signal measured at two antennas separated in the azimuth direction, the component of sea surface velocity orthogonal to the direction linking the two separated antennas, can be derived. This technique is currently only available on airborne imaging radar systems. It will be adopted on the ERS satellite in the near future.

Generally, each type of observational technique has its own limitations and can only provide measurements of a part of the characteristics of oceanic currents. A complete observation system requires a number of mutually complementary observational techniques.

The research described in this thesis focuses on the strategies and methods for improving the reliability and accuracy of the sea surface velocity field estimation from consecutive Sea Surface Temperature (SST) images.

1.2 Velocity Estimation from Consecutive Satellite Images

The sea surface velocity field can be estimated from either a single thermal infrared satellite image or a time-sequence of sea surface temperature (SST) or sea surface colour images. As the research described in this thesis will concentrate on the estimation of the sea surface velocity field from consecutive images, the techniques for

estimation velocity field from a single image will only be briefly introduced in an overview in Chapter 2.

In the techniques for estimating sea surface velocity field from consecutive satellite images, the SST or sea surface colour patterns are used as the tracer. Based on the assumption that the tracer is passively advected by the flow field, the velocity field is estimated by either tracking the movements of homologous tracer features or determined from time-differential of tracer concentrations based on energy conservation equations.

The earliest efforts at sea surface velocity field estimation from remotely sensed consecutive tracer images is termed the subjective feature tracking technique, in which the displacements of corresponding features of tracer patterns from a sequence of geographically co-registered images were visually identified and measured manually. The main disadvantage of the subjective feature tracking technique is its time and labour intensity.

To be able to process large amounts of data and achieve an automated and operator independent advective velocity estimation computational procedure, many so-called objective estimation methods were promoted.

The maximum cross-correlation (MCC) technique is one of most frequently employed techniques for the sea surface velocity field estimation from consecutive images. This approach tracks the movements of the homologous SST features by searching and identifying the maximum cross-correlated features.

The inverse model method is another frequently used technique. The basis of the inverse model method is the requirement that the estimated velocity field must satisfy certain sea surface physics principles using a least squares estimation. *Kelly* [1989] formulated a scheme based on a two-dimensional non-diffusive thermal conservation equation with a bi-linear representation of surface heat fluxes and vertical entrainment.

With the minimisation of the energy, divergence and vorticity the model gave a plausible total velocity field.

1.3 Factors Affecting the Reliability and Accuracy of Estimation

To gain accurate information of sea surface velocity field from consecutive AVHRR thermal images, two aspects of investigations are required:

1. Improving the reliability and accuracy in tracing the displacement of the SST patterns in consecutive images (i.e. optimisation of the determination of displacement of SST patterns)
2. Understanding the relation between the movement of surface temperature patterns determined from the consecutive AVHRR thermal images and the movements of ocean currents (i.e. the interpretation of the determined SST pattern displacements).

The work described in this thesis focuses on the investigation of the strategies and methods to improve reliability and accuracy of the determination of the SST pattern displacements. In other words, the research described in this thesis concentrates on the first aspect mentioned above.

Technically, previous estimations are based on two relatively simple techniques — the MCC method and the inversion method, using thermal conservation equation. Due to the complexity of the advective and non-advective physical processes of ocean currents, air-sea inter-affects, and thermal gradient distribution of SST patterns, the reliability and accuracy of the estimation can be affected by a number of factors.

In the MCC method, the quality of the determination can be affected by the following factors:

- As most previous MCC techniques track the motion of SST features with the non-rotate fixed-shape template, then the displacement caused by rotation and deformation are not resolved, thus, decreasing the cross-correlation corresponding to a correct SST feature pair, and increasing the chance of a mis-match.

- Non-advective physical processes such as spatially variant heat exchange and diffusing, change the intensity gradient of the sea surface pattern, and superimpose an additional decrease in the correlation. These effects can become more serious with an increased time-separation.

- The sea surface temperature pattern field tends to be dominated by large scale features such as jets and rings. The temperature gradients within these features are usually relative weaker, sometimes even isothermal. The features are generally highly auto-correlated along isothermal directions (i.e. along the edges of the SST pattern), while, the sub-image within the large scale patterns generally have a low signal to noise ratio. The investigation described in Chapter 5 of this thesis found that the cross-correlation function of the consecutive images corresponding to such patterns is frequently multi-peaked and of longish distribution. Consequently, the longish and multi-peak distributed correlation function introduces a large uncertainty into the displacement determination when using the correlation value alone as the criterion, as is the case in the MCC method.

- The use of independent fixed-shape template in the MCC method also allows trade-off in window size selection. To gain sufficient information, large template windows are required. However, the use of the large template window causes the over-smoothness of the resultant field in the areas of strong velocity shear.

There are mainly two sources of uncertainty and error in the estimation using inversion method based on the differential form of the thermal conservation equation.

- The inversion using the differential form of the thermal conservation equation is a under-determined system. The displacement determination relies on additional constraints, the resultant field can vary when the weight of the constraints change. This introduces an uncertainty into the estimation. To gain a realistic estimation, other data sets may required as the control or reference set.

- The inversion, using the differential form thermal conservation equation, uses only long wavelength image components. In section 7.4 of Chapter 7 of this thesis, it will be demonstrated that the exclusion of high frequency image components can increase

estimation error. The study in section 7.4 also demonstrates that this problem can be solved by using iterative processing with large to small elementary subsets.

Besides the above error sources, undetected cloud is also a source of erroneous estimations.

1.4 Motivation and Strategies Used in the Research to Improve Estimation Reliability and Accuracy

The general purpose of the research described in this thesis is to investigate the strategies of improving the reliability and accuracy in the determination of the displacement of SST patterns from consecutive AVHRR thermal images.

The research firstly investigated the general form of the cross-correlation function of SST patterns, and its variation due to different pre-filtering and correlation computation methods. The investigation described in Chapter 5, found that the uncertainty due to the multi-peak and longish distribution of the correlation function is a major source of erroneous estimation, and the unresolved rotational and deformation further distorts the correlation function distribution and introduces erroneous estimates.

Therefore, the research specifically concentrated on resolving the uncertainty in the estimation due to the multi-peak and longish distribution of the cross-correlation function, and the error in the correlation function computed using a fixed-shape template due to the unresolved rotational motion and deformation.

Based on the understanding of the factors which affect the displacement determination, then a comprehensive algorithm based on the relaxation labelling technique and jointed-patch least squares matching technique was developed. The basic strategies used to improve the reliability and accuracy of pattern displacement tracing in the algorithm are:

- Integrating additional contextual information with the measure of similarity of features (e.g. cross-correlation) to resolve the uncertainty in the correlation function. This is using a relaxation labelling technique to give a reliable displacement field

results, then the estimated field using the relaxation process is further refined with a jointed-patch least squares matching (JPLSM) technique.

- Resolving rotational motion and deformation using a bi-linearly flexible template in the proposed JPLSM scheme.

Besides these, an algorithm based on the Förstner operator for the partially cloud contaminated pixels detection was also developed.

1.5 The Organisation of the Thesis

- Chapter 2, firstly, very briefly provides a background on the ocean currents. Then a overview on the current techniques for the determination of the displacement field from satellite imagery is given. Finally, a discussion on the value of the consecutive SST images in ocean currents observation is given.
- Chapter 3, reviews and compares the previous MCC technique based displacement determination schemes.
- Chapter 4, develops a partially cloud contaminated pixels detection algorithm based on the Förstner operator.
- Chapter 5, studies the cross-correlation function distribution of SST features and its variation due to different pre-filtering and correlation computation methods.
- Chapter 6, develops a displacement determination algorithm based on the relaxation labelling method to reduce the uncertainty due to the multi-peak and longish distribution of the correlation function.
- Chapter 7, proposes and tests a scheme for a resultant field refining process based on a jointed-patch least squares matching method (JPLSM), to further improve estimation accuracy by using joined bi-linearly flexible templates to resolve the deformation due to the straining motion and rotational motion. The chapter further illustrates the inherent relation between the proposed JPLSM scheme and the inverse model method, and discusses the necessity of using an iterative process with large to small elementary computational units.
- Chapter 8, offers conclusions. The main points from the thesis are summarised. Contributions are discussed with suggestions for further study.

Chapter 2

Background and Overview on Oceanic Current Observation Techniques Using Remote Sensed Imagery

2.1 Introduction

It has been known that information on ocean current is crucial for understanding of global transportation of thermal energy, marine organism and momentum. As well, the precise information on current field at various depths has become more and more important for numerous modern ocean-related industries and applied sciences, such as, shipping, fishing, ocean engineering, ocean pollution monitoring and ocean geology. The history of current observation can be traced back to Columbus who was the first to use instruments to determine the direction of the current flowing north of the Equator. Data on currents collected over decades provide a general picture of ocean circulation. However, despite the advent of modern technology, knowledge of ocean currents are based on ship navigation records and ship borne temperature and salinity measurements. Because such observations are spatially and temporally sparse, the only way one could attempt to draw a current map was to lump together observation records from all the expeditions ever made, often spanning years or even decades. Therefore, the movements of ocean waters at any given moment were virtually unknown.

With the advent of modern electronics since 1960's, the electronic transistor has greatly changed the techniques of instrument set up, maintenance, and data retrieval. Equipped with a multitude of new techniques, such as moored arrays of current meters, STD/CTD (salinity temperature depth/conductivity temperature depth) temperature salinity profiles, XBT (bathythermograph), SOFAR (sound fixing and ranging) float and other methods, the oceanographers, during 1970's, improved remarkably the knowledge on ocean circulation through a series of ocean experiment programs, such as USSR

POLYGON (1970), US-UK Mid Ocean Dynamics Experiment (MODE-I, 1971-1974), English, French and German co-operative program North East Atlantic Dynamics Study (NEADS, 1976-1979) and the joint US-USSR program POLYMODE (1975-1978). However, unlike the atmosphere, for which environmental observations are performed routinely by a global synoptic satellite and on-land station monitoring system, the inhospitable conditions of the oceans and the prohibitively high costs prevented the establishment of a long-term large-scale routine observations with a sufficient spatial-temporal density based on these sea-born observational techniques.

The advent of modern observation technologies since the 1970's, especially space technology, have opened up the possibility of investigating the ocean on a global scale with an integrated composite systems of satellites, buoys, moorings, drifters and ship based observations. The remote sensing of the ocean surface brought novel information on surface temperature and colour, surface topography, surface roughness, sea ice and wind stress. This information was gradually assimilated into oceanographic research and have become important components in ocean studies. Also, satellites and aircrafts are used to read out information from buoy networks and trace the motion of drifters.

The introduction of modern observation techniques into oceanographic research changed the experimental design and observational strategies, and has allowed a large and dense (spatially and temporally) investigation of the intricate mechanisms of oceanic phenomena. With the help of the advanced observational techniques, the nearly continuous monitoring has made possible the study of transient phenomena, such as eddies, internal waves and the temporal structure of the ocean.. However, measurements from space can observe only directly the sea surface. Therefore, sea based observations will still be needed to complete a top-to-bottom observational system, required for 3-dimensional ocean circulation estimation, as *Wunsch* [1993] has suggested. The use of satellite or aircraft drifter positioning techniques, electronic transistors and acoustic tomography techniques has remarkably changed the sea-based observation network design and data retrieving. The improvements have made sea-based observation systems more cost-effective.

Generally, each type of observational technique has its own limitations and can only provide measurements of a part of the characteristics of oceanic currents. A complete observation requires a system of mutually complementary observational techniques.

2.2 Ocean Currents Structures

The oceans exhibit structures and movement on all scales from the molecular on up to the size of the container in which they reside (i.e. the ocean basin). The wavenumber spectrum of these oceanic processes is not very well known as yet. However, through a series of oceanographic experiments during the last decades, oceanographers have gained certain useful knowledge. The following figures (Figure 2.1.a adapted from the TOPEX Working Group report [*TOPEX* 1981] and Figure 2.1.b from [*Maul et. al.* 1980]) are the summary of the frequency-wavelength of oceanic dynamic features and the distribution of circulation kinetic energy in frequency-wavelength space.

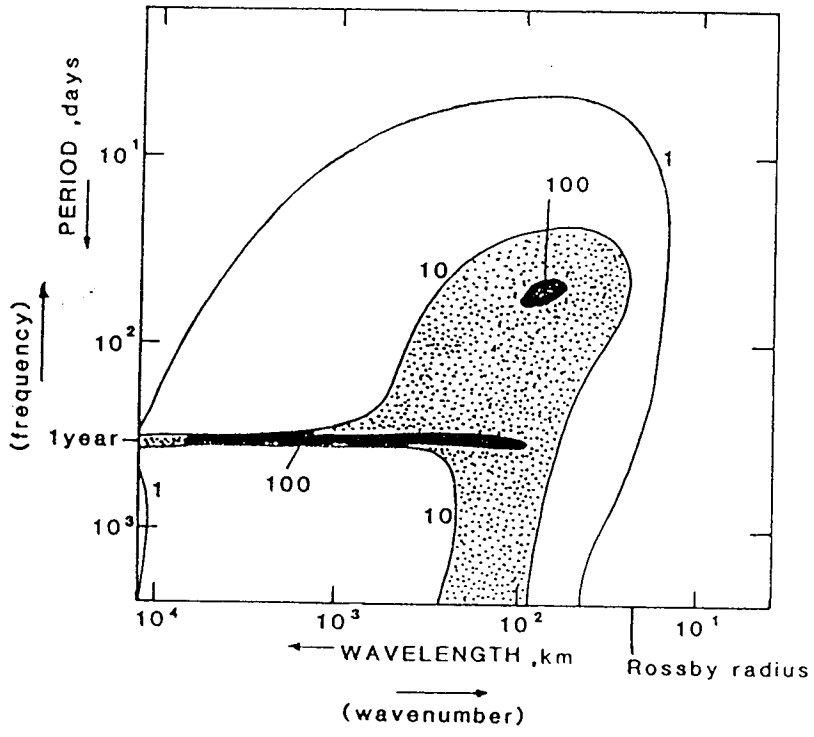

Figure. 2.1.a *Sketch of the frequency-spectrum of circulation energy at mid-latitudes, with arbitrary contour units (adapted from TOPEX* [1981])

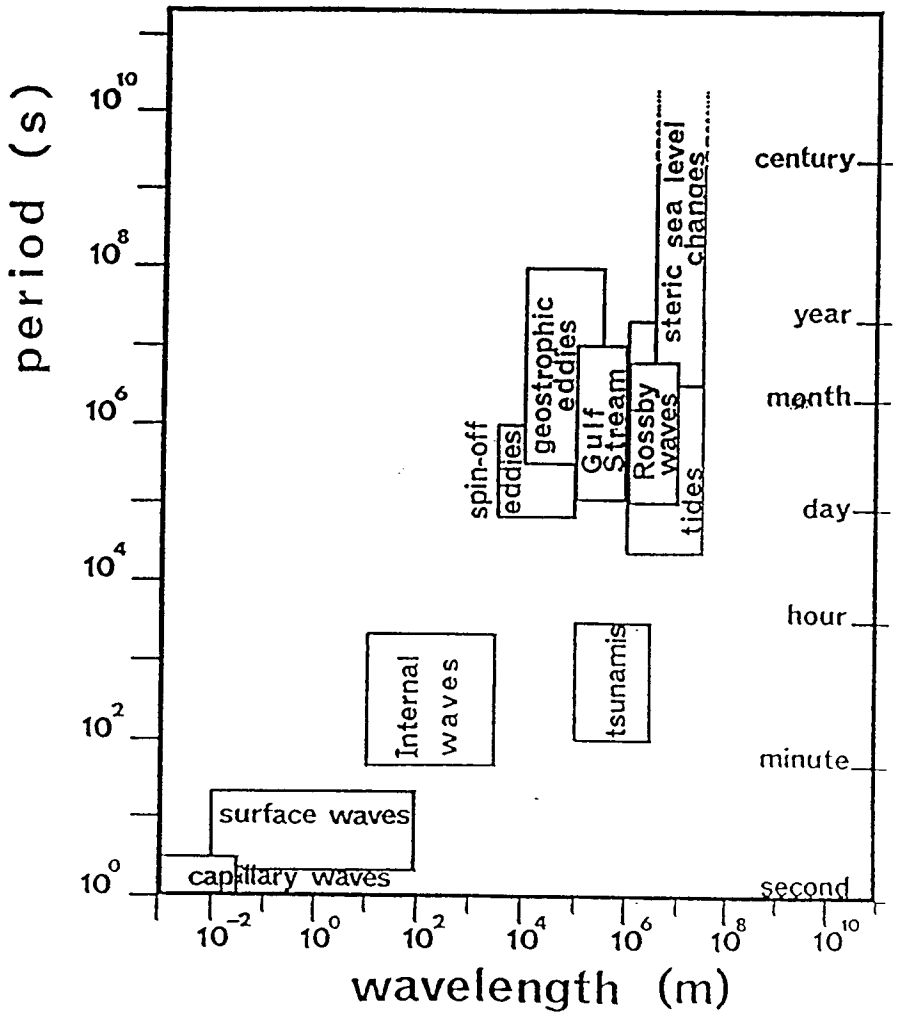

Figure. 2.1.b *Graphical summary of the frequency-wavelength regions of some important dynamic processes (adapted from Maul et al.,[1980])*

2.2.1 The Large Scale Steady Circulations and Mesoscale Oceanic Variabilities

To understand the ocean circulation and the distribution of its properties, it is convenient to split the subject into two parts — the large scale long-period mean circulation and the fluctuating part. Usually, currents on the basin-wide spatial scales, with temporal scales in the range from several years to several tens of years, are termed as large scale (or general, steady) mean ocean current, and by mesoscale variability, oceanographers refer to the phenomena on a spatial scale range 50-500 km and 1 day to 2 years on temporal scale [*Christou* 1990].

The global horizontal large scale, long period circulation system consists of a series of gyres (i.e. the closed rotational systems of current) as shown in Figure 2.2.

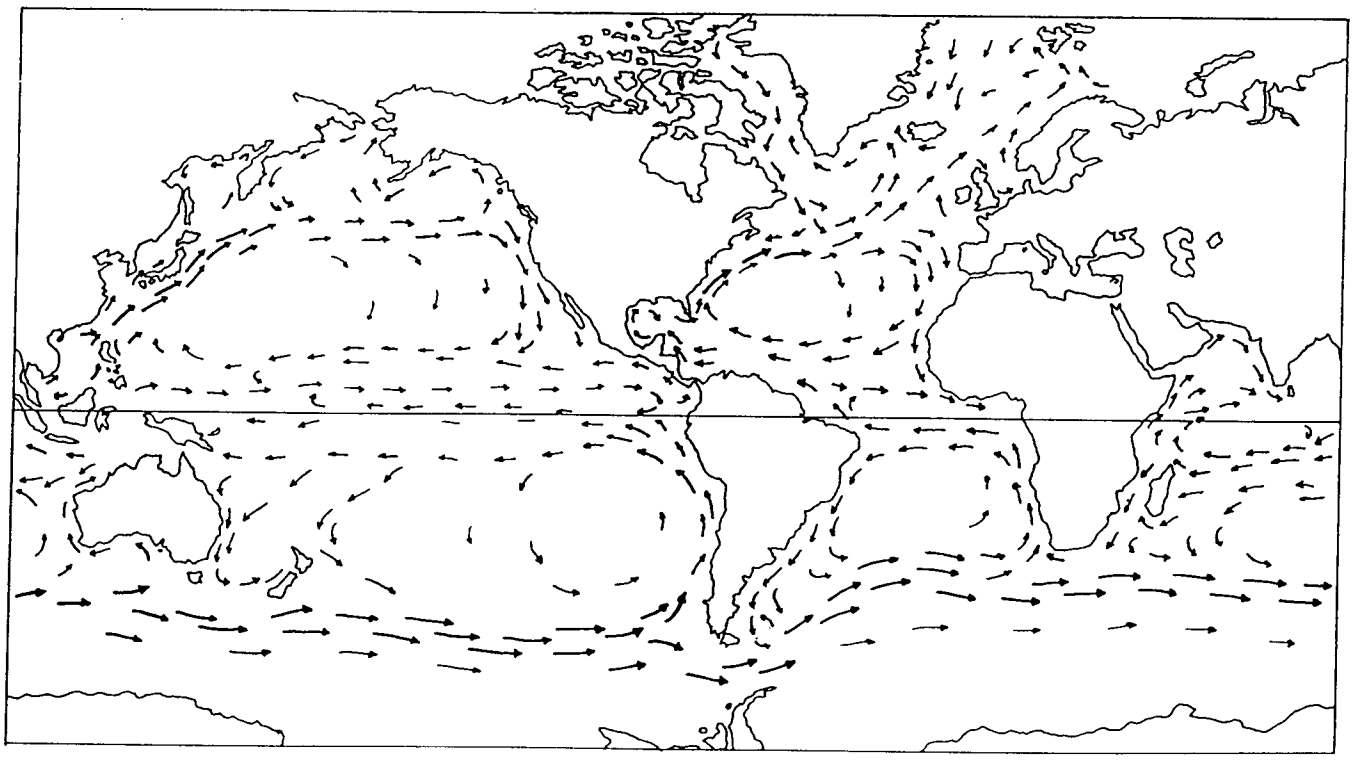

Figure 2.2 *The general circulation of the surface layer of the world ocean in July (after Robinson [1994])*

From the past few decades of oceanographic research, it is known that over great areas of the oceans there exists a variety of time-dependent mesoscale processes. These time-dependent fluctuations can have energy levels one or more orders of magnitude larger than those of the mean flow [*Holland et al* 1983], and also contribute dynamically to the large scale mean flow.

All types of variable flow are commonly referred to, by physical oceanographers, by the generic term eddies. In an analogy to atmospheric sciences, the general ocean circulation can be thought of as the climate of the oceans, while the eddy variability can be thought of as the internal weather of the oceans. The generic term eddies encompassed a large class of space and time variations. The spatial scales of variability can range from tens to hundreds and thousands of kilometres. Time scales can range

from weeks to months and years. The large scale ocean current variations are usually considered to be in approximate geostrophic balance [*Robinson*, 1983]. The phrase mesoscale eddies has been coined simply to indicate motions of less than the oceanic gyre scale with a typical mid-ocean spatial scale of 100 km, and with a life-time of the order of several months. these mid-ocean mesoscale eddies have swirl speeds of the order of 10 cm/s, which are frequently considerably greater than the long-term average flow [*Robinson*, 1983].

Figure 2.1.a shows the following:

- The high kinetic energy of variability at a period of one year, over a broad range of length scales, indicates the importance of annual fluctuations of the general circulation.
- The variabilities at length scales between 50 km and 500 km carries a large amount of energy, especially, the variabilities of a spatial scale 100 km and temporal scale about 100 days. The variability within this spatial/temporal range corresponds to the mesoscale eddy field.
- Little energy is found at length scales of less than around 50 km.

2.2.2 The Cause of Oceanic Circulation

The energy that drives the currents of the world's oceans is derived almost exclusively from the sun. Solar energy generates temperature differences at the Earth's surface and in the atmosphere that give rise to winds. The winds in turn are the major cause of the movements of surface waters in the oceans. In addition, the unequal heating of the ocean by solar energy further contributes to the movement of water masses as current.

The ocean circulations may be divided into two parts according to the type of primary driving-maintaining force — wind drive current and thermohaline. Water movement at the surface of the ocean is initiated by wind blowing across the water. The wind drags the water surface along through friction. As the water surface film is set in motion, it drags on the water layer beneath. The layer beneath then imparts motion to the water at lower levels until the entire surface zone (i.e. surface to thermocline about, 300-1000 m

thick) is in motion. Since the transfer of momentum from wind to the underlying water layer is not efficient, the kinetic energy from wind stress is lost with depth. Therefore, wind stress is the major force driving surface currents. The second major currents-generating force results from the effects of temperature and salinity difference in the oceans and it is called a thermohaline. Thermohaline effects are caused by the differences in sea water density that results from the differences in sea water temperature and salinity. The less dense water will be displaced laterally and upwards. Thermohaline effects are the main cause of deep water mass movement.

2.3 The Estimation of Sea Surface Velocity From Consecutive Sea Surface Temperature Images

2.3.1 The Categorisation of Velocity Estimation from Satellite Imagery

The sea surface velocity field can be estimated from either a single satellite image or a time-sequence of images of a tracer field.

There are two types of techniques for estimating velocity field from a single image:

- Qualitative flow trajectories analysis, in which the tracer patterns emanating from obvious source regions are qualitatively assessed from a single image acquisition. Flow directions (but not magnitudes) are mapped, often to observe seasonal current fluctuations from multiseasonal image sequences (see for example *Carlson* [1974], *Caraux & Austin* [1984], and *Mulhearn* [1987]).

- Inversion from a single sea surface temperature image, in which the sea surface geostrophic velocity field is estimated from a sea surface temperature gradient map which can be derived from a single AVHRR thermal infrared image. The techniques differ from the estimation techniques using consecutive tracer images. This type of single-image estimation is based on the geostrophic balance between the Coriolis force and the pressure gradient, caused by the gradient in the density field. Here, the surface temperature field is used as an argument of the density field rather than the

tracer field as is the case of consecutive images (see for example *Kelly* [1983] and *Essen* [1995]).

With qualitative flow trajectories analysis, oceanographers have revealed a large number of phenomena from remotely sensed images, especially the sea surface temperature patterns in frontal regions, *Mulhearn* [1987], for example, analysed the Tasman front with a sequence of infrared (sea surface temperature) images. However, this technique is difficult to computerise (automate), due to the complex knowledge involved in oceanographic interpretation of images, and, moreover, it can only yield the direction of the sea surface velocity vectors.

Kelly [1983] formulated an inversion method to determine the along-isothermal component of sea surface velocity from a single sea surface temperature image based on the thermal wind equation. This model empirically related the magnitude of the along-velocity component to the magnitude of temperature gradient using in situ velocity measurements.

The techniques for estimating sea surface velocity field from consecutive satellite images are the focus of this research, and they can be further categorised into two general approaches, they are —

- feature tracking, the Lagrangian measurements of tracer field displacements, which can be further categorised into two type of techniques – subjective feature tracking and correlation method. The feature tracking techniques estimate current by measuring the displacements of sea surface traceable features or patterns which passively move along with the current. This group of approaches consist essentially of matching the corresponding shifted (advected) tracer patterns between a pair of sequential images by searching and identifying the correspondent features.
- inverse model, the Eulerian measurements using a complete tracer field, which estimates the velocity field by least squares and requiring the estimated velocity to satisfy certain physical equations. The most basic of these being the energy conservation equation, which is based on the measurements of the time-differential and spatial-gradient of the tracer field.

The most basic assumption of both feature tracking and the inverse model is that ***the tracer is passively advected by the flow field***, so that the displacements of the tracer patterns (for feature tracking method) or the temporal variation in tracer concentration of each small spatially fixed unit (for inverse model method), reflect the movement of the current.

The remotely sensed tracers for sea surface velocity estimation are discussed by *Stow* [1988]. They are fluorescent dye, chlorophyll pigments, suspended sediments, surface temperature patterns and salinity distribution patterns. Among these, the sea surface temperature (SST) pattern sensed by NOAA/AVHRR thermal infrared band (11-12μm) is most widely employed. Besides the SST, the sea surface colour difference, caused mostly by phytoplankton pigment in the upper 5-15 m of the ocean has also been used. For example, images from the NIMBUS Coastal Zone Colour Scanner Channel 3 (540-560 nm) were used for surface current estimation by *Garsia and Robinson* [1989].

2.3.2 Early Attempts at Sea Surface Velocity Estimation from Satellite Images

The earliest efforts at sea surface velocity field estimation from remotely sensed consecutive tracer images was termed the subjective feature tracking technique, in which the displacements of correspondent features of tracer patterns from a sequence of geographically co-registered images were visually identified and measured manually.

Besides the basic assumption, i.e. that the tracers are passively advected by flow field, the subjective approach further requires that the tracer gradient among water parcels, and thus, the shape of sea surface tracer (e.g. temperature) patterns are not seriously distorted within a short period, so that the correspondence of advected features on time lapsed images can be identified and coupled. The estimations of the velocity field are inferred by tracking the motion of distinct features of sea surface temperature patterns on a pair of time lapsed images. The corresponding surface temperature features, on a pair of time lapsed images, were visually identified and the displacement of the features from one image to the next were determined by repeatedly displaying each of the images to subjectively estimate the movement of sea surface temperature patterns.

Using this technique *La Violette* [1984] estimated velocities around the Alboran Sea gyre. *Vastano et al.* [1984] tracked submesoscale features of the Oyashio front from a pair of 24 hours lapsed infrared images from the North Pacific. *Koblinsky, et al.* [1984] studied an offshore eddy in the California Current system, *Cracknell et al.*[1987] studied surface currents off the coast of Ireland, while, *Sheres et al.*[1990] also studied the eddy, coastal jet and incoming swell near Pt Conception, California using this technique. The estimated speeds were reported to be in good agreement with sea surface measurements. *Svejkovsky* [1988], using only the most identifiable features, determined that subjective estimates of surface velocities differ from the velocities of surface drifters with an *rms* difference of 0.06 m/s. This technique was expanded on by *Vastano et al.* [1985] who used the resulting velocity vectors to derive a two dimensional stream function expression for the advective surface velocity field. Invoking geostrophy, they further inferred a sea surface topography to match the stream function derived from satellite image estimated velocity vectors. The resultant "dynamic topography" provides a high spatial resolution synoptic sea surface elevation estimation which can possibly be compared with surface topography measured using satellite altimetry. This research showed the potential for simultaneously using satellite imagery data and altimeter data in sea surface current or topography estimation through data-model assimilation. However, the velocity vector estimation, the basis of this scheme, was still based on the manual subjective feature tracking technique.

The disadvantage of the subjective feature tracking technique is its time and labour intensity. This technique is completely subjective in the selection of surface temperature features. So, the reliability of the results is subject to the operator's ability to locate the same features in each of the sequential images, and their oceanographic knowledge, which may be involved in the interpretation of the correspondence among advected and distorted features. However, the involvement of human knowledge can avoid significant unreasonable estimates which is the main advantage over the so-called objective estimation methods (e.g. Maximum Cross Correlation (MCC), and the inverse model method, which will be discussed further through out the remainder of the thesis). Visual inspection of the images results in an overall impression of the pattern of changes in the image pairs, forcing the search to be restricted to only "reasonable" areas and reduces

the chance of grossly incorrect displacements. Rotation in features can also be followed more easily by eye [*Tokmakian et. al.* 1990], and it is unlikely that these human capabilities can be fully simulated by computers in the near future.

2.3.3 The Maximum Cross Correlation Method

To be able to process large amounts of data and eliminate the inherent human bias (which is the one of the primary purposes of objective estimation), many methods were promoted to achieve an automated and operator independent advective velocity estimation computational procedure. The conventional objective estimation schemes for mapping sea surface velocity fields from consecutive satellite remote sensed thermal infrared images, can generally be categorised into two main approaches, objective feature tracking techniques and inverse models based on the thermal conservation equation.

The most widely used algorithm for velocity estimation, based on feature tracking, is the Maximum Cross-correlation Coefficient (MCC) technique. The MCC technique was originally developed for cloud motion tracking from sequential visible images of the Applications Technology Satellite ATS-1 by *Leese et. al.* [1971], and was first adopted by *Emery et al* [1986] to estimate sea surface advective velocities of currents of the British Colombia coastal ocean, from a sequence of Advanced Very High Resolution Radiometer (AVHRR) thermal infrared images.

The basic assumption of the technique is that the shape of current-advected tracer patterns (e.g. temperature patterns) are not seriously deformed within a certain short temporal interval, so that a pair of similar patterns in the image pair can be considered as two shifted versions of an identical pattern. This group of approaches consist essentially of searching and identifying the maximum cross-correlated features. Two consecutive satellite images are co-registered to the same coordinate system. The first image is divided into contiguous small windows termed template windows. Each template is moved pixel by pixel through the "search window" in the second image and compared each other, and the similarity between the feature in template window and the features in search window are measured with correlation coefficients. Then, the region

of the maximum correlation is selected as the shifted feature. Therefore, the displacements is determined with the spatial lag between the centre of template in first image and the centre of the corresponding best matching sub-image in second image.

2.3.4 The Inverse Model Method

The basis of the inverse model method is the requirement that the estimated velocity field must satisfy certain sea surface physics principles using a least squares estimation. The dynamic model involved in the computation can vary from case to case dependent on the type of data employed in the estimation. Several inversion methods to infer velocity field have been used for oceanography studies with hydrographic data (e.g. *Wunsch* [1978]), altimeter data (e.g. *Gaspar & Wunsch* [1989] and *Mesias & Strub* [1995]) and AVHRR thermal infrared images (e.g. *Kelly* [1983], [1989] and *Kelly & Strub* [1993]). In the current research, the focus will be on the method of inferring velocity field from consecutive AVHRR thermal infrared images. *Kelly* [1989] formulated a scheme based on a two-dimensional non-diffusive thermal conservation equation with a bi-linear representation of surface heat fluxes and vertical entrainment. With the minimisation of the energy, divergence and vorticity the model gave a plausible total velocity field. The basis of this method is the temperature conservation equation, which was simplified in this application as (e.g. *Kelly* [1989]) —

$$-\frac{\partial T}{\partial t} = u\frac{\partial T}{\partial x} + v\frac{\partial T}{\partial y} + S.$$

where T is the sea surface temperature, t stands for time, u and v are the components of sea surface velocity vector in x direction and y direction respectively, S is a term containing the temperature variation due to the non-advective physical processes.

The equation describes the basic physical processes which cause the change in thermal energy content for a spatially fixed small unit on the sea surface. The left hand side of the equation is temperature change with respect to time, and the first and second terms, on the right hand side of the equation, are the advection of thermal gradient, i.e. the temperature change of the small unit caused by advection, while the third term models the entrainment of water from below and the affects of surface air-sea heat fluxes. In this approach, the thermal energy variation caused by horizontal and vertical diffusion

was considered to be negligible, and the heat exchange due to the entrainment of water from below and air-sea heat flux were considered to be of a much larger spatial scale than that caused by advection.

The study area is divided into a grid of units and the velocity of each unit is required to satisfy the simplified temperature conservation equation. However, with thermal conservation equations alone, the total velocity field cannot be estimated. The equation for each unit has two unknowns, two components of velocity vector in both the x and y directions (or the magnitude and orientation of vector). It is an under-determined system. The along-isothermal component (i.e. the component parallel to the local temperature gradient) is in null space. Therefore, the system does not have a unique solution if no additional constraints are applied. Additionally, the solution of regions where the temperature gradient is small may be extremely sensitive to the noise of the temporal-differential term $\frac{\partial T}{\partial t}$ and the error in the term S, the heat exchange due to non-advective physical processes. To solve this under-determined problem and to achieve a plausible total velocity field, additional constraints such as the minimisation of horizontal divergence and the minimisation of kinetic energy used in *Kelly*'s [1989] model, or in *Kelly & Strub*'s [1993] model, are needed. Although this under-determined system can be solved by incorporating additional constraints, the use of different constraints or varying the relative size of the weighting factors among the constraints, may lead to different solutions. Thus, it may be necessary to refer to other velocity data and to adjust the relative size of the weighting factors among the constraints to get a 'realistic' estimation of the velocity field. However, the inversion method has the advantage that, as a least squares tool, it can be employed flexibly to determine the velocity field with different types of measurements, and to assimilate different types of measurements within multiple physical constraints.

2.3.5. Factors Affecting the Displacement Determination, Interpretation

As was mentioned in section 1.3, due to the complexity of the ocean currents, further investigations are required in both optimisation of the determination of displacement of SST patterns, and the interpretation of the determined displacements.

The factors which affect the reliability and accuracy of the determination of the displacements of the SST patterns have been discussed in section 1.3. For the MCC method, they are briefly as follows:

- The unresolved rotation, straining, and non-advective physical processes.
- The uncertainty in the determination of displacement due to the multi-peak and elongated distribution of the correlation function. This form of distribution will be discussed in Chapter 5.
- The trade-off in the selection of template window size.

For the inverse model method, these are mainly two sources of uncertainty and error:

- The under-determination of the thermal conservation equation system
- The exclusion of high frequency image components, when using the differential form of the thermal conservation equation.

The undetected cloud contamination can further degrade the determination. The temporal separation of the image sequence is also crucial, due to the accumulation of the unresolved advective and the non-advective physical processes.

The problems related to the second aspect (i.e. the interpretation of the relation between the determined SST feature displacement field and the surface current) are:

Most research has found that the displacement field estimated from consecutive AVHRR and ocean colour images agree well with in situ data (e.g. see examples mentioned in section 2.3.2). However, disagreements between AVHRR estimates and other data were found in some studies. For example :

Kelly et al. [1992] found that the estimations of velocity field from AVHRR images qualitatively agree with the in situ data and altimetry profile. The AVHRR estimates have comparable directional accuracy to other observation techniques, however, the estimates systematically underestimate the magnitude. They suggested that the

underestimation of the velocity, particularly in the jets (i.e. narrow current with high speed), is inherent in the assumptions used to derive the velocity from the AVHRR data, rather than a limitation of a particular method. They believe that the small scale SST features near the jet move more slowly than a water parcel. The understanding of the physical processes which cause the underestimation may require further study based on large number of AVHRR images and in situ data. However, in some cases, this underestimation may be estimated statistically by comparison with other data. The results from *Kelly et al.* [1992] have illustrated this possibility. Once good estimates of the underestimation are achieved then this problem may be solved.

Besides the underestimation in magnitude, because the AVHRR thermal infrared bands only measure the sea surface temperature in the upper 15μm of the ocean, *Mulharn* [1987] found that the sea surface temperature patterns cannot always distinguish the northern edge of a ring (as in the Tasman front region) and he suggested that "when it is close to the front, since a ring may only pinch off beneath the surface. A ring close to the front often interacts with it, forming a meander at some times and at other times pinching off".

These two examples illustrate the limitations in the estimation using consecutive AVHRR images. However, on the other hand, the difference between the movements of SST patterns measured using AVHRR images and under-surface currents measured by in situ data, may reveal the difference between the surface and the deeper layer of the ocean currents, and it may improve our knowledge of the physical processes of ocean currents. Therefore, this should not be regarded as a disadvantage of the AVHRR data.

The better understanding of these differences (ie. the difference between the movements of SST features and the water parcel in *Kelly et al.* study [1992], and the different forms of a ring in *Mulharn's* study [1987]) is also subject to the improvement in the reliability and accuracy of the SST feature displacement determination.

The work described in this thesis focuses on the investigation of the strategies to improve reliability and accuracy of the determination of the SST pattern displacements.

The reasons for why the current techniques need to be improved will be discussed in Chapter 5.

To improve the reliability and accuracy of displacement determination, a two step multiple-information global matching algorithm is proposed. It is based on the relaxation labelling method and the jointed-patch least squares matching method. In the proposed algorithm, a reliable estimation of the displacement field is firstly yielded using a relaxation labelling technique by integrating the correlation information and the contextual information of the velocity field. Then the estimated field is further refined using a jointed-patch least squares matching technique. The algorithm is proposed to optimally integrate related information, where, spatial consistency and compatibility among the neighbouring grid points under certain constraints, are introduced into the estimation, and to maximise the resolution of the displacement due to rotational motion and the deformation of SST patterns in consecutive images.

As *Tokmakian et al* [1990] have commented, the objective methods do not use the benefits of human sight. Basically, the objective methods eliminate the use of visual estimation from the over-all SST pattern movement. Even the most advanced, current computer pattern recognition techniques cannot simulate human vision sight. However, the optimum use of available information and knowledge will certainly improve the reliability of estimation. Details of the algorithm developed as part of this research and the results, will be provided in Chapters 6 and 7 respectively.

2.4 The Value of the Displacement Field Determined from AVHRR Images

Like any other observation technique, the capacity to determine sea surface velocity from consecutive satellite images is limited by a number of factors that are inherent in the data.

The first limitation in the determination of ocean velocity field is that both the feature tracking methods and inversion methods, combined with a thermal conservation equation, are limited in application to the regions of relative strong SST gradients or strong phytoplankton concentration gradients, when using AVHRR thermal infrared

images or ocean colour images, respectively. Fortunately, most dynamic regions, such as the Gulf Stream, Kuroshio and East Australia current, are associated with strong sea surface temperature gradients, and along coastal regions, rich ocean colour patterns, caused by phytoplankton pigments, can usually be found .

The second limitation is that the electromagnetic radiation measured by the optical sensors barely penetrates the sea surface. Apart from the visible blue wavelength, which may penetrate up to 30 m depth, the satellites observe only the surface skin of the ocean. In particularly, the AVHRR thermal infrared bands (11-12μm) only measure the sea surface temperature in the upper 15μm of the ocean. Compared with AVHRR thermal infrared images, the ocean colour images from the NIMBUS Coastal Zone Colour Scanner Channel 3 (540-560 nm) which measures the sea surface colour difference caused mostly by phytoplankton pigment have the advantage of representing the upper 5-15 m of the ocean (e.g. *Tokmakian et. al.* 1990).

The third limitation is that visible and thermal infrared electromagnetic radiation cannot penetrate clouds. Therefore, the continuous observation of surface circulations with techniques based on these images are further limited by the cloud cover conditions of the study area. This problem is particularly serious in tropical and polar regions. For the Tasman front region 30^0 S - 38^0 S and 150^0 E - 158^0 E, 3 months statistics of the cloud maps from newspapers shows that approximately 3.8 days per month are relatively cloud free, which agree with the statistics shown in *Mulhearn* [1987]. Considering that a large amount of variability is found at temporal scales over 100 days (see Figure 2.1a), the images at this coverage frequency are still valuable tools for tracking most of the variation.

Besides these three limitations, the image-derived displacement field represents a combination of both the geostrophic mean and shorter-term wind-driven surface current [*Cracknell et al.* 1987]. Therefore, we should be aware that the displacements determined from consecutive AVHRR images may also include the drifting of sea surface features.

Although, the application of the visible and thermal infrared band images in ocean circulation observation is limited by the intensity gradients of features, cloud coverage, and the thin penetration, they can provide an intuitive, high resolution, synoptic view of horizontal structures of currents. This is the unique advantage of sea surface colour and SST images over other observations.

The positive aspect of the limited penetration of AVHRR data should also be noted, as has been discussed in section 2.3.5.. In some situations, the current may have a different form on the surface from that at a deeper layer as reported by *Mulharn* [1987]. Due to the thin penetration, the different formats of the current on the surface and at deeper levels can be revealed by comparing the displacement determined from AVHRR images with the ship borne data measured at deeper layers. In this sense, the limited penetration has its value in such studies.

Therefore, the question is not whether the SST image is useful for velocity field estimation but how to use them appropriately.

2.5 Summary

Currently, there are two types of observational data available for sea surface current determination from space-borne remote sensing systems and one available from airborne system. They are respectively

- satellite altimetry sea surface topography which can provide measurements of sea surface height gradients and geostrophic currents.
- consecutive SST or sea surface colour images, where the velocity field structure can be determined from either the displacements of SST/colour patterns (the feature tracking method) or the variation in energy concentration of a spatially fixed unit based on the energy conservation equation (the inversion method)
- radar interferometry images which can provide radial velocity components of sea surface currents

The velocity field derived from AVHRR images or sea surface colour images can provide a high resolution, synoptic view of the structure of surface currents. Previous research has shown that oceanic dynamic variabilities of the scale of 50-500 km, especially the variability at a scale of 100 km and frequency of about 100 days, carries a large amount of energy. Therefore, the AVHRR/ ocean-colour images are very valuable data for the observation of fine structures of these variabilities.

Due to the limited penetration of the electromagnetic radiation measured by AVHRR thermal infrared bands, the displacement field determined from SST images has also value in revealing the different form of currents on the surface and at depth, by comparing it against other data measured at different depths.

Chapter 3

The Basis of Maximum Cross Correlation Method and Previous Research

3.1 The Basis of the MCC Method

This group of approaches consists essentially of searching and identifying the maximum-cross correlated subareas on a consecutive image pair. Two consecutive satellite images are corregistered to a co-ordinate system. The first image is divided into contiguous or partially overlapping small windows termed template windows. Each template is moved pixel by pixel around a much large "search window" in the second image. The centre of the search windows coincide with those of corresponding template windows at initial position. The cross-correlation coefficients between the template window and each subarea of the search window covered by the template are then calculated with the following equation (see *Wahl et al.*, 1990, for example)—

$$\rho_{sp}(\eta,\xi) = \frac{\sum_{i=1}^{n}\sum_{j=1}^{m}[p(i,j)-E_p][s(i+\eta,j+\xi)-E_s(\eta,\xi)]}{M_s M_p} \qquad (3.1)$$

Where, (i,j) and $(i+\eta,j+\xi)$ are the co-ordinates relative to the centre of each search window (also the centre of the template window), $P(i,j)$ and $s(i+\eta,j+\xi)$ are the intensity function of the template and the subarea with spatial lag (η,ξ), $Es(\eta,\xi)$ is the mean of grey-level value of the subarea, and Ep is the mean of grey-level values of the template window, n and m stand for the number of rows and columns of the template (also the subarea) respectively, M_S and M_P are the standard deviations of the subarea and the template window respectively. They are given by

$$M_s = \sqrt{\sum_{i=1}^{n}\sum_{j=1}^{m}[s(i+\eta,j+\xi)-E_s(\eta,\xi)]^2}$$

and

$$M_p = \sqrt{\sum_{i=1}^{n}\sum_{j=1}^{m}[p(i,j)-E_p]^2}$$

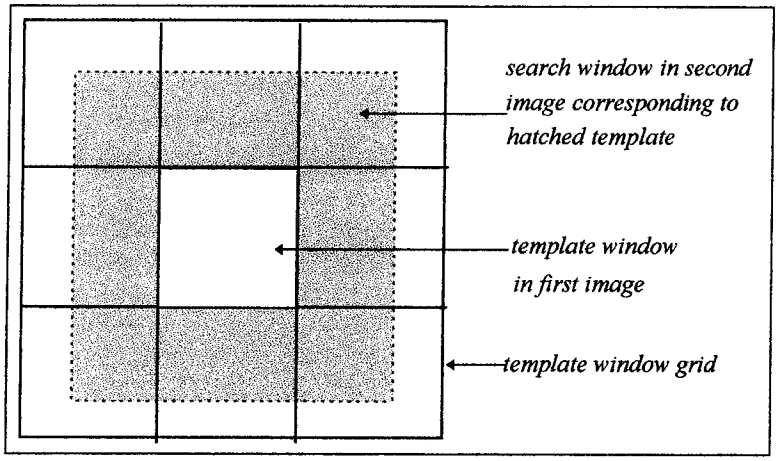

(a)

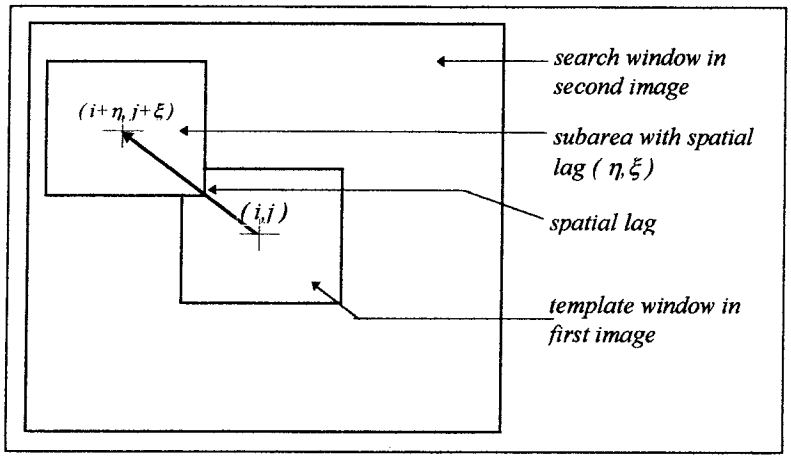

(b)

Figure 3-1 *(a) The overlap between template window (first image) and search window (second image), (b) The relation among template window, search window and the spatial lag between template window and sub-search-window.*

By this definition, the cross-correlation coefficient, ρ , $-1 \leq \rho \geq 1$ is a function of spatial lag (η, ξ),. If the signal in the subarea is an exact spatially lagged version of the signal in the template window, the correlation coefficient at this spatial lag will be the maximum value 1, and the coefficient will drop as the signals become more dissimilar. Hence, the cross-correlation coefficient is a measure of the similarity of two signals at a given lag. By moving the template window pixel by pixel throughout the search window and

calculating the cross-correlation coefficient at each position (η, ξ), the MCC method assumes the subarea of the maximum cross-correlation coefficient to be the shifted version of the feature contained in the template window. The average velocities of each template window are then calculated from the spatial lag between the centre of the template and the centre of the corresponding best correlated subarea and the time separation between the images, as follows —

$$v = \frac{\sqrt{(\eta_{max} \cdot \Delta x)^2 + (\xi_{max} \cdot \Delta y)^2}}{\Delta t} \tag{3.2}$$

where η_{max} and ξ_{max} are the spatial lag of maximum correlation, Δx and Δy are the pixel size in the row and column direction respectively, and Δt is the time interval between consecutive images. The direction of motion θ is given by

$$\theta = \arctan\left(\frac{\xi_{max} \cdot \Delta y}{\eta_{max} \cdot \Delta x}\right) \tag{3.3}$$

In most previous research, a square template was generally used. The choice of the size of the template window and the search magnitude of search radius will be discussed in section 3.3

Due to possible strong rotational motion and straining of current systems, the homologous features on sequential images are generally more or less deformed, which will consequently decrease the ability to determine the correlation between consecutive images. To eliminate erroneous determinations of correlated images, the estimated vectors are examined by a threshold of the correlation value, and optionally, also examined by an additional consistency threshold (i.e. spatial next-neighbour filtering).

To improve the correlation accuracy, in some MCC schemes (for example, *Tokmakian et al.* [1990], and *Kelly et al.* [1992]), a high-pass filter was applied to SST images before the cross correlation computation (see *Emery et al.* [1986] for example), or the SST gradient images were used in the correlation computation. These applications are discussed in following sections.

3.2 The Use of Feature Enhancing Pre-processing

Previous research has shown that the success of feature enhancement pre-processing may vary from case to case. *Emery et al.* [1986] successfully determined sea surface velocity field using MCC method from a sequence of temperature gradient images computed from AVHRR thermal images. The temperature gradients, $|T(x,y)|$ were computed using a unweighted central difference, the magnitude of which is given by :

$$|T(x,y)| = 1/(2\Delta h)\{[T(x-\Delta h,y)-T(x+\Delta h,y)]^2+[T(x,y-\Delta h)-T(x,y+\Delta h)]\}^{\frac{1}{2}} \quad (3.4)$$

where x and y are the coordinates of the pixel, T is the temperature of the pixel Δh is the distance between two pixels.

Garcia & Robinson [1989] estimated velocities directly from visible Coastal Zone Colour Scanner (CZCS) images without preprocessing. *Wu et al.* [1992] found that the gradient images were distinctly noisy, and did not produce more coherent velocity fields than those computed directly from SST images. *Emery et al.* [1992] found that, for the series of images of the Gulf Stream, the use of gradients did not yield meaningful results. The reason is probably due to the weaker SST gradient of the eastern Pacific compared with those found in satellite images from the western Atlantic used by *Emery et al.* [1986]. *Tokmakian et al.* [1990] compared MCC velocity estimation from raw SST images, the images pre-processed with a 23×23 running average high pass filter, and the SST gradient images. Their test showed that the estimations from raw SST images were of lower difference (between estimated velocity and a control data set), and gave the highest maximum cross-correlation value compared with the other two types of images. Use of high-pass filtered images produces similar difference (between the estimates and control vector set) to those determined from raw SST images, except all cross-correlations were lower in value, while the use of SST gradients resulted in not only lower maximum cross-correlation values but an increased difference as well.

It is worth noting that all of the above estimations and tests were based upon the MCC computed with non-rotational and fixed-shape templates. *Kamachi* [1989] developed and tested a MCC method with rotational registration (computed cross correlation with rotational fixed-shape template). In his study, the comparison of the resultant velocity

field from raw tracer images and their gradient images showed that the use of the gradient filter improved estimation significantly (in the case of computing cross correlation with rotational registration).

These previous works show that the benefit of using feature enhancing pre-processing may vary from case to case, apparently depending on the strength of the gradient and spatial spectrum of SST signal. It seems also to be related to the cross-correlation computation method. In other words, it depends on whether the unresolved rotational motion and deformation is large enough to distort the distribution of correlation value computed using a simple non-rotate and fixed-shape template.

3.3 The Template Window Size and Search Radius

The principal criterion in the determination of template windows size is that the windows should be large enough to contain sufficient information, but small enough to resolve the important mesoscale motion structure, such as the jets. The optimal size may vary from case to case, according to the spatial scale of SST features and the enhancement pre-processing. Therefore, the size of the template used in previous research was found to be quite diverse. *Emery et al.* [1986], for example, applied a 22×22 pixel template window directly to the satellite infrared temperature (the raw SST) images, but the weak cross correlation maxima yielded incoherent velocity patterns. When a template of the same size was applied to the SST gradient images, the MCC method resulted in a generally spatially coherent vector field. *Garcia & Robinson* [1989] applied a 20×20 pixels template on a series of CZCS images. The choice of the size of the template in their study was guided by an examination of the histogram of maximum cross correlation. The 25×25 pixels templates were applied on SST images pre-processed with a cosine high pass filter with wavelength of 30 km (equivalent to about 28 pixels for AVHRR images) in *Kelly & Strub*'s study [1992], while *Wu et al.* [1992] and *Tokmakian et al.* [1990] applied larger templates on raw and high-pass filtered SST images. They were 32×32 pixels and 50km×50km (1.1 km per pixel for AVHRR images, and it is equivalent to about 45×45 pixels) respectively. The tests of *Tokmakian et al.* [1990] showed that smaller 25 km×25 km (about 22×22 pixels) templates produce unacceptably

high difference between estimated velocities and field data and thus 50km×50km templates were used. *Emery et al* [1992] found that increasing template size partially addresses the problem of the weak variability in the central thermal structure of mesoscale eddies associated with the Gulf Stream. Results showed a much more coherent velocity field of a cold-core ring with 30×30 pixels templates compared with those with a 15×15 pixels template. *Kamachi* [1989] concluded that the optimal template window size for the MCC method with rotational registration is approximately the eddy diameter between the maximum velocity points.

These previous works show that the choice of template size is determined on a case-by-case issue. It basically depends on the spatial scale of the patterns being dealt with. Generally, the larger template contains more oceanographic information and so has a better chance of containing distinctive features. Consequently, it yields a relatively reliable estimation. However, the estimated velocity is derived from the window averaged spatial lag between the template positions in the first image and the targeted sub-image in the second image. While the sea surface velocity field may contain some important small or narrow structures, such as jets, they may only be 20-40 km in width. An increase in template size may sacrifice structural accuracy. Furthermore, for the non-rotational fixed-shape template, increasing the size may also decrease the cross-correlation value due to the unresolved rotational and straining motions and consequently increase the chance of mis-estimation. Ideally, increasing the template size should not change the cross-correlation between a signal and its purely shifted version. Therefore, the choice of the template size is seen to be a trade-off between containing sufficient traceable SST features and resolving smaller motion structure. The advantage in this regard of a least squares matching technique, with joined flexible templates, will be illustrated in Chapter 7.

The selection of a search radius is determined by the possible maximum velocity of the study region, time interval of the consecutive images and the template window size. It can be approximately determined as

$$L_S = 2\, v_{max}\, \Delta T + L_t \tag{3.5}$$

where L_S denotes the length of the search window of each direction, v_{max} stands for the possible maximum velocity in interest area, ΔT is the time interval of the consecutive images, and L_t is the length of the template window. *Tokmakian et al.* [1990] found that the large search radius may also increase the chance appearence of multi-correlation-peaks which may lead to mis-interpretation. They suggested solving this problem with more intelligent search strategies.

3.4 The Previous Studies on Rotational Effect

Kamachi [1989] examined the limitations of the MCC method for flow fields with rotational motion. He tested both the cases in which eddy size was much smaller than the radial displacement and also when the eddy size was larger than the radial displacement.

For the case in which the eddy size is much smaller than the radial displacement, the MCC algorithm with non-rotate and fixed-shape templates treats such eddy (usually the eddy is smaller then the template) as a particle in the large scale oceanic flow field. *Kamachi* examined the effects of the rigid-body rotation, straining motion and diffusing on the cross-correlation coefficient with ideal images. His investigation showed that the cross-correlation coefficient decreases as unresolved rigid-body rotation increases. When the angle is smaller than 50^0, the correlation coefficient of two rotated homologous features is larger than a typical correlation value significance threshold of e.g., 0.4 [*Emery et al.*,1986]. The investigation also showed that unresolved straining motion decreased the cross-correlation. The investigation on the effect of diffusion showed that it changes the tracer distribution without change to the horizontal shape, and consequently its effect is almost insignificant. The superimposed effects of rotation and deformation makes the detectable time interval more restricted.

In the case of a large eddy flow, where the size is equal to or larger than the radius of deformation, the eddy cannot be regarded as a particle in the flow field. To resolve the rotational motion *Kamachi* developed the so-called "MCC method with rotational registration". The algorithm resampled corresponding sub-areas in the second image with a rotational window before cross-correlation computation. Investigation showed that, with rotational registration, the rotational motion for the flow fields larger than the radius

of deformation could be detected, and the use of this method made possible the adoption of sequential images with longer time separation. They also found that small increases in the rotational step, improved the estimation accuracy.

This test provided support for the conclusions of *Vesecky et al.* [1987]. In an investigation of rotation and deformation of sea ice with synthetic aperture radar images he stated that rotations of greater than 15^0 reduced the capabilities of the MCC search. The necessity for rotational motion to be resolved in the MCC method is also supported by *Tokmakian et al.* [1990].

Although, most researchers are aware of the effect of unresolved rotational and straining motion, the rotational registration method has not been widely adopted. The reason for this may be as claimed by *Kelly et al.* [1992]. Firstly, *Kamachi's* [1989] rotational registration method is based on a brute force (cover-all) search strategy. Therefore, the additional rotational search made the slow MCC search process even slower. The computational expense prohibited its widespread use. The second drawback suggested by *Kelly et al.* [1992] is that additional searches increase the chance of erroneously high correlation.

3.5 The Effects of Non-Advective Physical Processes

For two dimensional incompressible flow in an oceanic, well mixed layer (i.e. $\frac{\partial T}{\partial z} << \frac{\partial T}{\partial x} or \frac{\partial T}{\partial y}$), the thermal energy variation of a spatially fixed small unit on the sea surface can be expressed using the thermal conservation equation, in the following form [*Wahl et al.* 1990] —

$$\frac{\partial T}{\partial t} = \vec{u}_h \cdot \nabla_h T + k_h \nabla_h^2 T + w\frac{\partial T}{\partial z} + k_Z \frac{\partial^2 T}{\partial z^2} + S \qquad (3.6)$$

Where T is temperature, t stands for time, $\vec{u}_h$ is the horizontal fluid velocity, w is the vertical velocity component, S is the sum of individual heating source and sink term and k_H and k_z are horizontal and vertical eddy diffusivity respectively. The first term on the right hand side of the equation is the thermal energy change caused by advection, the

second term is the contribution of horizontal diffusion and the third term models the effects of heat exchange with the atmosphere and vertical mixing. The first two terms are respectively the thermal energy change due to the horizontal advective motion and diffusion, the third is change due to vertical advection, the fourth is due to vertical diffusion, and fifth is mainly due to the air-sea thermal energy change.

Wahl et al. [1990] quantitatively analysed the sensitivity of SST image-derived velocity due to non advective processes, with idealised models, and found that —

The vertical mixing was strongly related to the sea surface wind speed. Over most of the world's oceans, and during most of the year, the mean wind speed is generally less than 10 ms^{-1} and under these conditions, SST is largely determined by diffusion and air-sea exchange. At high wind speeds, intense vertical mixing can occur and the thermal gradient pattern can be destroyed. Under these conditions, valid estimates of near sea surface velocities cannot be obtained from a time series of SST images.

The effect of diffusion is critically dependent upon the turbulent diffusivity and the temperature gradient. Based upon the work of *Okubo and Ozmidov* [1970], the desired range of turbulent diffusivity is $0.1 \leq k_H \leq 10$ m^2/s. For these values of k_H and for the typical temperature gradient range of $0.2^0 \leq \nabla_h T \leq 1.0^0$ C/km, diffusion has little or no effect on the correlation function structure. This evaluation agreed with the results of *Kamachi* [1989]. For higher values of k_H (>100 m^2/s), there is pronounced degradation in correlation. Also, if the separation of image sequence exceeds 24 hours, the importance of diffusion increases.

In the absence of cloud cover, atmospheric heat exchange at the sea surface is spatially invariant over a few degrees of latitude. Ideally, the effect of spatially invariant heating may be de-meaned during the correlation computation. However, the magnitude of the heat exchange is not a constant over time of day and season. This temporal variation, coupled with the mean advective flow, can complicate velocity estimation from SST images. *Wahl et al.* [1990] tested this effect on a series of synthetic images generated with idealised heating and advection models, showed that the correlation for pure

advection tends to asymptotically approach zero, whereas, coupled with spatially invariant heating, the correlation converges to zero with damped oscillation when spatial and time lag increases. The test also showed the seasonal dependence of this effect. The initial rate of decrease in correlation in summer is greater than that in winter which is consistent with the fact that the diurnal heat exchange in summer is greater than that in winter.

Regional spatial variation in heating at the sea surface is caused by the attenuation of radiative fluxes by clouds. The spatially and temporally uneven cloud coverage during the time interval spanned by two cloud free images causes spatially variant thermal exchange. The uneven heating changes the original SST structure perceived in the first image. Consequently, it may influence the calculation of the sea surface velocity. During the day, when the shortwave flux dominates the heat budget, clouds have a spatially variant cooling effect on the sea surface thermal structure because of the backscattering of the incoming solar radiation. The long wavelength radiation emitted from the sea surface is absorbed by clouds, and partly reradiated back to the sea surface, which enhances the spatial variation in heat exchange. Both the magnitude and structure of the spatial heat flux variation are functions of cloud type and amount. Cirrus clouds tend to be higher and less structured than stratus clouds. They attenuate less incident solar flux than stratus clouds, because they have smaller surface area and absorb less long wavelength flux from the sea surface than stratus clouds, and also because they contain less water vapour. Examinations showed that the cirrus clouds do not significantly alter the spatial and temporal correlation in both summer and winter, whereas stratus clouds can drastically change the correlation scale spatially and temporally. Therefore, this effect may interfere with the interpretation of thermal gradient advection.

It should be noted that, although most researchers are aware of the effect of sea-air heat exchange on velocity estimation, proper calibration was not applied in their studies. The reason for this may be as follows. Firstly, as the competing mechanisms, such sea-air heat exchange, are strongly dependent on temporal separation, *Emery et al.* [1992] suggested that over shorter time intervals between images, where the MCC method was demonstrated to be more reliable, these competing mechanisms are less likely to be

significant contributors to the change in SST. Therefore, shortening the time separation of image sequence may be an efficient way to control these effects. Secondly, the proper calibration on these competing mechanisms may also be prevented by their complexity. For example, the calibration of the effect of surface heating and cooling requires information on the cloud type, spatial scale, location, cover period, and the knowledge of atmospheric heat exchange and diurnal heat exchange. Furthermore, an important question still remains open — do these thermal exchanges merely produce an overall bias or do they have a smaller scale impact, leading to significant mesoscale change in the infrared SST pattern [*Emery et al.* 1992]. It should be noted that it is impossible to correct for air-sea heat exchange, and further that short time intervals between images can also be a problem as they filter out small velocities.

3.6 The Correlation Computation and Search Strategy

The cross-correlation coefficient can be either computed directly using the equation 3.1 (see for example, *Emery et al.* [1986]), or using fast Fourier transform (FFT). *Ninnis et al.* [1986] applied the FFT algorithm for correlation computation in pack ice motion estimation from AVHRR images. *Collins et al.* [1988] also employed FFT for correlation computation in ice motion estimation from synthetic aperture radar (SAR) images. The FFT method is faster but imposes two restrictions. Firstly, for the highest efficiency, window sizes must have dimensions of powers of 2. If the window does not fit this criteria, it must be padded to expand its size to the next power of 2. The second restriction is that all of the values contained in the window must be used, [*Emery et al.* 1992], whereas, in most cases, the images are more or less contaminated by bulky or broken cloud. These contaminated pixels must be masked out of the correlation computation. Therefore, the FFT correlation computation has not been widely employed in sea surface velocity estimation.

The search strategy in the MCC method are based on a brute force, in which the template moves pixel by pixel throughout the search window, calculating cross-correlation values at each position, then the maximum is chosen. *Kelly et al.* [1992], using a two step coarse-to-fine search strategy, improved search speed by a factor of 8. However, in

comparison to the MCC brute force method, the search efficiency can be further improved by a search strategy approach as is employed in the joint-patch least squares matching scheme (see chapter 7 for example).

3.7 The Correlation Significance and Vector Spatial Consistency Examinations

The low correlation caused by unresolved advective and non-advective physical processes such as rotational motion, straining and spatially variant thermal exchange may lead to erroneous estimates of velocity vectors. Thus, the estimated vectors must be examined with a correlation significance threshold. Many researchers found that the significance test alone may not be sufficient to eliminate erroneous estimates for some cases. Therefore, a vector consistency test was applied on estimated vectors after correlation significance examination (see, for example, *Kelly et al.* 1992 and *Emery et al.* 1992).

Two different methods were used in correlation significance threshold determination.

Tokmakian et al. [1990] empirically determined the significance threshold by applying the MCC method to images separated by approximately one year, assuming all correlations between the images to be random. The threshold was determined at the 95 percentile value, for all of the maximum correlations found between the images. *Kelly et al.* [1992] used a similar method to determine the significance threshold.

The significance threshold can also be determined based on a statistical method, such as that described by *Kreyszing* [1970], which was employed by *Wu et al.*[1992]. For estimated correlation ρ of a template of N degrees of freedom, there exists a t-distributed variable, such that:

$$t = \frac{\rho\sqrt{N}}{\sqrt{1-\rho^2}} \tag{3.7}$$

The probability distribution of $P(t \leq c)=1-\alpha$ gives a measure of the probability that two signals with a cross-correlation ρ and N degrees of freedom are not significantly

correlated, when the corresponding variable t is smaller than a threshold c, where, 1-α is referred to as the confidence level, or according to *Wu et al.* [1992], α is the significance level (for example 1%, 5%, 10% etc). Given a significance level α, the threshold c, can be determined. The correlation value ρ_c corresponding to threshold c can be inversely calculated from equation (3.7) with $t = c$, and N degrees of freedom. Then, ρ_c is taken as the threshold of the significance test. If the maximum cross correlation of a search area is lower than this threshold, the correlation between template and the sub-image in the second image is considered as insignificant, and therefore the estimated vector should be rejected.

The principle behind this method appears to have been employed by *Emery et al.* [1986], *Wahl et al.* [1990], *Emery et al.*[1992]. However, the method of determination of degrees of freedom (DOF) was different to that used by *Wu et al.* [1992].

In time series analysis (see *Haykin* 1983 for example), for an uncorrelated sample set, the degrees of freedom N is the sample size minus 2. However, when the elements within the sample set have a certain degree of correlation, N is a measure of the number of equivalent independent samples, and its value relates to the auto-correlation of sample set. For the case of one dimensional signal analysis, DOF is defined as the total length of the time series divided by the decorrelation time τ_0. For a time series $S(t)$, as the time lag Δt increases, the correlation between $S(t)$ and $S(t+\Delta t)$ decreases. Decorrelation time is the time lag for the time series becoming uncorrelated. The τ_0 can be determined from the autocorrelation of the time series such that, for any time lag $\tau > \tau_0$, the magnitude of the autocorrelation function falls below some prescribed value. However, for a two dimensional signal, an equivalent method for the determination of DOF does not seem to have been established [*Wu et al.* 1992]. *Emery et al.* [1986], *Wahl et al.* [1990], *Emery et al.*[1992] determined the DOF as follows:

$$N = \frac{\text{total number of the pixels in a template}}{l} \tag{3.8}$$

where the l is the average decorrelation length. The average autocorrelation matrix of all templates was computed, then the average length from the autocorrelation centre to the

first autocorrelation zero crossing (i.e. the curve autocorrelation variable equals zero) on the both X and Y axes, are employed as the average decorrelation length.

By making an analogy to the 1-D time series analysis, *Wu et al.* [1992] proposed a decorrelation measure termed the decorrelation area (DCA) for 2-D data analysis. The DCA is defined as one fourth of the area, which centres on the autocorrelation peak, and within which the magnitude of the correlation function is above a prescribed value. The reason for DCA being one fourth of the area is that an autocorrelation function is centre-symmetric. Then, the DOF was determined by

$$N = \frac{\text{total number of the pixels in a template}}{d} \tag{3.9}$$

where d is the DCA in number of pixels.

Wu et al. [1992] tested the estimated MCC velocity field with the correlation significance threshold computed with both *Emery*'s *et al.* [1986] method and their own method, and found that the threshold value calculated with *Emery*'s method is too low in some cases.

Many researchers found that the correlation significance test alone cannot sufficiently eliminate all mis-estimates. Therefore, a vector coherency test was applied to the estimated velocity field after the significance test. The test assumed that the velocity field varies smoothly from grid to grid. *Kelly et al.* [1992] tested a vector field with a 3×3 subgrid. The vector that differed from its subgrid mean by more than 3 standard deviations was replaced by a new vector calculated by searching a smaller region around the mean displacement. A similar test was employed by *Emery et al.* [1992].

Although these tests can eliminate a large number of mis-estimates, many studies (see for example, *Emery et al.* 1992) showed that many can still remain undetected. The following study shows (see chapter 5 for an example) that in many cases the vector field can be incoherent throughout the whole neighbourhood (i.e. there is not a smooth transition from vector to vector), rather than there being just one or two incoherent vectors. In these situations the coherency test may fail. *Tokmakian et al.* [1990], *Wu et al.* [1992] and this study show that in many cases, in the cross correlation function a second

correlation peak exists, or sometimes even multipeaks may exist. The following study also shows that, due to the high auto-correlation along the SST pattern edges, there usually exists a elongated highly correlated area (i.e. the corresponding cross-correlation values along the direction of the edges are usually high, and not significantly different from each other). This is similar to the situation when shifting a linear feature along its direction to a number of different positions, the correlation values between the original and these shifted versions are equally high. In other words, the motion along the linear feature cannot be detected, if there is no other traceable features on the linear feature.

In both the studies mentioned, the test of correlation significance only provides a measure of similarity. When the correlation function has a multi-peak or elongated distribution, i.e. the correlation function has more than one element of correlation values which are almost as high as the maximum, the test does not provide any confidence that the sub-image where maximum correlation value occurs, correlates with the template better than the remainder of the sub-images (which have correlation values almost as high as the maximum). Therefore, in these cases, the correlation value alone is no longer a reliable criterion, and multiple choices may exist in each grid point for some areas (where, the multi-choices for each grid point may exist throughout the whole neighbourhood). These situations introduce a large uncertainty into the MCC estimation. To eliminate the uncertainty, a multi-criteria estimation is required.

These characteristics of the correlation function are the primary motivation for the current research of developing an algorithm to integrate the correlation information and the contextual information of the displacement field, based on a relaxation labelling technique for velocity estimation from consecutive images. This algorithm will be discussed and tested in chapter 6.

3.8 Evaluation of the MCC Estimation Method

The above studies have shown that the quality of estimated results depends not only on the estimating method but also the data condition, such as the strength of deformation and the magnitude of the gradient of the SST patterns. Thus, the quality of estimation is

case-dependent. However, general statements on MCC estimation quality can be drawn from the following evaluations.

Emery et al. [1986] compared MCC estimates with the drifters measurements obtained from experiments in the same period, and the geostrophic balanced dynamic topography derived from in situ conductivity, temperature, and depth measurements. The comparison was supported by both these two types of in situ measurements with excellent agreement. *Garcia et al.* [1989] computed sea surface velocities of the eastern English Channel and St. George Channel with the MCC method, using 24 hours apart images from the Coastal Zone Colour Scanner (CZCS) on Nimbus 7. The results were also found to be consistent with the estimates from sea surface drifters.

Tokmakian et al. [1990] evaluated the MCC estimation with both quasi-geostrophic model generated synthetic images, and AVHRR and CZCS images. The results showed that the MCC method successfully determined the surface velocity field in some instances and failed in others, and that the time separation of images was critical to the estimation quality. The best separation for MCC estimation is between 4-12 hours. The strength of the SST gradient also affected the quality of estimation. The use of rotational registration and averaging estimated velocity field, derived from multiple image pairs, improved the quality. They also found that the *rms* difference between MCC estimates and ADCP (Acoustic Doppler Current Profiler) measurements, was much higher than the value of 0.06 m/s estimated with the subjective feature tracking method by *Svejkosky* [1988]. Some of the *rms* difference is due to the variability in the image data, but it may also be due to the MCC method itself. The investigations of that study revealed a number of disadvantages of the MCC method, when compared to the subjective method. In the subjective method the tracking of features from one image to the next are subjectively selected and only those most distinctive features are used. The feature rotation can also be followed more easily by eye. Visual inspection of the images results in an overall feeling for the changes in location, shape of SST patterns among the image sequences. Therefore, only those " reasonable" features are selected as the homologous feature in the first image. In contrast to the subjective method, the MCC method removes the advantages of human insight.

The MCC is a simple image matching algorithm which was adopted by *Emery et al* [1986] for sea surface velocity estimation 11 years ago. Logically, the more information included in an estimation, the more reliable the results. However in contrast, the MCC estimation is based only on local correlation values and leaves a large amount of image information unused. Both *Tokmakiam et al.*[1990] and *Wu et al.* [1992] have shown the necessity of including more information in the estimation. Recent developments in computer based image matching and pattern recognition techniques have provided a number of algorithms that include multiple sources of information. Researchers in other fields of image matching applications, such as digital terrain model estimation, have shown that the estimation quality can be improved by properly including additional information. These estimation schemes, which are based on relaxation labelling and global least squares matching techniques, can easily include neighbouring information, a-priori knowledge, and constraints based on oceanographic phenomena.

Kelly et al. [1992] compared MCC estimates to inverse model estimates, altimeter velocity estimates and a large amount of in situ data. The main results of this evaluation are as follows:

- The MCC and inverse model estimates are statistically similar.
- The estimates from both methods resolved the flow pattern qualitatively well.
- The AVHRR estimates were of comparable directional accuracy to other in situ data.
- There is underestimation in magnitude for both the MCC and inverse model methods.
- Both MCC and inversion estimations provided a conceptual structure of currents.

Their results basically agree with the other evaluations by the researchers previously mentioned, except for the underestimation in magnitude found in the estimates from consecutive SST images. They suggested that the underestimation of the velocity, particularly in the jets, is inherent in the assumptions used to derive the velocity from the AVHRR data, rather than a limitation of a particular method. They believe that the small scale SST features near the jet move slower than a water parcel. The understanding of the physical processes which cause the underestimation may require further study based on larger numbers of AVHRR images and in situ data. However, if the underestimation is

systematic, it may be statistically estimated and calibrated by comparisons with other data.

Kelly et al. [1992] calculated a linear regression between AVHRR estimates $\hat{u}$ and the GEOSAT altimetry geostrophic velocity u_g , $\hat{u} = au_g + b$ and the squared correlation coefficient, ρ^2. They found the regression coefficient "a" was less than 1 (about 0.56 for MCC estimates and 0.44 for inversion estimates) and that the regression results agreed with comparisons among AVHRR estimates and other in situ data. Therefore they concluded that the AVHRR velocities were underestmated. Logically, they have implied that there is a systematic relation between AVHRR velocity estimates and altimetry velocity (i.e. the linear relation $\hat{u} = au_g + b$ in that case), and that this relation is statistically significant, otherwise, the regression and the conclusion based on the regression were not meaningful.

If a systematic relation does exist and is significant, the regression equation $\hat{u} = au_g + b$ is itself the calibration equation in that case. Although it was not explicitly declared and discussed in their paper, they have in fact promoted a possible method for underestimation examination and calibration.

From their study (i.e. *Kelly et al.* [1992]) we can learn as follows:

- the estimates may need to be carefully tested with data from other sources such as the altimetry velocity and drifts.
- if a systematic bias exists, it must be separated from random errors in velocity estimates and treated differently from the random error, when assimilating AHVRR estimates with the data from other sources. Otherwise, the assimilation results will be biased.

3.9 Summary

The estimation of sea surface velocity field from consecutive AVHRR thermal infrared images using the MCC technique have reported varying success. The factors which may affect the estimation quality come mainly from two sources:

Firstly, the mis-estimations caused by physical processes which are not resolved in the MCC estimation model.

- The sea surface temperature pattern advected by the velocity field consists of the superposition of translation, straining motion and rotation instead of purely translation. However, the MCC technique which tracks the motion of feature with the non-rotated fixed-shaped template, implicitly assumes that the sea surface temperature pattern is a rigid body, and the spatial displacement of features are driven only by the non-rotate advective process. With a non-rotated fixed-shape template window, the displacement caused by rotation and deformation cannot be resolved, thus, decreasing the cross-correlation corresponding to a correct SST feature pair, and introducing the chance of a mis-match.
- Non-advective physical processes such as spatially variant heat exchange and diffusion, change the intensity gradient of the sea surface pattern, and superimpose an additional decrease in correlation, and these effects depend critically on their scales of processes.

These effects can become more serious with an increased time-separation.

Secondly, the MCC method is a simple image matching algorithm. To estimate complex sea surface velocity field from SST images, more sophisticated pattern recognition and image matching techniques many be required in many cases. The main sources of mis-estimation, due to the simplicity of the MCC matching scheme, would be as follows:

The sea surface temperature pattern tends to be dominated by large scale features such as jets, and rings. The temperature gradients within these features are usually relative weaker, sometimes even isothermal. Consequently, the templates located on edges show high auto-correlation along the isothermal direction, while the templates located within features generally have a very low signal to noise ratio. This leads to a number of trade-offs in the computational scheme design, such as, in the template window size selection, between requiring the template to contain sufficient traceable features and to resolve

small motion structures. The difficulties in the correct selection of these parameters may consequently cause mis-estimations.

Furthermore, multi-peaks in the cross-correlation function have been found in anumber of sea surface velocity estimations (For example see *Wu et al.* [1992] and *Tokmakian et. al.* [1990], and other image correlation applications (For example see *Lin. Z. J.* [1988]). This indicates that velocity estimation using the maximum cross-correlation alone as a criterion, is not reliable in many cases. The uncertainty due to multi-peak and elongated distribution of correlation function will be illustrated and discussed in chapter 5.

Besides these error sources, the undetected cloud can also cause erroneous estimations and these will be discussed in Chapter 4.

Chapter 4

Partial Cloud Contaminated Pixel Detection with Förstner Operator

4.1 Introduction

Cloud contamination of sea surface temperature images is a major source of error in estimation of sea surface velocity from consecutive AVHRR thermal infrared images. In particular, the partially cloud contaminated pixel is difficult to detect with simple static temperature threshold methods. A multi-criteria algorithm based on the Förstner operator is proposed in this chapter to remove this effect from AVHRR thermal infrared images. In the algorithm, both the local gradient spatial structure and intensity structure are measured, and tested with three thresholds. This algorithm is not only sensitive in cloud detection, but also effective in preventing mis-interpretation.

Clouds dominate the errors introduced into satellite observation of Sea Surface Temperature (SST). Thin clouds and sub-pixel clouds require most consideration, particularly, cirrus clouds which are much colder than the sea surface. Even small amounts of undetected, scattered cirrus clouds can add large errors to estimates of SST (*Stewart* 1985, *Simpson et al.* 1990). In turn, the error in SST leads to erroneous estimates in velocity field from consecutive SST images. A number of automated schemes for detecting cloud contamination from multiple channel data have been developed (e.g. *Saunders* 1986, *Simpson et al.* 1990). Generally, the multiple channel cloud screening schemes are more capable of distinguishing between contaminated and useful pixels, than detecting contamination in a single channel. However, in our study, only the thermal infrared channel images (AVHRR channel 4) are available. Therefore, multi-channel cloud screening is not possible. This is the primary motivation for developing this algorithm. However, the proposed algorithm has also a general value

since the usual multi-channel techniques can fail in discriminating cloud edges from surface thermal structure by night, or for day time images in the case of sunglint.

Massive bulky clouds are generally much colder than the underlying sea surface. Therefore, these cloud pixels can be detected and masked from AVHRR thermal infrared image with simple temperature thresholding methods. When the image covers a large spatial region, clouds in a high latitude portion of the image may be warmer than the water in low latitude parts. In this case, the image can be divided into a few sections along the latitude direction. Then, a regional temperature threshold is applied to each section. With temperature thresholding, most bulky clouds can be detected. However, sub-pixel clouds and the cloud pixels on the edges of bulky clouds usually remain undetected with such simple thresholding methods. Because these pixels may only be partially covered by clouds, broken clouds and edges of bulky cloud, they are often characterised by a temperature lower than the underlying sea water, but may be higher than some portions of sea surface water within the section. Thus, it is hard to distinguish them from SST features by simple temperature thresholding alone.

However, three characteristics of these undetected clouds can be noted. First, scattered cloud pixels may be warmer than some parts of the water not far from them, but colder than the directly underlying sea surface. Second, they are often characterised by a high gradient magnitude in temperature compared to the direct underlying sea surface. Third, after temperature thresholding, most of the undetected clouds are small broken clouds that are characterised as point-type features, which are associated with incoherent gradient directions over a small neighbourhood.

The difficulty in detecting these part cloudy pixels, is that the edge features and corner point features of SST patterns may also have a high gradient magnitude, the same as the scattered cloud pixels. Therefore, a multiple criteria testing is necessary to separate these pixels from the SST features. The following algorithm was developed based on the Förstner operator which has the advantage that it is able to classify the underlying feature by measuring gradient strength and coherency of gradient direction within a small window.

4.2 The Methodology

The individual character of broken clouds in terms of gradient strength, coherency of gradient direction (i.e. the degree of the gradient direction differences between adjacent pixels), and local intensity difference, may be similar or indistinguishable from the corresponding characteristics of edge or corner features of SST patterns. Edges of SST patterns may also have similar strong gradient magnitude as broken clouds. However, unlike cloud pixels, most SST pattern edges are associated with a coherent gradient direction. Thus, they may be separated from cloud pixels by testing both gradient magnitude and coherency of gradient direction over a small neighbourhood. Corner-type features of SST patterns may have similar characteristics in both the gradient magnitude and the gradient direction coherency as the cloudy pixels. Thus they may be difficult to distinguish using magnitude and direction coherency tests. However, they can be located where the second order differential of intensity is zero, using the Förstner operator as a point feature detector. Thus, the intensity value of a corner-type feature of a SST pattern approximately equals the local average intensity in a small window (3×3 or 5×5), while the intensity of cloud pixels are more likely to be much lower than the local average. Therefore, they could be distinguished by testing the difference between the intensity of candidate pixels from other pixels within the small window. In this algorithm we required the intensity of the cloud pixel candidate to be lower than any other pixel in the window.

A multi-criteria test was designed based on the measurements in gradient magnitude, the gradient direction coherency and intensity difference, where the gradient magnitude, the gradient direction coherence, and the location of the cloudy pixel within a small window are measured by the Förstner operator. The Förstner operator was originally designed for three different tasks, detecting distinct points, least squares matching and detecting the centre of circle-type features. It has been extended for precise edge detection by *Trinder et al.* [1993] with sub-pixel accuracy. For further details on the method, the reader is referred to [*Förstner*, 1987]. The operator has the advantage that it is able to classify the underlying features, such as edges, corners, blobs and the centres

of circular features. The Förstner operator can locate a distinct point by determining the intersection of all edge elements within a window by least squares estimation, when the roundness and size of the error ellipse of the intersection of edge elements satisfies certain requirements. The edge element at a point (x_{ij} , y_{ij}) is defined as a line through this point oriented in the direction of the gradient of the point, which is of a form—

$$x\cos\theta_{ij} + y\sin\theta_{ij} - l_{ij} = 0 \tag{4.1}$$

where l_{ij} is the normal distance between the line and the origin, and $cos\theta$ and $sin\theta$ can be represented by the local gradient

$$\cos\theta = \frac{g_x}{\sqrt{g_x^2 + g_y^2}} \qquad \sin\theta = \frac{g_y}{\sqrt{g_x^2 + g_y^2}} \tag{4.2}$$

If a distinct point exists in a window, it is the intersection of all edge elements of this window, that is all edge elements pass through this point. Let the coordinates of the estimated intersection be (x_0,y_0). Thus, the observation equation of an edge element through point (x_{ij},y_{ij}) with the intersection point (x_0,y_0) is of a form—

$$v_{ij} = x_0 \cos\theta_{ij} + y_0 \sin\theta_{ij} - l_{ij} \tag{4.3}$$

Where v_{ij} is the distance between the edge element and the estimated intersection. Each observation equation is given a weight P_{ij} proportional to the absolute gradient squared $\left|\nabla g_{ij}\right|^2$. By minimising $\sum_{i,j} p_{ij} v_{ij} v_{ij} = \min$, the normal equation of a window, with a form as follows, can be derived:

$$\begin{bmatrix} \sum g_x^2 & \sum g_x g_y \\ \sum g_x g_y & \sum g_y^2 \end{bmatrix} \cdot \begin{bmatrix} x_0 \\ y_0 \end{bmatrix} = \begin{bmatrix} \sum g_x^2 x + \sum g_x g_y y \\ \sum g_x g_y x + \sum g_y^2 y \end{bmatrix} \tag{4.4}$$

where the sums have are taken over all pixels within a window. The solution of the equation gives the coordinates of the intersection point. By orthogonalization, three other important measures from the normal equation matrix **N** can be determined:

1. The semi-axes of the error ellipse, E and F can be derived from the eigenvalues of matrix $\mathbf{N}^{-1}$, μ_1 and μ_2 with $E=\sigma_n\sqrt{\mu_1}$ and $F=\sigma_n\sqrt{\mu_2}$, where $\mu_1 > \mu_2$, and the σ_n is the variance factor, $\sigma_n = \frac{\sum_{i,j} p_{ij} v_{ij} v_{ij}}{n-2}$, where n is the number of the observation

equations. Förstner designed a parameter, W, based on these eigenvalues to measure the relative size of the error ellipse of the underlying feature, and this measure reflects both the gradient strength and the consistency of gradient orientation of the features within the window.

$$W = \sigma_n / (E^2 + F^2) = 1/(\mu_1 + \mu_2) = det\,\mathbf{N} / tr\mathbf{N} \tag{4.5}$$

Where $det\mathbf{N}$ and $tr\mathbf{N}$ are the determinant and the trace of the normal equation matrix **N** respectively.

2. The roundness of the error ellipse can be directly measured by the value

$$Q = 1 - \left[(F^2 - E^2)/(F^2 + E^2)\right]^2 = 4\,det\mathbf{N} / (tr\mathbf{N})^2 \tag{4.6}$$

The roundness measure Q ranges between 0 and 1. When the window lies on a extremely distinct point, the error ellipse is a circle, Q=1. Conversely, if the window lies on an ideal edge, one of the semi-axis is equal to 0, then Q=0. The roundness measure can be used to avoid selected points lying on edges.

3. The direction of the major axis of the error ellipse can be derived from

$$\tan 2\phi = \frac{2\sum g_x g_y}{\sum g_x^2 - \sum g_y^2} \tag{4.7}$$

If the window lies on an edge, ϕ is the direction of the edge, or if the texture within the window has a predominant direction, the above equation gives this direction.

In this cloud pixel screening algorithm, W and Q were used as the gradient magnitude and direction coherence measures respectively. Using these two measures with an intensity difference measure DT, the algorithm determines a pixel as a cloud pixel when $W > W_{thre}$, $Q > Q_{thre}$ and $DT < DT_{thre}$. The intensity difference measure DT is defined as the difference of the intensity values between the candidate pixel and its neighbouring pixel of lowest intensity within a small window (this criteria requires the intensity of a cloud candidate pixel of the lowest intensity within a window). The selection of the thresholds will be discussed in the next section. Then the coordinates of the cloud pixels are determined from the normal equation.

4.3 Results and Discussion

In order to understand the performance of individual criterion, the algorithm was investigated on a series of AVHRR thermal infrared images, (but only the results on the image shown in Figure 4.1 are presented in this chapter) with a wide range of threshold values and window size combinations. For this study, no other cloud data set was available for the evaluation. However, most of the cloud contaminated pixels can be visually determined on images. Therefore, the algorithm performance was evaluated by visual comparison.

Before the detection of partial cloud pixels, the regional temperature thresholding was applied to remove the bulky clouds. The images were separated into three sections. The threshold of each section was determined by measuring the lowest intensity value of the surface water within the section. The results of thresholding are shown in Figure 4.1. The detected cloud pixels are coloured white. The undetected broken clouds remain a dark grey colour.

The results show that most of the bulky clouds are detected in this process, due to the large temperature difference between these relatively large clouds and the surface water. However, a large amount of broken cloud and the cloud pixels along the bulky cloud border remain undetected, because the intensity values of these pixels were higher than or equal to some portion of water in its section.

The following detection of broken clouds is based on three criteria, the gradient magnitude measured with equation (4.5), the coherency of gradient direction measured with equation (4.6) and the intensity difference between the candidates and their neighbourhood. In this study, we investigated the effect of window size and gradient magnitude threshold, the effectiveness of the error ellipse roundness criterion and the performance of the intensity criterion. In this procedure for detecting scattered clouds, the pixels which have been flagged as cloud in the temperature thresholding step, were excluded from the W, Q and the intensity difference calculations.

Figure 4.1. *The image with a cloud mask determined with temperature thresholding. The detected cloud pixels are masked with white. The undetected broken clouds remain a dark grey colour.*

4.3.1 The Effect of Window Size and Gradient Magnitude Threshold

In this part of the test, the threshold of error ellipse roundness was fixed at 0.6. A value of 0.6 was chosen as tests in section 4.3.2 have found this to be the best value for total performance. The intensity difference threshold was 0 (i.e. this threshold requires the candidates of the lowest intensity among its neighbourhood, except for pixels that have been flagged as cloud). The window size used in this investigation ranged from 3×3 to 7×7. The W value varies widely with the variation of window size. However, the ratio between it and the (W values) average of the entire image domain, is less sensitive to the window size variation. Therefore, the threshold of the W value, W_{thre}, was selected based on the average of the entire image domain $W_{average}$, and it ranged from 0.5 $W_{average}$ to 1.5 $W_{average}$. The obviously mis-detected pixels were visually determined. The results are presented in Table 4.1 and Figure 4.2-a and Figure 4.2-b. Table 4.1 shows the numbers of detected cloud pixels and the numbers of obviously misinterpreted pixels in the screening processing with different window size and gradient strength threshold. For all pictures, the pixels flagged as cloud in the temperature thresholding step are shown in black, the broken clouds detected with this algorithm are shown in white, and the

obviously mis-interpreted pixels are highlighted with circles. The broken cloud mask shown in Figure 4.2-a was computed with 3×3 window and a gradient strength threshold of 1.0 $W_{average}$. The Figure 4.2-b was computed with the gradient strength threshold of 0.7 $W_{average}$ and 5×5 window.

***Table 4.1**. The numbers of detected cloud pixels and the numbers of obviously mis-interpreted pixels in the second step of the screening processing, with different window size and gradient strength threshold.*

	3×3 window		5×5 window		7×7 window	
	identified (pixels)	mis-identified (pixels)	identified (pixels)	mis-identified (pixels)	identified (pixels)	mis-identified (pixels)
0.5 $W_{average}$	----	----	5390	5	6022	5
0.7 $W_{average}$	----	----	4836	1	5359	1
1.0 $W_{average}$	3771	4	4262	0	4983	0
1.3 $W_{average}$	3352	1	3922	0	----	----
1.5 $W_{average}$	3165	0	3737	0	----	----

The test results show that:

- processing with a larger window has relatively less chance of mis-interpretation. Therefore, a relatively lower gradient strength threshold can be chosen which enables the algorithm to detect the cloud pixels of weaker gradient.
- with the same level of W value threshold, the processing with a larger window is able to detect more cloud pixels. The reason for this is that some of the broken clouds span a few pixels. Thus, they may determined as linear features in the case of a small window but as point features when using larger windows. Both the tests using 5×5 and 7×7 windows give very good results, and the tests using 7×7 windows are marginally better than the cases of 5×5 windows.

However, enlarging the window increases the computation time, and the algorithm is designed to detect the point type cloud contaminated pixels. To avoid the cases, in which the detect window contains more than one point type contaminated pixel, a window larger than 7×7 pixels was not adopted in this study.

Figure 4.2.a *Image with cloud mask computed with* 3×3 *window, gradient strength threshold* W_{thre}=1.0$W_{average}$. *and error ellipse roundness threshold* Q_{thre}=0.6. *The intensity criterion was applied. The misinterpreted pixels are marked with white circles*

Figure 4.2.b *Image with the cloud mask computed with* 5×5 *window, gradient strength threshold* W_{thre} = 0.7$W_{average}$. *and error ellipse roundness threshold* Q_{thre} = 0.6. *The intensity criterion was applied. The misinterpreted pixels are marked with white circles*

4.3.2 The Effectiveness of Error Ellipse Roundness Criterion

To investigate the effectiveness of the criterion based on error ellipse roundness, a cloud mask was computed with roundness threshold Q_{thre} = 0.1. The balance of the parameters were chosen to be the same as those in the computation of Figure 4.2-b. Where the 5×5 window was used, the gradient strength threshold was chosen as W_{thre}= $0.7\ W_{average}$ and the intensity criterion were also applied. The obviously mis-interpreted pixels were visually determined and highlighted with circles. The roundness threshold Q_{thre} = 0 was not chosen, because, from equation (4.7), it can be seen, that when and only when $det\mathbf{N}$=0, the roundness measure Q will equal zero Q=0. In this case, the location of the candidate pixel cannot be determined from equation (4.4) because of the singularity of the normal matrix. Figure 4.3 shows many pixels along the borders of SST patterns were mis-interpreted as cloud points, compared with only one obviously mis-interpreted pixel in Figure 4.2-b. This result indicates the ellipse roundness test is effective in preventing the mis-interpretation of the points on SST pattern borders, which also have strong gradients.

Figure 4.3 *Image with the cloud mask computed with* 5×5 *window, gradient strength threshold* W_{thre}= $0.7W_{average}$, *and error ellipse roundness threshold* Q_{thre}=0.1. *The intensity criterion was applied. The misinterpreted pixels are marked with white circles*

4.3.3 The Performance of the Intensity Criterion

In the following test, a cloud mask was computed without the intensity criterion. The balance of the parameters are the same as those in the mask computation shown in Figure 4.2-b. where the 5×5 window was used. The gradient strength threshold was set as W_{thre}= *0.7* $W_{average}$ and the error ellipse roundness threshold set as Q_{thre} = 0.6. The result is shown in Figure 4.4. Six additional mis-interpreted pixels were found in the lower-right portion of the image compared with Figure 4.2-b. This indicates that the intensity criterion is effective in reducing the chance of mis-interpretation.

Figure 4.4 *Image with the cloud mask computed with* 5×5 *window, gradient strength threshold* W_{thre}= 0.7$W_{average}$, *and error ellipse roundness threshold* Q_{thre}=0.6. *The intensity criterion was not applied. The misinterpreted pixels are marked with white circles*

4.3.4 The Test Applied to Images Acquired at Night

The proposed algorithm was tested on a number of images, Figure 4.5 shows the results of the algorithm applied to an image acquired at night. The image used for the test shown in Figure 4.5 was acquired 12 hours after the image used in the tests described in 4.3.1 to 4.3.3.. Figure 4.5 shows that most of the cloud contaminated pixels were detected. However, there are still a number of cloud contaminated pixels that were not

detected which remain dark grey and which are marked with white circles in the figure. From the image, we can see that the differences between the grey value of these undetected cloud pixels and the grey value of background features (the sea surface temperature features) are relatively small. Therefore, they were more difficult to detect.

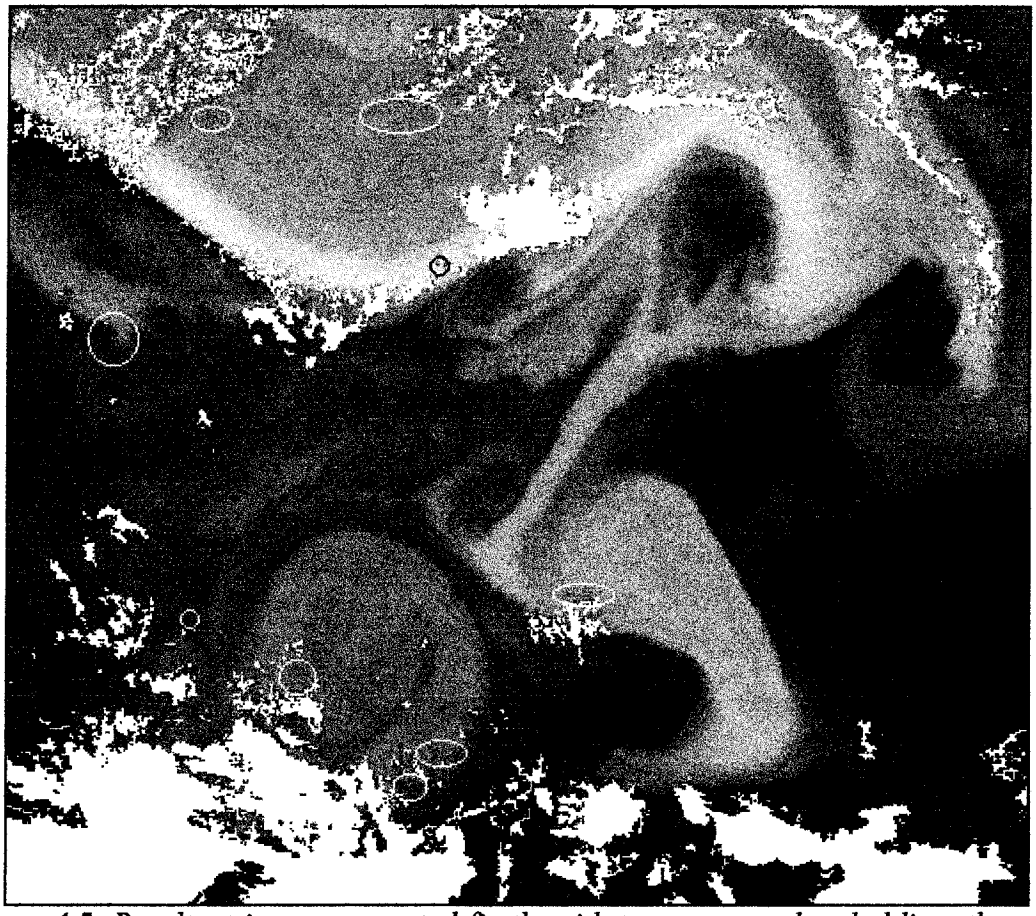

Figure 4.5 *Resultant image computed firstly with temperature thresholding, then with the proposed partial cloud contaminated pixel detection algorithm (with 5×5 window, gradient strength threshold* W_{thre}= $0.7W_{average}$, *and error ellipse roundness threshold* Q_{thre}=0.6. *The intensity criterion was applied). The detected cloud pixels are marked with white. The undetected cloud pixels are marked with circles. The image used for the test shown in the figure was acquired at night and about12 hours later then the image shown in Figure 4.1 to 4.4.*

4.4 Summary

A multi-criteria algorithm for masking partially cloud contaminated pixels in AVHRR thermal infrared images was proposed in this study. The algorithm developed is especially designed as a pre-processor for the sea surface velocity estimation from consecutive SST images. In the algorithm, the local gradient magnitude and coherency of gradient direction are measured with the Förstner operator. These measures (i.e. *W*

and Q), and the difference of the intensity value between the candidate pixel and the neighbouring pixels of the lowest intensity within the window (i.e. DT), are tested against three criteria. The experimental results show that with regional temperature thresholding and multi-criteria broken cloud screening, a majority of cloud contaminated pixels can be detected. Our investigation also shows that the multi-criteria screening produce a relatively better result with a combination of 5×5 or 7×7 windows, gradient strength threshold W_{thre}= $0.7\ W_{average}$, error ellipse roundness threshold Q_{thre} = 0.6 and the use of the intensity criterion. With this algorithm, a small portion of cloud pixels still remain undetected. Those pixels that remain undetected are generally characterised by relatively weak gradients, thus, it is more difficult to separate them from the features of the SST pattern features. However, on the other hand, due to their weak gradient, their affect can be effectively removed with by smoothing without a significant affect on the contrast of SST features.

Although the algorithm was designed for the detection of point type cloud contaminated pixels, the majority of cloud pixels on the border of the bulky cloud clusters were also detected. This is probably because the proportion of the cloud contamination of these pixels varies widely (i.e. gradients among these pixels varies widely). Thus these pixels were detected as point type pixels rather than as edge pixels. However, a complete detection for both point type and edge type cloud contamination pixels still needs further study.

The thresholds used in the algorithm were determined empirically based on test results. The automated optimisation of the thresholding requires further study. However, these empirically determined thresholds resulting from this research may be used to initialise an automated optimisation process, for example, in a heuristic refining process.

The contextual information remains unused in the proposed algorithm. This source of information can be used to improve the detection accuracy in future studies, especially for on-edge cloud pixels detection. The contextual relation between the candidate pixel and the detected bulky cloud cluster can also be a valuable source of information.

Chapter 5

Study of the Cross-correlation Function of SST Features and Its Variation Due to Different Pre-filtering and Correlation Computation Methods

5.1 Introduction

In former research, a number of different pre-filtering schemes and MCC matching schemes (basic and the scheme with rotational search) have been used. The performances of each pre-filtering and matching scheme were reported, and have been reviewed in Chapter 3. A scheme which performs positively in some cases may affect the estimation negatively in the others. The purpose of this chapter is to understand why these pre-filtering schemes and MCC matching procedures perform differently from case to case. The distribution structure of the correlation function is crucial to the reliability and accuracy of the estimation. In this chapter, we will examine the way different pre-filtering and matching schemes vary the correlation function structures, and consequently, affect the velocity estimation reliability and accuracy.

5.2 Image Data Description

The evaluations are made with a pair of NOAA AVHRR thermal infrared images and a set of synthetic SST image sequences. The AVHRR thermal images, shown in Figure 5.1 and Figure 5.2, are observed at respectively 4:36 and 16:04 Greenwich time, 8 December 1991, with about 12 hours time separation. The images cover a domain from E 153^0-160^0 in longitude and S 33^0-38^0 in latitude, and were co-registered in the CSIRO Marine Laboratories, Hobart, Australia, and this image pair will be refer to real images. The images cover the western part of the Tasman Front, and contain a number of interesting phenomenon, such as current fronts and eddy features. Unfortunately, we were unable to find simultaneous in situ data for this evaluation. Thus, the assessment of the absolute quality of the estimated velocity field using these two images is

impossible. The quality of the estimations derived from the image data are assessed by comparing the estimated displacement with a displacement field estimated using a subjective feature tracking method. The displacement field determined using the subjective method was also used to derive a series of synthetic images extending in time on from the AVHRR images of Figure 5.1, to assess the absolute accuracy of the determination of the displacements of SST features.

The synthetic images were derived by iterative resampling (shifting) the image shown in Figure 5.1 based upon a model velocity field. To make the variation of SST features in the synthetic images sequence as close to reality as possible, the model velocity field used to derive the SST field is firstly determined by a subjective tracking method (i.e. a SST feature tracking method using visual feature identification and manual measurement of displacement). The subjectively determined velocity field is fitted to a stream function, Ψ, of a two dimensional Fourier series form, using a least squares method presented in *Vastano et al.* [1985] and using the following observation equations —

$$\Psi = \sum_n \sum_m A_{n,m} \sin\frac{n\pi x}{L_x} \sin\frac{m\pi y}{L_y} \tag{5.1}$$

$$u = \frac{\partial \Psi}{\partial y} = -\sum_n \sum_m \frac{m\pi}{L_y} A_{n,m} \sin\frac{n\pi x}{L_x} \cos\frac{m\pi y}{L_y} \tag{5.2}$$

$$v = \frac{\partial \Psi}{\partial x} = -\sum_n \sum_m \frac{n\pi}{L_x} A_{n,m} \cos\frac{n\pi x}{L_x} \sin\frac{m\pi y}{L_y} \tag{5.3}$$

where, x (column) and y (line) are coordinates in pixel, u and v are visually determined velocity components in the x and y direction respectively, L_x and L_y are the dimensions of the rectangular region enclosing the image domain, and $A_{n,m}$ is the series coefficient to be determined. From the derived stream function, the velocity at each pixel was then determined from equations 5.2 and 5.3 by substituting the coordinates of the pixel. Using the pixel-by-pixel velocity field, a displacement field of 3 hours interval (i.e. $d(i,j) = v(i,j) \times 3$) was then derived. Under the assumption that the velocity field is temporally constant over 24 hours, a sequence of synthetic SST images of 3 hours separation (3, 6, 12, 15, 18, 21 and 24 hours) were derived through iteratively resampling (with bilinear interpolation) the AVHRR thermal infrared image shown in

Figure 5.1, using the calculated displacement field. The synthetic images of 12 hours and 18 hours respectively are shown in Figures 5.3, and 5.4. The vectors at the grid points of the velocity field (determined based on visuals method described previously), that were used for synthetic image derivation are superimposed on the image, and are shown in Figure 5.3.

The variation due to the major advective physical processes such as shifting, rotation and deformation of SST features are simulated in the synthetic image sequence. As the effect of bilinear interpolation in the iterative resampling processes is similar to the oceanic diffusion process, a small temporal step (3 hours) in the displacement calculation and the iterative resampling processes were applied to simulate the oceanic diffusion process.

The sum of partial the derivatives of equation (5.2) and (5.3) with respect to x and y equals zero (i.e. equation (5.4)). This implies that the stream function (5.1) and velocity described with equation (5.2) and (5.3) defines a velocity field which is 2-dimensional incompressible.

$$\frac{\partial u}{\partial x}+\frac{\partial v}{\partial y}=-\frac{\partial^2 \psi}{\partial x \partial y}+\frac{\partial^2 \psi}{\partial y \partial x}=0 \qquad (5.4)$$

The use of this assumption is equivalent to assuming that the velocity field is horizontally non-divergent, which means that no water goes to or comes from under surface.

The purpose of this study is to evaluate the method of velocity field determination rather than the velocity field itself. In other words, in this study the interest is in how to accurately track the SST features and not on how the SST features flow. Therefore, this non-divergence approximation should not affect the results of the study. The other approximation made in the synthetic image generation is that a time constant model velocity field is used. This assumption can be reasonably made, because, firstly, the equivalent time span of this synthetic image sequence is short (24 hours, and actually only the synthetic image of 12 hours and 18 hours were used in the following studies), and thus the velocity field should not vary significantly. Secondly, as explained above, these images are generated for testing the feature tracking method rather than a study of

Figure 5.1 *NOAA AVHRR thermal infrared image observed at Greenwich time* 4:36, 8 *December* 1991. *The image covers E* 153^0-160^0 *in longitude and S* 33^0-38^0 *in latitude.*

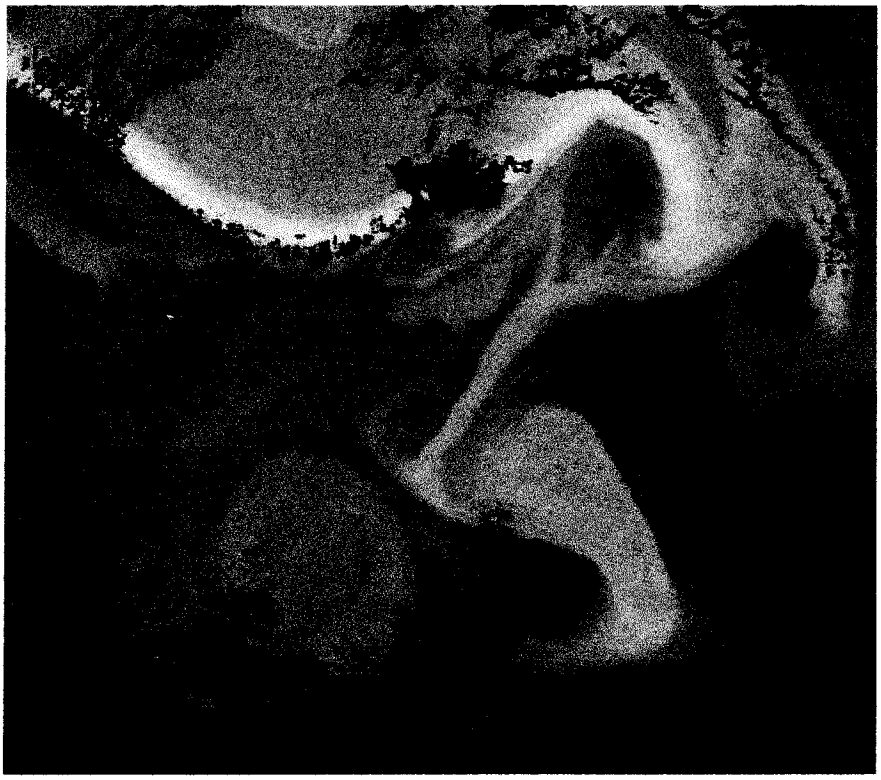

Figure 5.2 *NOAA AVHRR thermal infrared image observed at Greenwich time* 16:04, 8 *December* 1991 *from the same area as Figure 5.1*

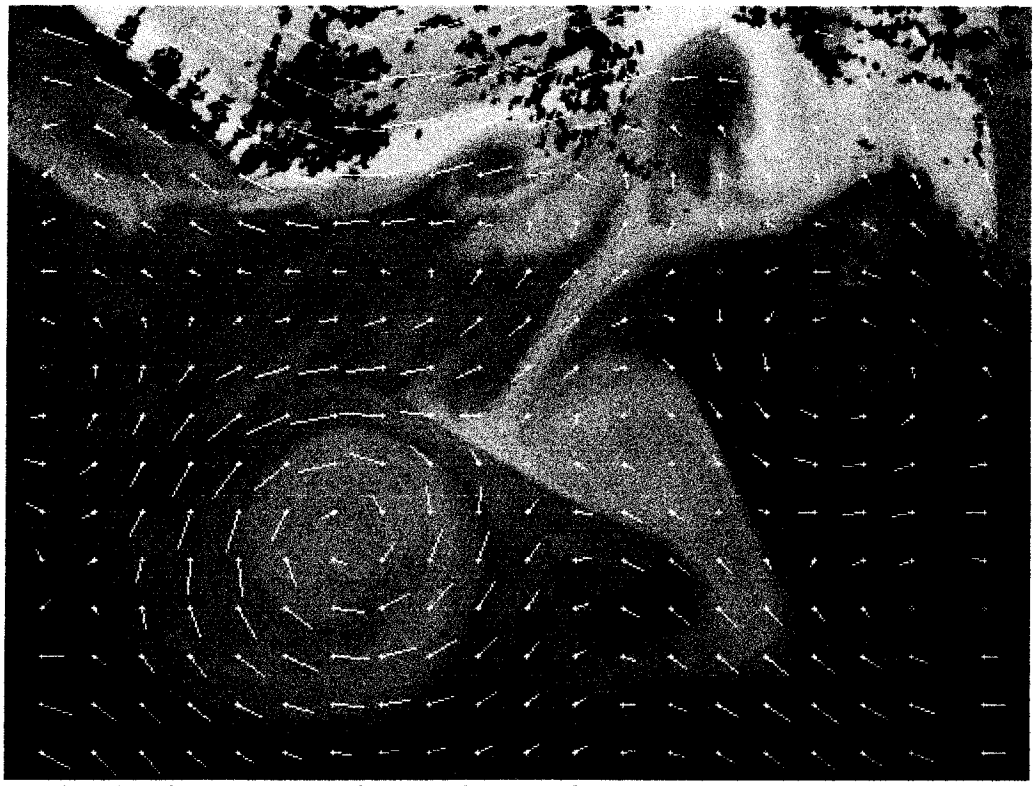

Figure 5.3 *Synthetic image of equivalent* 12 *hours time separation from the image shown in* Figure 5.1. *The superimposed vectors •— are the velocity field used for synthetic image generation, where the • are the grid points (the locations of the centre of templates and the centre of corresponding search areas in MCC computation) the length of the symbol "—" indicates the displacement of* 12 *hours.*

Figure 5.4 *Synthetic image of equivalent* 18 *hours separation from the image shown in Figure 5.1*

the velocity field. Thus, minor variations of the velocity field should not affect the outcome of this study.

We should be aware that the non-advective physical processes, which may affect the SST field in the real world, are not simulated in synthetic image generating, such as vertical mixing, advection, surface heating and cooling *etc.* *Wahl et al.* [1990] have estimated the effect of some of these non-advective factors using idealised models. They found the spatially uneven heating and cooling may have a relative large effect on image correlation. Another difference between synthetic images and observed or real images is that the noise in real images is random from image to image, while, in the process of synthetic image generation, the noise in the original image are advected along with the SST features. In other words, the noise becomes a part of the features. Besides the non-advective physical processes and noise, undetected cloud contamination is also a major source of error in velocity estimation in the case where real images were used. Similar to the noise, in the synthetic image generating process, the cloud contaminated pixels are shifted from one synthetic image to another along with the SST features.

5.3 Problems and background

The filtering process removes components of a certain frequency in the original image and enhances others. The purpose of filtering, for velocity estimation with the methods based on the MCC technique and other feature tracking techniques, is to make the SST features more traceable. The SST image is usually dominated by large scale and nearly piece-wise patterns (nearly isothermal inside the patterns). The small scale features inside the patterns and along the borders usually have very weak gradients. Previous research (see *Van Woert* [1982] for example) has found that the along-isotherm velocity component, the component parallel to the SST border, is generally larger than the cross-isotherm component. In other words, the SST images are dominated by the features parallel to the dominant moving direction. It is analogous to the situation of tracing the movement of a linear feature or the rotation of a circle. The cross-feature displacement of a linear feature can be easily determined, while the along-feature displacement is not traceable if there is no distinguishable small feature on the linear feature that reveals the

displacement. It is also true that it will not be possible to determine the rotation of a circle if there is no small feature on the border of the circle or inside the circle that reveals its position. Therefore, small, weak features may play an important role in along-isotherm component determination. To make these weak features more distinguishable, and thus traceable, a number of different high-pass filters have been used in previous research.

The distribution of the cross-correlation function between a feature and its shifted version is not only determined by the similarity and spatial lag between these two features, but is also determined by the shape of the features (assuming that the original feature and it shifted version have identical shape). If the features are dominated by short wavelength components, then they de-correlate quickly when the spatial lag increases, and yield an abrupt change in the cross-correlation function, thus the variation of the cross-correlation value is more sensitive to the displacement between two features (i.e. a small displacement can cause a relatively large variation in the cross-correlation value). Conversely, a feature and its shifted version which are dominated by long wavelengths in the frequency domain, de-correlate slowly when the displacement between the two increases, and generates a flat cross-correlation function, which is less sensitive to displacement. The use of a high-pass filter on an image enhances small features and improves their traceability, and the high pass filtered images are dominated by high frequency components, thus the variation in correlation values are more sensitive to the spatial lag between the homogeneous features.

This increasing sensitivity may affect the subsequent matching process between two similar images, either positively or negatively. The positive aspect is that it may improve the accuracy of the measurement of the displacement between homologous features. The negative aspect is that it also makes the matching process more sensitive to biases due to unresolved displacements and deformations between the feature and its advected version, so that it degrades the correlation value between homologous features in two images. However, the ocean surface current is a very complex phenomenon. It consist of a wide range of dynamics such as advection, rotation, straining, diffusion and mixing. These oceanic dynamic phenomena are of various spatial and temporal scales.

Some of them, as yet, are not well understood. Therefore, it is difficult to include all of these dynamics into the estimation model, and consequently, some of the displacements and deformations remain unresolved. The estimation scheme must be capable of tolerating these unresolved displacements and deformations. It requires a trade-off between enhancing small features and keeping the matching scheme at a certain level of tolerance to the unresolved displacements and deformations.

5.4 Methods

To investigate the dominant frequency of most traceable features and their corresponding sensitivity to the unresolved displacement and deformation in the subsequent MCC matching process, in the following sections of this chapter:

1. A series of filters described in section 5.4.1 were used to produce images which are dominated by high, medium and low frequencies, respectively.
2. Each pair of filtered images was then used to derive the velocity field using both the basic MCC method and the MCC method with rotational search described in section 5.4.3.
3. The resultant velocity fields derived from the synthetic images, are compared with the control velocity field which was originally used to generate the synthetic images.
4. The quality of the resultant velocity fields estimated from the real images are also tested against the control velocity field, because simultaneous in situ data are not available.

Because the control velocity field was determined by subjective feature tracking using the same image pair, and generally, the resultant field derived by using the subjective feature tracking method is more reliable than the MCC method, the comparison should give a reasonable measure of quality of estimation. However, it should be noted that the displacement vectors derived using the subjective feature tracking method, are determined by tracing the most distinguishable features, and generally are not located at the grid points described in Figure 5.3. The displacement values of the control field at the grid points are interpolated by least squares fitting. Therefore, due to errors in the control field caused by both subjective feature tracking and the interpolation, the

comparison between the resultant field estimated using the real images and the control field, can only be used as a check on significant erroneous estimates.

5.4.1 Filters

The gradient images are formed with a 3×3 window (see Figure 5.5). Four groups of gradients are computed with the Robert's operator. The gradients in two directions are then averaged separately, to reduce the noise (the gradient directions of a noisy pixel are incoherent with its neighbours). The magnitude of the averaged gradient is used as the image value of the central pixel of the window. The gradient magnitudes range from 0 to about 20 within a 0-255 range. Thus, the range of image values of the gradient images are linearly stretched to a range of 0 to 255. The SST gradient magnitude images computed with this filter are dominated by very high frequency components. They are used here to illustrate the influence of the high frequency components in the MCC matching process.

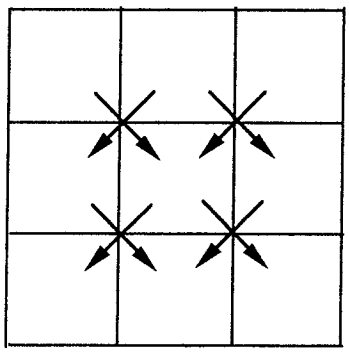

Figure 5.5 *The gradient computation window and Robert's Gradient*

A "high-pass" filter is used to produce images which contains high and medium frequency components. The high-pass filtering is accomplished in two steps. First, a centred 25×25 pixel average of the original image is computed using a running average low pass filter. The low pass filtered image is then subtracted from the original image to produce the high pass filtered image as used in *Tokmakian et al.* [1990].

The low frequency images are produced with a running average low-pass filter of 25×25 window.

5.4.2 Cloud Contamination Detection

The cloud contamination is a major error source in velocity estimation from consecutive images. A number of automated schemes for detecting cloud contamination from

multiple channel data have been developed (e.g. *Saunders* 1986, *Simpson et al.* 1990). Generally, the multiple channel cloud screening schemes are more capable of distinguishing between contaminated and useful pixels, than detecting contamination in a single channel. However, in this study, only the thermal infrared channel images (AVHRR channel 4) are available. Therefore, multi-channel cloud screening is not possible. In this research, an algorithm was developed in chapter 4 to detect the cloud contaminated pixels from single band thermal infrared images. The detected cloud contaminated pixels are masked in the filtering and matching processes. The cloud contaminated pixels are detected using the method described in chapter 4.

5.4.3 Correlation Computations (Matching Schemes)

Two correlation computation methods are used here. One computes the correlation coefficients with non-rotate template, as was discussed in Chapter 3 section 3.1. It will be referred to as the basic MCC method hereafter. The other computes the correlation using a MCC method with rotational registration (rotational search) similar to the method used in *Kamachi* [1989]. It will be referred to as the rotational MCC method hereafter. The rotational MCC method not only searches for the maxima by computing and comparing the correlation value at every location of the search area, but also searches the rotational displacement at each location in the search area by rotating the resampling window by several different angles. The correlation values between the template and each rotationally resampled sub-images are computed. Then, the maxima is employed as the correlation value of that position (see Figure 5.6) .

This search strategy is not very efficient, and there are a number of ways to improve the it. The least squares matching method is one, where a sampling window iteratively approaches the best matching sub-area, rather then the brute force strategy which computes the correlation value over-all the search area and then chooses the maxima. However, to illustrate the whole structure of the correlation function of each search area and the relationship with the corresponding SST feature, the brute force strategy is still used in this chapter. To save computation time, the rotational resampling is only applied to the areas of significant rotational motion, such as the areas within the circles as shown in Figure 5.7 Plate B. To compare the full features of displacement fields

estimated with different computational combinations, the estimates of low correlation value are not eliminated using correlation significant test and coherency test.

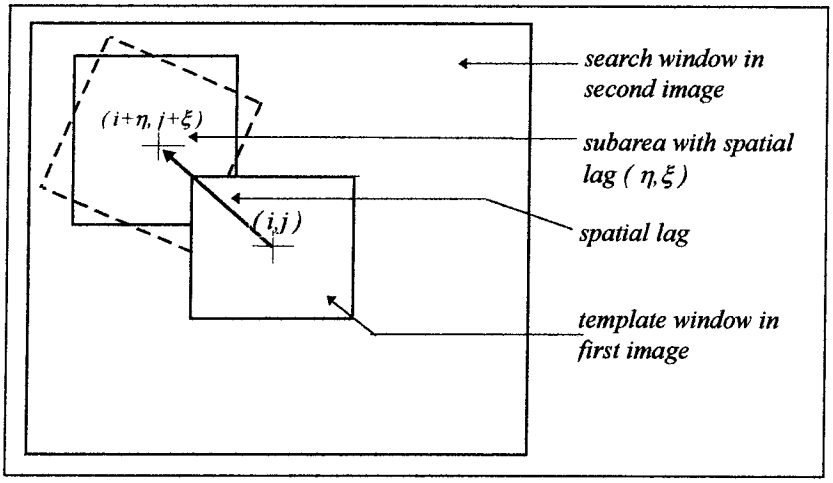

Figure 5.6 *Illustration of the geometry of rotational MCC method.*

5.5 The Results Computed Using Synthetic Images

Initially the effect of the pattern tile (template) size are tested. The pattern tile size was varied from 31 to 51 pixels. The search radius in the second image is determined with the maximum velocity and image time separation. In this test, a search radius of 32 pixels in all directions is used for the image pair of equivalent 12 hours separation and 48 pixels for the 18 hours pair. The search radius is the distance between the centre of the template in the first image and the centre of the most distant sub-area in the corresponding search area in the second image. To reduce the effects due to the other sources, such as the unresolved rotational effect etc, the correlation coefficients are computed using the rotational MCC method. The images are pre-processed with a running average high pass filter of a 25×25 pixel window. The test results are shown in Table 5.1.

In this study, the correlation threshold was set to 0 to view the full features of the resultant vector field and the correlation function distribution. The mean MCC value provided in Table 5.1, is the mean value of the maximum cross correlation coefficient at all grid points including the positions of low SST gradients. In the table, the *rms dm* is the root mean square of the difference in the magnitude of the displacement (velocity ×

time separation) vectors magnitude, between the control velocity field, which was used for generating the synthetic images, and the measured velocity field. The *rms dα* is the root mean square of the difference in angle between the control velocity field and the measured field. *n* stands for the number of erroneously estimated vectors. The estimated vector of an error with a magnitude great than 7 pixels, or an error in the orientation of larger than 30^0 are counted as an erroneous estimate. These two thresholds (7 pixels and 30^0) were selected as they were considered as reasonable practical limits when the results of Table 5.1 considered.

Table 5.1 *The results of the test on the effects of different pattern template sizes.*

	12 *hours separation*			18 *hours separation*			
pattern tile size	31	41	45	31	41	45	51
mean MCC	68	66	64	65	58	58	58
rms dm	4.7	4.0	3.8	12.0	8.8	6.6	6.0
rms dα	30^0	23^0	23^0	48^0	41^0	31^0	31^0
n	14	7	7	30	23	15	13

The results shows that the mean MCC drops slightly when the template size is increased. At the same time, the number of erroneous estimated vectors and root mean square difference in magnitude and direction improve significantly when the template size increases from 31 pixels to 41 pixels, for the images of time separation 12 hours, and from 31 to 45 for the image pair of 18 hours separation. When the template size is increased from 41 pixels to 45 pixels, the variation in the above 4 measures are not very significant for 12 hours separated images. For the 18 hours separated images, the measures do not vary significantly when the template size is increased from 45 pixels to 51 pixels. The results also show that the cross correlation drops and the erroneous estimates increase as the time separation of the images increases. This is because the rotational MCC method uses fixed-shape resampling window. The deformation due to straining will therefore still remain unresolved. Our test shows that, generally, the larger template contains more information, therefore improving the estimation of the MCC. However, we should also be aware that the vector computed with the MCC methods (including the basic method and the method with rotational search) is the average value

of the area covered by the template. The larger template may bias the estimates in the region of large velocity gradients, such as the area where the jet passes through. The optimal template size also depends on the scale of the traceable SST features, which may vary from case to case. For the synthetic images used in this study, the 45 pixels template is considered an appropriate size to balance these effects.

The performance of the basic MCC method and the MCC method with rotational search, and the effect of different filtering on the correlation distribution and the resultant displacement vector field, are firstly evaluated using 12 hours and 18 hours separated synthetic image pairs. The filters used here are described in section 5.4.1.

The resultant velocities are compared against the velocity field used to generate the synthetic images. In a similar manner to the tests on the inspection of template size selection, the difference between the retrieved displacement vector fields and the control field, are measured with the mean maximum correlation coefficient (MCC), root mean square difference in magnitude *rms dm*, orientation *rms* $d\alpha$, and the number of erroneous estimates, *n*. Again, in the rotational MCC computation, the rotational search is only partially applied to the areas of strong rotational motions marked with circles in Figure 5.7, and the basic MCC is used in the balance of the area to save computation time for raw, high-pass filtered, and low-pass processed images. For gradient images, the rotation resampling are both partially applied and applied in the entire image frame. The comparison of results using image pairs of time separation 12 hours and 18 hours are shown in Table 5.2 and Table 5.3 respectively. A part of the resultant displacement vector field are shown in Figures 5.7 to 5.11.

Plates A and B of Figure 5.7 are the estimated displacement (velocity × time separation) field computed using unfiltered (raw) synthetic image pairs of 12 hours separation with the basic MCC and rotational method applied, respectively. The two plates of Figure 5.8 show the estimated fields by applying the basic and rotational MCC method to the 12 hours separated high-pass filtered image pair. Plate A, B and C of Figure 5.9 show, respectively, the displacement field computed using the basic method, the partial rotational method (rotational resampling applied to the partial image frame) and the full

rotational method (the rotational resampling was applied to the entire image frame) with 12 hours separated gradient image pair. Figures 5.10 and 5.11 show the resultant displacement fields using the 18 hours separated high-pass filtered image pair and the gradient image pair, with the same computation combinations as those applied to the 12 hours separated images.

Table 5.2 *Results using the synthetic images of equivalent time separation of* 12 *hours.*

		mean MCC	*rms dm*	*rms dα*	*n*
unfiltered image	basic MCC	0.76	4.7	34^0	16
	rotational MCC	0.77	4.2	25^0	8
low-pass filtered image	basic MCC	0.96	7.8	62^0	51
	rotational MCC	0.97	7.4	54^0	37
high-pass filtered image	basic MCC	0.61	5.3	38^0	17
	rotational MCC	0.66	4.0	23^0	7
gradient image	basic MCC	0.41	4.9	45^0	26
	rotational MCC (partially applied)	0.46	4.3	31^0	13
	rotational MCC (fully applied)	0.48	3.8	19^0	6

Table 5.3 *Results using the synthetic images of equivalent time separation of* 18 *hours.*

		mean MCC	*rms dm*	*rms dα*	*n*
unfiltered image	basic MCC	0.74	10.0	51^0	31
	rotational MCC	0.76	6.8	41^0	18
low-pass filtered image	basic MCC	0.87	9.9	64^0	45
	rotational MCC	0.87	9.8	44^0	35
high-pass filtered image	basic MCC	0.54	9.8	58^0	34
	rotational MCC	0.58	6.6	31^0	15
gradient image	basic MCC	0.40	16.0	71^0	63
	rotational MCC (partially applied)	0.42	10.3	53^0	36
	rotational MCC (fully applied)	0.46	10.0	41^0	25

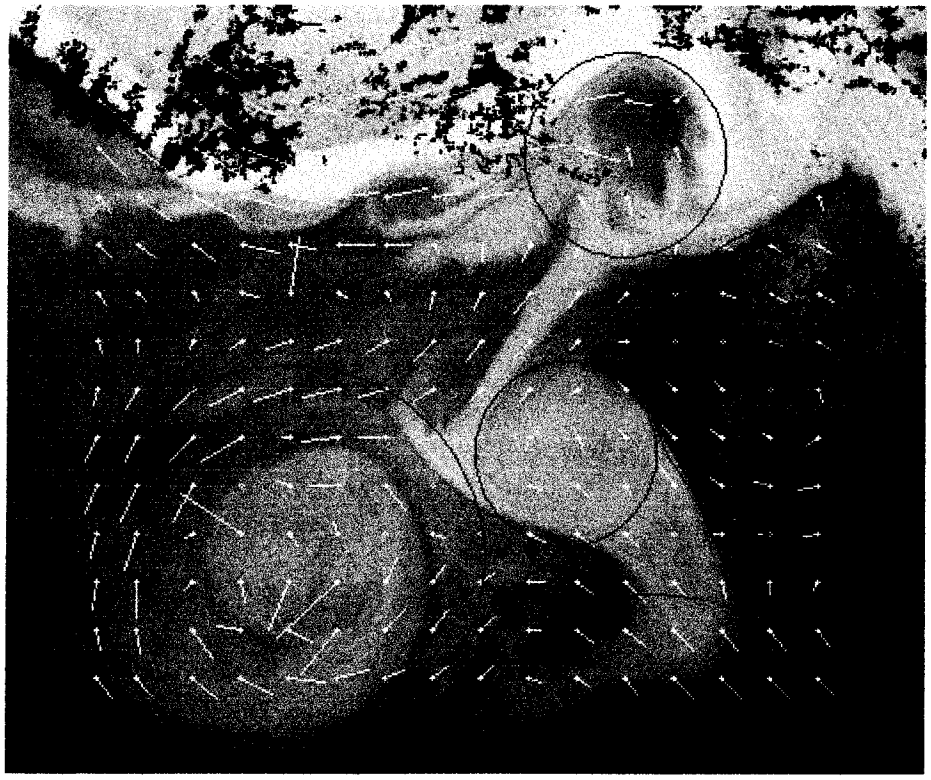

Figure 5.7 Plate A, *The estimated displacement field computed using an unfiltered synthetic image pair of* 12 *hours separation and the basic MCC method*

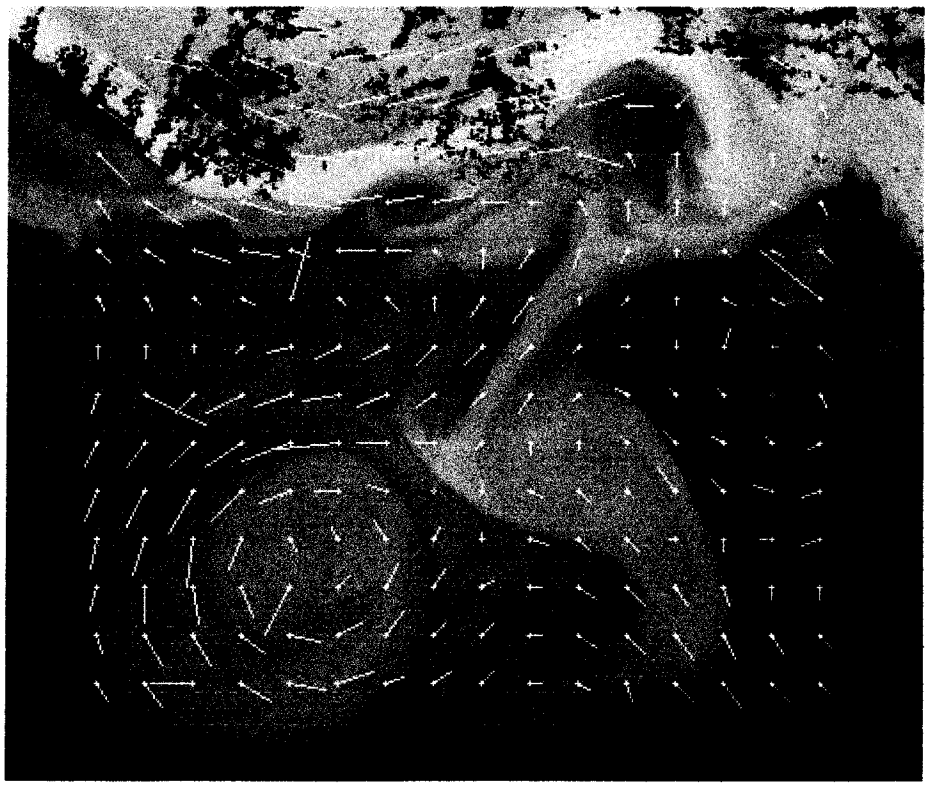

Figure 5.7 Plate B, *The estimated displacement field computed using an unfiltered synthetic image pair of* 12 *hours separation and* the *partially applied rotational MCC method*

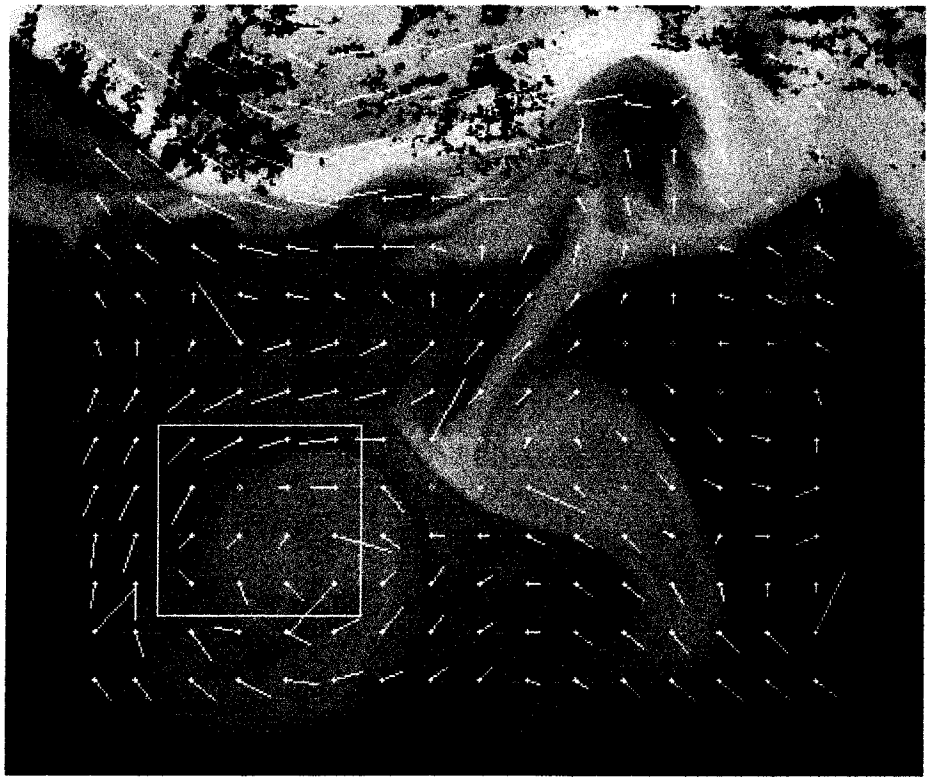

Figure 5.8 Plate A. *The estimated displacement vectors using the basic MCC method and the* 12 *hours separated high-pass filtered image pair. The white square relates to data displayed in Figure 5.14.*

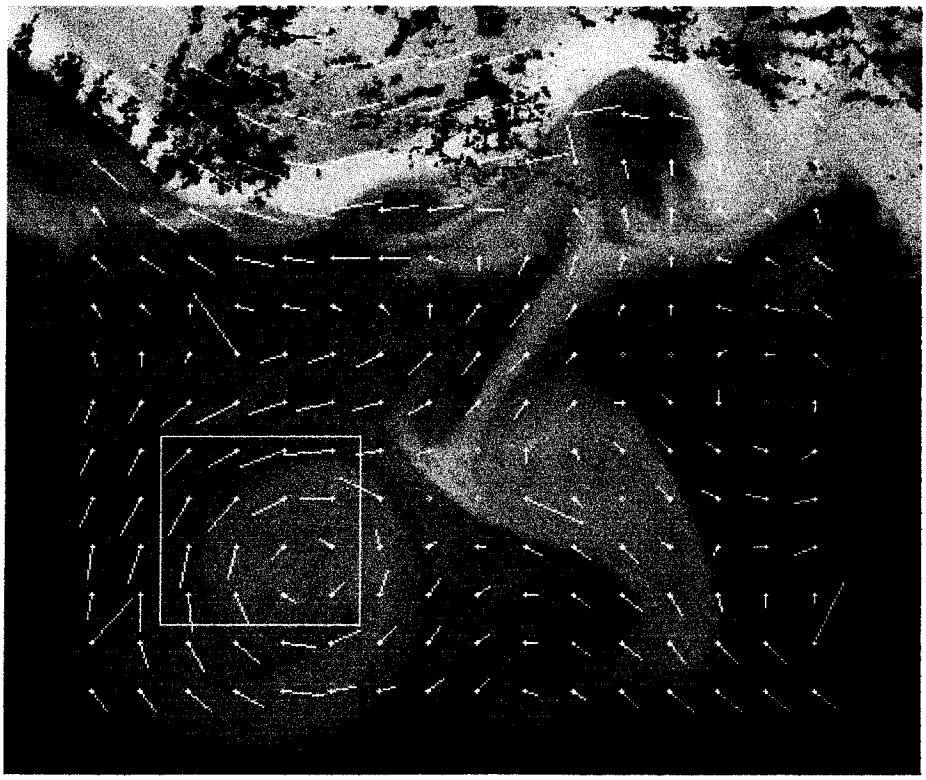

Figure 5.8 Plate B. *The estimated displacement vectors using the partially applied rotational MCC method and the* 12 *hours separated high-pass filtered image pair. The white square relates to data displayed in Figure 5.14.*

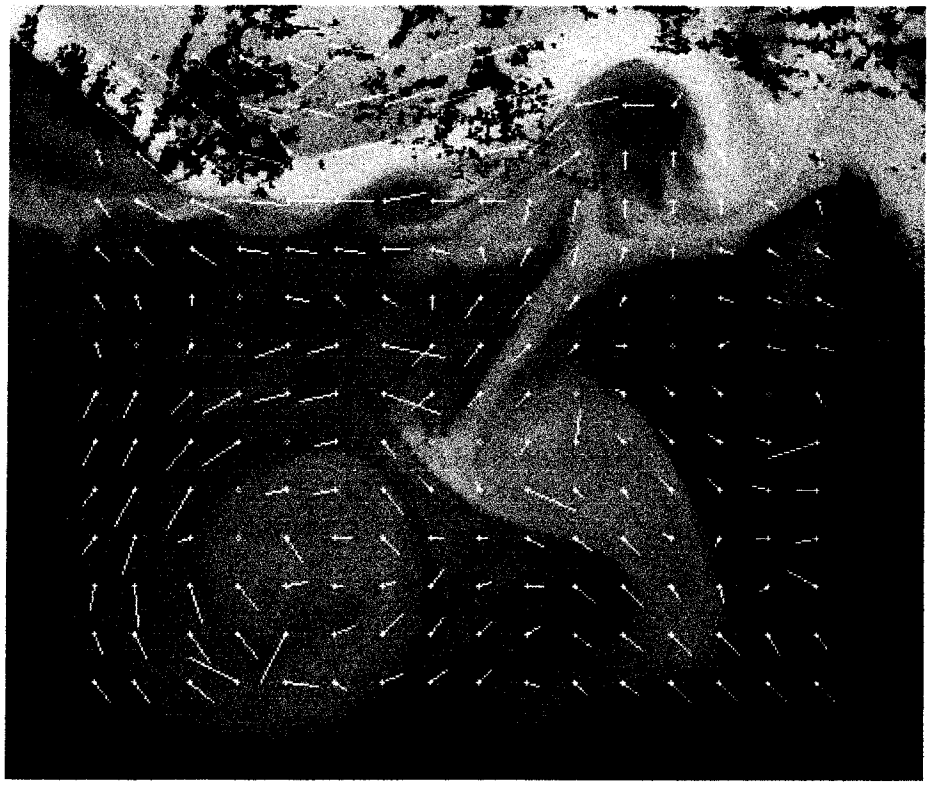

Figure 5.9 Plate A. *The resultant displacement vector field using the basic MCC method and gradient images of* 12 *hours separation.*

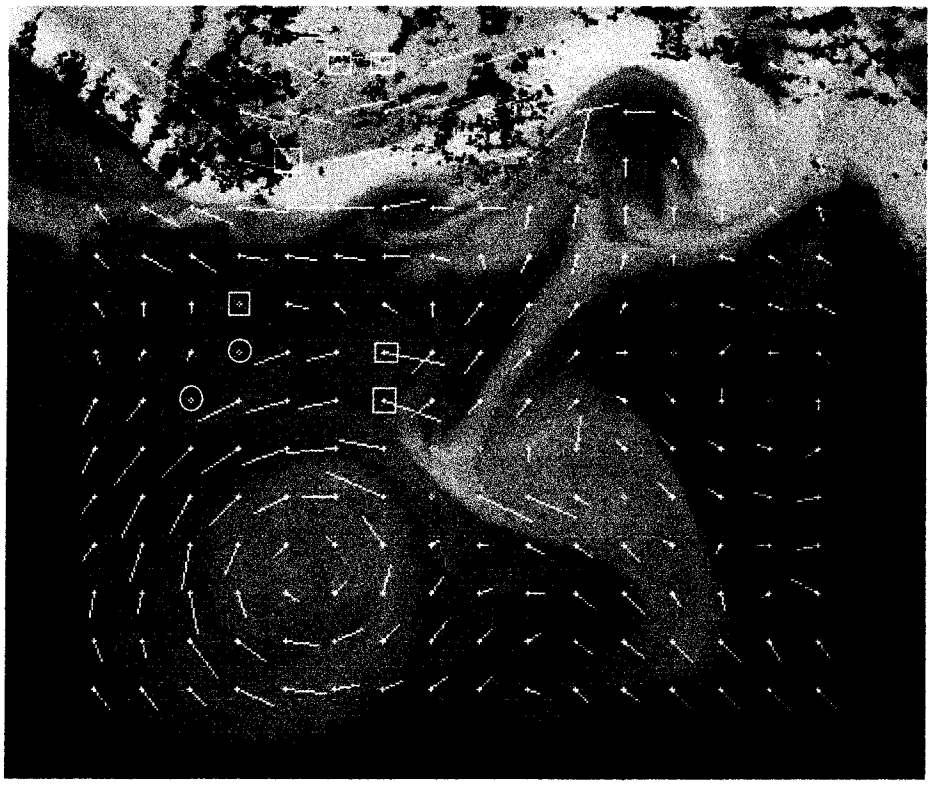

Figure 5.9 Plate B. *Resultant displacement field computed using the partially applied rotational method and gradient images of* 12 *hours separation.*

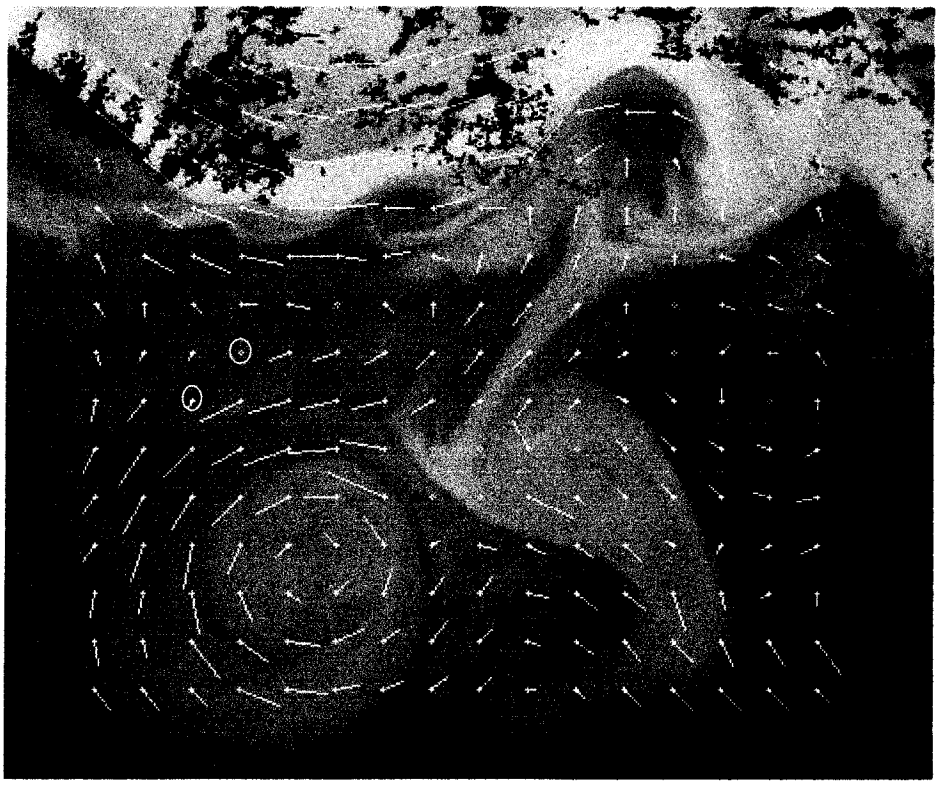

Figure 5.9 Plate C. *Resultant displacement field computed using the fully applied rotational method and gradient images of* 12 *hours separation*

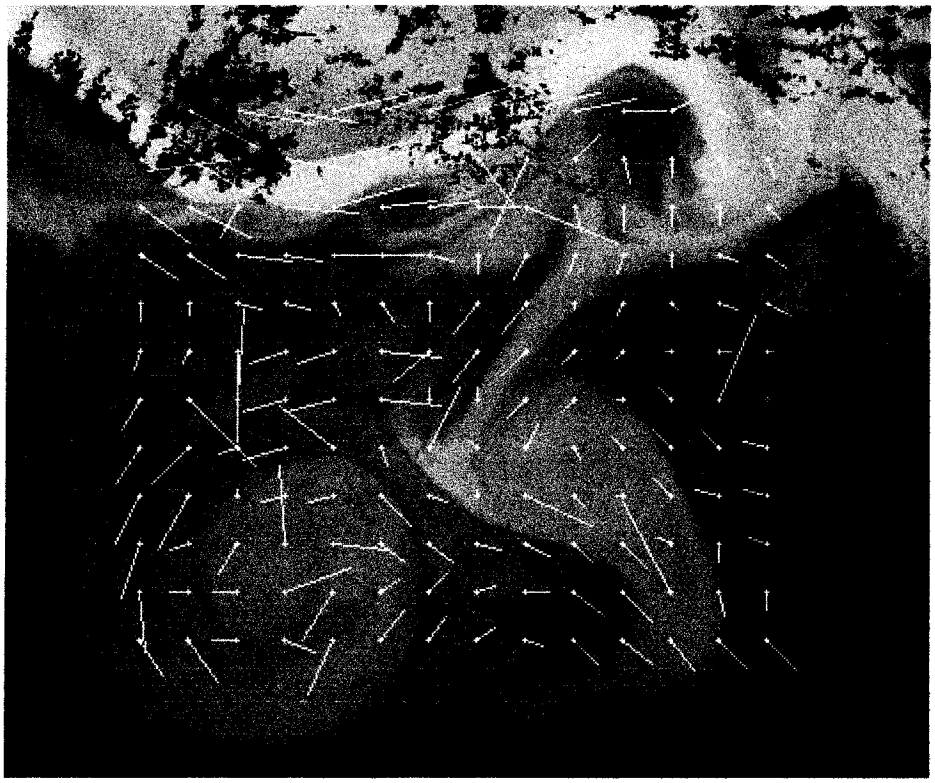

Figure 5.10 Plate A. *The resultant displacement field computed using the basic MCC method and the 18 hours separated high-pass filtered image pair.*

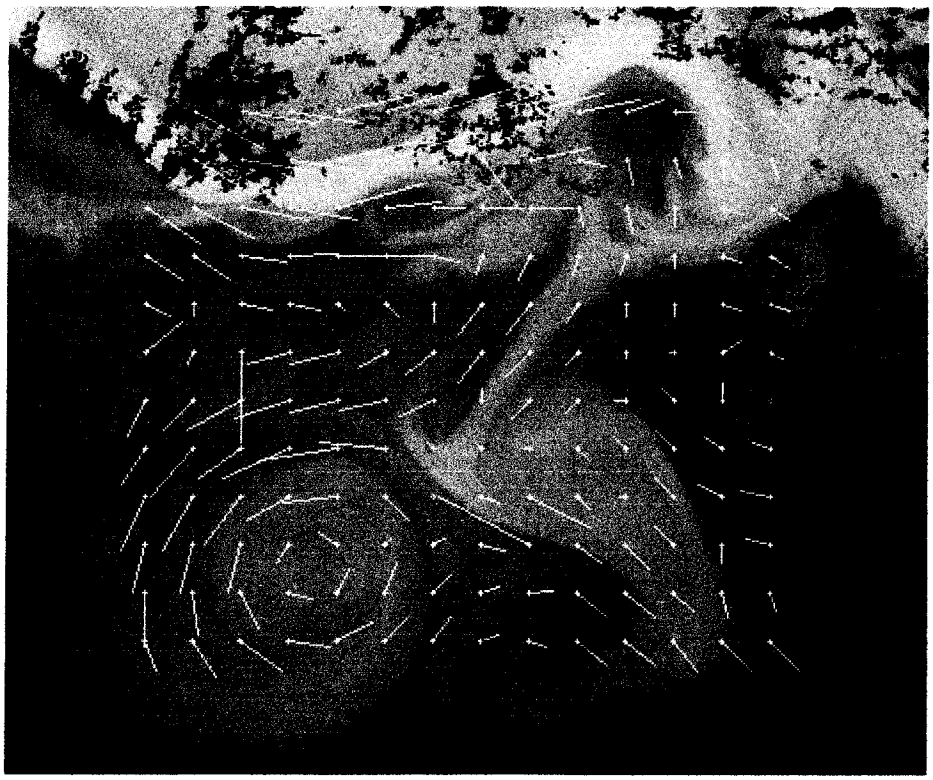

Figure 5.10 Plate B. *The resultant displacement field computed using the partially applied rotational method and the* 18 *hours separated high-pass filtered image pair*

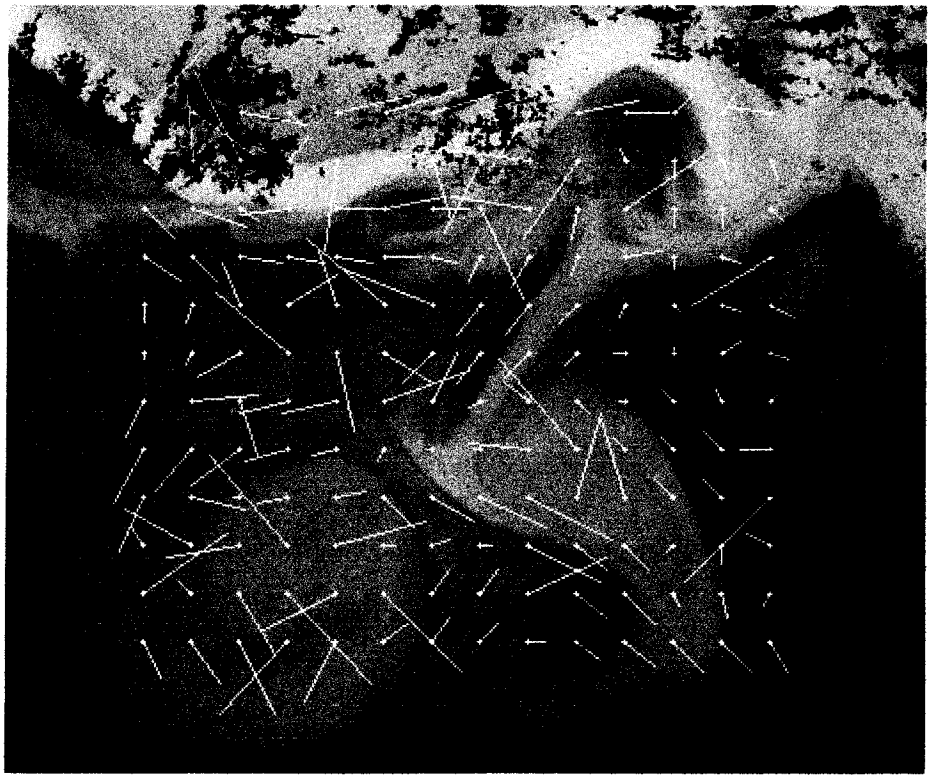

Figure 5.11 Plate A. *The displacement field computed using the basic method and the* 18 *hours separated gradient image pair.*

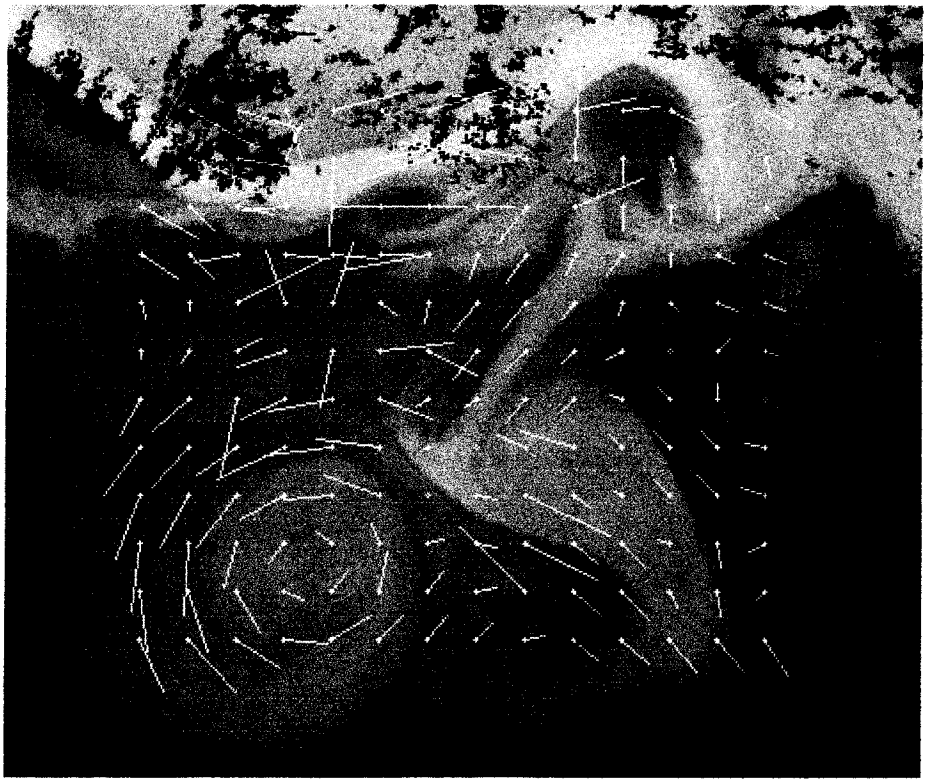

Figure 5.11 Plate B. *The displacement field computed using the partially applied rotational method and the* 18 *hours separated gradient image pair.*

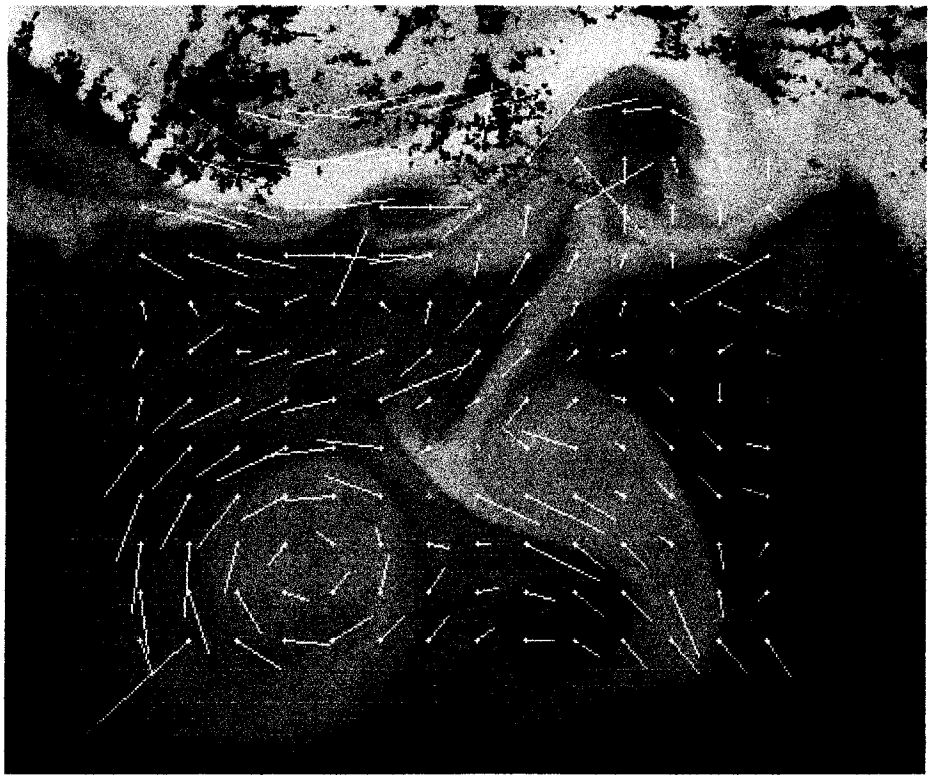

Figure 5.11 Plate C. *The displacement field computed using the fully applied rotational method and the* 18 *hours separated gradient image pair.*

5.6 Results Computed from Real AVHRR Thermal-Infrared Images

An investigation is also made using the real NOAA AVHRR thermal infrared images, presented in Figure 5.1 and 5.2. The estimations using synthetic images are the "best case" test. As described in section 5.2, compared with retrieving the velocity from synthetic images, the velocity estimation using real AVHRR thermal infrared images suffers from additional effects due to the non-advective physical processes, such as the effect of uneven surface heating and cooling and mixing etc. Furthermore, in the real image sequence, noise is totally random and the clouds move at speeds and directions different from the SST patterns.

In the computations using real images, the cloudy pixels are detected using the method described in chapter 4, and are masked, so that they do not contribute to the correlation value. Subtracting the cloud pixels from the correlation computation is equivalent to reducing the template size. When the masked cloud pixels reach a certain percentage in a template or the corresponding sub-area in the second image, the information contained in the template or the sub-area may be insufficient. Therefore, in the tests using real images, the estimated velocity was not accepted when the cloud contamination reached a certain level. The rejection of estimated velocity due to cloud contamination is based on following rules:

1. If the contamination in a template reaches 20%, the velocity at that grid of the template located is not computed, that is the entire correlation matrix is not computed.
2. If the contamination in the template is less than 20%, then the contamination in each sub-area is tested, as well as the sum of the contamination in the corresponding template-sub-area pair. If either the contamination in a sub-area or the sum of the contamination in the template and the sub-area reaches 20%, the correlation value at that position is not computed, which is equivalent to eliminating the corresponding element from the correlation matrix. If the percentage of eliminated elements due to the cloud contamination in the correlation matrix is over 20%, the corresponding estimated velocity at that grid is not accepted.

The evaluation was performed using both the basic and the rotational MCC methods on the raw images, high-pass processed images and gradient images. For the computations

using raw images and high-pass filtered images, the rotational resampling was partially applied, while the rotational resampling was applied to the entire image domain for the case using gradient images.

Unfortunately, simultaneous in situ data was not available for this evaluation. Thus, an assessment of the absolute quality of the estimated displacement field is impossible. The quality of the estimations with the real image data are assessed by examining the consistency of the estimated vector field. The grids used in this study are about 26km apart. As shown in Figure 2.1.a and 2.1.b, the dominant oceanic related features such as the eddies, geostrophic eddies and streams are of spatial scales greater than 50 km, therefore it can be reasonably assumed that the velocity field is smoothly varying from grid to grid over this distance. The consistency of a vector with its neighbourhood is measured using the difference between the vector and the average of its 8 neighbouring vectors. The *rms* consistencies of the vector fields are as shown in Table 5.4. The evaluation also compared the estimated displacement fields against the control velocity field used in the evaluation of the synthetic images. Because the control field is based on measurements determined by subjectively tracking the features of the same real image pair used in this evaluation (the method was introduced in section 5.2), it should be a good reference field for this evaluation. The comparison is again measured with the mean MCC, *rms da*, *rms dm*, and the number of erroneous estimates, *n*. The computed results are shown in Table 5.4. The displacement field computed using the rotational method and the raw images is shown in Figure 5.12, and the computed field using the high-pass filter processed images is shown in Figure 5.13.

Table 5.4 *Test results on a real image pair with a time separation of about* 12 *hours*

		mean MCC	*rms dm*	*rms dα*	*n*	*rms consistency*
raw image	basic MCC	0.70	9.0	71^0	51	13.1
	rotational MCC	0.72	7.3	62^0	44	11.0
high-pass filtered image	basic MCC	0.46	8.5	69^0	42	11.6
	rotational MCC	0.48	5.5	50^0	25	9.6
gradient image	basic MCC	0.37	9.8	68^0	45	15.7
	rotational MCC	0.44	8.0	53^0	25	11.3

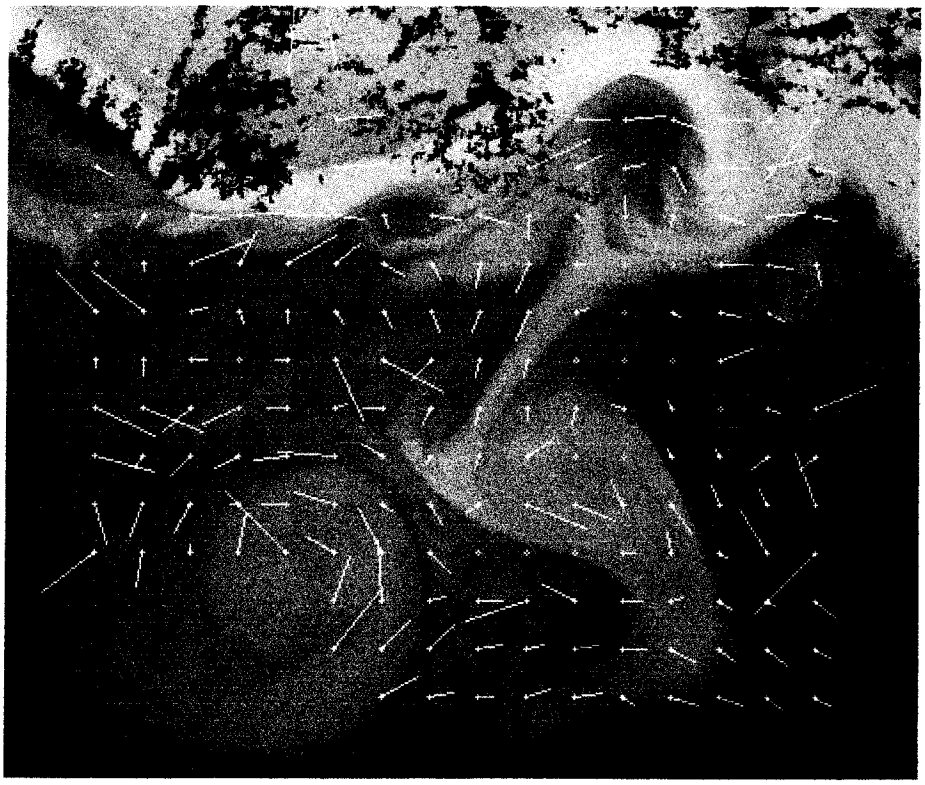

Figure 5.12 *The estimated displacement field using raw real images of* 12 *hours time separation and the rotational method*

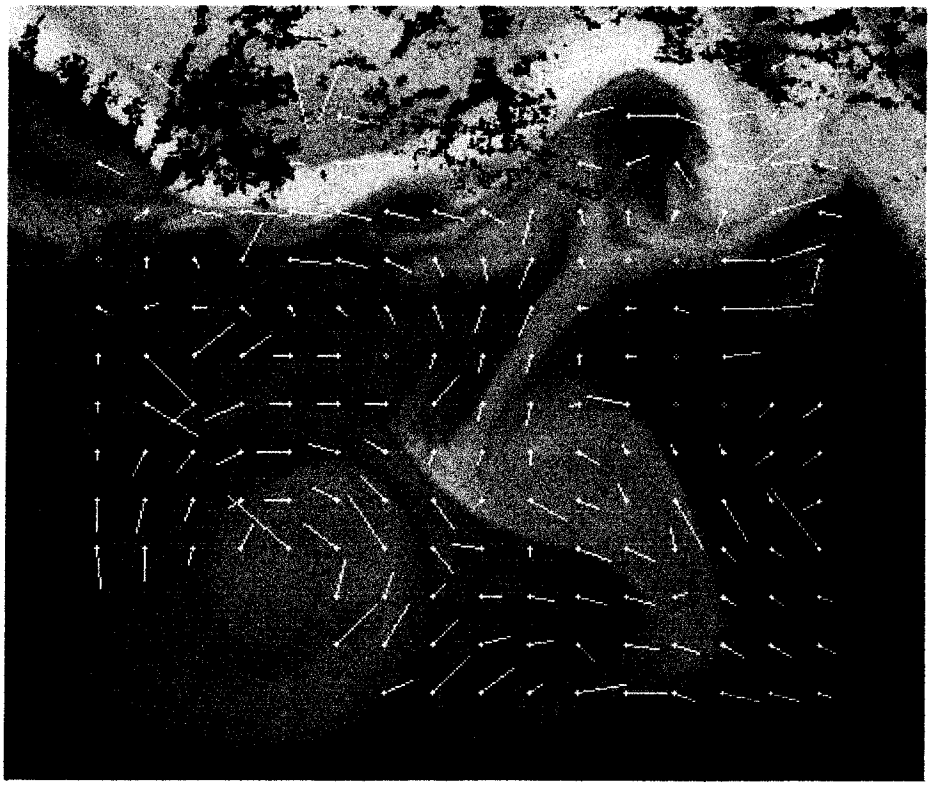

Figure 5.13 *The displacement field estimated using* 12 *hours separated high-pass filtered images and the rotational method*

5.7 Discussion

5.7.1 The Performance of the Rotational MCC Method

The results presented in Table 5.2 and 5.3 and the resultant displacement fields shown in Figures 5.7 through to 5.11, show that with the same images, the rotational MCC method significantly improves the quality of the resultant velocity field compared to those using the basic MCC method. For example, compare the velocity field in Plate Bs (and Plate Cs, for the cases using gradient images) against that of Plate As of Figures 5.7 to 5.11. For the image pairs of 12 hours separation, erroneous estimates are reduced on average by 11, and reduced by 20 on average for images of 18 hours separation. These results strongly indicate that the rotation motion has a significant effect on the correlation value in strong dynamic areas. Therefore, the including this part of the motion into the estimation model helps improve the estimation quality. It is especially true for the image sequence of a relative long time separation.

5.7.2 The Variation in Correlation Distribution Due to the Use of the Rotational Method

The comparison of the correlation matrices resulting from the basic method and the rotational method shows that the rotational computation does not change the basic structure of the correlation matrix distribution, but enhances the correlation value at the correct position. Plate A and Plate B of Figure 5.14 are the correlation functions computed using the basic and the rotational method, respectively, with the same image pair (high-pass filtered 12 hour separated images). Each square represents a correlation matrix (the correlation value distribution of a search area) of a template/search-area pair. The correlation values are coded in colours ranging from blue, green, yellow, orange to red in ascending order. The maxima of each search area is marked with a white cross. The vector field corresponding to these 16 correlation matrices (search areas) are shown in plate A and B of Figure 5.8 and marked with a square. Plate B of Figure 5.14 shows that the maxima are shifted to their correct position when the rotational method is used, while the basic structure of the correlation function remains unchanged. The correctness of the positions of the maximas is measured by a comparison between the corresponding estimated displacement vectors shown in Figure 5.8 (marked with a square) and the vectors in the control field.

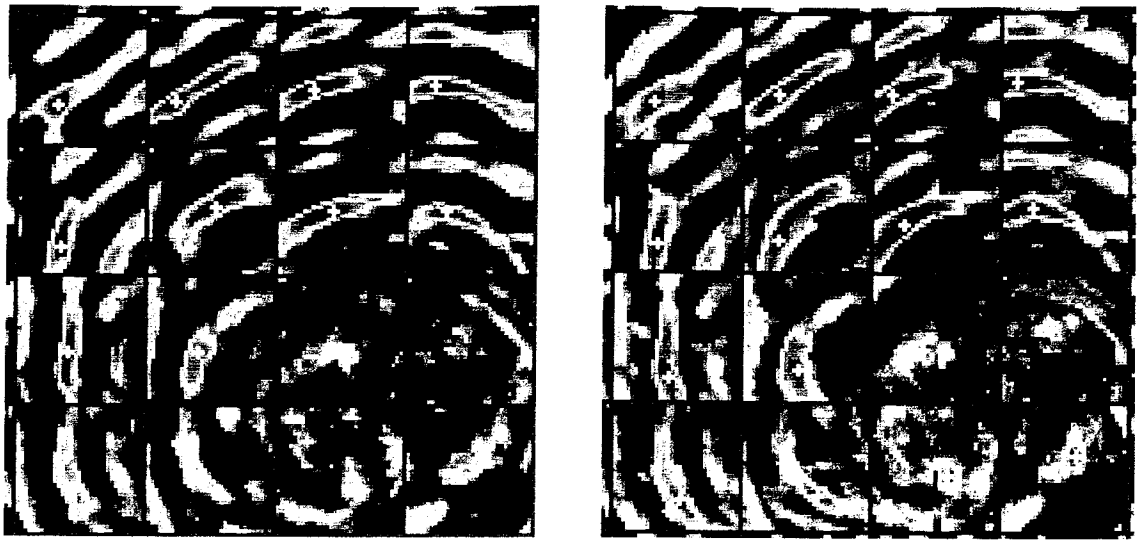

Plate A Plate B

Figure 5.14 *Plate A shows the values of the correlation matrices computed using the basic MCC method. Plate B shows the correlation matrices using the rotational method. The image used in this comparison is the* 12 *hours separated high-pass filtered image pair. The correlation values are coded in colours ranging from blue, green, yellow, orange to red in ascending order. The maxima of each search area is marked with a white cross. The corresponding computed displacement fields are shown in Plates A and B of Figure* 5.8, *respectively (the areas marked with a square)*

5.7.3 The Variation of Effectiveness of the Rotational Method

The results presented in section 5.5. also show that the effectiveness of the rotational method varies when the predominant frequency of the input images is changed. The unfiltered image contains a whole range of features of different frequency, but dominated by the long wavelength components. The 25×25 running average low-pass filter removes the features of spatial scale less than 25 pixels, and the processed image contains only the low frequency features. The high-pass with 25×25 running average window removes the components of spatial scale larger than 25 pixels. The gradient computation with a 3×3 window removes most of the features except those with high frequency, such as the borders of the SST patterns.

To view this effect, the number of erroneous estimates in the areas of strong rotational motion are counted and given in Table 5.5. When the rotational search is applied, the motion estimation with the gradient images gains the largest improvement. The number of erroneous vectors drops from 35 to 10, a 75% drop, for the 18 hours separated

gradient images, compared to a drop from 34 to 21, 41%, for the case using the same correlation methods (basic and rotational) on a low frequency image pair.

Table 5.5 *Variation in the number of erroneous estimates due to different matching schemes and different pre-filtering methods, and the percentage reduction in erroneous estimates from basic to rotational MCC.*

		number of erroneous estimates in the areas of strong rotational motion			
		unfiltered raw image	*low-pass image*	*high-pass image*	*gradient image*
12 *hour separation*	*basic MCC*	13	32	14	17
	rotational MCC	4	18	4	5
reduced		9 (69%)	14 (56%)	10 (71%)	12 (71%)
18 *hour separation*	*basic MCC*	25	34	26	35
	rotational MCC	9	21	7	10
reduced		16 (64%)	13 (41%)	19 (73%)	25 (75%)

5.7.4 The Effect of Correlation Function Distribution on the Quality of the Resultant Field

This study also found that pre-filtering changes the sharpness of the correlation function distribution. When the SST features are dominated by short wavelength components, they de-correlate fast, thus yielding an abrupt change in the correlation function. Conversely, the signal from the long wavelength dominated components, de-correlates slowly and generates a flat correlation function. As an example, the correlation functions were computed using the 12 hours separated raw images, the high-pass filtered images, the low-pass filtered images and the gradient images, and these results are shown in plates A, B, C, and D of Figure 5.15 respectively. The rotational method was used in these computations. Again, each box used in the these plates corresponds to a correlation matrix of a template/search-area pair. The correlation values are coded in colours in the same way as described for Figure 5.14.

Generally, the features dominated by high frequency components provide more accurate measurement of the movement of the SST patterns, however, their cross-correlation value is more sensitive to the unresolved deformation due to the abrupt de-correlation. In contrast, the correlation value of the long wavelength components are relatively less sensitive to the unresolved deformations and rotations. However, because the

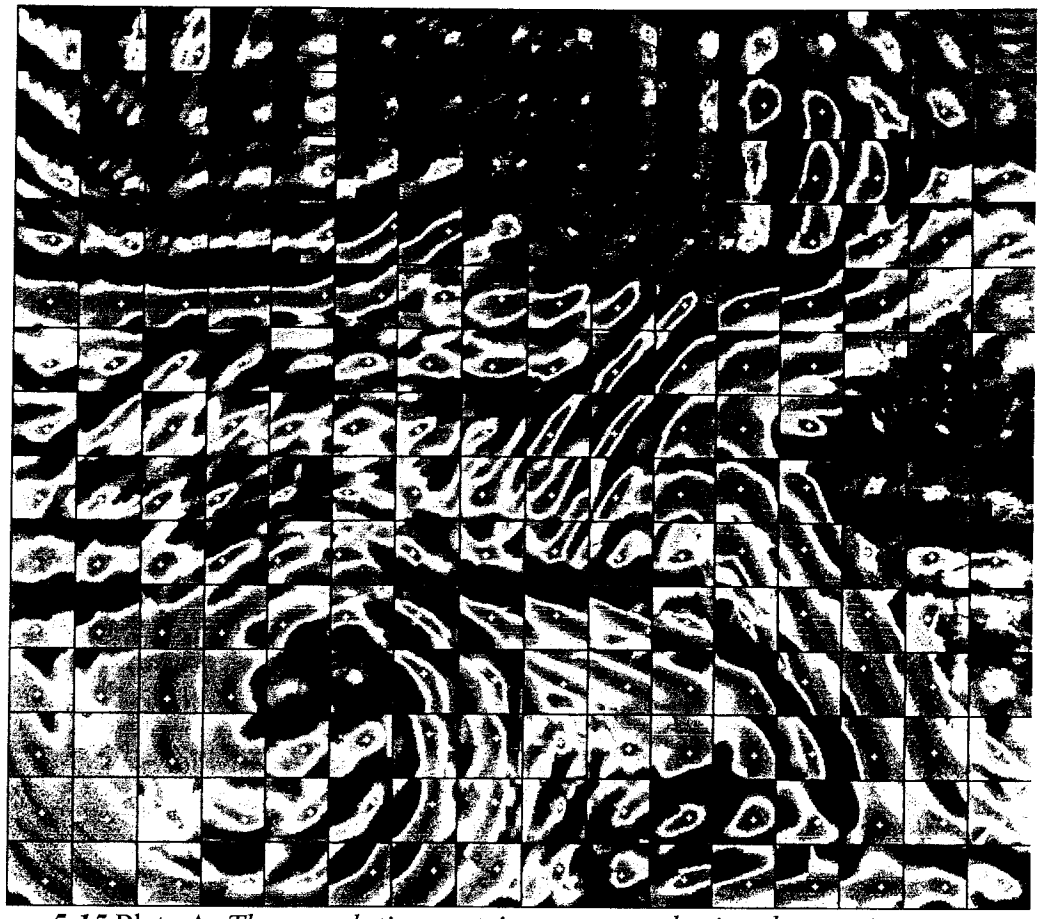

Figure 5.15 Plate A. *The correlation matrices computed using the raw images*

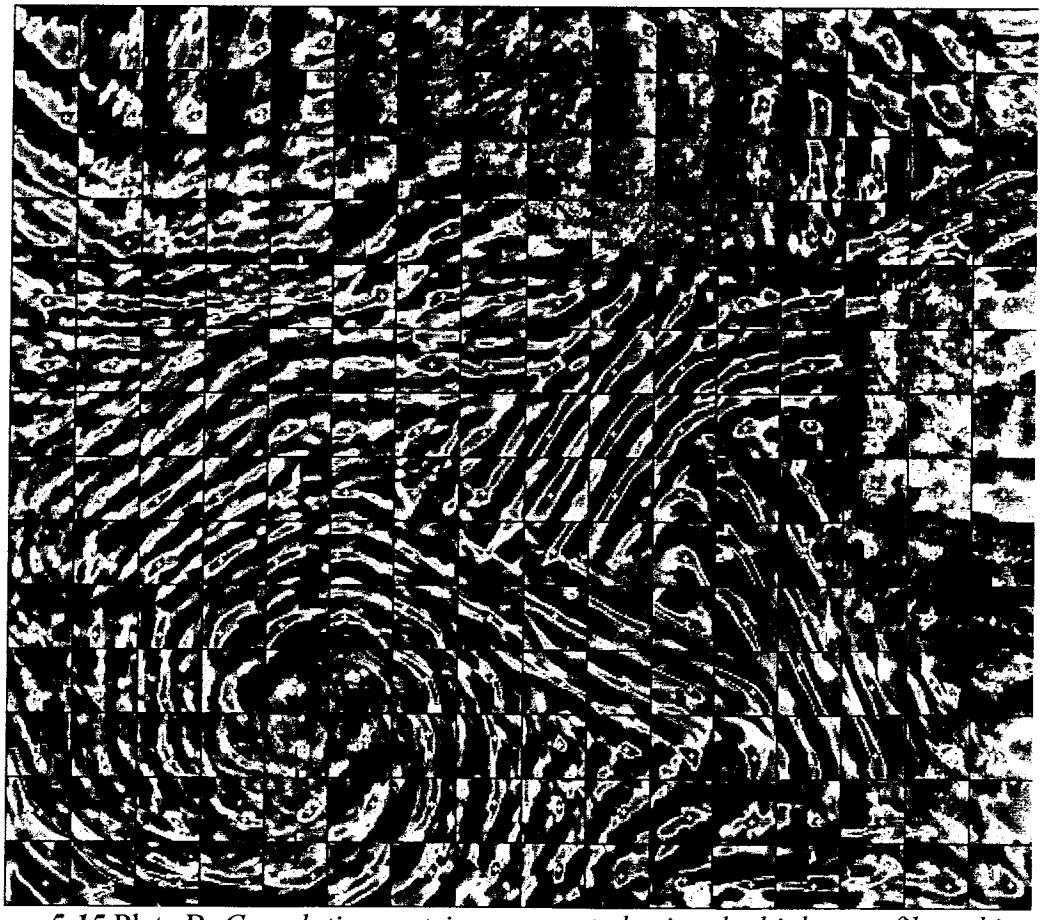

Figure 5.15 Plate B. *Correlation matrices computed using the high-pass filtered images*

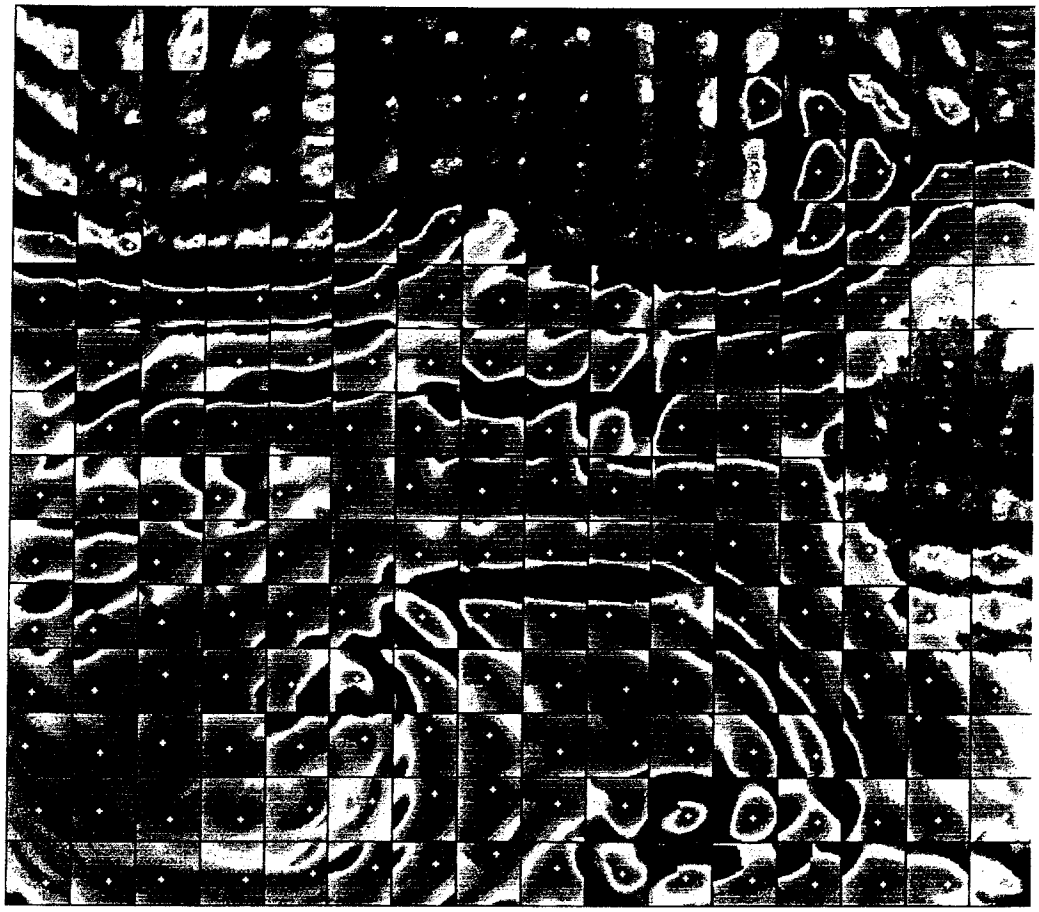

Figure 5.15 Plate C *Correlation matrices computed using the low-pass filtered images*

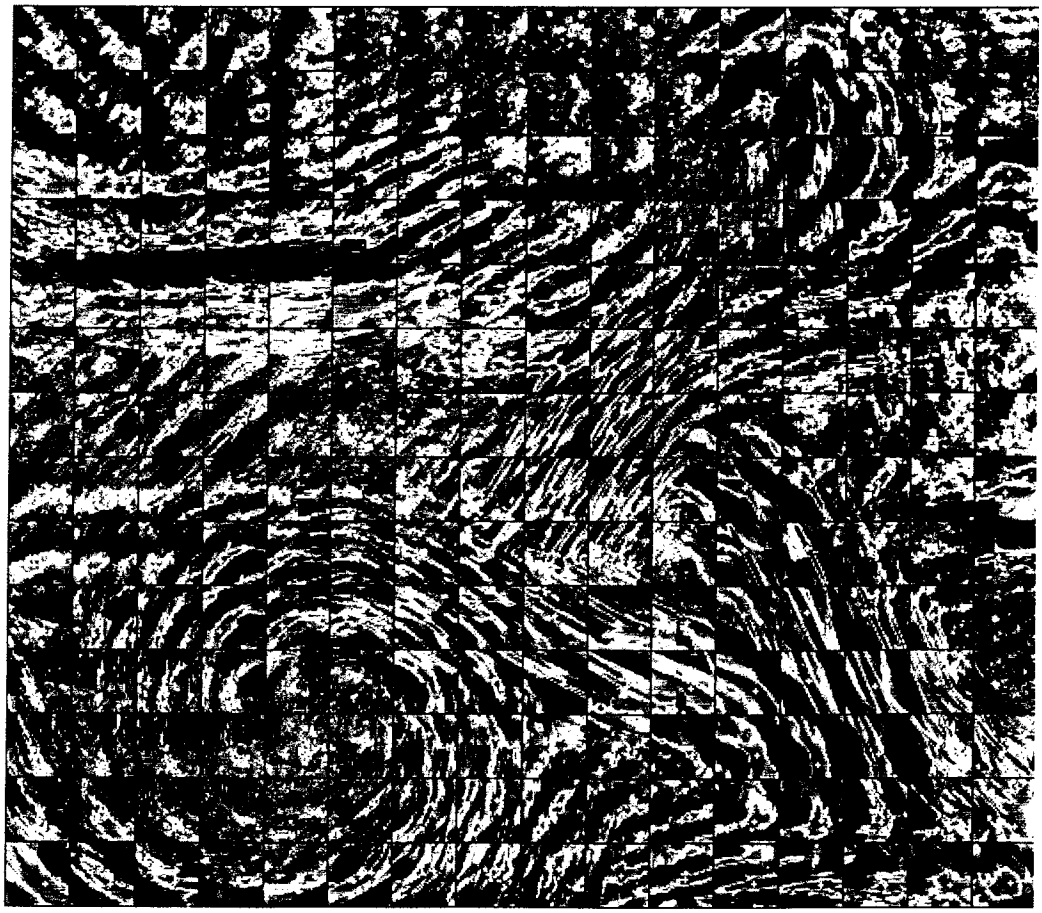

Figure 5.15 Plate D *The correlation matrices computed using the gradient images*

correlation functions are flat, and exist as an area of almost evenly high correlation values around the maxima — the maxima is therefore not significantly different from the others, thus, possibly allowing less accurate movement measurement. Additionally, the SST image is usually dominated by large scale and nearly piece-wise patterns (nearly isothermal inside the patterns) as shown in Figures 5.1 and 5.2, and this is also reported in *Kelly et al.* [1992]. The small scale features inside the patterns and along the borders are usually very weak in gradient. The high-pass filter enhances these small features and provides relatively better results. The use of the high-pass filter gives more significant improvement in the case where real images are used.

The purpose of using low-pass filter processed images in this study is to understand the characteristics of the correlation function distribution of low frequency components and their contribution to the matching process, rather than a belief that they can provide better results. The results using low-pass filtered images show, firstly, that the subsequent correlation procedure has many templates around the piecewise patterns, such as the jet and ring, which contain inadequate features to trace the movement along the isothermal direction, thus, yielding a large number of erroneous displacement estimates. Secondly, Figure 5.15 plate C shows that the correlation distribution corresponding to the low-pass filtered images is extremely flat, and a large number of correlation matrices have areas around the maxima where the correlation value is almost as high as the maxima. This is due to the extreme high auto-correlation of the long wavelength components of the SST features. Therefore, this type of correlation function has a high probability of providing erroneous estimates. Thirdly, due to the slow de-correlation, the correlation value changes little when the rotational method is applied (e.g. the average MCC value changes from 96 to 97 for the 12 hours separated images and from 95 to 96 for the 18 hours separated images). The rotational method does not improve the quality of the estimation as efficiently as when high frequency images were used. The rotational method only reduces the erroneous estimates by 41% for the case using the 18 hours separated images, and by 56% for the case using images 12 hours apart.

At the other extreme, the gradient computation using a 3×3 window removes most of the features of the SST images and leaves only the borders of the SST patterns where

there are high gradients. Therefore they only contain very high frequency components. The test results shows that the gradient images produce a worse estimation than images computed with the high-pass filtered images and the raw images, although the rotational matching method significantly improves the displacement estimation quality. This is due to the following two reasons.

Firstly, because the SST images are dominated by large scale features (low frequency components), the gradient computation process removes most of the signal of the images, therefore, yielding very noisy resultant images (noise is generally of high frequency, and enhanced in the gradient computation). This may not be a significant error source in the cases using synthetic images because, in the synthetic image generating process, the noise in the original image is advected along with the SST features and becomes part of them. While, in the case of real images, the noise in the subsequent images are random. The low signal to noise ratio may reduce the quality of the estimation.

The second reason that the gradient images yield relatively more erroneous estimates than the raw images and the high-pass filtered images is that the gradient images computed using a 3×3 window are dominated by extremely high frequency signals (features). Thus the correlation values are extremely sensitive to the unresolved deformation or displacement due to the abrupt de-correlation. The rotational MCC matching resolves the displacement due to rotational motion, but the deformation due to the straining motion still remains unresolved, because the shape of the resampling window used in the rotation search is fixed. When the gradient images are used, the unresolved straining deformation degrades the correlation values more sensitively than in the case of an unfiltered image or images processed with the 25×25 pixels running average high-pass filter.

To investigate the high sensitivity of the gradient image to a small displacement deformation, the displacement fields were computed by applying rotation search to the entire image domain (it will be referred to as full rotational search hereafter) and also applying it to only those areas of strong rotational motion which are marked with black

circles in Figure 5.7 plate A (it will be referred to as partial rotation search). The resultant displacement fields using partial rotational search and full rotational search on gradient images are shown in Figures 5.9 plate B and C respectively. The results show that, when the rotational search was fully applied, the resultant field shown had only 6 erroneous estimates for the image pair of 12 hours separation, which is similar to the case when using the high-pass filtered images. While, when the rotational search was only partially applied to the same image pair, 6 additional erroneous vectors occurred in the areas where the rotational search was not applied, which are marked with small squares in Figure 5.9 plate B (the full rotational method yielded 2 erroneous vectors in these areas, which are marked with small circles in both Figure 5.9 plate B and C, against 8 resulting from the partial rotational method). This effect can be seen from the resultant displacement fields shown in Figures 5.11 Plate B and C, which are computed using partial rotational search and full rotational search on gradient images of 18 hours separation. The full rotational search reduces the total number of erroneous estimates by 9, compared to that computed using the partial rotational search.

The high sensitivity of the gradient images to the unresolved rotation and deformation is also shown by a comparison of the resultant fields using the same partial rotational method applied to gradient images, raw images and high-pass filtered images. The resultant field for the high-pass filtered images has 3 erroneous vectors in the non-rotational-search areas. Use of gradient images yielded 8 additional erroneous vectors, giving a total of 11 bad vectors in these areas. The computed field from the raw images has 4 erroneous estimates in the non-rotation-search areas. This comparison shows that, in the non-rotational-search areas, the displacement and deformation due to rotational motion is relatively small. In these areas, the unresolved displacements and deformations resulting from the basic non-rotational computation can be tolerated when using high pass filtered, and raw images. However, they have a much higher chance of causing erroneous estimations when using gradient images. Furthermore, as mentioned previously, the rotational search can only resolve the displacement due to rotational motion. Therefore, when the deformation due to straining motion increases as the time separation increases, again due to the high sensitivity to the deformation, the estimated vector field using gradient images can be much worse than that computed using raw

images and high-pass filtered images, even when the rotational search was fully applied. (The computation using images of 18 hours separation shows the resultant field has 18 erroneous vectors for the case using raw images, 17 for that using high-pass filtered images, and 25 for the field computed using gradient images, even when the rotational resampling was applied to the entire image domain.).

Additionally, in the real image sequence, the noise is entirely random and because it is predominantly high frequency, it may be significantly enhanced in the gradient computation process. Therefore, as the results show in table 5.4, the resultant field using gradient images is very inconsistent and has a large number of erroneous vectors compared with the results using (real) raw images and (real) high-pass processed images.

The high-pass filtering enhances the small scale features and yields sharply defined correlation functions compared to those computed with the raw images (see Figure 5.13 Plate A and B). For the synthetic images, the use of the high-pass filtering slightly reduces the number of erroneous estimates compared to those computed with the raw images (reduction of 1 for the image pair of 12 hours separation, and 3 for the 18 hours separation). The high-pass filtered images yield relatively lower correlation values than when raw images are used, However, when the rotational method is applied, the increase in correlation values for the high pass filtered images is greater (larger) than for the raw images. For example, the mean maximum correlation value increases from 0.61 to 0.66 compared to 0.76 to 0.77 in the case of raw images (for the 12 hours separated images). This is because the high-pass filtering increases the sensitivity of the correlation value to the displacement and deformation. Generally, the raw and high-pass filter processed images (using 25×25 window) produced relatively better estimations in this study. Although the rotational search increased the correlation values, the mean correlation value 0.66 is still quite low, and this is due to the noise which is enhanced by high pass filtering and unresolved deformation of SST features due to straining motions. The tests in Chapter 7 showed that by resolving the deformation with bilinear flexible template the average correlation value was increased to 0.88 (see Table 7.2, section 7.5.1).

Table 5.2 and 5.3 also shows that the mean correlation values from high pass filtered images were lower than raw images. This is because the long wavelength components were removed in high pass filtered images. The correlation value of long wavelength components are less sensitive to the spatial lag and deformation between the homogeneous features. Thus, the long wavelength components contribute to the high correlation value, but they are less traceable than small features (short wavelength components). This is evident from the tests using the low pass filtered images, where the average correlation value was 0.97, it was much higher than that from the high pass filtered images (0.66), however, the displacement field derived from low pass filtered images had much more erroneous estimated vectors (37) than that derived from high pass filtered images (7). Therefore, the higher correlation values of raw images and low pass filtered images, which contain long wave length components, do not necessarily provide better resultant vector field than high pass filtered images.

In the case of using real images, the results in Table 5.4, Figures 5.12 and 5.13 show that the velocity field estimated using high-pass processed images is more consistent than that estimated using raw images. These results differ from the evaluations using synthetic images, where the resultant velocity fields using raw images is not significantly worse than those computed using high-pass filtered images. However, when using real raw images, the resultant velocity field (of 44 erroneous vectors) is significantly less consistent than that using the high pass filtered images (of 25 erroneous vectors). As has been mentioned previously, the non-advective processes are not simulated in the synthetic images, while, when using real raw images, these processes can degrade the estimation. However, a part of these non-advective processes may have relatively large spatial scales, compared with those due to mesoscale advective motions. When a high-pass filter is applied, part of the effects due to these non-advective processes (which are of large spatial scales) are removed, thus generating a relatively better velocity field estimation.

5.7.5 The Effect of Time Separation

Besides the matching methods and the dominant frequency of the input images, the study also shows that the time separation of the images sequence is also crucial to the

quality of the estimation of the velocity vector. The number of erroneous displacement vectors for image pairs of 18 hours separation are almost doubled compared with those obtained from 12 hours separation, when processed with the same computation combination. For example, with the raw images, the total erroneous estimates increased from 16 for the velocity field computed using the basic MCC method and 8 for that using the rotational method, to 31 and 18 respectively when the time interval increases from 12 hours to 18 hours. Therefore, the increased time interval generates an unacceptably inconsistent velocity field when the rotational MCC method was not applied.

5.7.6 Erroneous Estimates Due to the Form of the Correlation Function Distribution

Both the tests using synthetic images and real images show that the high-pass filtering makes the small features more traceable, and the rotational resampling resolves the displacement due to the rotational motion, thus, both processes significantly increase the quality of the estimation as shown in Table 5.2 and 5.3, and discussed in previous sections. However, a large number of erroneous estimates still resulted. These erroneous estimations were mainly due to the poor correlation between the homogeneous features in subsequent images, cloud interruption, and the multiple-peak and elongated distribution of the correlation matrix. Among these, the multiple-peak and elongated distribution of the correlation matrix are the main error sources. For example, in the resultant vector field computed using high-pass processed real images and the rotational MCC method, there were a total of 25 erroneous estimates. Among these, only 1 was due to the cloud interruption, and 3 due to the poor correlation, while the multiple-peak and elongated distribution of the correlation matrices caused 21 erroneous estimates. Figure 5.16 shows the distribution structure of the correlation matrices computed using high-pass filtered real images and the rotational MCC method. Where, the colour coding is the same as that used in Figure 5.14 and Figure 5.15 (i.e. the correlation values are coded in colours ranging from blue, green, yellow, orange to red in ascending order). The maxima of each matrix are marked with white cross. The elements rejected due to cloud cover are white. The matrices corresponding to the erroneous estimates are marked with a white frame.

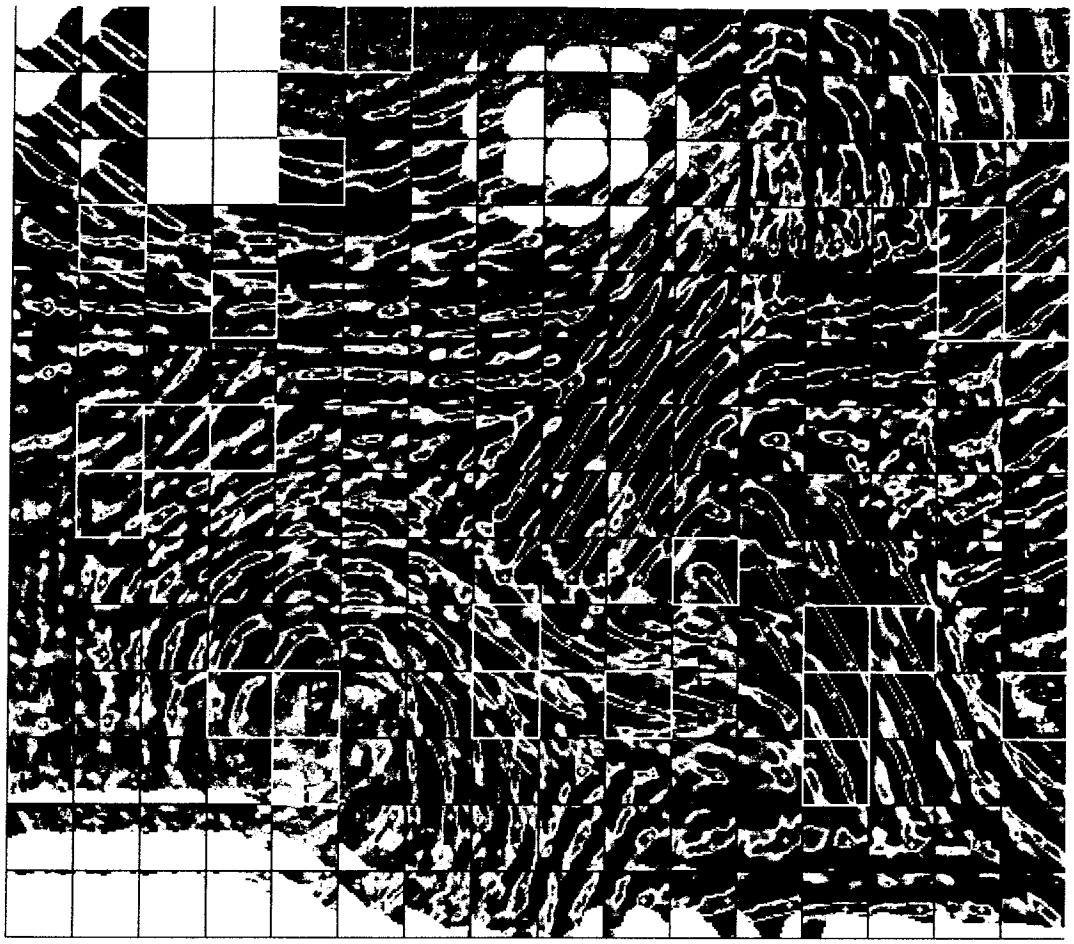

Figure 5.16 *The cross-correlation matrices computed using the rotational method and high-pass filtered* 12 *hours separated real images. The elements which were rejected due to cloud cover are coloured white, and the matrices corresponding to the erroneous estimates, are marked with white frames.*

Figures 5.15. Plate B, C and D, and Figure 5.16, show that there are a large number of correlation matrices of an elongated distribution form. The comparison between these figures and the SST image shown in Figure 5.1 shows that the elongated directions are parallel to the SST patterns borders which are of strong gradients such as the jet, in the up image domain and the eddy in low-left image domain. Since borders of these SST patterns are of a large gradient in the cross-border direction and the length of these borders are much longer than the template size, they are similar to linear step features in a template. If there are not sufficient traceable small features on these borders, or the gradients of the small features are not sufficiently strong, there may be a large number of sub-images in the search area from the second image, containing a similar pattern as the template as shown in Figure 5.17, and the correlation values corresponding to these

sub-images may be equally high. Since the gradient of gray values is strong in the cross border direct, the correlation value will decrease rapidly when the sub-image is away from the border. Therefor, the cross-correlation matrices corresponding to these features usually have a multiple-peak or elongated distribution form and the elongated direction is usually parallel to the direction of the borders.

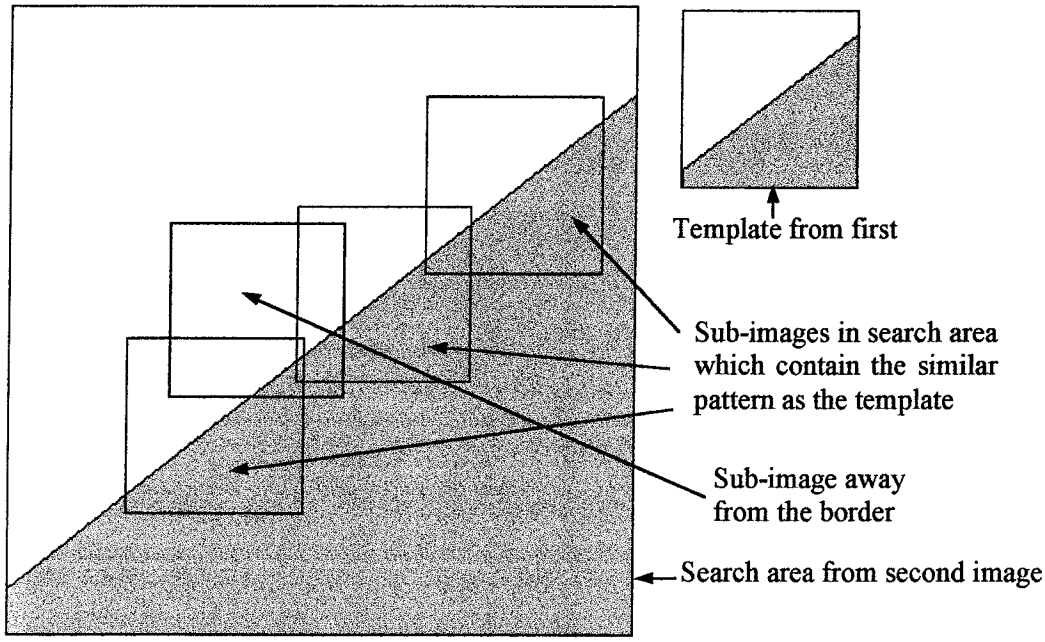

Figure 5.17 *Sketch for the cause of elongated distribution form in correlation matrix*

These types of correlation matrices have a large number of elements of almost equally high correlation values, and the maxima can easily shift from one element with high correlation value to anther with similar correlation value, due to the influence of a small amount of unresolved displacement and deformation or noise, thus resulting in erroneous estimates. The use of high-pass filtering increases the traceability of the small features, and the rotational search increases the correlation value of the rotated homologous features, which partially address the problem. However, the tests also show that, the use of high-pass filtering and the rotational search method do not change the basic multi-peak and elongated distribution structure of the correlation function. The insignificant difference in correlation value among these elements introduces uncertainty into the estimation. Thus, in these cases, the magnitude of the correlation value alone cannot provide a reliable measure, and it is essential to include neighbouring information through contextual constraints.

In a number of previous research studies, a vector coherency (a contexture constraint) test was applied to the estimated velocity field. The test assumed the velocity field should vary smoothly from grid to grid. *Kelly et al.* [1992] tested a vector field with a running 3×3 sub-grid. The vector located in the centre of the sub-grid which differed from its sub-grid mean (computed with 8 nearest neighbouring vectors) by more than 3 times that of the sub-grid standard deviation, was replaced by a new vector calculated by searching a smaller region around the mean displacement. A similar test was employed by *Emery et al.* [1992]. These studies show that the vector coherency test can eliminate large numbers of mis-estimates. The tests described in this chapter and a number of other studies (see *Emery et al.* 1992, for example) show that the vector field can frequently be incoherent throughout the whole neighbourhood rather than at just one or two isolated points. In this situation, a large percentage of the vectors used to compute the sub-grid mean may themselves be the "bad" estimates. Consequently the coherency test may yet fail due to the poor reliability of the reference set, the sub-grid mean.

There are a number of optimisation techniques that can be used to reduce the uncertainty by introducing contextual information into the estimation. In the following two chapters, two techniques will be considered to reduce the estimation uncertainty and improve the estimation reliability and robustness.

5.8 Summary

Both the studies using the synthetic images and the real images reveal three main facts:

1. The rotational search is essential in high dynamic areas, such as the frontal area which may have strong eddies and rings. Especially, when the temporal separation increases to 12 hours and above, the unresolved displacements and deformations due to rotation and straining may significantly degrade the estimation of the displacement field. The tests in this chapter show that the inclusion of the rotational motion into the estimation model significantly improves the quality of the results. Tests also

show that the effectiveness of using the rotational MCC method increases as the frequency of the SST features increases.

2. The use of a high-pass filter of 25×25 to 35×35 window, can enhance the traceability of small features, and consequently, improve the estimation quality. However, it also reduces the tolerance to unresolved displacement and deformation. Therefore, when the high-pass filter or gradient operator is used, the use of the rotational search is even more necessary.

3. Due to the high auto-correlation along the border of the SST patterns, the corresponding cross-correlation function frequently has a multi-peak or elongated distribution. This form of distribution of the correlation function introduces a high uncertainty into the estimation of displacement field, and consequently, results in erroneous estimates. The rotational search and high-pass filtering partially addresses this problem, but both techniques cannot change the basic (the multi-peak or elongated) distribution structure. A correlation function of such distribution cannot alone provide a reliable measure for the displacement determination, and additional information is essential to resolve the uncertainty..

Chapter 6

Improving Estimation Reliability with Relaxation Labelling

6.1 Introduction

The study in Chapter 5 has shown that a large number of the correlation matrices are of multi-peak or elongated distribution due to the high auto-correlation of the borders of SST patterns, and the correlation matrices of such form introduce uncertainty in homogeneous feature correlation. The use of high pass filtering and rotational search improves the estimation quality. These two techniques partially addressed the problem, but does not change the basic multi-peak and elongated distribution structure of a correlation function. In these situations, the magnitude of correlation value alone cannot provide a reliable measure. Therefore, it is essential to include extra information to reduce the uncertainty and improve the reliability. The contextual relation is a valuable information source to reduce the these effects.

In a number of previous research studies (for examples, *Kelly et al.* [1992] and *Emery et al.* [1992]), a vector coherency (a contextual constraint) test was applied to the displacements estimated using MCC method . The test assumed that the velocity field should vary smoothly from grid to grid. These researchers showed that the vector coherency test can effectively eliminate mis-estimates in some cases. However, the vector field can frequently contain a large percentage of erroneous vectors in a sub-grid. In this situation, the sub-grid mean, which is used as the reference for the coherency test, may be the "bad" estimation itself. Consequently the coherency test may yet fail due to the poor reliability of the reference set.

There are a number of optimisation techniques that can be used to reduce the estimation uncertainty and increase consistency such as the relaxation labelling and the dynamic programming. In this chapter, a new approach based on relaxation labelling techniques

is proposed and tested to reduce the uncertainty due to the multi-peak or elongated distribution of the correlation matrix. The new approach, first computes the correlation distribution of each search area, that the correlation value of each position of the search area is computed, using the correlation computation method with rotational searching which has been described and tested in Chapter 5. Then, the computed correlation matrices (the correlation distribution function) are scanned, to identify and search for the multi-peaks and the ridge of the elongated correlation clusters, which are usually of high correlation value. The identified elements, the multi-peaks and elements on the ridge of the elongated correlation patterns, are selected as the initial candidates for the relaxation process. Then a relaxation approach is applied to iteratively reduce the ambiguity among the multiple candidates, and optimise the estimation based on both the compatibility of contextual relation and correlation value. Finally, a refining process, also based on relaxation labelling technique, is then applied to further improve the quality of estimation. The candidate selection and relaxation processes themselves are very fast. However, since the correlation distribution is computed using brute force strategy as that used in MCC method, this step is extremely time consuming. To improve the computation efficiency, the feasibility of using the correlation distribution coarsely determined with a leap-frog strategy for this approach, is also tested in this chapter.

6.2 The Basis of the Relaxation Labelling Process

6.2.1 The Mathematical Framework of the Relaxation Labelling Process

Relaxation labelling processes are a class of parallel, iterative approaches for reducing ambiguity and increasing consistency of a relational net. The relaxation labelling approach was popularised by *Rosenfeld et al.* [1976]. Since then, it has been widely employed for image classification, edge enhancement, feature enhancement, stereo matching for digital terrain model (DTM) generation and some high-level image interpretation. A comprehensive review has been given by *Kittler et al.* [1985].

There are two sources of information employed in the relaxation labelling processes:

1. the initial probability of labels, the measure of likelihood or certainty of each candidate is appropriate for a node in a relational net, and
2. the compatibility relationships among candidates at neighbouring nodes.

Assume that there are a set of objects $A=\{a_i \mid i=1,2,...n\}$ with specified neighbourhood relations holding over this set. The object set forms a relational net and each of the objects can be viewed as a node of the net. In this application, the grid is viewed as a relational net and the grid points are the nodes of the relational net. Attached to each of the objects (nodes) is a set of labels (the candidate velocity vectors in our case) $\Lambda_i=\{\lambda_k \mid k=1,2,...m\}$, where each candidate indicates a possible interpretative assertion of that node. Each of these candidates has an initial measure of likelihood or certainty to indicate the degree that the candidate λ_k is appropriate for the node a_i. This measure is denoted by $P_i=\{p_i(\lambda_k) \mid k=1,2,..m,\}$

The probability estimates for each label are iteratively updated on the basis of the probabilities distributed over the label sets on neighbouring nodes. These probabilities interact through a compatibility function defined over pairs or groups of candidates on neighbouring nodes. The compatibility can either have a form of correlation coefficients between a candidate λ_k on node a_i and candidate λ'_l on node a_j, denoted by $r_{ij}(\lambda_k, \lambda'_l)$, $-1 \le r_{ij}(\lambda_k, \lambda'_l) \ge 1$ [e.g. *Rosenfeld et al* 1976], or a form of conditional probability $p_{ij}(\lambda_k \mid \lambda'_l)$, $0 \le p_{ij}(\lambda_k \mid \lambda'_l) \ge 1$ [e.g. *Peleg*, 1980]. The compatibility can be measured either on the basis of an apriori model (for example, a physical model) or statistics. It is these compatibility measures which provide the means for incorporating heuristic knowledge into the process. The initial probabilities $P^0_i=\{p^0_i(\lambda_k) \mid k=1,2,..m,\}$, can be obtained either based on some sort of a posteriori information, or assigned a uniform value, in the absence of any a posteriori information.

Based on the initial probabilities of each label and mutual compatibilities, the relaxation labelling process iteratively updates the probability of each label to achieve an unambiguous and consistent labelling of the relational net. The foundational updating scheme (with a first order compatibility function) of the non-linear probabilistic

relaxation labelling process suggested by *Rosenfeld et al* [1976] is formulated as follows.

Assume, an arbitrary node a_i within a relational net which has m_i candidates λ_k k=1,2,...m_i . The node a_i has n related neighbours a_j j=1,2,..n and each neighbouring node has m_j candidates λ'_l l=1,2,...m_j. The supporting evidence, or contextual influence, given to a label λ_k on node a_i by candidates λ'_l l=1,2,...m_j on node a_j is given by —

$$q_{ij}^t(\lambda_k) = \sum_{l=1}^{m_j} r_{ij}(\lambda_k, \lambda'_l) p_j^t(\lambda'_l) \tag{6.1a}$$

and the total support for this candidate provided by all of its related neighbours is given by —

$$q_i^t(\lambda_k) = \sum_{j=1}^{n} c_{ij} q_{ij}^t(\lambda_k) = \sum_{j=1}^{n} c_{ij} \sum_{l=1}^{m_j} r_{ij}(\lambda_k, \lambda'_l) p_j^t(\lambda'_l) \tag{6.1b}$$

where the c_{ij} are the weights which satisfy $\sum_{j=1}^{n} c_{ij} = 1$ and insure that $q_i^t(\lambda_k)$ is in the range [-1,1]. Then the probability of the candidate λ_k on node a_i being updated is given by following equation —

$$p_i^{t+1}(\lambda_k) = \frac{p_i^t(\lambda_k)[1 + q_i^t(\lambda_k)]}{\sum_{k=1}^{m} p_i^t(\lambda_k)[1 + q_i^t(\lambda_k)]} \tag{6.1c}$$

where the superscript t is the iteration number, $r_{ij}(\lambda_k, \lambda'_l)$, $-1 \le r_{ij}(\lambda_k, \lambda'_l) \ge 1$ denote the first order compatibility coefficient between candidate λ_k at node a_i and the candidate λ'_l at node a_j. The probability of each candidate on each node is updated iteratively, until no further changes occur. It is required that the sum of the initial probabilities of all labels on a node satisfy $\sum_{k=1}^{m} p_i^0(\lambda_k) = 1$ for every note a_i and the equation (6.1c) insures the updated probabilities still satisfy the condition $\sum_{k=1}^{m} p_i^t(\lambda_k) = 1$ for every i and t.

It is possible to define the compatibility function and the support function in terms of higher order combinations of neighbouring candidates. In second order combination cases, the support function and the updating equation have the following form—

$$q_0^t(\lambda_l) = \sum_{s=1}^{S} c_s \sum_{k=1}^{m_i} \sum_{n=1}^{m_j} r_{i,0,j}(\lambda'_k, \lambda_l, \lambda''_n) p_i^t(\lambda'_k) p_j^t(\lambda''_n) \qquad (6.2a)$$

$$p_0^{t+1}(\lambda_l) = \frac{p_0^t(\lambda_l)[1+q_0^t(\lambda_l)]}{\sum_{l=1}^{m_0} p_0^t(\lambda_l)[1+q_0^t(\lambda_l)]} \qquad (6.2b)$$

where S is the number of the combinations of neighbouring nodes, c_s are the weights which satisfy $\sum_{s=1}^{S} c_s = 1$ to insure $q_j^t(\lambda_k)$ within the range [-1,1], and $r_{i,0,j}(\lambda'_k, \lambda_l, \lambda''_n)$ denotes the compatibility of candidate vector λ_l at node a_0 against candidate vector λ'_k at the neighbouring node a_i and λ''_n at a_j. The relaxation process in this proposed approach is of second order neighbouring combinations.

6.2.2 Convergence and Equilibrium Point of Relaxation Process

The probability relaxation schemes have been demonstrated in many applications, to have a capability to increase the consistency and reduce the ambiguity of the labelling of a relational network. However, its formal convergence properties were not given by *Rosenfeld et al.* [1976]. *Zucker et al* [1978] have shown that the process, with an updating scheme as described in equation (6.1c) or (6.2c), could converge in following cases, and if the process converges, then following one of following cases results:

Case 1: $p_i^t(\lambda_k) \neq 0$ for all i and k and $Q_i^t = \beta I$, where β is a scalar, and I is an identity matrix, and Q_i^t is m×m diagonal matrix which contains the total supporting coefficients for each label attached on node a_i.

$$Q_i^t = \begin{bmatrix} q_i^t(\lambda_1) & 0 & \dots & 0 \\ 0 & q_i^t(\lambda_2) & \dots & 0 \\ \dots & \dots & \dots & \dots \\ 0 & 0 & \dots & q_i^t(\lambda_m) \end{bmatrix}$$

case 2: $p_i^t(\lambda_\alpha)=0$ for some labels λ_α (but not all), $1\leq \alpha \geq m$. The corresponding $q_i^t(\lambda_\alpha)$ are arbitrary, however the remaining $q_i^t(\lambda_k)=\beta$ for $k\neq\alpha$.

case 3: $p_i^t(\lambda_\alpha)=1$ for exactly one label λ_α , $1\leq \alpha \geq m$, and $p_i^t(\lambda_k)=0$ for all $k\neq\alpha$. This corresponds to a unique interpretation case.

The equilibrium points can be illustrated as follows. If the process converges after iteration "t+1", the updated probabilities of all labels at all nodes satisfy

$$[p_i^{t+1}(\lambda_k) - p_i^t(\lambda_k)] = 0 \qquad \text{for every } i \text{ and } k \qquad (6.3)$$

Practically, the relaxation process is terminated when this difference smaller a sufficient value ε. Substituting updating scheme (6.1c) into equation (6.3), gives the following relationship:

$$p_i^t(\lambda_k)\left[\frac{1+q_i^t(\lambda_k)}{\sum_{k=1}^{m} p_i^t(\lambda_k)[1+q_i^t(\lambda_k)]}-1\right]=0 \quad \text{for every } i \text{ and } k \qquad (6.4)$$

Since $\sum_{k=1}^{m} p_i^t(\lambda_k)=1$, the expression in the bracket of equation (6.4), becomes the following condition for every i and k, where $p_i^t(\lambda_k)\neq 0$.

$$q_i^t(\lambda_k)=\sum_{k=1}^{m} p_i^t(\lambda_k)q_i^t(\lambda_k) \qquad \text{for every } i \text{ and } k \qquad (6.5)$$

Since this expression is a constant for all i and k, and $\sum_{k=1}^{m} p_i^t(\lambda_k)=1$, if $p_i^t(\lambda_k)\neq 0$ for all i and k (the case 1), then the requirement expressed by equation (6.5) implies that $Q_i^t=\beta I$. For case 2, in which $p_i^t(\lambda_\alpha) = 0$ for some candidates λ_α, $1\leq \alpha \geq m$, and the probability $p_i^t(\lambda_k) \neq 0$ for other candidates λ_k $k \neq \alpha$ (i.e. The node a_i has m candidates λ_k, k=1...m. Among these m candidates, the probabilities corresponding to some candidates λ_α becomes zero after t iterations, where the subscript α used to denote the candidates with zero probability). The equation (6.5) implies that the $q_i^t(\lambda_k) = \beta$ for candidates λ_k with $p_i^t(\lambda_k)\neq 0$ (where the β is a scalar, a constant, as previously defined), while the $q_i^t(\lambda_k)$ can be arbitrary, for the candidates λ_α with probability $p_i^t(\lambda_\alpha) = 0$. The case 3, in which

$p^t_i(\lambda_\alpha)=1$ for exactly one label λ_α , $1\leq \alpha \geq m$, and $p^t_i(\lambda_k)=0$ for all $k\neq\alpha$., satisfies the condition described by equation (6.5). Since on each node a_i has only one candidate probability of 1 (i.e. one candidate is appropriate for one node), this is a unique interpretation case. Detailed discussion of the equilibrium points of the updating scheme expressed within the equation (6.1a),(6.1b) and (6.1c) can be found in *Zucker et al.* [1978].

Generally, the processes could converge to both unambiguous and ambiguous interpretations. In an unambiguous interpretation, each node has only one possible label, while, when the neighbouring contribution approaches a constant, the process converges to an ambiguous interpretation. The intuitive sense of this situation is that the network contains insufficient local information suitable for further resolving the ambiguity. In such cases, additional information is required or control should be passed to another process.

6.3 The Design of the Relaxation Approach for Velocity Field Estimation

The proposed approach consists of four processing steps:

1. correlation distribution computation
2. correlation distribution feature identifying and candidate selection
3. approximate relaxation process
4. refining process

The flowchart of these processes is shown in Figure 6.1. The details of each step will be discussed as follows.

6.3.1 Grid and Correlation Computation

As for the MCC method, in the new approach, the image domain is divided into a grid. Each node of the grid associated with a sub-image from the first image, is named as a pattern tile, and a search area defined in the second image (see Chapter 5 for the details). The nodes of the grid are 24 pixels (about 26 km) apart from each other in this

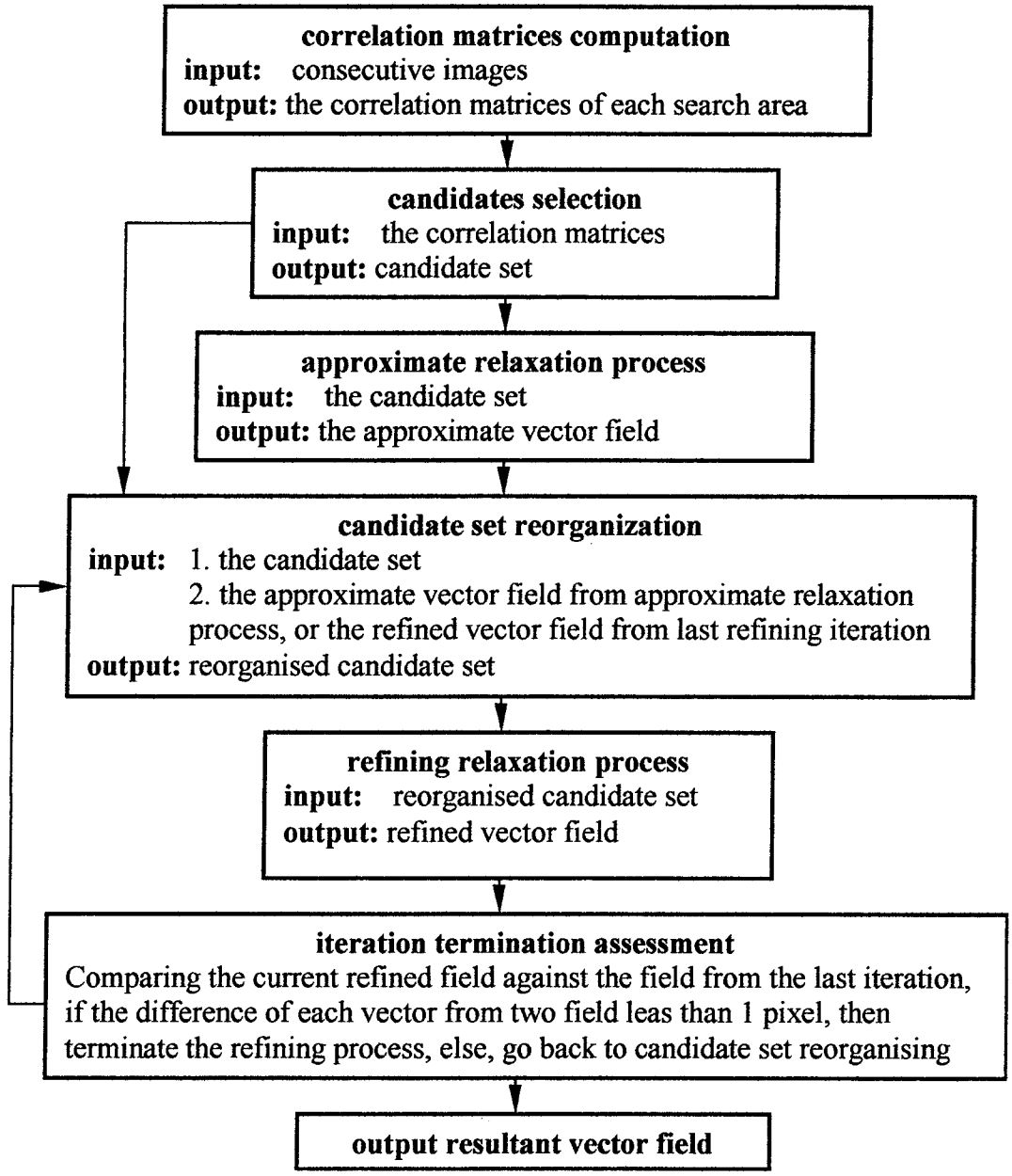

Figure 6.1 *The flowchart of relaxation estimation scheme*

study. The pattern tile is 45×45 pixels, the size of the search area being defined according to the possible maximum displacement. The approach firstly computes the correlation value of every position of each search area with a rotational correlation computation method as described in Chapter 5 (see also *Kamachi* [1989] for details). To include all possible estimates, the approach records the correlation value of the entire search area, rather than simply selecting the search-area-maxima as the estimates of the corresponding node, as in the MCC method. The recorded correlation values of a search

area forms a correlation matrix for each element of the matrix, corresponding to each position of the search area, which represents the cross-correlation function distribution within a search area. Then, the computed correlation matrices are input to the candidate selection step.

The subsequent steps — the candidate selection, the relaxation and the refining, are very fast processes. However, the computation efficiency of the approach is limited by this extremely time-consuming correlation matrix computation step, due to its brute force search strategy. To improve the computational efficiency, in this chapter, the relaxation process, based on the candidates selected from matrices coarsely computed using the leap-frog strategy, is tested.

6.3.2 Candidate (Label) Selection and Initial Probability

As has been shown in chapter 5, the correlation function frequently has a multi-peak and elongated distribution. The peaks or the ridge of the elongated distributed correlation clusters are usually of almost of equal correlation value. Thus, all the displacements corresponding to these elements are the possible estimates of a node. Generally, each node is associated with more than one candidate. Then, the optimal estimate of each node is determined from the selected candidate set by the relaxation process, based on the correlation value of each candidate and the compatibility with the candidates at its neighbouring nodes.

Theoretically, all peaks and the elements along the ridge of the elongated clusters should be selected as the candidates due to their almost equally high correlation values. However, if two candidate elements are spatially locate too close to each other, the corresponding candidate vectors would also be similar. The compatibility values of these two candidate vectors would be also very similar to each other. If the initial probabilities of these two candidate vectors are also similar, the equation (6.1a) (6.1b) (6.1c) would update the probabilities of these two candidates in similar way, thus, the process could converges to a ambiguous equilibrium point described in case 2 in section 6.2.2 (ie. There are more one candidate equally appropriate to one node, and the relaxation process based on *Rosenfeld et al* [1976] scheme may not able to

"discriminate" which one is better). Thus, it is essential to have a distance between adjacent candidates. However, if the interval is too large, the selection process may miss the correct candidate. Because the results of the relaxation process can be easily refined with further processing such as a least squares matching method, the procedure generally requires less precise, but correct initial estimates. In other words, the focus of this process is correctness rather than accuracy. The approach only requires the peaks of each cluster and the elements along the ridge of elongated clusters to be selected as the candidates. The selection is further constrained to require the candidates to be separated from each other by a certain distance. The candidate selection is implemented using a matrix scanning process which consists of histogram analysis and cluster analysis.

The first step of the scanning process is histogram analysis. The analysis process firstly generates a histogram of population of elements at each correlation level above a basic correlation threshold N(c), where c is the correlation value N is the number of elements of a correlation value c. The basic correlation threshold is determined using a empirical method similar to that used in *Tokmakian et al.* [1990] by applying the MCC method (without rotational search) to 4 unrelated images. The images are separated by 6 months to 2 years and geographically separated by 250km to 500 km, assuming all correlations between the images to be random. The images were organised into 6 combinations (pairs). The 80 percentile value for all of the maximum correlations found between the images was used as the basic correlation threshold. When the high-pass filtered (with 35×35 window) images were used, the value was 0.42, and in following test the basic correlation threshold was set at 0.45. In contrast to the correlation significance test in the MCC method, the basic correlation threshold is only used to exclude the elements which are significantly not correlated. Therefore the threshold value should be lower than in the significance test. Since the selected candidates will be processed by the relaxation process, the accuracy of the determination of this threshold is much less crucial than in the significance test of the MCC method.

If the population of elements of correlation values above the basic correlation threshold is greater than 1/10 of the total number of elements of the matrix, the process then adaptively adjusted upwards the correlation threshold, based on the histogram N(c), to

let only the top 1/10 of the elements of the highest correlation values pass this threshold, and only the elements of a correlation values greater than the increased correlation threshold are considered in the subsequent cluster analysis. When the population of the elements of correlation values greater than basic correlation threshold is less then 1/10 of the total number of elements of the correlation matrix, the elements of correlation value above the basic correlation threshold are passed onto the subsequent analysis.

The cluster analysis is designed to identify the characteristics of the distribution of the correlation function, and provides the following information

- whether the matrix is multi-cluster distributed
- if the matrix has a multi-cluster distribution, then how many clusters exist
- the population of each cluster
- the shape of each cluster

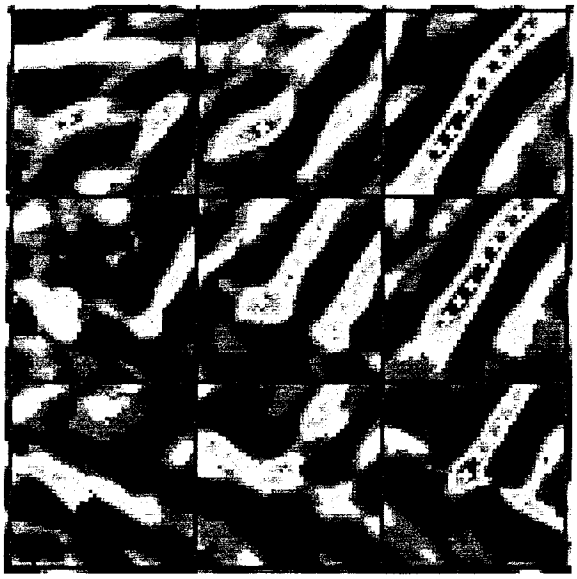

***Figure* 6.2** *The selected candidates based on the full resolution correlation matrices computed using rotational MCC method for* 18 *hours (equivalent) separated high-pass filtered synthetic images. In the figure, each square is a correlation matrix, the correlation value are colour-coded ranging from blue, green, yellow, orange to red in ascending order. The selected candidates are marked with white crosses.*

If a cluster is of elongated distribution, then the process searches for the ridge of the cluster and selects a candidate at specific intervals starting from the cluster maxima along the ridge of the pattern. The interval between the candidates is designed to avoid

the relaxation process converging to an ambiguous equilibrium for the reason discussed in the beginning of this section. As the resultant field will be refined by a least squares method, and the focus of the relaxation process is the correctness rather than the accuracy of displacement field, the selection of the interval between the candidates is not very crucial to the final result. To approximately determine the candidates' spatial interval, three candidate sets were selected from full resolution correlation matrices with intervals respectively 5 pixels, 7 pixels and 10 pixels apart, and tested using the relaxation process described in sections 6.3.3 to 6.3.5. Tests show that in all these three cases the process converges, and the resultant fields are identical. However, the computation using the candidate set selected with 5 pixels interval takes about twice as long as the cases using candidate sets with 7 and 10 pixels intervals, due to the fact that the closer the candidate, the more ambiguous the candidate set. In the tests described in this chapter, the interval of 7 pixels was empirically chosen for selecting candidates from full resolution correlation matrices, and 2 elements (i.e. correlation matrix elements) for the cases using coarse correlation matrix determined with the leap-frog method. This method computes the correlation value of every 5th position of a search area, rather than every position, when the leap-frog step is set at 5. When the leap-frog step equals 5 and the candidate interval is 2 elements apart, it is equivalent to an interval of 10 pixels in the full resolution correlation matrix case. Then the coordinates in the correlation matrix (r,c) of these selected candidates are converted to corresponding displacement vectors (dx,dy). As an example, the selected candidates based on the correlation matrices computed using the rotational MCC method with 18 hours separated high-pass filtered synthetic image is shown in Figure 6.2.

The initial probability of the candidate vectors at each grid point are calculated based on their correlation value. Because the approach is based on the scheme suggested by *Rosenfeld et al* [1976], which requires the sum of the initial probabilities of candidates of a node to be equal to 1, the initial probability of a candidate λ_k at node i is calculated using the following equation:

$$p_i(\lambda_k) = \frac{\rho'_i(\lambda_k)}{\sum_{k=1}^{m_i} \rho'_i(\lambda_k)} \tag{6.7}$$

where $$\rho'_i(\lambda_k) = s(\rho_i(\lambda_k) - \rho_{\min}) + \rho_{\min}$$

and $\rho_i(\lambda_k)$ is the correlation value the candidate λ_k at node a_i, m_i is the number of candidates at a_i, ρ_{min} is the minimum correlation value among the selected candidates of that the node is associated with, and s is the a scaling factor, which controls the differences between the initial probabilities of selected candidates.

The relaxation procedure is based on two sources of information, the initial probability and the compatibility among the candidates of neighbouring nodes. Generally, the larger the differences among the initial probabilities of the candidates of a node, the lower the degree of the initial ambiguity of the relaxation process, and the initial probabilities may contribute more to the relaxation process in the first a number of iterations. For the relaxation process based on *Rosenfeld et al.* [1976] scheme, when only one candidate has an probability equals 1, among the candidates of a node, while, the probabilities attached to the rest candidates equal to zero is a unique (unambiguous) interpretation case, as the case 3 discussed in section 6.2.2. Therefore, when initial probabilities of a node have a distribution close to this unique interpretation case, this node is nearly unambiguous. At least in the first few iterations the candidate of initial probability nearly equals 1, can have a significant influence on the relaxation process. At the other extreme, if all candidates of a node have equal initial probability, $p_i(\lambda_k) = \frac{1}{m_i}$, k=1,2,...,m_i, then the initial probabilities do not convey any information, and the relaxation procedure is based solely on the compatibility among the candidates. Because the initial probabilities deliver the valuable information of the basic structure of the estimating field, it may be preferred to use a large s to influence the relaxation process, allowing convergence to a consistent field closer to the initial status. Alternatively, because the initial probabilities contain a certain degree of error, the use of a large s value may also strengthen the influence of candidates of the erroneous high-correlation value (or erroneous high-initial-probability). Therefore, the question to resolve is whether the relaxation process has a capacity to adjust the erroneous initial status when a large value of s is used, in other words, whether the magnitude of the scaling coefficient s can affect the result of the relaxation process. This will be tested in a series of experiments given later in this chapter.

In the cases of real images, the grids (nodes) may be situated in cloud covered areas, where the corresponding correlation matrices cannot be computed. Therefore, the previous method cannot provide candidates and associated initial probabilities for these nodes. Hereafter, these nodes are named as "no-apriori information" nodes. The treatment of no-apriori information nodes will be discussed in the following section .

6.3.3 Neighbourhood Structure and Compatibility Function in the Approximate Relaxation Process

As has been discussed in section 6.2, in a relaxation process of second order neighbourhood candidate combinations, the compatibility function $r_{i,0,j}(\lambda'_k,\lambda_l,\lambda''_n)$ provides a measure of the compatibility of the candidate vector λ_l at node a_0 with candidate vector λ'_k at neighbouring node a_i, and λ''_n at a_j. The compatibility function plays a role in a similar way to the constraint equation in the least squares computation. For the ocean surface velocity field estimation, theoretically the compatibility function can be designed on the basis of physical models, such as the momentum conservation equation, continuity equation *etc.* or some approximation assumptions, such as the smoothness of the velocity field which is used in the proposed approach. However, the compatibility function and the support function based on these models contains the higher order neighbourhood candidate combinations (orders higher than 3, ie. the compatibility function, supporting function, and updating function are based on a combination of more then 4 neighbouring nodes, rather than a combination of 3 neighbouring nodes as the case of second order combination described by equation (6.2a) and (6.2b)), therefore, increase computational complexity and computing costs.

The appropriateness of the assumption of smoothness of the velocity field to the specific problem depends on the gradient of the velocity shear of the area and the density of the grid points. The relatively dense grids used in the study are 24 pixels (about 26 km) apart. Although, the spatial scale of some oceanic processes is not very well known yet, through a series of oceanographic experiments during the last decades, oceanographers have found that the variabilities at length scales great than 50 km carries most of the dynamic energy especially, the variabilities of a spatial scale 100 km (see Maul et al. [1980], TOPEX [1981] for example). This part of processes are most

important for understanding oceanic currents. It is reasonable to assume that the velocity or the displacement field due to this part processes should vary smoothly in most parts of image domain at such a grid scale. The estimated field in the area of large velocity shear gradients may be over-smoothed in the approximate relaxation process and may need to be refined. Thus, in this study, the compatibility function in the approximate relaxation step is designed based on the assumption of the smoothness of the velocity field, and the function uses the magnitude of the second order difference of 3 neighbouring candidates (see equation (6.8)) as the measure of the smoothness. The compatibility function and the support function contain the second order combination of neighbouring candidates.

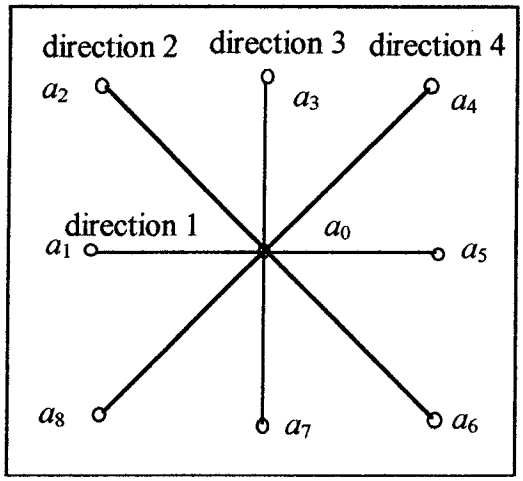

Figure 6.3 *The neighbourhood structure for the compatibility and support function*

For the compatibility function and support function based on the second order difference, we further define the relation net to possess a neighbourhood structure as shown in Figure 6.3, where each node of the grid a_0 relates only to its 8 immediate neighbouring grid points, a_1, a_2 ... a_8. The contextual information contained by the far neighbours is not directly passed onto it through the compatibility coefficient, but conveyed through the iterative procedure. Each node is attached to a set of candidate displacement vectors (or velocity vectors) which are selected in the way described in section 6.3.2. Each of the candidate vectors has an initial probability determined from the cross-correlation value computed using the rotational correlation method. With the a_0 as the center, these 9 related nodes can be organised as 4 groups in 4 directions as shown in Figure 6.3. For example, in the horizontal direction, there is a group of nodes

a_1, a_0 and a_5. In this approach, only the compatibilities in each of these 4 directions are computed.

For a direction which contains nodes a_i, a_0 and a_j, and each of these node is attached to a set of candidates λ'_k k=1,2...m_i, λ_l l=1,2...m_0 and λ''_n n=1,2...m_j respectively, then the compatibility of a candidate λ_l at a_0 with candidates λ'_k and λ''_n at neighbouring nodes a_i and a_j — $r_{i,0,j}(\lambda'_k,\lambda_l,\lambda''_n)$, is derived based on the magnitude of the second order difference of these three candidates, $d_{i,0,j}(\lambda'_k,\lambda_l,\lambda''_n)$ in the approximate relaxation process. The magnitude of the second order difference is given by the following equation:

$$\begin{aligned} d_{i,0,j}(\lambda'_k,\lambda_l,\lambda''_n) &= \left\|(\vec{\lambda}'_k-\vec{\lambda}_l)-(\vec{\lambda}_l-\vec{\lambda}''_n)\right\| \\ &= \sqrt{(x_k-2x_l+x_n)^2+(y_k-2y_l+y_n)^2} \end{aligned} \tag{6.8}$$

where, the x_k , y_k , x_l , y_l, and x_n , y_n are the components in the x and y direction of vectors λ'_k , λ_l, and λ''_n respectively. Then, the second order difference is converted to the compatibility coefficient using the following function:

$$r_{i,0,j}(\lambda'_k,\lambda_l,\lambda''_n) = 2\exp(\frac{-d^2_{i,0,j}}{2\sigma^2}) - 1 \tag{6.9}$$

The compatibility coefficients computed with equation (6.9) satisfy the rules described in *Rosenfeld et al* [1976], being —

1. The compatibility function is defined within the range $-1 \le r_{i,0,j}(\lambda'_k, \lambda_l,\lambda''_n) \ge 1$.
2. When the $d_{i,0,j}(\lambda'_k,\lambda_l,\lambda''_n)$ = 0, the vectors vary smoothly, and the compatibility coefficient $r_{i,0,j}(\lambda'_k, \lambda_l,\lambda''_n)$=1.
3. As the difference among the candidates $d_{i,0,j}(\lambda'_k,\lambda_l,\lambda''_n)$ increases, the compatibility coefficient $r_{i,0,j}(\lambda'_k, \lambda_l,\lambda''_n)$ decreases towards -1.

The parameter σ in the compatibility function (6.9) affects its sensitivity to the difference of vectors and convergence speed of the relaxation procedure. If σ is large, the differences among the compatibility coefficients of the candidates of a node will be small, and the relaxation procedure will converge slowly. Conversely, if σ is small, the

process may converge faster, and the local compatibility and local initial probability information will predominate. When the local initial probability (i.e. the initial probability of candidates) information is not correct and the erroneous candidates have extremely large initial probabilities, the correct candidates at the node of the outstanding erroneous candidates, and the candidates attached to the nodes around it, may be eliminated before the global contextual information is conveyed into the neighbourhood. To balance the sensitivity, a variable σ is used in this approach. Initially, a relatively large σ is used to allow the relaxation process to convey contextual information globally, then, the magnitude of σ is gradually reduced, to increase the sensitivity of the compatibility function. The *rms* magnitude of the second order difference among all the candidates of the entire image domain is used as the initial value of σ, and it is updated iteratively by the new *rms* difference after each iteration. As the wrong candidates are gradually eliminated in the iterative procedure, the *rms* difference will become smaller. To gain a approximate idea of the *rms* magnitude of second order differences of a no-error displacement field, the mean and the *rms* magnitudes of the second order differences of the control displacement field of 18 hours separation was computed using equation (6.8). The mean magnitude of the second order differences of this field is 3 pixels, and the *rms* magnitude of second order differences is 16 pixels. This means that even in an error free field can still have about 32 % second order differences greater than 16 pixels and about 10% greater than 2×16 pixels. And when the *rms* magnitude of the second order difference becomes smaller than 15 pixels, the relaxation process is likely to approach towards a correct equilibrium point. To prevent σ becoming further smaller, a σ equal to 1.6 times the *rms* difference is applied. The equation (6.9) gives a negative value, when $\frac{-d_{i,0,j}^2}{2\sigma^2}$<-0.7, and gives positive value when $\frac{-d_{i,0,j}^2}{2\sigma^2}$>-0.7. Therefore, when σ =1.6 × (*rms* difference), the equation (6.9) gives negative values to the candidate vectors of second order difference $d_{I,o,j}$ > 2 × (*rms* difference). It means that only 10% of the candidates are negatively supported when the *rms* magnitude of the second order differences becomes smaller than 15 pixels.

The use of the second order difference of vectors as the measure of the smoothness of a field rather then the first order difference, is based on the following two reasons.

Firstly, as mentioned previously, the compatibility function acts as a constraint. The use of the first order differences as the smoothness measure forces neighbouring vectors to be the same. However, the compatibility function, based on second order differences, only constrains the shear of neighbouring vectors to be the same. It allows the neighbouring vectors to be different, but constrains them to vary smoothly.

Secondly, compatibility based on the second order candidate combination contains contextual information derived from 2 neighbouring nodes (there are a total of 3 nodes involved in the compatibility computation). In comparison to the relation net structure using first order difference, where only one neighbouring node is involved in each compatibility coefficient computation, the relation net structure using second order difference is strengthened, and therefore, the reliability of estimated compatibility should be enhanced.

Also the compatibility function defined by equation (6.9) constrains the magnitudes of the second order differences, among the neighbouring vectors of the resultant field, to be zero in four directions as shown in Figure 6.3. Since, equation (6.9) increases as the second order difference $d_{i,o,j}$ decrease, and when the second difference $d_{i,o,j}= 0$ equation (6.9) reaches maxima 1, the equation (6.9) supports the candidates which satisfy $d_{i,o,j}= 0$ more than those with $d_{i,o,j} \neq 0$. However, the second order differences are not strictly equal to zero. As mentioned previously, the *rms* magnitudes of the second order difference of the control displacement field (i.e. a error free displacement field) of 18 hours separation can be up to 16 pixels. Therefore, the correct compatibility function should have the following form:

$$r_{i,0,j}(\lambda'_k, \lambda_l, \lambda''_n) = \exp\left(\frac{-[d_{i,0,j}(x) - \bar{d}_{i,0,j}(x)]^2}{2\sigma^2} + \exp\left(\frac{-[d_{i,0,j}(y) - \bar{d}_{i,0,j}(y)]^2}{2\sigma^2}\right) - 1 \quad (6.10)$$

Where, the $\bar{d}_{i,0,j}(x)$ and $\bar{d}_{i,0,j}(y)$ are the optimal second order differences, in x and y directions respectively, among the vectors at nodes i, 0 and j. However, they are not known until the optimal vector field is determined, and thus, they are approximated as

zero in the approximate relaxation process. This approximation can smooth the resultant vector field, because the equation (6.9) gives more support to the candidates with smaller second order differences. The effect of over-smoothing can be refined iteratively. The refinement of the resultant vector field will be discussed in section 6.3.5.

6.3.4 The Updating Scheme of the Relaxation Process

The support function for a net of the neighbourhood structure shown in Figure 6.3 and the compatibility defined by equations (6.8) and (6.9) is of the following form —

$$q_0^t(\lambda_l) = \sum_{N=1}^{4} \frac{1}{4} \sum_{k=1}^{m_i} \sum_{n=1}^{m_j} r_{i,0,j}(\lambda'_k, \lambda_l, \lambda''_n) p_i^t(\lambda'_k) p_j^t(\lambda''_n) \qquad (6.11)$$

where N is the number of combinations of neighbouring nodes (each node has a total of 4 combinations with its neighbours in 4 directions), m_i , m_0 and m_j are the number candidates on the nodes a_i, a_0 and a_j respectively, and λ'_k, λ_l and λ''_n stand for the candidates on nodes a_i , a_0 and a_j. The $q^t_0(\lambda_l)$ is the total support from all candidates of 4 combinations of neighbouring nodes to the candidate λ_l on node a_0. in the tth iteration. The $p^t_0(\lambda_l)$, $p^t_i(\lambda'_k)$ and $p^t_j(\lambda''_j)$ are the probabilities of λ'_k, λ_l and λ''_n in the tth iteration.

The updating equation used in this approach is different from the updating scheme defined by equation (6.2b). In the latter updating scheme, the situation, where a node can contain no correct candidate, is taken into the account. Due to the possible bias in correlation values computed in the first step of the approach, for some nodes, none of the selected candidates are consistent with the candidates at their neighbouring nodes. In other words, none of the candidates of that node are correct. These nodes are named as zero-matching nodes. The relaxation process should be able to reject all these incorrect candidates. To handle the zero-matching situation, *Hsi-Jian Lee* and *Wen-Ling Lei* [1990] add a pseudo candidate to each node and define the pseudo candidate to correspond to the zero matching case of the node. In this study, a similar technique is used to handle the zero matching situation. Here, we note the zero matching candidate at all nodes as 0 and define their initial probability $p^0_i(0) = 0$. These candidates have no compatibility coefficients, and only play a role in probability normalisation. The

probabilities of normal candidates and the zero-matching candidates are updated by equations (6.12a) and (6,12b) respectively, as follow:

$$p_0^{t+1}(\lambda_l) = \frac{p_0^t(\lambda_l)[1+q_0^t(\lambda_l)]}{p_0^t(0) + \sum_{l=1}^{m_0} p_0^t(\lambda_l)[1+q_0^t(\lambda_l)]} \tag{6.12a}$$

$$p_0^{t+1}(0) = \frac{p_0^t(0)}{p_0^t(0) + \sum_{l=1}^{m_0} p_0^t(\lambda_l)[1+q_0^t(\lambda_l)]} \tag{6.12b}$$

When a node contains no correct candidate, the total support from its neighbouring nodes given by equation (6.11), will be negative, then the sum of the probabilities of non-zero-matching candidates of that node decreases, and thus, the probability of zero-matching candidate of this node, given by equation (6.12b), increases.

The relaxation process may converge at an ambiguous equilibrium point, which corresponds to the situation in which a number of nodes may have more than one candidate surviving. Hereafter, the node that has more than one candidate selected by the relaxation process, is referred to as a multi-matching node. For the current application, the multi-matching nodes may be categorised into the following two classes.

1. The remaining candidates (at a node) are very similar to each another. Therefore, the compatibility value r and supporting value q of these candidates have very little difference, so that the relaxation process may not be sufficiently sensitive to distinguish the differences among these candidate. This situation may be avoided by increasing the separation of candidates in the candidate selection procedure (see section 6.3.2) and by increasing the sensitivity of the compatibility function to the second order difference of neighbouring vectors (i.e. decreasing the value of parameter σ, see section 6.3.3). Also, because these candidates are similar to one another, it may be reasonable to take the average of these remaining candidates as the final estimate of the node.
2. The remaining candidates of a node are completely dissimilar. The intuitive sense of this situation is that the network contains insufficient information, provided by the applied compatibility model, for further resolving the ambiguity. For this situation,

additional information is required. Further ambiguity reduction can be undertaken by applying additional compatibility constraints to those resultant ambiguous neighbourhoods. Theoretically, this class of ambiguous interpretation can occur in the relaxation process, however, it did not appear in the current study.

Previous studies (for example see *Levy*, 1988) found that, in some situations the candidate set may contain more then one consistent set, and the relaxation process improves the initial labelling in the first few iterations, but later, it slowly drifts away from the initial converging direction and gives results far from what was expected. Theoretical considerations explain why the scheme proposed by *Rosenfeld et al* [1976] may produce unexpected results and a practical treatment to circumvent this problem has been provided by *Levy* [1988]. *Levy* [1988] proposes to constrain the labelling process by setting the label probability to zero, under a certain threshold, which is equivalent to eliminating these candidates from the process. By setting them to 1, when the probability close to 1, these probabilities will not be modified by the iterative procedure, and therefore the candidates which contain useful information will have much more influence to the procedure. This treatment is adopted in the approach developed in this research.

6.3.5 The Refining Relaxation Process

The refining relaxation process is applied in this scheme for the following two reasons:

- It will be demonstrated that the approximate relaxation process can adjust the inconsistency contained in the candidate set, conveyed by the biases in the correlation values, and the resultant field will consistently and faithfully reflect the basic structure of the estimating vector field. However, it may be over-smoothed in the areas of strong velocity shear gradients.
- The use of the leap-frog procedure can reduce the computation time by a factor of $n \times n$, where the n is the leap-frog step in pixel units. For example, when computing every 5th position of the research area, computing time reduces to 1/25 of the computation time for a full resolution correlation matrix. However, due to the coarse sampling rate in the correlation computation, the position of the maximum

correlation of a search area may be "jumped over" in the correlation matrix computation. Therefore, the resultant displacement field based on the candidate set, selected from the coarse correlation matrices, must be refined.

The effect of the over-smoothing (ie. the first and second order differences among the neighbourion vectors of the resultant field from using the approximate relaxation process are smaller than those derived from the control field) is due to two sources. Firstly, to enable each pattern tile to possess sufficient information, large (45×45 used in this study) pattern tiles are used in the correlation matrix computation. The computed correlation value is the window average. Therefore, the correlation value reflects the information of the average movement (smoothed) of the SST features contained in the pattern tile. As the basic information source, the correlation matrices carry this effect into the relaxation process. The selection of the pattern tile size is a trade-off, as has been discussed in Chapter 4. This part of the effect cannot be solved in this refining process, and it will be discussed further in Chapter 7.

The second source of the over-smoothing is the approximation of the compatibility function, as has been mentioned in section 6.3.3. The proper compatibility function should have the following form, as defined by equation (6.10):

$$r_{i,0,j}(\lambda'_k,\lambda_l,\lambda''_n)=\exp\left(\frac{-[d_{i,0,j}(x)-\bar{d}_{i,0,j}(x)]^2}{2\sigma^2}+\exp\left(\frac{-[d_{i,0,j}(y)-\bar{d}_{i,0,j}(y)]^2}{2\sigma^2}\right)-1\right.$$

As the optimal second order differences $\bar{d}_{i,0,j}(x)$ and $\bar{d}_{i,0,j}(y)$ in equation (6.10) are unknown until the optimal vector field is determined, they are approximated as zero and equation (6.9) is used as the compatibility function in the approximate relaxation process. The compatibility function defined by equation (6.9) may over-smooth the resultant vector field.

The refining process designed in this thesis aims to reduce the over-smoothing due to the effect of the approximation in the compatibility function, and the effect of the leap-frog procedure. The process is an iterative loop and contains two steps in each iteration, candidate set reorganisation and refining relaxation process. Hence, there are two levels

of iterations, the refining iteration and the relaxation iteration, as shown in the flowchart in Figure 6.1.

The candidate set is reorganised based on two information sources — the original candidate set and the resultant vector field from the approximate relaxation process. It will be demonstrated, in following section 6.4, that the approximate relaxation process has capability of adjusting the random inconsistency in candidate sets due to the biases in the correlation matrices. The resultant vectors from the approximate relaxation process faithfully reflect the basic structure of the estimating field, although it is over-smoothed in the areas of strong variation in velocity shear. Therefore, this resultant field can provide the following two sets of information:

1. The approximations of the second order differences of the neighbouring vectors $\tilde{d}_{i,0,j}(x)$ and $\tilde{d}_{i,0,j}(y)$ which enable the process to approach a more accurate estimation using equation (6.10).
2. By comparing the estimated field derived from the approximate relaxation process, with the candidate vectors of the initial probability (the equivalent of the MCC estimates) of each node, we can gain knowledge as to whether the candidate vector of the maximum initial probability of a node is correct or not. If, at a node, the difference between the approximate relaxation estimate and the candidate vector of the maximum initial probability (which is equivalent to the MCC estimate) is smaller than a certain value, it indicates that the MCC estimate and the relaxation estimate support each other. Therefore, the candidate vector of the maximum correlation value is a correct estimate of that node.

The candidate reorganisation reduces the candidate set by "freezing" the nodes where the candidate of maximum initial probability is confirmed as a correct estimate. In the case where the original candidate set is selected from the full resolution correlation matrices, if, at a node, the difference between the candidate of the maximum initial probability (which is equivalent to the MCC estimate at this node) and the approximate estimate from the relaxation process is smaller than a threshold (7 pixels is used in this study, as the spatial interval among candidates is 7 pixels), the candidate of the

maximum initial probability is selected as the only candidate of this node in the reorganised candidate set and it is given a probability 1.

In the case where the candidate set selected from the coarse correlation matrices, firstly, as is the case of using the full resolution correlation matrices, the vectors derived using relaxation method are compared to those estimated using MCC method. If two vectors match each other, then that vector is refined by computing the full resolution correlation values within a small search area around the end of the coarsely determined vector, using the rotational correlation method (refer to Figure 6.4). The position corresponding to the maxima of the small search area is used as the refined displacement. As in the case of using the full resolution correlation matrices, the refined vector is frozen in the reorganised candidate set by giving it a probability of 1, and defining it as the only candidate at that node.

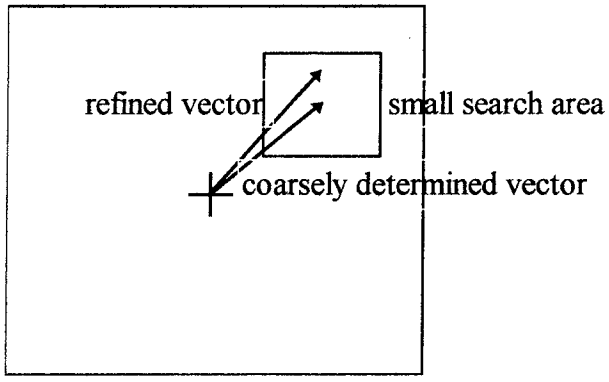

Figure 6.4 *The refining of the coarsely determined vector*

If, at a node, the candidate of maximum initial probability in the original candidate set does not match the estimate from the relaxation process, it indicates that the candidate of maximum correlation value is an erroneous vector, or the estimate from the approximate relaxation process is over-smoothed. Therefore, all candidate vectors of this node, and the initial probability attached to these candidate vectors, remain the same as the original in the reorganised candidate set, and these candidates will be passed onto the refining relaxation process.

In the refining relaxation process, equation (6.10) is used as the compatibility function. The $\tilde{d}_{i,0,j}(x)$ and $\tilde{d}_{i,0,j}(y)$ in equation (6.10) are computed from the resultant field using the approximate relaxation process initially, and they are then updated in each refining iteration using the resultant field of the last refining iteration. The neighbourhood structure, the support function and the updating equation are the same as in the approximate relaxation process. The resultant displacement field is then compared to the field that resulted from the last refining iteration. If the difference of the vectors of the two fields smaller than 1 pixel, then the refining process is terminated, otherwise, the process returns to the candidate reorganisation step, and start a new refining iteration.

6.4 Experimental Results and Discussion

The designed relaxation estimation approach was tested using both 18 hours separated synthetic image pair as shown in the Figures 5.1 and 5.4. and the real image pair of 12 hours separation shown in Figures 5.1 and 5.2. The details of the images have been described in section 5.2, Chapter 5.

The testes using the synthetic image pair are demonstrated and discussed respectively in sections 6.4.1, 6.4.2, and 6.4.3. The results of implementation using the real image pair are given in 6.4.4.

6.4.1 The Results of Candidate Selection

The full resolution correlation matrices and the candidates selected based on these matrices are shown in Figure 6.5. The coarse correlation matrices computed using the leap-frog strategy and the candidates selected from these coarse correlation matrices are shown in Figure 6.6.

The images were pre-processed with the high-pass filter of 25×25 pixels window, as described in section 5.4.1, Chapter 5. The correlation matrices are computed using the method of rotational search described in section 5.4.3, Chapter 5. The candidates are

selected using the correlation matrix distribution scanning process described in section 6.3.2. In both Figures 6.5 and 6.6, the correlation coefficient values are colour-coded with blue, green, yellow, orange to red in ascending order and the selected candidates are marked with white crosses in Figure 6.5, and marked with white dots in Figure 6.6.

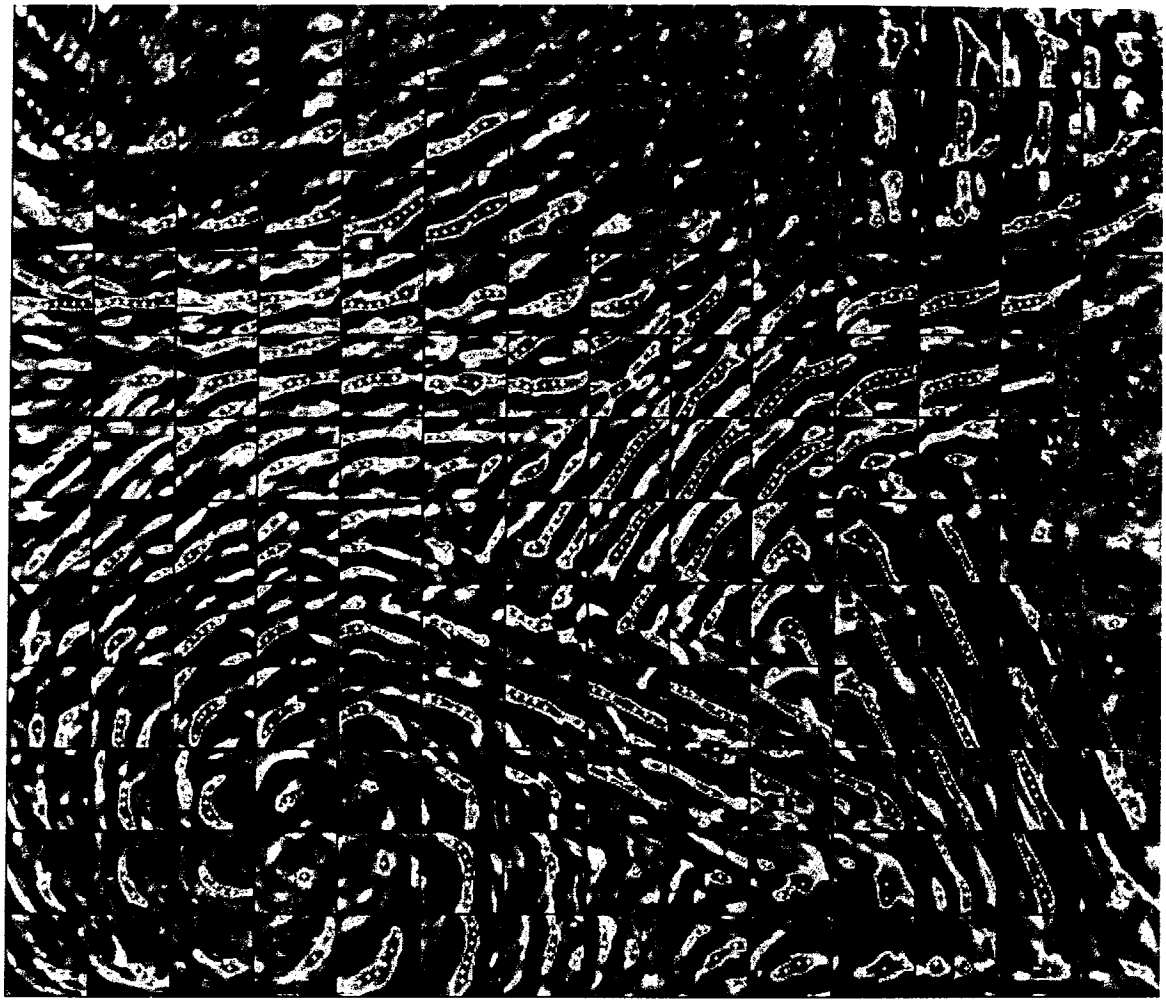

Figure 6.5 *The candidates selected using the correlation matrix distribution scanning process, and the correlation matrices computed using the rotational correlation computation method. The selected candidates are marked with crosses. The correlation coefficient value are colour-coded with blue, green, yellow, orange to red in ascending order.*

With the leap-frog strategy, in this test, the correlation distribution of each search area was coarsely determined by computing the correlation coefficients of every 5th position of the search area. The rotational search is also applied in this computation. The use of the leap-frog strategy reduces the computation time by 25. Figure 6.6 shows that the coarse correlation matrices contain the same basic distribution structure as the full resolution matrices.

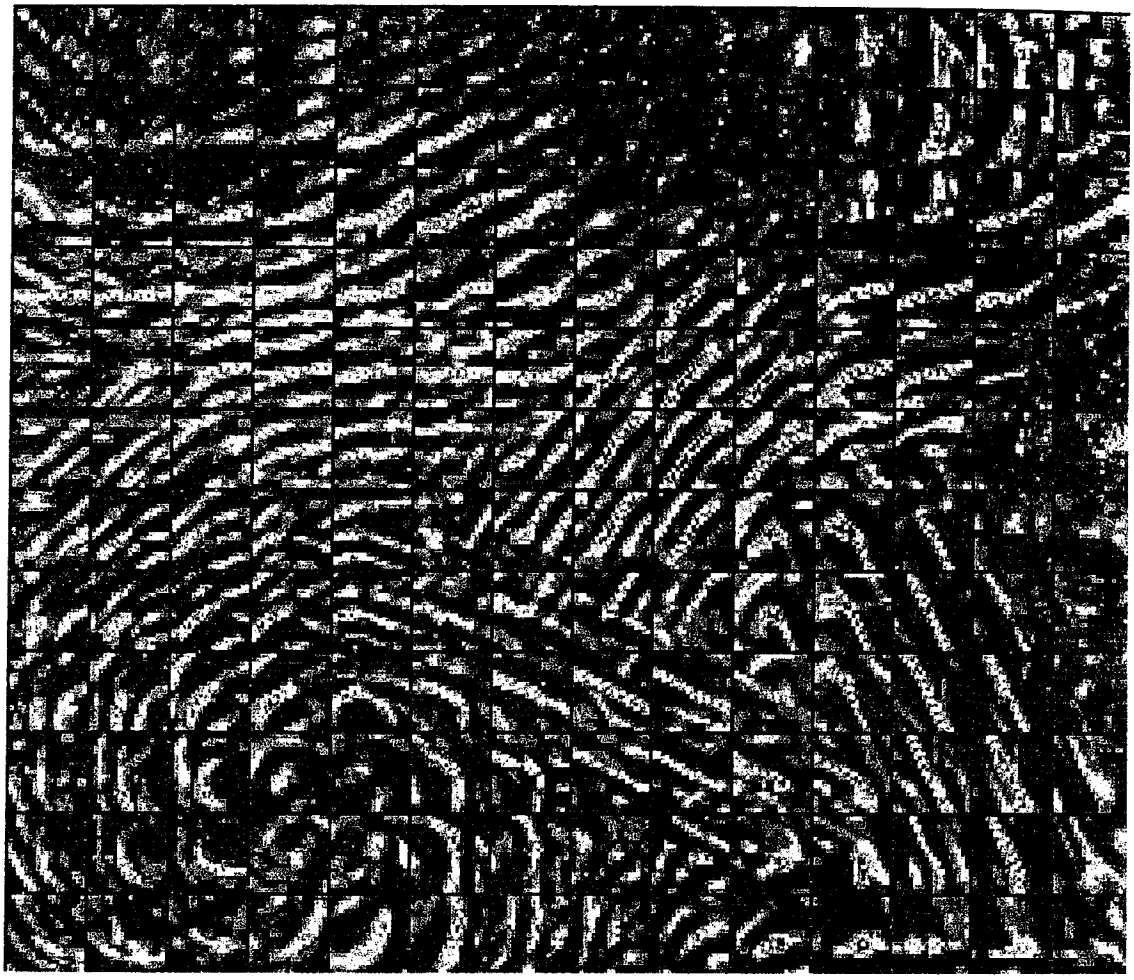

Figure 6.6 *The coarsely computed correlation matrices and the selected candidates based on these coarse correlation matrices. The selected candidates are marked with white dots.*

6.4.2 The Experimental Results of The Approximate Relaxation Process

The experiments in this section aim to investigate the following:

1. The effect of the scaling factor s in equation (6.7) on the relaxation process.
2. The capability of the relaxation process to handle the candidate set containing large numbers of erroneous candidates with high correlation value.
3. The feasibility of using the candidate set from the coarsely determined correlation matrices.

(a) The Test of the Effect of the Scaling Factor

The relaxation procedure is based on two sources of information.

- The initial status of the candidate set. The candidate vectors of each node and their probability deliver the possible structure of the estimating field, and provides the initial convergence trend of the relaxation process.
- The compatibility among the candidate vectors of neighbouring nodes. This information influences the relaxation process through the compatibility and support functions, and plays a role analogous to the constraint among the neighbouring estimating vectors. It does not independently provide the information on the estimating field, but constrains the mutual relationship of the neighbouring vectors.

Generally, the initial status of the candidate set selected using the correlation value may be erroneous or ambiguous in some nodes. As has been shown in Chapter 5, the correlation distribution can be biased due to a number of effects. The multi-peak and elongated distribution of the correlation matrices introduce ambiguity into the determination of the optimal displacement. These biases and ambiguity in correlation values are conveyed to the candidate set. Figure 6.7 shows the candidate vectors of maximum initial probability at each node (which are equivalent to the MCC estimate of each node) of the candidate set shown in Figure 6.5. This candidate set contains 15 nodes where the erroneous vector is of maximum initial probability (due to the bias in the correlation value). The erroneous initial status and ambiguity contained in the candidate set is iteratively adjusted by the compatibility among the neighbouring candidates in the relaxation process. Specifically, in this application, they are adjusted based on the smoothness of the neighbouring candidate vectors.

The differences of the initial probabilities of the candidate vectors of a node, determine the differences of the influence among individual candidate vectors in the first a number of iterations of the relaxation process. Also, the magnitudes of the difference of the initial probabilities among the candidates, determines the initial status of the ambiguity in the convergence of the process. For example, if all the candidates have equal initial probabilities, all candidates equally contribute to the process, and the initial status of the convergence of the relaxation process is completely ambiguous. Therefore, the scaling

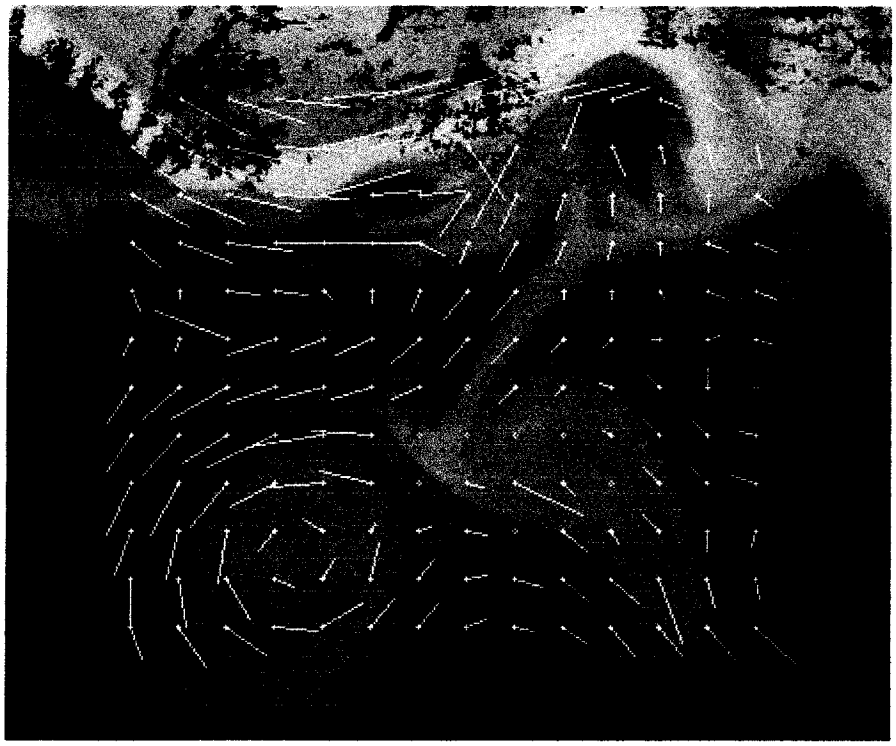

Figure 6.7 *The candidate vectors of maximum initial probability of each node (which are equivalent to the MCC estimates) from the candidate set displayed in Figure 6.5.*

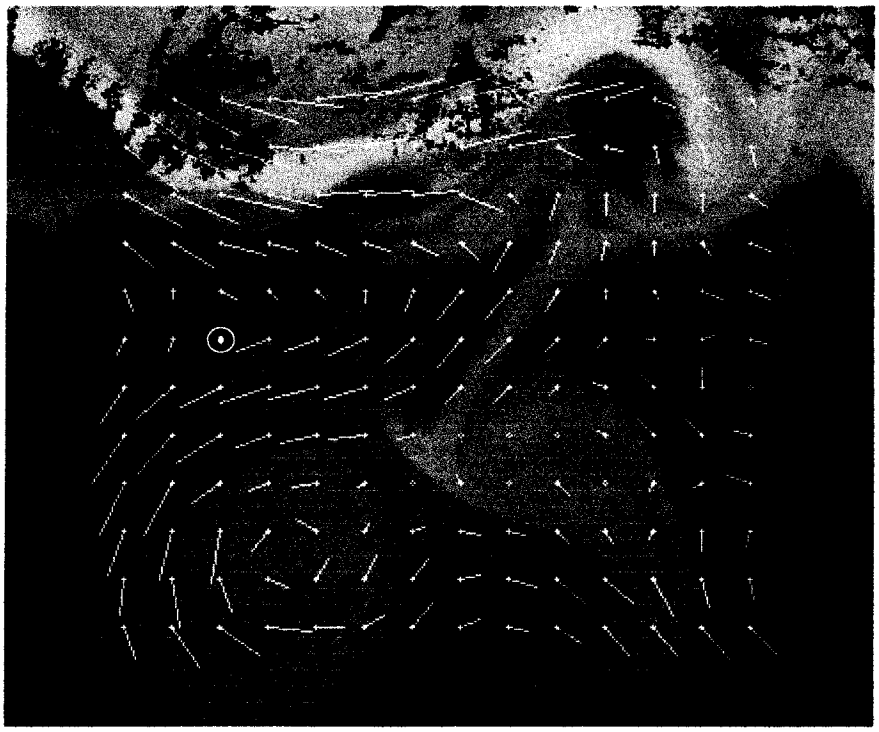

Figure 6.8 *The resultant vector field from the approximate relaxation process using the candidate set displayed in Figure 6.5.*

factor s in equation (6.7) can affect the initial status of the ambiguity in the convergence.

Because the initial probabilities are based on the similarity of the SST features in consecutive images and provide the valuable information on the possible structure of the estimating field, it may generally be preferable to use a relatively large s to strengthen the contribution of the correlation value, and to influence the relaxation process to approach to a set of vector field, which is not only consistent but also best satisfies the sense of correlation. However, on the other hand, because the initial probabilities contain a certain degree of error, the use of large s value may also increase the influence of the candidates of the erroneous high correlation value. Therefore, the question to resolve is whether the relaxation process is able to correct the erroneous initial status when a large scaling factor is used. In other words, it is necessary to test whether the use of a large scaling factor can affect the final results of the approximate relaxation process, even though it influences the initial status of the relaxation process.

The candidate set used in this test is computed using the full resolution correlation matrices as shown in Figure 6.5. The scaling factors used in this test are 1, 50, 100, and 150. Since this scaling factor is used only in the approximate relaxation step, it does not directly affect the refining process. In other words, if the resultant fields derived from the approximate relaxation step with different scaling factors are the same, they will be the same after the refinement process. Therefore, the refining process was not applied in this test. The differences among the corresponding resultant vectors derived with different scaling factors were computed to measure the effect of the scaling factor. The comparison found that the four resultant vector fields, computed with the different scaling factors, were identical (i.e. the differences among corresponding vectors equal 0). This result is different from what was primarily expected, and the primary intention of the design of the scaling factor (refer to point 3 on next page). The resultant fields which are all the same are as shown in Figure 6.8. It is worth mentioning that since the candidates (of a node) were selected to be 7 pixels apart, to avoid converging to an ambiguous equilibrium point, as mentioned in section 6.3.2, the difference between the corresponding resultant vectors derived with different scalings would only be zero or a

multiple of 7. The only difference was the number of iterations of the process required to reach convergence. When s = 1, the process took 45 iterations to complete the convergence, 37 iterations when using s = 50, and 40 iterations when using s = 100. The reason for this is that when the differences of the initial probabilities are small, the ambiguity of the initial status of the candidate set is large, and the process may take more iterations to reduce the ambiguity of the candidate set. The use of a scaling factor, s = 150, in this test, also made the process converge more slowly. The reason is that, the large scaling factor increases both the positive influence of the correct candidates and the influence of the erroneous high initial probability candidates, and requires more iterations to overcome such negative influences. The resultant displacement field, computed with initial probabilities and a scaling factor of 50 is shown in Figure 6.8.

The resultant field shown in Figure 6.8 was also compared with the control displacement field used to generate the synthetic images used for this test. The comparison found that:

1. The resultant field faithfully reflects the basic structure of the estimating displacement field, whith no significant inconsistent estimates being found. The direction of the estimated vectors basically match the corresponding vectors of the control field. The direction difference between the estimates and the vectors of the control field is less than 30^0.

2. According to it design, if all candidates at a node are not compatible with the neighbouring estimated vectors, the relaxation rejects all of them. For example, at node row 6, column 3 (marked with a white circle), due to the bias in the correlation value, the selected candidate vectors are all incorrect. All the candidates attached to this node were rejected.

3. As expected, due to the use of large pattern tiles in the correlation computation, and using equation (6.9) as the compatibility function, the resultant approximate displacement slightly over-smoothed areas of strong velocity shear gradients, compared with the control field. For example, 9 estimated displacement vectors in the core area of the ring (in the low-left image domain) are shorter than the corresponding vector of control field, the difference being greater than 7 pixels. The

rms difference between the estimated displacement field and the control field is 5.5 pixels. One of the intentions of the design of the scaling factor was primarily to reduce this over-smoothing effect by strengthening the influence of the correlation value. However, the test results in this section show that this intention wasn't successful, and this is one of the reasons for using the relaxation refining process.

(b) Test of the Robustness of the Relaxation Process

When the estimating fields where relatively turbulent or the time separation of the image pair is relatively long, the correlation value can be seriously biased. As has been discussed in Chapter 5, the rotational search can resolve the displacement due to the rotation motion of the currents, thus improving the estimation quality of the correlation distribution. However, due to the use of the fixed-shape pattern tile, the deformation due to the straining still remains unresolved. When estimating the field of strong velocity shear and a relatively long temporal interval of the image pair, the unresolved deformation can seriously bias the computed correlation distribution. The candidate set selected from the full resolution matrices, computed using the method with rotational search, contains 15 nodes where the erroneous candidate has the maximum initial probability. This should be considered as a "good" case, to test the capability of the relaxation process in handling a candidate set which contains relatively larger numbers of erroneous candidates of high initial probability. To test the capability of handling a case of "bad" initial conditions, two test candidate sets of erroneous initial condition, were created.

The first test candidate set was generated by using the candidate set shown in Figure 6.5, and adding erroneous candidates to 35 randomly chosen nodes. The position, length, orientation of the erroneous candidates were derived with computer generated random numbers, and the The added erroneous candidates were given an initial probability $p_{error} = p_{max} + 0.1$, where, the p_{error} is the initial probability of added erroneous candidates and the p_{max} is the maximum initial probability value of the original candidates at the node. That is the added erroneous candidate of an initial probability larger than the maximum initial probability of the original candidates at

those nodes. The candidates of the maximum initial probability at each node of this testing candidate set are shown in Figure 6.9.

To test the capability of the relaxation process handling the systematic bias in the candidate set, a test erroneous candidate set was created by adding systematically biased erroneous candidates to the basic candidate set. A total of 8 such erroneous candidates were added in a strong rotational area in the lower-left image domain (in the core area of the ring). The added erroneous candidates were given the initial probability $p_{error} = p_{max} + 0.1$. that is the initial probability was larger than the maximum initial probabilities of the original candidates at those nodes. The candidate vectors of the node-maximum initial probability of the test candidate set are shown in Figure 6.10.

The displacement vector fields resulting from the approximate relaxation process using two error-added candidate sets were compared with the approximate relaxation resultant field described in section 6.4.2 (a) as shown in Figure 6.8. The comparisons showed the following:

The resultant field computed using the candidate set with added random erroneous candidates is shown in Figure 6.11.a. It is identical to the field derived with approximate relaxation process using the original candidate set which is shown in Figure 6.8. The differences between corresponding vectors of the two fields was zero (as mentioned previously, the differences can only be 0 or a multiple of 7). This result indicates that the relaxation process can handle the candidate set containing randomly distributed inconsistent candidates of high erroneous initial probability.

The resultant field computed using the candidate set with added systematical erroneous candidates is shown in Figure 6.11.b, The comparison, between the resultant field derived from the erroneous candidate set and the original candidate set, showed that 6 added erroneous candidates were rejected by the relaxation process, while 2 still remained in the resultant field which are marked with white circles. These 6 rejected erroneous candidates located in the left part of the ring, were significantly inconsistent with the surrounding vectors. Therefore, although they were locally consistent, they can

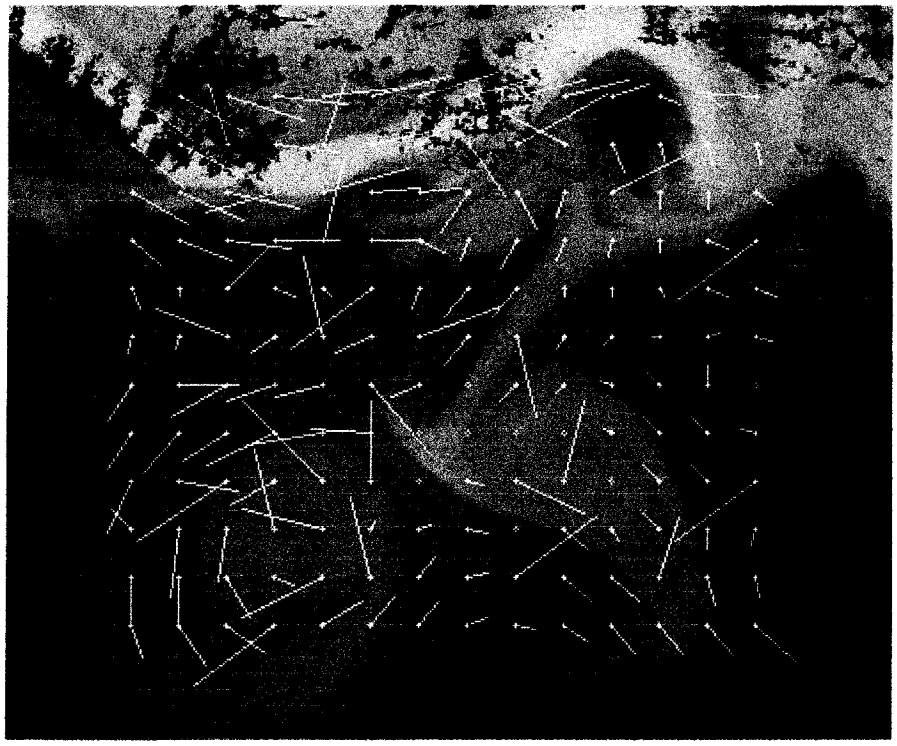

Figure 6.9 *The candidate vectors of the maximum initial probability of each node of the testing candidate set containing randomly added erroneous candidates.*

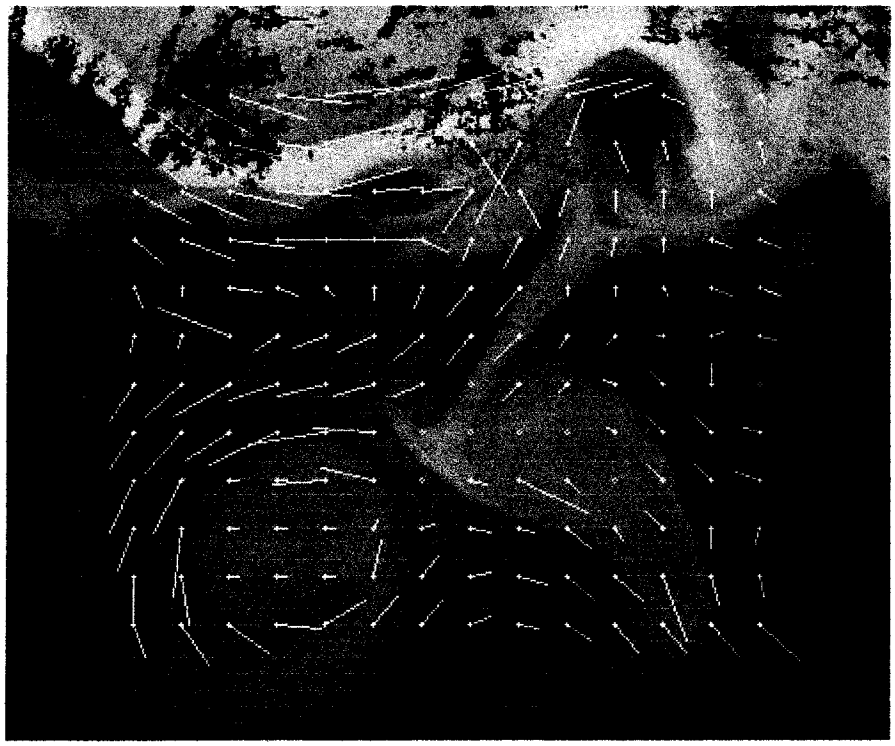

Figure 6.10. *The candidate vectors of the node-maximum initial probability of the testing candidate set containing systematic bias.*

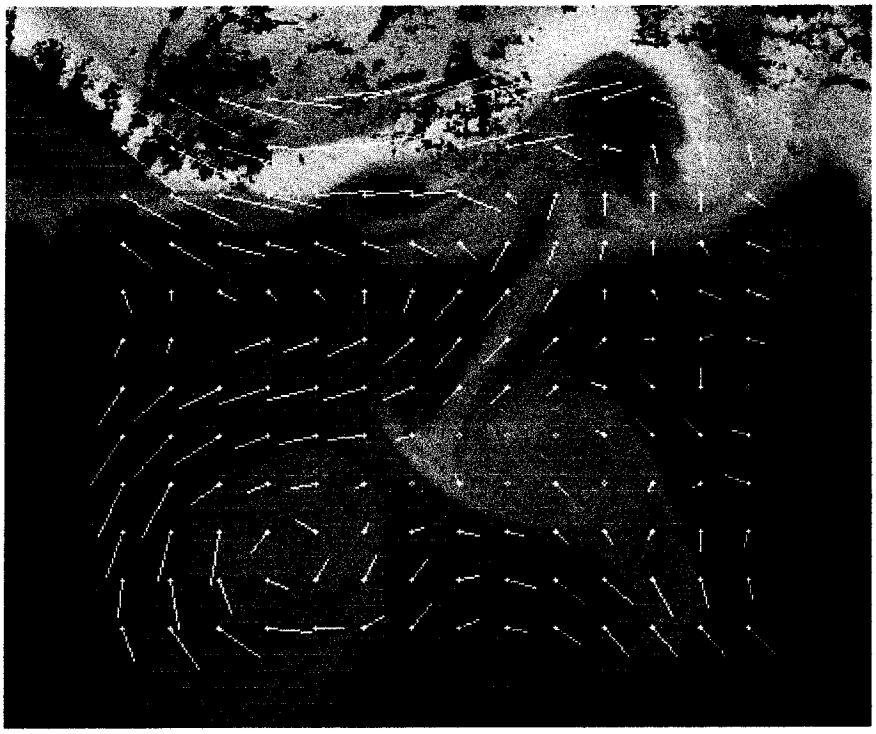

Figure 6.11.a *The resultant displacement vector field from approximate relaxation process using the candidate set containing added random erroneous candidates*

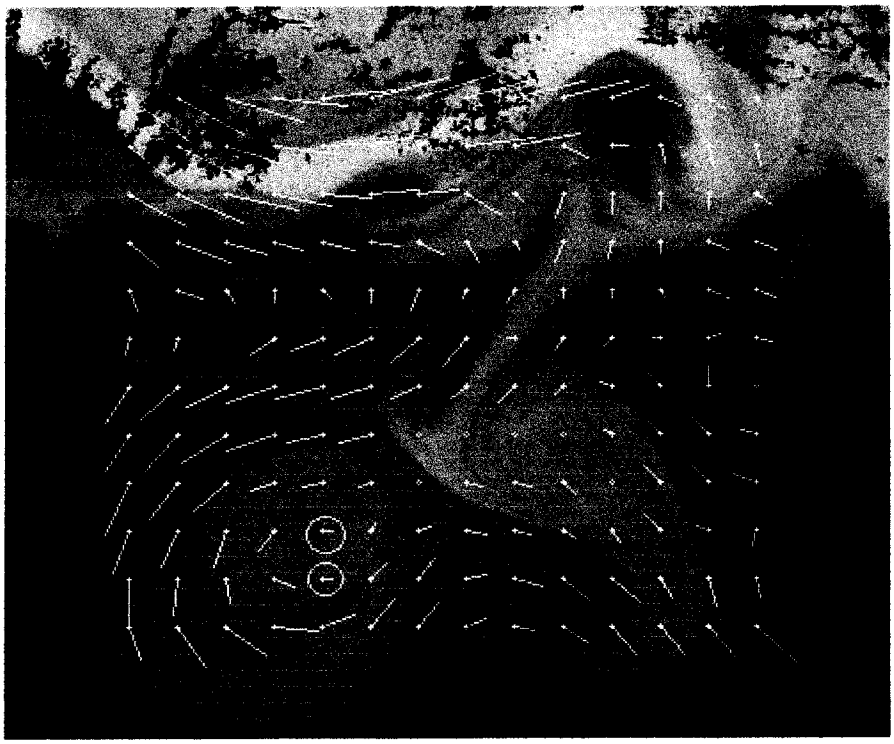

Figure 6.11.b *The resultant displacement vector field from approximate relaxation process using the candidate set containing added systematic erroneous candidate*

still be identified by the compatibility function and rejected through the relaxation process. However, the two remaining erroneous candidates were basically compatible with their surrounding vectors supported by the smoothness in the second order difference of neighbouring vectors, and thus, the process failed to identify and reject them.

(c) Test Using the Candidate Set Selected from Coarsely Determined Correlation Matrices

The candidate selection and relaxation labelling are very fast processes. However, the computation of the correlation matrix of each search area is based on brute force strategy, which computes the correlation coefficient of every position within a search area by moving the pattern tile pixel-by-pixel, and thus, is extremely time consuming. The key to improving the computational efficiency is reducing the computation time the correlation matrices. As has been shown in section 6.41 and Figure 6.5, the coarsely determined correlation matrices have the same basic distribution structure as the full resolution matrices. However, they are relatively noisier, and because the optimal matching position may be 'jumped over", the computed correlation matrices and the candidate selected based on such correlation matrices may not contain the optimal vector of the estimating field. The candidate of the maximum initial probability of each node selected based on the coarsely determined correlation matrices is shown in Figure 6.12. From the figure it can be seen that this candidate set contains more inconsistent displacement vectors than those shown in Figure 6.6, which is selected based on the full resolution correlation matrices. Therefore, the feasibility of using the candidates selected from coarsely computed matrices for the estimation raises the issue as to whether the relaxation process has a capability can handle the erroneous candidate set .

The resultant displacement vectors derived from the approximate relaxation process are shown in Figure 6.13. The vector field was compared with the resultant field computed, using the candidate set from the full resolution correlation matrices which is shown in Figure 6.8. The comparison showed that the *rms* difference between the corresponding vectors of the two resultant fields was 3.2 pixels, and a visual comparison of the two images also showed that the two fields are very similar except vectors at row 9, column 6, row 10, column 6, and row 12, column 4, which are marked with white circles in

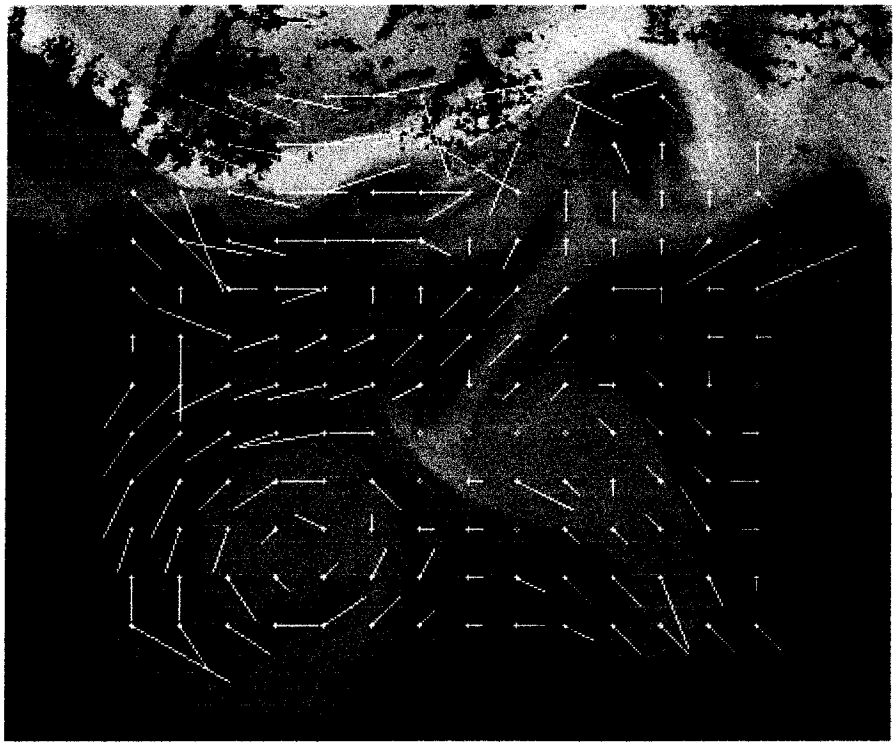

Figure 6.12 *The candidate displacement vectors of maximum initial probability of each node selected based on the coarsely determined correlation matrices.*

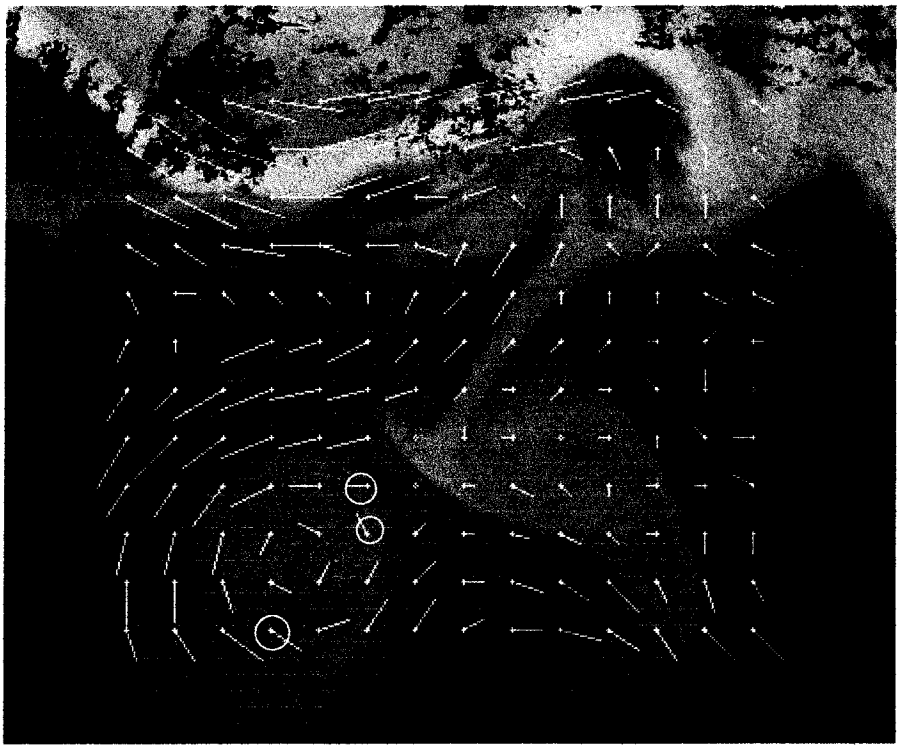

Figure 6.13 *The resultant displacement field from approximate relaxation process using coarse correlation matrices*

Figure 6.13. Therefore, the tests showed that it is feasible, using the leap-frog method, to save computation time in the correlation matrix determination.

6.4.3 The Test on the Refinement Process

The refinement process employed in this application was undertaken for two reasons as was mentioned in section 6.3.5.

Firstly, the resultant vector field derived from the approximate relaxation process may be over-smoothed. This is due to : the use of the large template in the correlation computation to gain sufficient information; and the use of the zero second order difference approximation in the neighbouring vector compatibility function (equation 6.9), because the actual or estimated value of this variable in the compatibility function is unknown at that stage.

Secondly, when the candidate set is selected from the coarsely determined correlation matrices, the maximum correlated position of a search area may not be covered by the leap-frog computation.

The iterative refinement loop described in section 6.3.5 was tested using the candidate sets selected from both the full resolution correlation matrices (shown in Figure 6.5) and the candidates from the coarse correlation matrices, (shown in Figure 6.6). The refinement processes took 3 iterations to reach convergence in both cases. The resultant displacements using these two candidate sets were almost identical (with a small *rms* difference 0.7 pixels), except for the displacement at node row 9 column 6, which is marked with a white circle in Figure 6.14. The estimate, in the case of using the coarsely determined correlation matrices, is closer to the corresponding displacement in the control field. The reason for this is that in the refining process, for coarsely determined correlation matrices, the refinement correlation search was applied. That is, computing the full resolution correlation distribution of a small area around the end of the vector in the refinement relaxation process has resolved, and then, located the maxima within this small area. This search process is not employed for full resolution

correlation matrices. This difference indicates that the refinement correlation search is helpful for both using full and coarse correlation matrices. The intuitive reason for this is that the selected candidates have a large separation, while the optimal position may be located between them. The resultant displacement field computed using the candidate set with full resolution correlation matrices is shown in Figure 6.14.

Figure 6.14 shows that after the refinement process, the over-smoothing in the resultant field, derived from the approximate relaxation process, is significantly improved as revealed by comparison with the field shown in Figure 6.11. The resultant field was also compared with the control field shown in Figure 6.15. The *rms* difference in magnitude of the two fields, *rms dm*, is 4.7 pixels and the *rms* difference in angle of the two fields, *rms da*, is 19^0. Compared with the MCC estimated displacement field, using the same image pair and processed with the high-pass filter and correlation method with rotational search, i.e. the best resultant field among the estimates based on MCC method, shown in Figure 5.10, which gaves 6.6 pixels *rms dm* and 31^0 *rms da*, the relaxation process improveed the *rms* diffrence in magnitude by 1.9 pixels (1.9/6.6=28%) and *rms* difference in orientation by 12^0 (12/31=38%). It is worth mentioning that since the relaxation process is not able to correct the error due to the bias in the correlation value caused by the use of a large pattern tile as discussed in the following paragraph, this improvement was achieved by reducing the number of estimated vectors with large error. The field derived with the MCC method had 15 vectors different from the control field by 7 pixels, while the relaxation process reduced this number to 4.

These 4 vectors, and the other 10 vectors which are different from the control field by 5 pixels (these erroneous vectors were not counted as erroneous vectors, in the MCC cases) vectors are marked with squares and circles in Figure 6.14. Most of these vectors have nearly the same direction as the corresponding vectors in the control field, and all these vectors are consistent with neighbouring vectors. The comparison with the field shown in Figure 6.7, which is equivalent to the MCC estimates as described in section 6.4.2, showed that the vectors marked with squares are the same as the MCC estimates. Further, the comparison showed that most of these vectors were located in the areas of

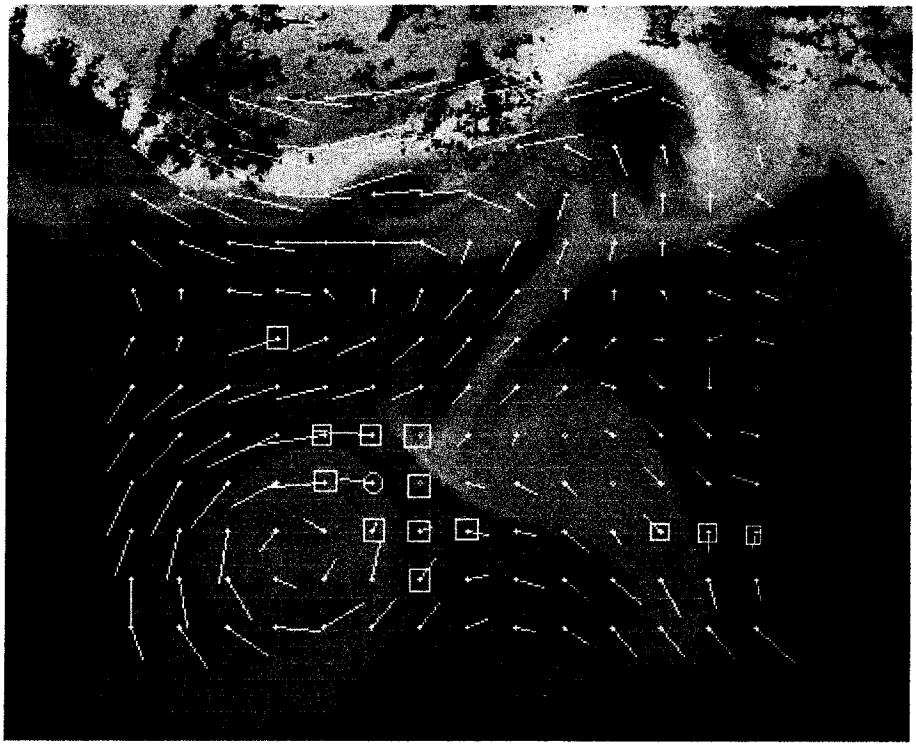

Figure 6.14 *The resultant displacement field after the refining process.*

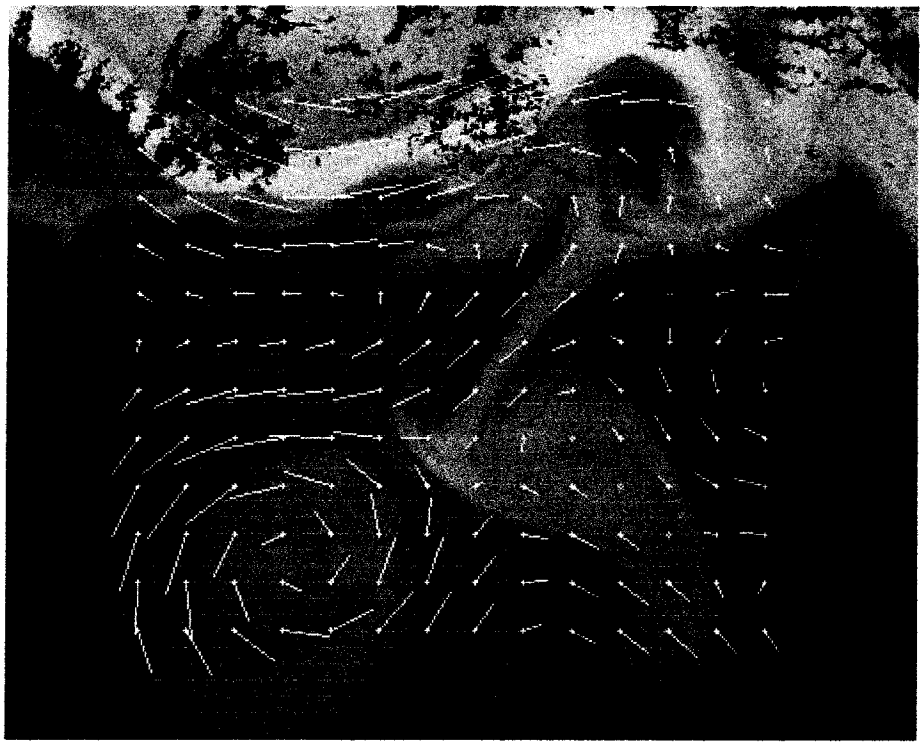

Figure 6.15. *The control displacement field*

strong velocity shear variation. This indicated that the error of most of these vectors were due to the bias in correlation value caused by the use of a large pattern tile. When these erroneous vectors were compatible with their neighbouring vectors in the sense defined by the compatibility function, the relaxation process was not able to correct the error. The vector marked with a circle in row 9, column 6, is shorter than the corresponding vector in the control field and the MCC estimate. This error is due to the over-smoothing effect of the compatibility function in the approximate relaxation process. Although the refining process reduces the effect, this vector is still over-smoothed.

6.4.4 Experimental Results Computed from Real Images

The proposed method was also tested using a pair of 12 hours separated AVHRR thermal images which are shown in Figures 5.1 and 5.2, respectively. As was the case for the tests using synthetic images, the images are preprocessed with the running-average high-pass filter with a 25×25 pixel window. The correlation matrices and the selected candidates are shown in Figure 6.16. The correlation matrices are computed using the method with rotational search. The leap-frog step used in the computation of the correlation matrices was 2 pixels, i.e. compute correlation value at every second position within a search area. The cloud contaminated pixels were detected and masked using the algorithm described in Chapter 4. Figure 6.16 shows that the cloud contamination disturbed the correlation distribution of some matrices. The optimal matching position may be located in these cloud-covered areas. To enable the relaxation process to approach the cloud-covered optimal positions, based on the contextual information provided by the neighbouring candidates, a series of pseudo-candidates, i.e. the candidates selected were not based on the correlation value, were added to the cloud-disturbed areas. The added pseudo-candidates were marked with black crosses in Figure 6.16. The pseudo-candidates were evenly distributed in 25 positions in the search area, and have equal initial probabilities of 1/25. When the entire search area or more than 20% of the pattern tile is covered by clouds, the matrix corresponding to this area contains no computed correlation value. It is feasible to exclude the nodes corresponding to these no-correlation-value matrices from the relaxation computation. However, this disturbs the contextual information. In this test, the 25 evenly distributed

and equally weighted (i.e. of the equal initial probability 1/25) pseudo-candidates were attached to each of these nodes, for example, see the correlation matrices at rows 1 to 3, and columns 3 and 4 from the upper-left corner of the figure. Because the pseudo-candidates at these nodes have been given equal initial probabilities, they do not deliver the information on the possible trend of the vectors at these nodes. Thus, they have no influence on the relaxation process for the neighbouring nodes, in the initial stage. The updating of their probabilities, in the first iteration is purely based on their compatibility with the candidates at neighbouring nodes and the probabilities of the neighbouring candidates. Once the probabilities of these pseudo-candidates are updated and the differences in probabilities established, the pseudo-candidates start to propagate contextual information. This treatment is only suitable for internal small areas, because the constraint of the contextual information becomes weaker as the distance increases. For this reason, this treatment was not applied in the test, to the cloud covered areas in the lower-left image domain.

The reason for not apply the large leap-frog step was that, in the upper image domain (i.e. the nodes at row 1, columns 2 to 8 and row 2, column 2 to column 8 from upper-left corner of the net), the gradients of the intensity of some SST patterns are relatively weak, and are contaminated by cloud. Most of the cloud contaminated pixels were detected. However, the masking out of these cloud contaminated pixels reduces the effective size of the pattern tile. Thus, a number of matrices in this area were every noisy and sharply distributed. The use of a large leap-frog step may have further biased the distribution of the matrices. Due to the sharp distribution of the correlation matrices, the use of a large leap-frog step increased the chance of jumping-over the position corresponding to the optimal vector. Thus, due to the poor image conditions, a relative small leap-frog step (2 pixels) was used in this test.

The candidate displacement vectors of maximum initial probability of each node are shown in Figure 6.17. The resultant field is shown in Figure 6.18.

As was mentioned in Chapter 5, because simultaneous in situ data were not available for the evaluation of the estimated field from real images, an assessment of the absolute

quality of the estimation is impossible. As for the evaluations in Chapter 5, the quality of the estimation for the real image data was assessed by examining the consistency of the estimated vector field, and by comparing it with the control field (at the status of 12 hours separation). The consistency of a vector with its neighbourhood is measured using the difference between the vector and the average of its 8 neighbouring vectors. Due to the existence of velocity shear gradient, the computed consistency will not always equal zero, even for the error-free displacement field of the study area. The *rms* consistency computed from the control displacement field with 12 hours separation is 7.2 pixels.

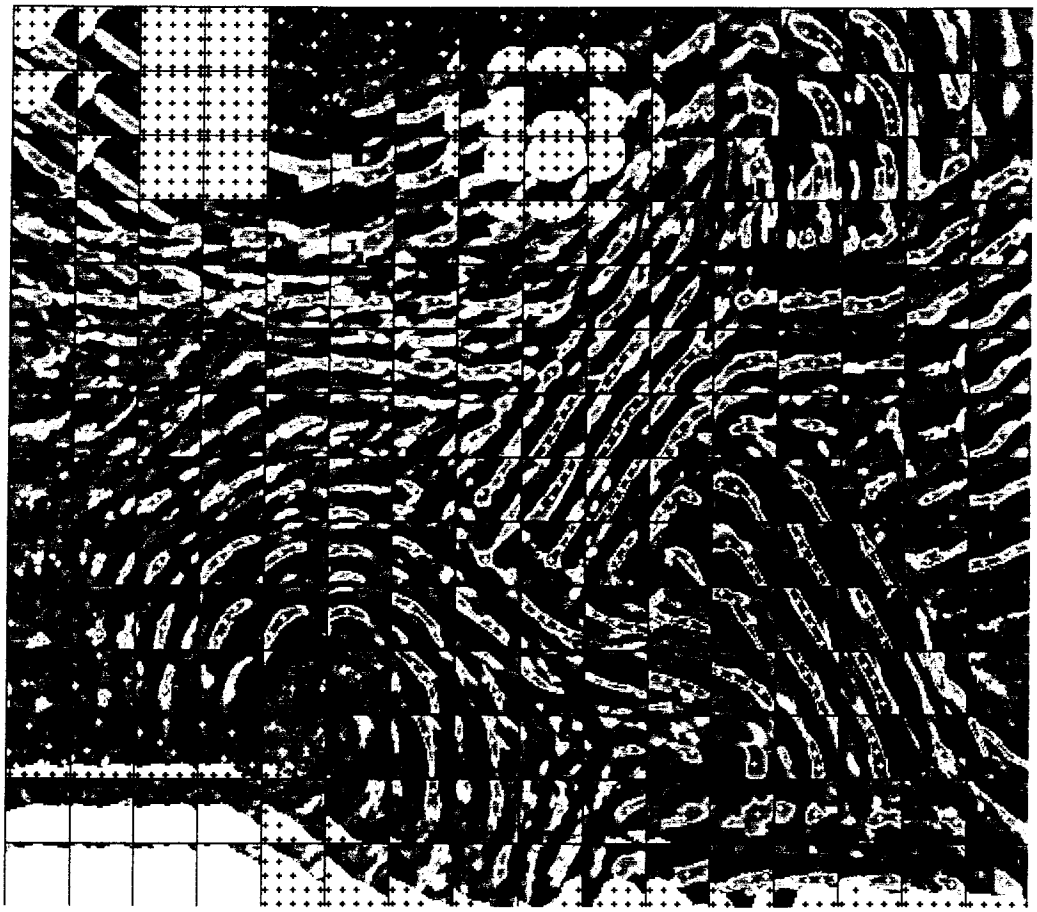

Figure 6.16 *The correlation matrices computed using real AVHRR thermal images with 12 hours separation and the selected candidates and the pseudo-candidates. The leap-frog step used in correlation computation is 2 pixels. The normal candidates are marked with white crosses and the pseudo-candidates are marked with black crosses.*

The comparison of Figures 6.17 and 6.18 shows an obvious improvement in consistency among the neighbouring estimates over that estimated field using the MCC method. The *rms* consistency of the displacement estimated using the MCC method and the same image pair is 9.6 pixels, while, it is improved to 8.1 pixels using the relaxation scheme,

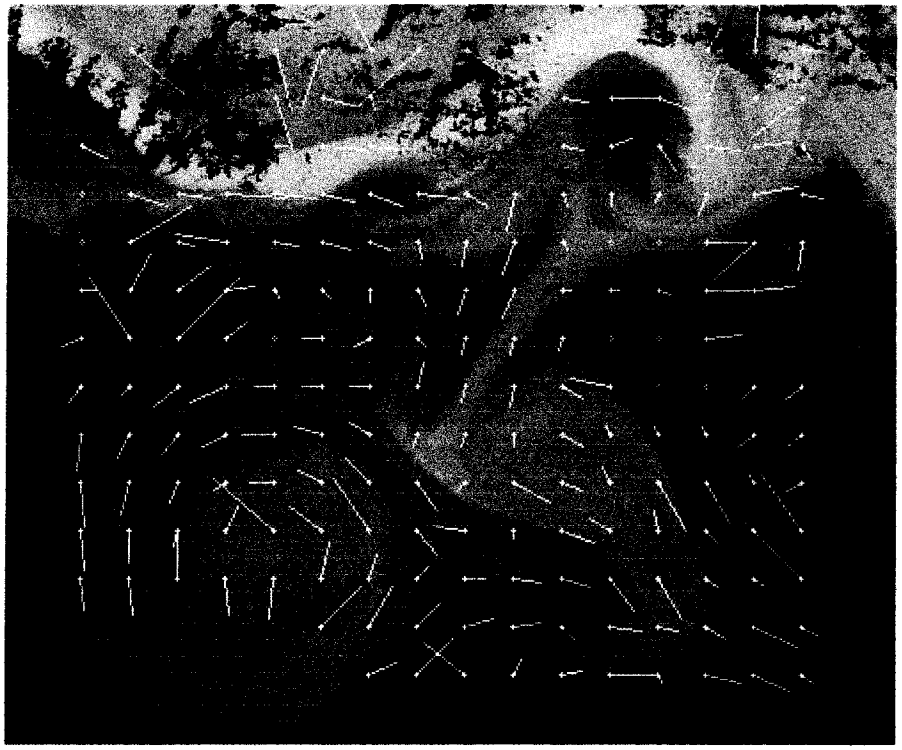

Figure 6.17 *The candidate displacement vectors of maximum initial probability of each node (equivalent to the MCC estimates) computed from 12 hours separated real AVHRR thermal image pair.*

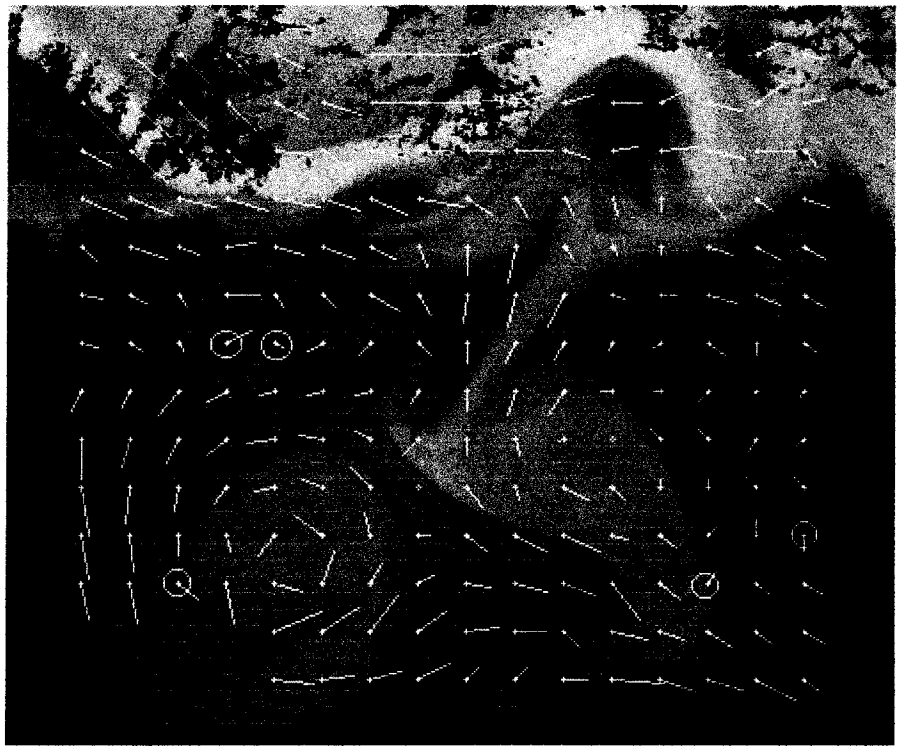

Figure 6.18 *The resultant field estimated using proposed relaxation scheme.*

and improved the *rms* consistency by 19% (1.5/8.1), this improvement is considered to be significant. As mentioned previously, since the relaxation process is not able to correct the error due to the bias in correlation values caused by the use of a large pattern tile as previously discussed, this improvement was due to the achievement in reducing the number of estimated vectors with large error. The field derived with MCC method had 25 vectors different from the control field by 7 pixels, and the relaxation process reduced this number to 5, which are marked with white circles in Figure 6.18.

Among these remaining erroneous vectors, displacement at row 7 column 4 is less consistent with the neighbouring vectors to its right side and below it. Figure 6.16 shows that among the selected candidates, based on the correlation distribution at this node, there is no candidate that is more consistent with its neighbouring vectors. This candidate was not eliminated by the process because it is still supported by the estimates above it and to the left. The survival of this candidate consequently affects the estimate to its right (the estimate at row 7 column 5). Both the marked estimates at row 11 column 16 and at row 12 column 14 are located in the area of a relatively large velocity shear. Therefore, they are compatible with some of the neighbours, while, inconsistent with the other neighbours. In these cases the estimates may be less accurate.

The search area corresponding to the displacement at row 12 column 3, from upper-left corner of the figure, is partially contaminated by cloud. According to the neighbouring estimated displacements, the optimal matching position may be located in the cloud covered area. Although, the pseudo-candidates were added in the cloud covered area, the relaxation process still selected the normal candidate which is less consistent with its neighbours. The reason for this is that, the pseudo-candidates are given a relatively low initial probability (1/25), while, the finally selected candidate had an initial probability of 0.29, This difference is further increased by the scaling factor, $s = 50$, in equation (6.7), and the fact that the displacement selected by the relaxation process is not entirely incompatible with its neighbours.

The resultant displacement field is also compared with the control field used for the synthetic images generation. The control velocity field is derived from the

measurements determined by subjectively tracking the features of the same real image pair used in this evaluation (the detailed description is given in section 5.2, Chapter 5). Therefore, it should be a good reference field for this evaluation. The comparison again measured the root mean square differences in angle, *rms da*, root mean square differences in magnitudes, *rms dm*, and the number of the significant erroneous estimates, n_1 and n_2, where, n_1 is the number of erroneous displacements that are different from the control field with error greater than 7 pixels or 30^0 in the orientation, and n_2 is the number of erroneous displacements that are different from the control field within 5 to 7 pixels or 22^0 to 30^0. The *rms da*, *rms dm* and the n_1 and n_2 derived from the comparison between the resultant displacement field from relaxation scheme and the control displacement field are shown in table 6.1. To illustrate the improvements, the comparison of results of the estimated displacement field using rotational MCC method and high-pass filtered real images, with the control field which has been shown in the Table 5.4 are also listed in the table 6.1.

Table 6.1 *The comparison of results between the resultant field from the relaxation method and the control displacement field, and the comparison of results between the estimated displacement field using the rotational MCC method and high pass filtered real images and the control field.*

	rms dm (pixels)	*rms da*	n_1	n_2
rtelaxation labelling	4.3	27^0	5	12
MCC method	5.5	50^0	25	*N/A*

This comparison also shows the obvious improvements in the estimation quality using the relaxation scheme.

6.5 Summary

To reduce the inconsistency of the estimated field and the uncertainty in estimation due to the multiple-peak and elongated distribution of the correlation function, an estimation scheme based on the relaxation labelling technique was proposed and tested. The proposed scheme estimates the displacement of SST features in consecutive images based on two sources of information — the correlation between the features in

consecutive images and the compatibility among the neighbouring candidate displacements. The compatibility is measured with the second order difference of neighbouring displacements.

The proposed scheme was tested using both a pair of synthetic images and a pair of real AVHRR thermal images. In this study, the following capabilities of the scheme were tested:

1. The reliability and robustness of handling the candidate set containing candidates of erroneous high correlation value.
2. The feasibility of using the candidate set from coarsely determined correlation matrices.

The experimental results showed the following:

1. The relaxation labelling scheme is capable of identifying and eliminating the candidates of erroneous high correlation, which are randomly distributed in the image domain. However, the proposed relaxation scheme is unable to eliminate the systematically biased candidates, of high correlation values, when the systematically biased neighbourhood is not entirely incompatible with its surroundings.
2. It is feasible to use the leap-frog strategy in correlation distribution computation to significantly reduce the computation time. The selection of the distance of the leap-frog steps is inherently a issue of sampling rate. The principle of this selection is based on maximising the reduction of the computation time, with a minimum bias in the computed correlation distribution. The experimental results in section 6.4.3 show that when the images are not too noisy, the coarsely determined correlation matrices with 5 pixels leap-frog steps, and a pair of high-pass filtered images with a 25×25 window, are of the same basic distribution structure as those in the full resolution correlation matrices. The estimated displacement field resulting from both the full resolution correlation matrices and the coarse correlation matrices are almost identical.

The experimental results also show that the resultant field derived from the proposed scheme was slightly over-smoothed in the areas of strong velocity shear gradients, due to the following effects:

1. The use of a large and fixed-shape template in the correlation computation to gain sufficient information. Also, because the shape of the template was fixed, the deformation due to the velocity shear is not resolved, and the estimated displacements with such a template are the average value of the displacement of features contained in the template.
2. The compatibility equation based on the assumption of smoothness of the second order differences among the neighbouring candidates. The accuracy of the assumption is subject to the balance between the density of the grid points and the magnitude of the velocity shear gradients.

The results of the experiments show that the refining process can effectively reduce the over-smoothing effect resulting from the inaccuracy of the compatibility equation used in the approximate relaxation. While the effect caused by the use of the large template is an inherent problem in the correlation computation using fixed-shape templates, this effect can be reduced by using flexible templates, and resolved by using joined-patch least squares matching, which will be discussed in the next chapter.

Chapter 7

Refinement of Estimation With Joined-Patch Least Squares Matching (JPLSM)

7.1 Introduction

The study in chapter 5 shows that SST fields are usually dominated by large scale piece-wise features, the cross-correlation function of such features are frequently of multi-peak and/or elongated distribution, and the differences among correlation values of these multiple peaks and other elements along the ridge of the elongated correlation functions are usually insignificant. Because of the similarity of correlation values of these elements, a small amount of unresolved rotational motion, deformation or noise can "shift" the location of maximum correlation value from the correct position to one of the other elements. This introduces uncertainty into the determination of the similarity among the features in the image sequence, and consequently the determination of displacements of SST features, and results in a large number of erroneous estimates. Enhancing the traceability of the SST features using a high-pass filter, and resolving the rotational motion with the rotational search can partially address the problem, and reduce the number of erroneous estimates.

However, the study also shows that the use of high-pass filtering can also enhances the sensitivity of the correlation scheme to the effect of unresolved deformations. It was showed in Chapter 5 that the deformation due to the straining motion cannot be resolved by the fixed shape template used in the MCC method, and the use of the rotational search does not change the basic structure of the correlation distribution. Thus these processes cannot solve the uncertainty in the estimation. Therefore, it is essential to introduce contextual information when the correlation value alone is not sufficient to indicate the significance of the similarity between the features in the image sequence, and so further reduce the effect of the unresolved motions.

The scheme based on the relaxation labelling proposed in Chapter 6 uses both the information on the correlation distribution and the contextual information. The study shows that the integration of multi-information sources significantly improves the consistency of the estimated displacement field and the robustness of the scheme. The improvement in the robustness consequently enables the use of the relative large search step (i.e. the leap-frog strategy), and significantly reduces the computational expense. The study also shows a few aspects requiring improvement as follows:

1. Because the computation of the correlation distribution used in the relaxation scheme is the same as that used in the MCC method, the deformations of the SST features in the image sequence remain unresolved due to the use of the fixed shape template.
2. For the same reason as in the MCC method, to gain sufficient information, the large template window had to be used. The studies in Chapter 5 and 6 show that the use of large templates can cause over-smoothing of displacements in the areas of strong velocity shear. This trade-off in the template size selection is remain unresolved.
3. The compatibility function in the relaxation scheme proposed in Chapter 6 acts in a manner to similar constraints in the least squares technique. However, the influence of the compatibility function on the relaxation process is not as easily controlled as when using the least squares technique where the influence of a constraint can be controlled by applying different weights. The study also shows that the simplified compatibility function is a source of over-smoothing of the estimated displacement field, although the refinement process described in section 6.3.5 significantly reduces this effect.

To further improve the estimation quality, a refinement scheme based on a least squares matching technique, which was originally designed for the digital terrain model estimation from stereo pair of airborne photos or SPOT images by *Rosenholm* [1985], is proposed in this chapter. In the proposed scheme, the shape of the templates (referred as patches hereafter) are automatically varied bi-linearly to fit the shift, rotation and deformation of the features in the second image. These patches are joined together, to convey the contextual information. The joined flexible patches are similar to a rubber

sheet. The flexibility of this "rubber sheet" can be controlled by the weights of the constraints.

By using a joint flexible patch net, the following advantages of the proposed scheme can be expected:

- The deformation due to the straining motion is expected to be resolved.
- Not only can both the information on the similarity of the SST feature in image sequence and the physical constraints be integrated, but also the influences of the constraints can be controlled.
- The difficulty caused by the trade-off in the selection of the size of template can be effectively resolved.

7.2 The Basis of The Least Squares Matching Method

Least Squares matching is a correlation technique, which was developed and has been used by photogrammetrists (eg. *Förstner* 1982, *Gruen* and *Baltsavias* 1988 and *Rosenholm* 1985) for the determination of digital elevation models (DEM or DTM) from airborne or satellite image pairs. In the least squares matching process, the first image is divided into an array of template windows in a similar approach to the MCC method. However, the method of searching in the least squares matching technique is different from that in the MCC method. The process directly determines the displacement vectors, and the approach determining the best match of sub-images in the second image is based on iteratively refining the displacements. The shape of the template or the sample-widow on the second image is automatically adjusted bi-linearly, according to the deformation of corresponding SST features in the second image, in a similar way to changing the shape of a rubber template to match a deformed corresponding pattern. In the MCC based technique, the shape of the window is fixed, which causes a trade-off in window size selection. The window should be large enough to contain sufficient information, and small enough to avoid over smoothing the estimated field in the region of strong velocity shear gradients, as has been discussed in Chapter 5 and Chapter 6. The advantage of using a bi-linearly flexible in the least

squares approach is that the deformations can be largely resolved. The least squares matching can be categorised into two groups, the single patch (window) least squares matching schemes and multiple patch matching schemes. In the single patch matching schemes, each window independently approaches their destination position, while, in the multiple patch matching schemes, the template windows are joined together and converge onto the destination positions simultaneously.

7.2.1 The Structure of Joined Patches

The scheme proposed in this chapter is based on the joined patch matching technique developed by *Rosenholm* [1985] for the DEM determination using stereo image pairs. The scheme divides the first image into rectangular templates which are always joined together when they approach their best match locations as shown in Figure 7.1. The displacements of the corners of each patch are the unknowns to be determined.

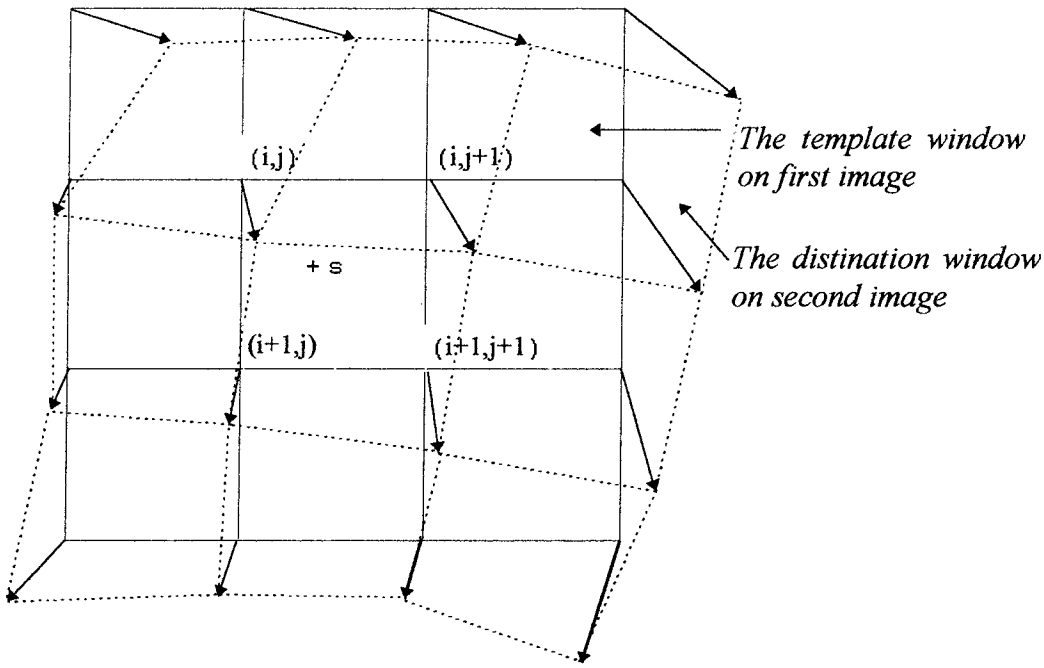

Figure 7.1 *The geometry of the template windows and displacement vectors*

In the proposed scheme, the adjacent patches overlap each other by one pixel as shown in Figure 7.2, in which each little square stands for a pixel. The displacements at the corners of the patches are common to 4 adjacent patches. For example, in Figure 7.2,

the displacement at the top-left corner of patch 4 is common to those at the low-right corner of patch 1, the low-left corner of patch 2 and the top-right corner of patch 3. Therefore, for an area of $n \times m$ patches, the number of displacements to be determined is $(n+1)(m+1)$, i.e. $2(n+1)(m+1)$ unknowns to be determined. For example, as shown in Figure 7.1, for an area of 9 patches (3 rows and 3 columns of patches), there are a total of 16 displacement vectors to be determined.

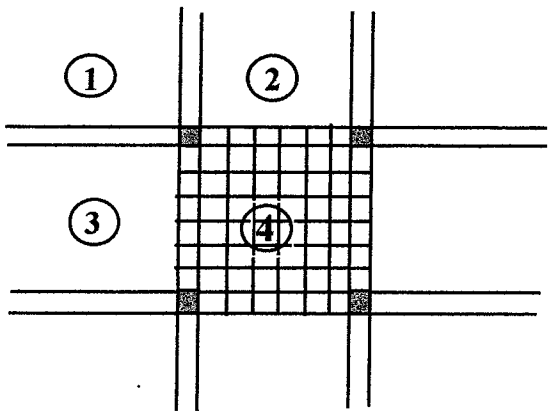

Figure 7.2 *The joining structure of the patches.*

In the proposed scheme, each patch is further divided into an array of elementary subsets or sub-images for forming an observation equation (7.6), discussed in section 7.2.3. In other words, an elementary subset has an observation equation. The necessary size of the elementary subset is controlled by the expected maximum spatial lag of corresponding features contained in the template patch on the first image, and the sub-image resampled from the second image, i.e. the possible maximum refinement of the displacements to be determined, $d\Delta x_s$, $d\Delta y_s$. In the first iteration, because the approximate displacements are less accurate, the spatial lags between the features in the template patch and their counterpart in the resampled sub-image are relatively large. Thus, large elementary subsets are used. When the estimated displacements approach their optimal values in subsequent iterations, the size of the elementary subset is reduced as the $d\Delta x_s$, $d\Delta y_s$ are gradually reduced. The detailed discussion on the reason for varying the size of the elementary subsets will be given in section 7.4.

As the proposed scheme is designed to refine the resultant displacements derived from the relaxation labelling estimation, the residuals of displacements are expected to be about 5 to 7 pixels. Therefore, the sizes of the elementary subsets were 5×5 pixels , and 3×3 pixels for the first 2 iterations respectively, then subset 2×2 pixels in size was used until the iterative process converges. The adjacent elementary subsets have a 1 pixel overlap with each other. In this study, patches are of the size 25×25 pixels. The numbers of elementary subsets in each patch are respectively 6×6=36, 12×12=144, and up to 24×24=576, when the elementary subset is of the size 5×5 pixels , 3×3 pixels, and 2×2 pixels.

7.2.2 The Transformation Model of the Template Window

The scheme employs a bi-linear transformation model to derive the displacement of a surface water patch contained in the template window. The displacement of the patch is parameterised with 4 independent displacement vectors of the four corners of the patch.

$$\Delta = [\, \Delta x_{i,j}\ \Delta y_{i,j}\ \Delta x_{i,j+1}\ \Delta y_{i,j+1}\ \Delta x_{i+1,j}\ \Delta y_{i+1,j}\ \Delta x_{i+1,j+1}\ \Delta y_{i+1,j+1}]^T$$

The displacements of each pixel in the patch are bi-linearly interpolated based on the displacement of the corners Δ, with equations:

$$\begin{aligned}
\Delta x_s &= [\Delta x_{i,j}(n-c_s)(m-r_s) + \Delta x_{i,j+1}(c_s-1)(m-r_s) + \Delta x_{i+1,j}(n-c_s)(r_s-1) \\
&\quad + \Delta x_{i+1,j+1}(c_s-1)(r_s-1)]/(n-1)(m-1) \\
\Delta y_s &= [\Delta y_{i,j}(n-c_s)(m-r_s) + \Delta y_{i,j+1}(c_s-1)(m-r_s) + \Delta y_{i,j+1}(n-c_s)(r_s-1) \\
&\quad + \Delta y_{i+1,j+1}(c_s-1)(r_s-1)]/(n-1)(m-1)
\end{aligned} \qquad (7.1)$$

Where s is an arbitrary pixel within the patch, located at the r_sth row and the c_sth column of the template window. n and m are the number of rows and columns of the template window in pixel units. s in the first image is advected to the position s' in the second image as shown in Figure 7.3. The displacement of s, i.e. the distance between s and s', is parameterised by the displacements of the four corners, Δ, using equation (7.1)

Equation (7.1) defines a projection, which projects each element of the template at location (x_s, y_s) to the position (x'_s, y'_s) in the second image, or conversely, projects the

elements at (x'_s,y'_s) in the second image back to the position (x_s,y_s) in the template. It is a projection between a rectangular (a square is used to simplify the computation) template and a general quadrilateral. In practice, the reverse projection is preferred to simplify the computation. In this scheme, the quadrilateral sub-image in the second image is projected into a rectangular resampled image. Then the computation as discussed in the following section, is undertaken between the two rectangular windows, the template and the resampled sub-image from the second image.

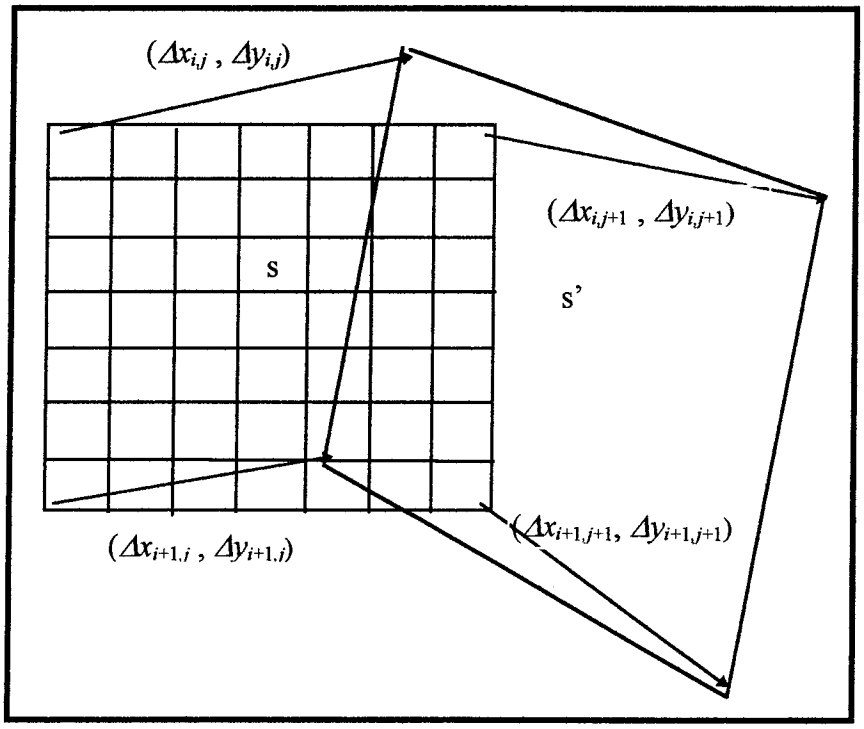

Figure 7.3 *The geometry of the template and its best match sub-image in the second image. One square represents one pixel.*

7.2.3 The Observation Equation

Let $I_1(x,y)$ be the discrete intensity function of the template in the first image obtained at time t_1, and $I_2(x,y)$ be the intensity function of the sub-image in the second image acquired by the satellite at time t_2. During the short period $\Delta t = t_2 - t_1$, the sea surface temperature (SST) patterns are transported along with the sea surface current. A small water parcel S (corresponding to an elementary subset) centred at (x_s,y_s) at moment t_1 is transported a distance $(\Delta x_s, \Delta y_s)$ to $(x'_s, y'_s) = (x_s + \Delta x_s, y_s + \Delta y_s)$ at t_2. The change of temperature of this small parcel is assumed to be negligibly

small during the short time interval. This is one of the most basic assumptions for estimation of sea surface current from consecutive images, as has been discussed in Chapter 2. The intensity values (x_s, y_s) in the first image and (x'_s, y'_s) in the second image satisfy the following equation:

$$I_2(x_s + \Delta x_s, y_s + \Delta y_s) + n_2(x_s + \Delta x_s, y_s + \Delta y_s) + I_d = I_1(x_s, y_s) + n_1(x_s, y_s) \quad (7.2)$$

where, $n_1(x_s, y_s)$ and $n_2(x_s + \Delta x_s, y_s + \Delta y_s)$ are the noise in the first and second images, and the term I_d is the intensity deformation due to the difference between the atmospheric conditions at the time of acquirement of the two images.

It is further assumed that an approximate estimation of the displacement field $(\Delta x^0_s, \Delta y^0_s)$ can been obtained by using some other techniques, such as the relaxation estimation described in Chapter 6, or the results of the previous iteration for the initial input to this scheme. Thus, the position of the water parcel S in the second image can be denoted as $(x'_s, y'_s) = (x_s + \Delta x^0_s + d\Delta x_s, y_s + \Delta y^0_s + d\Delta y_s)$ or $(x'_s, y'_s) = (x^0_s + d\Delta x_s, y^0_s + d\Delta y_s)$ with $(x^0_s, y^0_s) = (x_s + \Delta x^0_s, y_s + \Delta y^0_s)$, where the $(d\Delta x_s, d\Delta y_s)$ are the corrections to the approximate displacements, and are the $(\Delta x^0_s, \Delta y^0_s)$ are the approximate displacement derived from relaxation labelling process or last interation. When the least square matching starts with no apriori knowledge, i.e. when no approximate estimation of the displacement field is available, the iterative process starts from the same position as that of the template location (i.e. $(\Delta x^0_s, \Delta y^0_s) = (0,0)$ and $(d\Delta x_s, d\Delta y_s) = (\Delta x_s, \Delta y_s)$). Under these circumstances, the spatial lags between corresponding features in the two patches (i.e. the template window and the resampled window) are large. For a pair of images separated by 12 hours, the spatial lags can be up to 20 pixels. Whether the least square matching can provide the correct initial positions for optimal estimation for large spatial lags will depend on whether the template and the resample windows contain large spatial scale homogeneous features. A detailed discussion of this matter will be given in section 7.4. Following the discussion, reasons will be given to explain why the proposed scheme is preferably only for refining of the resultant field derived from the relaxation estimation.

In this proposed scheme, the displacement correction values ($d\Delta x_s$, $d\Delta y_s$) of an arbitrary elementary subset S centred at (r_s,c_s) in the patch are also defined by displacement correction values of the patch corners $\mathbf{d} = [\, d\Delta x_{i,j}\ d\Delta y_{i,j}\ d\Delta x_{i,j+1}\ d\Delta y_{i,j+1}\ d\Delta x_{i+1,j}\ d\Delta y_{i+1,j}\ d\Delta x_{i+1,j+1}\ d\Delta y_{i+1,j+1}]^T$ derived by the bi-linear equation (7.1) in which Δ replaced by $d\Delta$.

$$\begin{aligned} d\Delta x_s &= [d\Delta x_{i,j}(n-c_s)(m-r_s) + d\Delta x_{i,j+1}(c_s-1)(m-r_s) + d\Delta x_{i+1,j}(n-c_s)(r_s-1) \\ &\quad + d\Delta x_{i+1,j+1}(c_s-1)(r_s-1)]/(n-1)(m-1) \\ d\Delta y_s &= [d\Delta y_{i,j}(n-c_s)(m-r_s) + d\Delta y_{i,j+1}(c_s-1)(m-r_s) + d\Delta y_{i,j+1}(n-c_s)(r_s-1) \\ &\quad + d\Delta y_{i+1,j+1}(c_s-1)(r_s-1)]/(n-1)(m-1) \end{aligned} \tag{7.3}$$

Substituting $(x's, y's) = (x^0s + d\Delta x_s, y^0s + d\Delta y_s)$ into equation (7.2) and combining n_1 and n_2 as n gives the following equation:

$$I_1(x_s, y_s) = I_2(x_s^0 + d\Delta x_s, y_s^0 + d\Delta y_s) + I_d + n \tag{7.4}$$

Linearising equation (7.4) with first order Taylor series expanding at point (x^0s, y^0s), gives:

$$I_1(x_s, y_s) - I_2(x_s^0, y_s^0) = \frac{\partial I_2(x_s^0, y_s^0)}{\partial x} d\Delta x_s + \frac{\partial I_2(x_s^0, y_s^0)}{\partial y} d\Delta y_s + I_d + n + O \tag{7.5a}$$

where, O is the higher order terms of the series. Rewriting some of the terms in equation (7.5a) in simpler form as:

$$\Delta I_s = I_2(x_s^0, y_s^0) - I_1(x_s, y_s)$$

$$I_x = \frac{\partial I_2(x_s^0, y_s^0)}{\partial x} \qquad I_y = \frac{\partial I_2(x_s^0, y_s^0)}{\partial y}$$

$$v_i = -n - O$$

gives the rewritten equation (7.5a) in the following form:

$$v_s = \Delta I_s + I_x d\Delta x_s + I_y d\Delta y_s + I_d \tag{7.5b}$$

The equation (7.5b) is the observation equation of the elementary subset S. The displacement correction values of elementary subset S, ($d\Delta x_s$, $d\Delta y_s$), can be parameterised with the displacements of four corners, $\mathbf{d}$, by equation (7.3). Substituting equation (7.3) into equation (7.5b) gives the observation equation of the elementary subset S parameterised with the displacements of four corners, $\mathbf{d}$.

$$v_s = a_{i,j}\,d\Delta x_{i,j} + b_{i,j}\,d\Delta y_{i,j} + a_{i,j+1}\,d\Delta x_{i,j+1} + b_{i,j+1}\,d\Delta y_{i,j+1} + a_{i+1,j}\,d\Delta x_{i+1,j} + b_{i+1,j}\,d\Delta y_{i+1,j} + a_{i+1,j+1}\,d\Delta x_{i+1,j+1} + b_{i+1,j+1}\,d\Delta y_{i+1,j+1} + \Delta I_s + I_d \qquad (7.6)$$

where,

$$a_{i,j} = I_x(n\text{-}c_s)(m\text{-}r_s)/(n\text{-}1)(m\text{-}1) \qquad b_{i,j} = I_y(n\text{-}c_s)(m\text{-}r_s)/(n\text{-}1)(m\text{-}1)$$

$$a_{i+1,j} = I_x(n\text{-}c_s)(r_s\text{-}1)/(n\text{-}1)(m\text{-}1) \qquad b_{i+1,j} = I_y(n\text{-}c_s)(r_s\text{-}1)/(n\text{-}1)(m\text{-}1)$$

$$a_{i,j+1} = I_x(c_s\text{-}1)(m\text{-}r_s)/(n\text{-}1)(m\text{-}1) \qquad b_{i,j+1} = I_y(c_s\text{-}1)(m\text{-}r_s)/(n\text{-}1)(m\text{-}1)$$

$$a_{i+1,j+1} = I_x(c_s\text{-}1)(r_s\text{-}1)/(n\text{-}1)(m\text{-}1) \qquad b_{i+1,j+1} = I_y(c_s\text{-}1)(r_s\text{-}1)/(n\text{-}1)(m\text{-}1)$$

Where I_d is the intensity deformation due to the difference of atmosphere conditions between the images observation time. Generally, the surface temperature change due to the atmosphere effects can be reasonably assumed to be of much larger spatial scales than the temperature change due to the advection of the SST patterns, and can be effectively reduced by filtering out the very long wavelength components of both images (see *Kelly* [1989], and *Kelly & Strub* [1992]).

The observation equation with the gradients derived from the first image can also be derived by equivalently rewriting equation (7.4) as follows:

$$I_1(x_s - d\Delta x_s, y_s - d\Delta y_s) = I_2(x_s^0, y_s^0) + I_d + n$$

and linearising the left side of the equation to give:

$$I_1(x_s, y_s) - \frac{\partial I_1(x_s, y_s)}{\partial x} d\Delta x_s - \frac{\partial I_1(x_s, y_s)}{\partial y} d\Delta y_s = I_2(x_s^0, y_s^0) + I_d + n + O$$

This equation is of the same format as equation (7.5a) except the gradients and derived from the intensity function of the first image.

The intensity gradients and the intensity differences of each elementary subset are computed using the same methods as used in *Kelly* [1989] and *Kelly & Strub* [1992]. The intensity differences are computed as follows:

$$\Delta I = \overline{I_2(x,y) - I_1(x,y)} \qquad (7.7a)$$

where the overbar denotes the average over the elementary subset. The gradients are computed by linearising the intensity function over the elementary subset as a ramp with least squares fitting:

$$\xi = Ax + By + C - I(x,y) \tag{7.7b}$$

so that the gradient $I_x = A$ and $I_y = B$.

The displacement correction values at the corners of these joined patches are simultaneously determined, by minimising the sum of the squares of v of all the observation equations corresponding to the entire joined area.

The displacements are updated with the estimated corresponding correction values. The updated displacements are then used as the parameters to resample the sub-image in the second image for the new iteration. The position to be resampled in the second image of each element inside the patch, (x^{k-1}_s, y^{k-1}_s), is determined by equation (7.1) and based on the updated displacements of corners of the patch. The intensity value of the resampled elements are computed with bi-linear interpolation of the 4 nearest pixels around the position (x^{k-1}_s, y^{k-1}_s). The iterative process terminates when all the computed displacement correlation values are smaller then 0.5 pixel.

7.3 The Constraints

As has been mentioned previously, the SST images are frequently dominated by the large scale patterns. Although, each patch has up to 576 (24×24) observation equations, the observation equations derived, based on those large patterns, have a high chance of being correlated to one another. When the number of effective observation equations is less than the total number of the unknowns, the least squares problem is under-determined. In the test reported in this chapter, it was also found that some of patches may not be entirely singular, however, their normal equations are ill conditioned (i.e. a part of eigenvalues of the normal equation formed from those patches are close to zero) due to the SST gradients being predominantly in one direction. Some examples where the features contained in patches are not sufficient for the determination of the 6 or more affine transformation parameters have been given in *Gruen et al.* [1991].

In the proposed scheme, constraints are used to solve the problem of singularity or ill conditioning, which may be contained in the observation equations, and convey the contextual information. Three constraints are used which are respectively:

1. The joined patches
2. The smoothness of the second order difference among the neighbouring displacements
3. The incompressibility of the water volume

7.3.1 The Joined Patches

In the proposed scheme, the estimation is primarily constrained by joining the adjacent patches together through using common unknowns (displacements) for the four overlapped (1 pixel overlap with each other) adjacent patch corner (refer to the Figure 7.1 and Figure 7.2).

Firstly, the joined patches relieve the problem of singularity or ill conditioning of the normal equations by reducing the number of unknowns i.e. they reduce the requirement in the number of essential independent observation equations. For example, for an area of $n \times m$ patches, the number of unknowns is $6 \times n \times m$ in the single patch least squares matching, where the following linear transformation function is used in the displacement determination:

$$\begin{bmatrix} x_i' \\ y_i' \end{bmatrix} = \begin{bmatrix} a_1 & a_2 \\ a_3 & a_4 \end{bmatrix} \cdot \begin{bmatrix} x_i \\ y_i \end{bmatrix} + \begin{bmatrix} a_5 \\ a_6 \end{bmatrix} \tag{7.8.a}$$

where (x_i, y_i) is the position of an elementary subset in the first image about a local coordinate system which is centred at the centre of the template in the first image, (x_i', y_i') is the position of the corresponding elementary subset which contains the homogenous feature in the second image, and the $a_1, a_2, \ldots a_6$ are the transformation parameters of the patch. This linear transformation function plays the same role as the equation (7.1) in joined patch least squares matching. In contrast with the JPLSM method, in the single patch matching method the unknowns to be determined are the transformation parameters $a_1, a_2, \ldots a_6$ rather than the displacements at the four corners

of the patch. The correction of displacement to the elementary subset is derived from the derivative of equation (7.8.a), and has the following form:

$$\begin{aligned} d\Delta x_i &= x_i' - x_i'^0 = x_i da_1 + y_i da_2 + da_5 \\ d\Delta y_i &= y_i' - y_i'^0 = x_i da_3 + y_i da_4 + da_6 \end{aligned} \tag{7.8.b}$$

where the $(x_i'^0, y_i'^0)$ is the approximate position of the elementary subset derived by the last iteration. The observation equation of the elementary subset is then given by substituting equation (7.8.b) into equation (7.5.b), and it has a as follows:

$$v_i = \Delta I_i + I_x(x_i da_1 + y_i da_2 + da_5) + I_y(x_i da_3 + y_i da_4 + da_6) + I_d$$

Therefore, each patch has 6 unknowns da_1 , da_2 ,... da_6 to be determined. The number of the unknowns for the joined patches is $2\times(n+1)(m+1)$. Intuitively, each displacement away from edges of the joined area is common to four adjacent patches. In other words, the observation equations formed from four adjacent patches contribute to the determination of the displacements at a grid point. Thus it effectively strengthens the structure among the patches and therefore reduces the chance of singularity.

Secondly, the bi-linear transformation function defined by equation (7.1) has 8 independent parameters and it projects a rectangular template on to a general quadrilateral. In other words, it allows the rectangular sub-image contained in the template to deform to a general quadrilateral sub-image in the second image. In this way, the patches move together but each one deforms independently. In comparison, the transformation function defined by equation (7.8.a) has only 6 independent parameters, it projects the rectangular template to a parallelogram. Obviously, it only allows for those cases where the rectangular sub-image in the first image deforms to an arbitrary parallelogram in the second image. Therefore, the bilinear transformation function (i.e. the equation (7.1)) enables the matching process to resolve the deformation better than the transformation function defined by equation (7.8).

7.3.2 The Smoothness of the Second Order Difference among the Neighbouring Displacements

The smoothness of the displacement field is measured by the second order difference of displacements of three neighbouring grid points. For an arbitrary inner grid point, the

second order difference of optimal displacements of neighbouring points in the x and y directions are constrained to be minimum in the least squares process:

$$\xi = -\Delta x_{i-1,j} + 2\Delta x_{i,j} - \Delta x_{i+1,j} \quad \xi = -\Delta y_{i-1,j} + 2\Delta y_{i,j} - \Delta y_{i+1,j}$$

$$\xi = -\Delta x_{i,j-1} + 2\Delta x_{i,j} - \Delta x_{i,j+1} \quad \xi = -\Delta y_{i,j-1} + 2\Delta y_{i,j} - \Delta y_{i,j+1} \qquad (7.9.a)$$

where, the Δx's, Δy's are the optimal displacements, and the ξ's are the residuals to be minimised in the least squares process. As defined previously in section 7.2.3, the optimal displacements are the sum of approximate displacements Δx^0's, Δy^0's and their correction $d\Delta x$'s and $d\Delta y$'s:

$$\Delta x_{i-1,j} = \Delta x^0_{i-1,j} + d\Delta x_{i-1,j} \qquad \Delta y_{i-1,j} = \Delta y^0_{i-1,j} + d\Delta y_{i-1,j}$$

$$\Delta x_{i,j} = \Delta x^0_{i,j} + d\Delta x_{i,j} \qquad \Delta y_{i,j} = \Delta y^0_{i,j} + d\Delta y_{i,j} \qquad (7.9.b)$$

$$\cdots\cdots\cdots$$

$$\Delta x_{i+1,j} = \Delta x^0_{i+1,j} + d\Delta x_{i+1,j} \qquad \Delta y_{i+1,j} = \Delta y^0_{i+1,j} + d\Delta y_{i+1,j}$$

Substituting equations (7.9.b) into (7.9.a) gives the following four smoothness constraint equations:

$$\xi = -d\Delta x_{i-1,j} + 2d\Delta x_{i,j} - d\Delta x_{i+1,j} - (\Delta x^0_{i-1,j} - 2\Delta x^0_{i,j} + \Delta x^0_{i+1,j})$$

$$\xi = -d\Delta y_{i-1,j} + 2d\Delta y_{i,j} - d\Delta y_{i+1,j} - (\Delta y^0_{i-1,j} - 2\Delta y^0_{i,j} + \Delta y^0_{i+1,j})$$

$$\xi = -d\Delta x_{i,j-1} + 2d\Delta x_{i,j} - d\Delta x_{i,j+1} - (\Delta x^0_{i,j-1} - 2\Delta x^0_{i,j} + \Delta x^0_{i,j+1}) \qquad (7.9.c)$$

$$\xi = -d\Delta y_{i,j-1} + 2d\Delta y_{i,j} - d\Delta y_{i,j+1} - (\Delta y^0_{i,j-1} - 2\Delta y^0_{i,j} + \Delta y^0_{i,j+1})$$

For the points on the edge of the grid, the neighbouring vectors are constrained by two equations in either the x direction or the y direction correspondingly.

The smoothness constraint influences the unification of the gradients of the neighbouring displacements. As that has been discussed in Chapter 6, compared with the smoothness constraint based on the first order difference of displacements, which forces the gradients of neighbouring displacements to be zero, the smoothness constraint based on second order difference of displacements has an advantage over that based on first order differences. It resolves the variation among the neighbouring displacements. However, it still forces the variation of the gradient of the neighbouring

displacements to be small. Therefore, the suitability of this constraint to the estimation at hand is dependent on three aspects:

1. Whether the estimating field has strong variation in the velocity gradients.
2. The density of the computation grid.
3. Because the direct estimates are displacements, and the differences of the gradients of neighbouring displacements are accumulated as the time separation increases, the suitability of the constraint is also subject to the time separation of the image sequence.

The grid density used in the scheme in this chapter is the same as that used in Chapter 6, i.e. the points are 24 pixels (about 26 km) apart. The study in Chapter 6 shows that when the smoothness constraint based on second order differences of the neighbouring displacements are employed as the compatibility function for this grid density is appropriate to estimate the displacements of an 18 hours separated image sequence for most part of the image domain. However, the constraint may over-smooth the estimates in areas of strong variation in velocity gradients due to the imperfection of the constraint as discussed previously. Even after the refining process described in Chapter 6, the negative effect of the constraint may still remain in some parts of the estimated field. Therefore, the influence of this constraint should be minimised in the least squares matching process to prevent the over-smoothing effect. However, on the other hand, as discussed in *Gruen et al.* [1991], in some cases, the features contained in patches are not sufficient for the determination of all transformation parameters, i.e. the displacements at four corners in the proposed scheme, and the least squares problem can be under-determined because the number of effective observation equations is less than the total number of the unknowns, or is ill conditioned, i.e. a part of the eigenvalues of the normal equation formed from those patches are close to zero, due to low contrast in grey values. The smoothness constraint and the incompressibility constraint discussed in the next section (7.3.3) are designed to solve this under-determined or ill-conditioned problem. To balance solving the singularity and preventing the over-smoothing effect, in principle, these two constraints are only applied to the under-determined and ill-conditioned patches, and this is implemented by giving a very small weight to the

constraints where the grid points are surrounded by patches of good condition, while a larger weight is given to the grid points around a patch of ill condition. The detailed discussion on the determination of the weights of the constraint will be given in section 7.3.4..

7.3.3 The Constraint Based on the Incompressibility of Water Volume

This constraint is based on the fact that the principle direction of the movement of the water in the ocean is horizontal (i.e. the vertical movements of the ocean water are much smaller than the horizontal movements). The average velocities of vertical water movements accompanying wind-driven currents in the open sea do not exceed 10^{-5} - 10^{-6} cm s^{-1} [*Tolmazin* 1985]. It is therefore, reasonable to assume that the water parcel in the open ocean is approximately 2 dimensionally incompressible.

The incompressible constraint used in this scheme requires the area of the best matching sub-image in the second image to be equal to the area of the sub-image contained in the template of the first image. In other words, the area of the sub-image in the template does not change when it shifts, rotates and deforms. It is assumed that the sub-image contained in a rectangular template in the first image is deformed to a general quadrilateral in the second image as shown in Figure 7.4. Letting the coordinates of the corners of the template in the first image to be $(x_{i,j}, y_{i,j})...(x_{i+1,j+1}, y_{i+1,j+1})$, the length of the sides of the square template to be s, the displacements of these corners are respectively $(\Delta x_{i,j}, \Delta y_{i,j})$ ... $(\Delta x_{i+1,j+1}, \Delta y_{i+1,j+1})$, the diagonals of the quadrilateral in the second image are d_1 and d_2 , and the angle between the two diagonals is θ, then according to the 2-D incompressible assumption, the constraint can be given as follows:

$$s^2 - \frac{1}{2} d_1 d_2 \sin\theta = 0 \tag{7.10}$$

where,

$$d_1 = \sqrt{(\Delta x_{i+1,j+1} + s - \Delta x_{i,j})^2 + (\Delta y_{i+1,j+1} + s - \Delta y_{i,j})^2}$$

$$d_2 = \sqrt{(\Delta x_{i+1,j} - s - \Delta x_{i,j+1})^2 + (\Delta y_{i+1,j} + s - \Delta y_{i,j+1})^2}$$

$$\theta = \tan^{-1} \frac{\Delta y_{i+1,j} + s - \Delta y_{i,j+1}}{\Delta x_{i+1,j} - s - \Delta x_{i,j+1}} - \tan^{-1} \frac{\Delta y_{i+1,j+1} + s - \Delta y_{i,j}}{\Delta x_{i+1,j+1} + s - \Delta x_{i,j}}$$

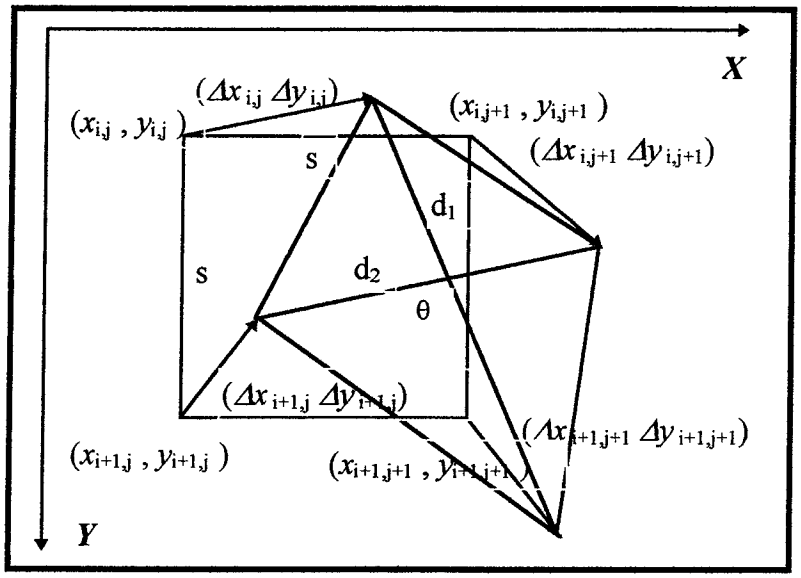

Figure 7.4 *The geometry of the incompressibility constraint.*

Denoting the displacements estimated in the previous iteration by $(\Delta x^{o}_{i,j},\Delta y^{o}_{i,j})$ ... $(\Delta x^{o}_{i+1,j+1},\Delta y^{o}_{i+1,j+1})$, and linearising the equation (7.10) gives the error equation of the constraint:

$$\begin{aligned}\xi = &-Dy_2 d\Delta x_{i,j} - Dx_2 d\Delta y_{i,j} + Dy_1 d\Delta x_{i,j+1} - Dx_1 d\Delta y_{i,j+1} - Dy_1 d\Delta x_{i+1,j} \\ &+Dx_1 d\Delta y_{i+1,j} + Dy_2 dx_{i+1,j+1} + Dx_2 dy_{i+1,j+1} - (2s^2 - d_1 d_2 \sin\theta)\end{aligned} \tag{7.11}$$

where,

$$Dx_1 = \Delta x^{o}_{i+1,j+1} + s - \Delta x^{o}_{i,j}$$

$$Dy_1 = \Delta y^{o}_{i=1,j+1} + s - \Delta y^{o}_{i,j}$$

$$Dx_2 = \Delta x^{o}_{i,j+1} + s - \Delta x^{o}_{i,j+1}$$

$$Dy_2 = \Delta y^{o}_{i+1,j} + s - \Delta y_{i+1,j}$$

Although, it is possible to exclude from the analysis the vertical velocity and assume the water parcel to be 2 dimensionally incompressible without introducing any major error, the constraint influences the system results of a non-divergent field. The information on divergence/convergence of the velocity field may still be valuable (it may be small but useful) to the studies of meso-scale circulations in coastal regions. Therefore, the proposed scheme only applies this constraint to the patches which are singular or ill conditioned in principle, and this is implemented by giving very small weights to the

constraints corresponding to the patches of good inversion condition and relatively larger weights to those corresponding to singular and ill conditioned patches. This is the same procedure as used for the treatment of the smoothness constraint in section 7.3.2.

7.3.4 The Scaling and Weighting of the Constraints.

The system of equations of this least squares matching scheme consists of three parts, the observation equations based on equation (7.6), the smoothness constraint equations, and the equations based on the incompressible constraint. These are denoted as $\mathbf{Ax}=\mathbf{L_a}$, $\mathbf{Bx}=\mathbf{L_b}$, and $\mathbf{Cx}=\mathbf{L_c}$ respectively and their weight matrices as $\mathbf{P_a}$, $\mathbf{P_b}$ and $\mathbf{P_c}$ respectively, where $\mathbf{P_a}=\mathbf{I}$ ($\mathbf{I}$ is an identity matrix) is used in this scheme and $\mathbf{P_b}$ and $\mathbf{P_c}$ are diagonal matrices with elements of magnitude ranging from 0 to 1. The normal equation of the system is of the following form:

$$(\mathbf{A}^T\mathbf{A}+\mathbf{B}^T\mathbf{P_b}\mathbf{B}+\mathbf{C}^T\mathbf{P_c}\mathbf{C})\mathbf{x}=\mathbf{A}^T\mathbf{L_a}+\mathbf{B}^T\mathbf{P_b}\mathbf{L_b}+\mathbf{C}^T\mathbf{P_c}\mathbf{L_c} \tag{7.12}$$

There is a great disparity in the number of equations between that of $\mathbf{Ax}=\mathbf{L_a}$ and $\mathbf{Bx}=\mathbf{L_b}$ and $\mathbf{Cx}=\mathbf{L_c}$. In part $\mathbf{Ax}=\mathbf{L_a}$, there are up to 24×24 equations corresponding to each patch, while, each patch has only one incompressibility constraint equation, and each grid point has only up to 4 smoothness constraint equations. Considering the typical intensity gradients are between ±3-6 pixel^{-1} (for the 8 bit image data with intensity value ranges of 0-255), the magnitude of coefficients in matrix $\mathbf{A}^T\mathbf{A}$ can be of the order of 10^4 to 10^5, while, the coefficients in $\mathbf{B}^T\mathbf{B}$ are between -2 and 4, and the coefficients in $\mathbf{C}^T\mathbf{C}$ are about 500 to 2000. The great difference in the magnitude of the coefficients among the matrices, especially between $\mathbf{A}^T\mathbf{A}$ and $\mathbf{B}^T\mathbf{B}$ may make the contribution due to the measurements contained in $\mathbf{A}$ and $\mathbf{L_a}$ too dominant in the results. Therefore, to balance the contributions of each part of the equations, the $\mathbf{B}^T\mathbf{P_b}\mathbf{B}$ and corresponding $\mathbf{B}^T\mathbf{P_b}\mathbf{L_b}$ and $\mathbf{C}^T\mathbf{P_c}\mathbf{C}$ and corresponding $\mathbf{C}^T\mathbf{P_c}\mathbf{L_c}$, are scaled by S_b and S_c respectively which play a role equivalent to weights, and they are computed with the following equations:

$$S_b = \frac{tr(\mathbf{A}^T\mathbf{A})}{tr(\mathbf{B}^T\mathbf{B})} \quad \text{and} \quad S_c = \frac{tr(\mathbf{A}^T\mathbf{A})}{tr(\mathbf{C}^T\mathbf{C})} \tag{7.13}$$

where *tr*( )'s are the trace of the matrices. The S_b and S_c computed based on the image condition used in the tests described in section 7.5 are approximately 2.0×10^4 and 10 respectively.

As discussed in *Gruen et al.* [1991], in some cases, the features contained in patches are not sufficient for the determination of all transformation parameters, i.e. the displacements at four corners in the proposed scheme, and the least squares problem can be under-determined because the number of effective observation equations is less than the total number of the unknowns, or ill conditioned, i.e. a part of eigenvalues of the normal equation formed from those patches are close to zero, due to low contrast in grey value. The smoothness constraint and the incompressibility constraint discussed in next section (7.3.3) are designed to solve this under-determined or ill-conditioned problem. To balance solving the singularity and preventing from the over-smoothing effect, in principle, these two constraints are only applied to the under-determined and ill-conditioned patches, and this is implemented by giving a very small weight to the constrains where the grid points surrounded by patches of good condition, and a larger weight to the grid points around a patch of ill condition.

As discussed previously in section 7.3.2 and 7.3.3, in some cases, patterns contained in patches are not sufficient for the determination of all transformation parameters (see *Gruen et al.* [1991], for example), and the least squares problem can be under-determined or ill conditioned, i.e. a part of eigenvalues of the normal equation formed from those patches are close to zero. To solve the singularity, and at meantime prevent from the negative effects of the constraints due to the approximations discussed previously, in principle, these two constraints are only applied to the under-determined and ill-conditioned patches.

In leaner algebra, the singularity or the degree close to singularity of a leaner system can be measured by the eigenvalues or the condition number derived from eigenvalues of the system. The proposed scheme uses a condition number defined in *Branham* [1990], which is of a form as follows:

$$cond(A_{ij}^{T}A_{ij})=(\lambda_{max}/\lambda_{min})^{1/2} \qquad (7.14)$$

where, A_{ij} is the coefficient matrix of error equations of patch (i,j), and λ_{max} and λ_{min} are the maximum and minimum eigenvalues of the matrix $A_{ij}^T A_{ij}$ respectively. When the normal equation is singular, the minimum eigenvalue λ_{min} is zero, and thus the condition number equals infinity. When the normal equation is in an ideally good condition (i.e. all of eigenvalues are equal), the condition number reaches its minimum, and equals 1. In the proposed scheme, the condition number of each patches is computed individually, (i.e. patches are considered as independent of each other, and not joined together in the condition number computation), and each patch has 8 unknowns. The coefficient matrix of normal equations of each patch $A_{ij}^T A_{ij}$ in equation (7.14) is formed by 24×24 error equations based on equation (7.6). The eigenvalues of the coefficient matrix is computed firstly. If the matrix is not singular, then the condition number is computed to measure the degree close to singularity of the matrix.

The detailed discussing about the determination of the weight of each constraint equations will be given in section 7.5.1 and 7.5.2. Briefly, each inner grid point has 4 adjacent patches, and each patch has a condition number. The weight of the smoothness constraint of centred at this grid point is determined based on the maximum condition number of these four patches. As four grid points involved in a incompressibility constraint equation (equation 7.11) are the four corners of a patch, the incompressibility constraint of each patch is simply determined based upon the condition number corresponding to this patch. Since all patches are joined together in JPLSM, the displacements of each grid point are determined by the information from adjacent patches. The displacements of an inner grid point is determined from four patches. However, the grid points on the edge of grid have only two adjacent patches, and the grid points at corners of the grid have one patch connected to this point. In comparison with the inner points, these point have less information for the determination of displacements. Therefore, it is reasonable to give relatively larger weights to the smoothness constraints and incompressibility constraints related to these grid points, to strengthen the linkage between these points and their neighbouring grid points, and convey information among these points and from their nearest neighbouring inner grid points onto these points.

7.4 The Error of Using a First Order Differential Approximation over a Large Elementary Sub-Image

In this section, the relation between the proposed least squares matching scheme and the inverse model method developed by *Kelly* [1989] is firstly illustrated, and then, the error of using the differential form of the thermal conservation equation over a large elementary subset for velocity estimation using a large elementary subset is discussed. Based on the discussion, the reasons for using the iterative procedure with elementary subsets varying from large to small in the proposed scheme, is explained.

7.4.1 On the Relation between the Proposed Scheme and the Inverse Model Method

The relation between the proposed scheme and the inverse model can be viewed by comparing equation (7.5b) with the differential form of the energy conservation equation, which is the basis of the inversion method for the velocity field estimation from consecutive thermal images (see section 2.5.4 and also refer to *Kelly* [1989] and *Kelly et al.* [1992]). The two equations are of the same form, although they are derived differently from the image matching point of view and the physical point of view. When the initial size of the elementary subset equals the size of the patch (i.e. each patch possess only one elementary subset), and the initial displacements (Δx^0 , Δy^0) are equal to zero, the first iteration of the proposed scheme is the inverse model method. In other words, the proposed least squares matching scheme can be viewed as an iterative inverse model method as developed by *Kelly* [1989]. As has been discussed in Chapter 2, there are two types of methods for the objective estimation of velocity field from consecutive satellite images — the methods based on feature tracking (image matching using feature similarity) and the inversion methods based on the energy conservation equation. The least squares matching scheme elegantly unifies these two methods.

7.4.2 Error from Using the Differential Form of the Energy Conservation Equation over a Large Elementary Subset

The error from using the differential form of the thermal conservation equation (as well as equation (7.5b) equivalent) for velocity estimation with a single iteration may come from a number of sources. The following discussion is restricted to the error due to the

image components being of a spatial scale smaller than the displacements which are neglected by the linear approximation due to the use of the differential form of the equation.

To simplify the discussion, consider a one dimensional case as shown in Figure 7.5, where the $T_1(x)$ is the temperature spatial distribution of a water body at moment t_1. The water body shifts a distance $u(t_2 - t_1)$ in the temporal interval $t_2 - t_1$ with a velocity u. The temperature distribution of the water body at moment t_2 is denote by $T_2(x)$ in the figure. As shown in Figure 7.5, the water body between x_c and x_d which is in the window at moment t_1 moves out of the window at t_2, and the water body between x_a and x_b which is outside the window at $t_1$moves into the window at t_2. As discussed previously in Chapter 2, all methods used to determined current velocity field from consecutive SST images assumes that the temperature of the water body does not change when it is shifted, i.e. the temperature values marked with a, b, c, d, remain the same when they flow to positions a', b', c', d'. Due to the incompressibility of the water body, the displacements a $\rightarrow$ a', b $\rightarrow$ b', c $\rightarrow$ c', d $\rightarrow$ d' are all equal to $u(t_2 - t_1)$. Thus, $T_2(x) = T_1(x - u(t_2 - t_1))$. The sub-image contained in the window is an elementary subset used to form the observation equation.

Precisely, because the window (i.e. the elementary subset) is of a certain size, the change of the thermal energy (i.e. the integration of temperature with respect to distance x in the one dimensional case) contained within the window, ΔT is given by the follow integral:

$$\Delta T = \int_{x_b}^{x_d} [T_2(x) - T_1(x)]dx \tag{7.15}$$

Considering the relation $T_2(x) = T_1(x - u\Delta t)$, where $\Delta t = (t_2 - t_1)$, the equation can be rewritten as follows:

$$\Delta T = \int_{x_b}^{x_d} T_1(x - u\Delta t)dx - \int_{x_b}^{x_d} T_1(x)dx$$

Replacing the integral unit dx of the second integral of the right side of the equation with $d(x - u\Delta t)$, and considering the relation $x_a = x_b - u\Delta t$ and $x_c = x_d - u\Delta t$, the equation becomes:

$$\Delta T = \int_{x_a}^{x_c} T_1(x)dx - \int_{x_b}^{x_d} T_1(x)dx$$

Further, consider that the two integrals are partially overlapping each other, over the part between x_b to x_c, and the equation can be rewritten as follows:

$$\Delta T = \left(\int_{x_a}^{x_b} T_1(x)dx + \int_{x_b}^{x_c} T_1(x)dx\right) - \left(\int_{x_b}^{x_c} T_1(x)dx + \int_{x_c}^{x_d} T_1(x)dx\right)$$

Since the integrals over interval x_b to x_c from first and second parentheses have opposite sign, they cancelled each other, and the equation has a form as shown in following:

$$\Delta T = \int_{x_b}^{x_d} [T_1(x) - T_2(x)]dx = \int_{x_a}^{x_b} T_1(x)dx - \int_{x_c}^{x_d} T_1(x)dx] \qquad (7.16)$$

The equation means that the change of the thermal energy contained in the window is equal to the energy flows into the window minus the energy flows out of the window.

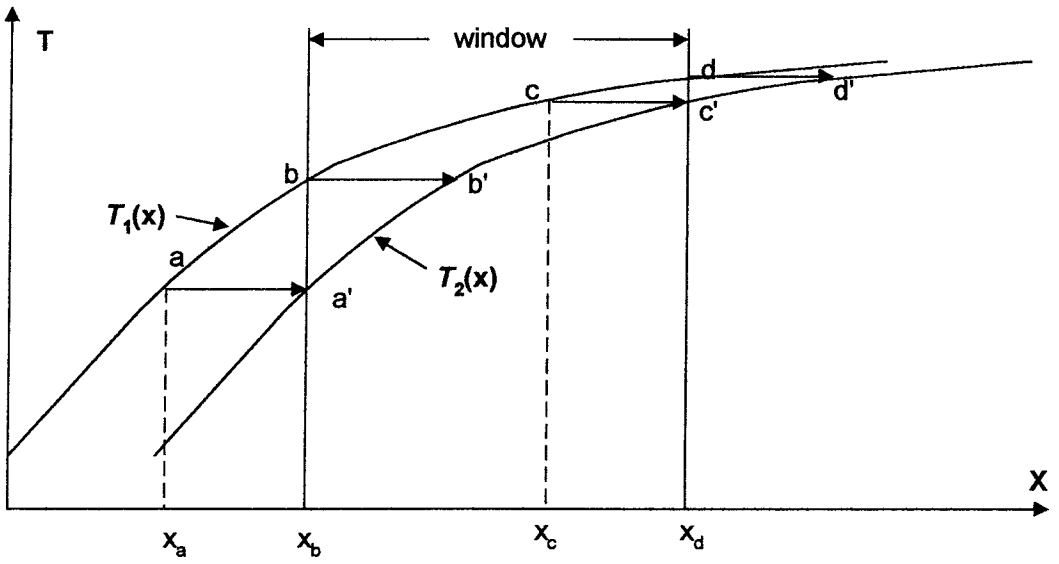

Figure 7.5 *The variation of the temperature function in an elementary subset*

To use the differential form of the energy conservation equation, the window is treated as an elementary unit and the following approximations have to be made:

- Temperature gradients are constant over the water body within the window at moment t_1 and the water flows into the window during Δt (i.e. the water over the distance x_a to x_d in figure 7.5). It is equivalent to assuming the temperature is linearly distributed over the interval x_a to x_d.

- The velocities within the interval x_a to x_d are approximately uniform.

Kelly [1989] computed the temperature gradient by a least squares fit of the temperature distribution function to a ramp over each window. Precisely, the least squares fitting should not only span the window but also should cover the water flowing into the window during the time interval, because this part of the water is also assumed to possess the same temperature gradient. However, because the velocity is the unknown and to be determined, the volume of the water, which is outside the window at moment t_1, and which will flow into the window during Δt, are not known before the velocity or displacement been determined. In this discussion, the same least squares fit as that used in *Kelly* [1989] is used, but assumes the interval for the gradient computation covers the window and the water flow into window during Δt (i.e. the interval x_a to x_d). For a one dimensional case, the error equations for each x with the distance x_a to x_d , are of following form:

$$v(x) = Ax + B - T_1(x) \tag{7.17}$$

where, $v(x)$ is the residual, which is a function of x, and varies depending on the difference between the temperature function $T_1(x)$ and its linear approximation at point x. Based on the least squares theory, $v(x)$ will satisfy the following:

$$\Sigma\, v(x)^2 = \min \quad \text{and} \quad \Sigma\, v(x) = 0 \tag{7.18}$$

where Σ is the sum over x_a to x_d, Their equivalent continuous expressions can be written as follows:

$$\int_{x_a}^{x_d} v(x)^2 dx = \min \text{ and } \int_{x_a}^{x_d} v(x) = 0$$

Using the least squares fit, the temperature function over x_a to x_d is approximated to a linear function as $T'_1(x) = Ax + B$, so that the gradient of this linear function $T'_x = A$. Substituting the relation $T_1(x) = Ax + B + \Delta T(x)$, where the $\Delta T(x) = - v(x)$, into the right side of equation (7.16) gives:

$$\int_{x_b}^{x_d} [T_2(x) - T_1(x)]dx = \int_{x_a}^{x_b} Ax + B + \Delta T(x)dx - \int_{x_c}^{x_d} Ax + B + \Delta T(x)dx$$

Considering the velocities over the area x_a to x_d are assumed to be uniform, therefore, $(x_b - x_a) = (x_d - x_c) = u\Delta t$, and the equation becomes:

$$\int_{x_b}^{x_d}[T_2(x)-T_1(x)]dx = -A(u\Delta t)(x_d - x_b) + \int_{x_a}^{x_b}\Delta T(x)dx - \int_{x_c}^{x_d}\Delta T(x)dx \qquad (7.19)$$

where the coefficient, A, is the gradient of the linear function, T'_x. The window is treated as an elementary unit in the inverse model estimation using the differential form of the energy conservation equation. Thus, both sides of equation (7.19) are divided by the size of the window (x_d - x_b) and Δt. The integral on the left side of the equation is divided by (x_d - x_b) to give the continuous form of the spatial average of the temperature change between Δt and further divided by Δt to give the finite difference form of the temporal derivative, as follows:

$$T_t = \frac{\overline{T_2(x)-T_1(x)}}{\Delta t} = \frac{\int_{x_b}^{x_d}[T_2(x)-T_1(x)]dx}{(x_d - x_b)\Delta t} \qquad (7.20)$$

and further denoting

$$\Delta = \frac{1}{(x_d - x_b)\Delta t}\left[\int_{x_a}^{x_b}\Delta T(x)dx - \int_{x_c}^{x_d}\Delta T(x)dx\right] \qquad (7.21)$$

equation (7.19) then becomes:

$$T_t = -T_x' u + \Delta \qquad (7.22)$$

Equation (7.22) is the one dimensional differential form of the energy conservation equation plus an error term due to the linear approximation. Equation (7.22) shows that the first term of the left side of the equation is only responsible for the thermal energy transfer T_t - Δ. While the T_t is actually derived from the difference $T_2(x)$ and $T_1(x)$ using equation (7.20). Therefore, when using the differential energy conservation equation T_t = $-T_x'u$ as the observation for the estimation, the estimated velocity has an error Δu = Δ/T_x'.

7.4.3 The Analysis of the Error Expressed with Equation (7.21)

Equation (7.21) shows that the magnitude of this error is related to the image power spectrum, i.e. the spatial frequency composition of the input image, window size and the displacements of consecutive images.

Firstly, equation (7.21) shows that the error comes from the difference between the integrals of the residual between the temperature function and its linear approximation over the distances (x_b - x_a) and (x_d - x_c). Due to (x_d - x_a) = (x_d - x_c) = $u\Delta t$, physically, the difference of these two integrals is the difference between the residual thermal energy (i.e. the energy neglected by the linear approximation) which flows in and out of the window during Δt respectively. In Figure 7.6, they are marked with a grey shading. Although, using the least squares fitting, the sum of the residuals $\Sigma\, v(x) = 0$ over the distance x_a to x_d , it does not guarantee the difference of these two integrals is equal to zero as is the case as shown in Figure 7.6. Here the difference of the two integrals is the sum of the two areas shaded grey, due to the opposite signs of the residuals over x_a to x_b and x_c to x_d. Therefore, this difference is highly dependent upon the image power spectrum. If the image is dominated by long (spatial) wavelength components, the linear function $Ax + B$ can give a good approximation. When the components of the wavelength are shorter than the length of window size + $u\Delta t$ (i.e. x_a to x_d in Figure 7.6), possessing significant energy, the linear approximation can significantly affect the estimation. In an extreme image which is dominated by such short wavelength components, the coefficient A of the linear function will approach zero (i.e. the areas shaded grey in Figure 7.6 will become very large). This is because the leaner least squares fitting process described by equations (7.17) and (7.18) act similarly to a low pass filter, and when the sub-image in the window contains no low frequency component, A equals zero. Therefore, when the input image contains only high frequency components, the inverse model method, using the differential form of the energy conservation equation, may not be able to provide even an approximate estimate of displacement field. In other words, to use the differential form of the energy conservation equation (equivalently to equation (7.5a)), the image should possess sufficient energy components of wavelengths longer than window size + $u\Delta t$. This is a condition of using the differential form of the energy conservation equation, as well as equivalently, the condition for using of the least squares matching for the sequential image displacement determination without a priori knowledge of displacement.

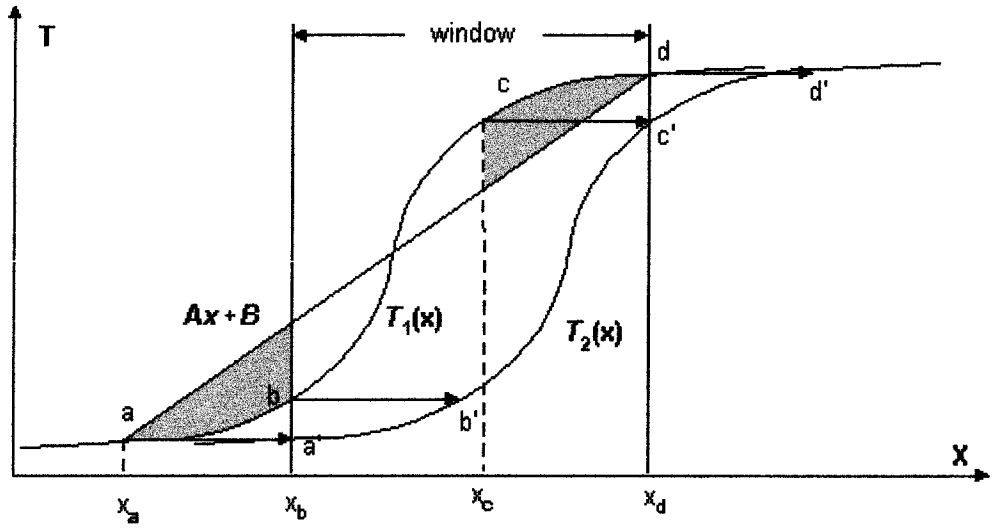

Figure 7.6 *The error due to the linear approximation of temperature function over elementary subset (shaded grey)*

Figure 7.7 *The image processed using a running average high-pass filter of 25×25 pixels window. The original image is shown in Figure 5.1.*

Fortunately, SST images are usually dominated by large piece-wise patterns. This is the basis of the feasibility of using the inverse model with the differential energy conservation equation. However, the components of short wavelengths in SST images

also possess a significant amount of energy. This is evidenced from the high pass filtered images with 25×25 pixels window as shown in Figure 7.7. The image shows the high pass filtered image retains almost all features of the SST patterns, and the studies in Chapter 5 have shown that using such high-passed images can even provide more accurate estimation than when using raw images with the estimation method based on feature tracking. This means that the components of the wavelengths shorter than about 25 pixels contain a significant amount of energy. Therefore, the ignoring of such a large amount of energy can cause significant errors in the estimation using inverse model method or equivalently the first iteration of the least squares matching with no a priori displacement knowledge.

Secondly, because the intervals of two integrals in equation (7.21) are equal to the feature displacement which is to be determined, $u\Delta t$, the error due to the linear approximation is also controlled by the image displacement.

Thirdly, in the equation, the difference of the two integrals is divided by the size of the window. This indicates that, for a given displacement and residual of linear approximation, the error can be relatively reduced by using a sufficiently large window. However, on the other hand, the window should be sufficiently small, for the reason that, the smaller the elementary unit (i.e. the window size + $u\Delta t$), the closer the linear approximation is to its original function. Therefore, the determination of the size of the window, the elementary subset in the proposed scheme, is controlled by the magnitude of the image displacements. When using the differential form of the energy conservation equation for the estimation, the temperature function of the water body which is in the window at the moment t_1, and that which will flow into the window during Δt, is assumed to be of constant gradient. In practice, as the displacements are unknown, this gradient is determined with a least squares fit over the window as proposed in *Kelly* [1989]. In other words, the temperature gradient of the water body which will flow into the window is extrapolated by assuming that it is of the same gradient as the water body inside the window at moment t_1. It is true that, no matter how large the window is, this part of the water is always outside the window at moment t_1, and its gradient is, therefore, the extrapolation of the gradient estimated from the

temperature distribution inside the window. However, increasing the ratio of the interval of the least squares fitting (i.e. the size of the window) over the distance of extrapolation (i.e. $u\Delta t$) can statistically increase the reliability of the extrapolation. As well, as mentioned previously, equation (7.21) indicated that, for the given displacement and residuals, the error due to the residuals of the linear approximation can be relatively reduced by using a sufficiently large window.

7.4.4. The Reasons for Using the Iterative Process with the Large to Small Elementary subsets

The analysis of the error expressed by equation (7.21) shows that the magnitude of the error due to the use of the differential form of the energy equation is related to:

1. The magnitude of the displacement of the consecutive images.
2. The magnitude of the residual between the linear approximation and its original temperature function, i.e. the intensity function of SST images, over the water bodies flow into or out of the window (the elementary image subset).
3. The essential size of the elementary image subset for the given displacement and the residual due to the linear approximation of the intensity function.

Obviously, the magnitude of displacement is the key factor to the error due to the use of the differential form over the large finite element. It controls the size of the elementary subsets and the residual of the linear approximation over the subset. When the displacement of the consecutive images is large, the large elementary subset is essential. Generally, the larger the elementary subset, the larger the residual of the linear approximation over the subset, and the residual reduces as the size of the subset reduces. This is the reason for the proposed scheme using the iterative procedure, and the large to small elementary subsets in the iterative processes. As described in section 7.2, the unknowns to be determined in each iteration are the lags of four patch corners between the template patch from the first image and the resampled image from the second image, using approximate displacements estimated in the previous iteration. The resultant lags are the correction value of the displacements between the template and the optimally matching sub-image in the second image. In the initial state, the approximate

displacements are less accurate or entirely unknown, thus, the lag between the template patch and the resampled patch are correspondingly large. Therefore, the large elementary subset should be used to suit the large spatial lag of the patches. Consequently, due to using the large subset, the error expressed in equation 7.21 can be un-ignorably large, especially, when the short wavelength components possess large energy. Thus, the resultant displacements need to be refined. As the estimated displacements are iteratively refined, the resampled patches gradually approach their optimal positions, and the spatial lag between the template patch and the resampled patch become smaller and smaller, thus, the smaller elementary subset should be used to reduce the residuals of the linear approximation.

If without apriori approximate displacement knowledge being available, the search of the least squares matching starts from the position where the template patch is located, i.e. Δx^0 and Δy^0 equal to zero. Under this circumstance, a large spatial lag between the sub-image resampled with $\Delta x^0 = 0$ and $\Delta y^0 = 0$ and the sub-image contained in template is expected. In the areas of relative strong currents, the maximum displacement for two 12 hour separated images can be over 20 pixels. Based on the above discussion, the large initial elementary subset should be used. *Kelly* [1989] suggested the size of the elementary subset should be at least larger than the displacement to be determined. Therefore, the elementary subset of a size over 20×20 pixels is required. This is about the size of the patch used in this study.

This analysis also shows that the error of using the first order differential approximation related to the spatial frequency composition of input image. If the image is dominated by the components of the wavelengths shorter than the size of the elementary subset, the least squares matching may not even provide the correct search direction in the first iteration, when initiating the search. This is an extra requirement to the image condition over those for the cases using the MCC method or relaxation method. It is generally feasible to initiate the search using the least squares matching, or equivalently the inverse model method, because the SST images frequently are dominated by long wavelength components. However, this extra requirement is an avoidable restriction to the estimation. Therefore, it may somehow make the least squares matching, or

equivalently the inverse model using the differential form of the energy conservation equation, not the best choice for the initiation of the search. Besides this, in the initial stage of the search, due to the large spatial lags of the corresponding patches, the search relies on the long wavelength components, thus the raw images or the low pass-filtered images are preferred. However, when the resampled patches approach their optimal positions, the long wavelength components contained in the template and the resampled patches are highly correlated, and then they do not contribute or contribute little to the further searching. Thus, to make the features more traceable, the high pass filtered images are preferred. This means that the images used for the estimation need to be switched from the raw image used for the initial search to the high-pass filtered images for accurate matching. This is not a problem for implementation. However, it does complicate the programming.

Furthermore, the study in Chapter 6 shows that, the relaxation method improves the consistency and robustness of the estimation by using both the correlation distribution information and the contextual information of the velocity field, although the resultant field in the areas of strong velocity gradient variation can be over-smoothed due to used of large and fixed-shape templates and the imperfection in the model used as the compatibility function. Contrarily, because in the initial iteration of the least square matching proposed in this chapter, which is equivalent to the inverse model method used in *Kelly* [1989] and *Kelly et al.*[1992], the number of observation equations is less than the number of the unknowns (the displacements vectors) due to the use of the large elementary subset, the inversion is under-determined, and extra constraints are necessary.

Kelly [1989] and *Kelly et al.* [1992] have shown that the weights of the constraints can largely affect the resultant field, while, the optimisation of the weights is not an easy task. This difficulty can be avoided by initialising the search using the relaxation method. In successive iterations of JPLSM, due to the reducing size of the elementary subset, the number of observation equations increases up to 24×24=576 in each patch. In the joined-patches least squares matching, the number of unknowns to be determined, for an area of $m \times n$ patches, is $(m+1)(n+1)$. On average, each patch has $(m+1)(n+1)/m \times n$

unknowns to be determined. The actual number of unknowns for each patch is less than 8. The inversion is not under-determined any more, except that the patches containing insufficient traceable SST features. In the refinement process, using the JPLSM algorithm, if there are more than 8 observation equations from the 576 observation equations of a patch that are linearly independent (i.e. the gradients of the corresponding subsets are not correlated to each other), all 8 unknowns of a patch are determinable and the system is not under-determined. Based on these concerns, the proposed scheme is designed only for refining the resultant displacement field estimated using the relaxation method. This choice is made purely on a preferential basis.

7.5 Experimental Results

7.5.1 The Experiment Using Synthetic Image Pair

The proposed joined-patch least squares matching scheme was firstly tested using an AVHRR thermal image shown in Figure 5.1 as the first image and a synthetic image shown in Figure 5.4 as the second image. The synthetic image is generated by iteratively resampling (driving) the image shown in Figure 5.1 using a velocity field based on the velocity vectors derived by subjectively tracking the SST features in a pair of real AVHRR thermal images shown in Figure 5.1 and 5.2. The detailed techniques used for the control velocity field determination and the synthetic image generating have been given in Chapter 5. The temporal interval between the image shown in Figure 5.1 and the synthetic image (they will be referred as the synthetic image pair hereafter) is equivalent to 18 hours. As the control velocity field is based on the velocity vectors determined from the real image pair, using a subjective feature tracking method, the SST field variation due to the major advective physical processes such as shifting, rotation and the straining motion, are simulated in the synthetic image. While, the SST variation due to the non-advective physical processes, such as the vertical mixing and the surface heating and cooling, are not simulated in the synthetic image.

In the experiment using the synthetic image pair, the cloud contaminated pixels were not excluded from the computation, for the reason that in the synthetic image

derivation, the cloud contaminated pixels in the original image are shifted along with the SST features, thus, these pixels actually become a part of the SST features.

The initial approximate displacement field was determined using the relaxation method proposed in Chapter 6. The input approximate displacement field is shown in Figure 6.14.

In the refinement process, the spatial lags of the SST features in the template sub-image and their counterparts in the resampled sub-image, using the approximate displacements are expected to be within 5-10 pixels. The long wavelength components contained in the two sub-images are already highly correlated, thus the further search process relies on the short wavelength components (i.e. the small scale features). To enhance the traceability of the small features, the image pair was preprocessed using a running average high-pass filter of 25×25 pixels window. The detailed description about the filter has been given in Chapter 5. The high-pass filtering also removes the non-advective physical process effects such as the vertical mixing and the surface heating and cooling which generally have much larger scale than 25×25 pixels (i.e. about 30×30 km). To reduce the effect of noise, the high-passed images were then smoothed using low-pass filter of 3×3 pixels window.

The sizes of the elementary subset used in the test are 5×5 pixels and 3×3 pixels for the first 2 iterations and 2×2 pixels for the successive iterations until the processing converges. The number of elementary subsets, equivalent to the number of observation equations, in each patch are correspondingly 6×6=36 and 12×12=144 for the first 2 iterations, and 24×24=576 for the successive iterations. The detailed description of the structure of the patch and the elementary subset have been given in section 7.2. The iteration was terminated when the resulted maximum displacement correlation value was less than 0.5 pixel.

As has been discussed in section 7.3.4, there is a great disparity between the number of observation equations and the number of constraint equations. To balance the contributions of the observation equations and the constraint equations, the $\mathbf{B}^T\mathbf{P}_b\mathbf{B}$ and

the corresponding $\mathbf{B}^T\mathbf{P}_b\mathbf{L}_b$, and $\mathbf{C}^T\mathbf{P}_c\mathbf{C}$ and corresponding $\mathbf{C}^T\mathbf{P}_c\mathbf{L}_c$, in equation (7.12) were scaled by S_b and S_c respectively. The scaling factors S_b and S_c were computed using equation (7.13), and in this test, are 1.3×10^4 and 8 respectively when the elementary subset is 2×2 pixels and each patch has 24×24=576 observation equations.

To understand the effect of the constraints, the least squares matching process was examined with three tests, giving different weights to the constraint. In the first test, all of the constraint equations were equally weighted with 1, and the condition of the patches were ignored. In the second test, all constraints were equally given a very small weight 0.001. In the third test, the weights of constraints were determined based on the condition number of the normal equation of each patch, which has defined in section 7.3.4. In this test the ratio of the maximum eigenvalue and the minimum eigenvalue $\lambda_{max}/\lambda_{min}$ was used as the measure of the inversion condition (i.e. the singularity, and the degree close to singularity). The computed $\lambda_{max}/\lambda_{min}$ of each patch, when the elementary subset was 2×2 pixels, are shown in the Table 7.1. In the table, the condition numbers are arranged as an array of the same order as the corresponding patches in the grid. The weight of the smoothness constraint of a grid point is determined based on the maximum condition measure, $\lambda_{max}/\lambda_{min}$, of the patches adjacent to it (each inner grid points has 4 adjacent patches, the grid points along the edge of the image domain have 2 adjacent patches and the grid points at the corners of image domain have 1 adjacent patch). For an ill-conditioned patch, and as shown in Figure 7.8, where the ill-conditioned patch is shaded grey, the smoothness constraints at the corners of that ill-conditioned patch were given large weights, to enhance the contextual relation with their neighbouring grid points marked with black dots.

In the test, when the maximum $\lambda_{max}/\lambda_{min}$, among the adjacent patches of a grid is larger than 2000, the smoothness constraints centred at this grid point were given a weight of 1. For the grid point of a maximum square condition number smaller than 2000, the weight is given by the following function:

$$p = \begin{cases} \left(\dfrac{\lambda_{max}/\lambda_{min}}{2000}\right)^2 & \text{when } \lambda_{max}/\lambda_{min} < 2000 \\ 1 & \text{when } \lambda_{max}/\lambda_{min} \geq 2000 \end{cases} \qquad (7.23)$$

Table 7.1 *The square condition number (i.e. the ratio of maximum eigenvalue over the minium, $\lambda_{max}/\lambda_{min}$) of the normal equation of each patch (computed using synthetic images)*

34.	33.	65.	278.	927.	139.	24.	15.	204.	100.	34.	152.	67.
170.	66.	82.	351.	1551.	693.	99.	117.	941.	155.	95.	137.	119.
163.	143.	403.	183.	114.	482.	127.	62.	101.	165.	43.	75.	1047.
33.	35.	90.	137.	74.	148.	309.	205.	411.	161.	196.	273.	46.
51.	55.	57.	54.	63.	66.	59.	292.	305.	129.	131.	49.	346.
38.	38.	64.	56.	44.	106.	370.	502.	171.	81.	94.	42.	97.
40.	212.	96.	183.	103.	150.	394.	108.	32.	38.	737.	58.	265.
48.	37.	159.	174.	69.	64.	111.	18.	28.	20.	1815.	1099.	65.
105.	123.	14.	29.	23.	193.	213.	620.	138.	60.	144.	513.	204.
48.	61.	16.	23.	77.	702.	133.	72.	137.	289.	148.	252.	197.
39.	69.	27.	26.	75.	192.	152.	31.	59.	70.	260.	37.	39.

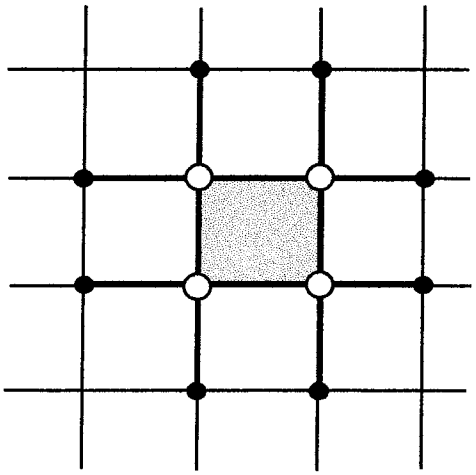

Figure 7.8 *The smoothness constraints around a patch of ill condition, where the ill-conditioned patch is marked with grey, the grid points connected to this patch are marked with white, and the grid points linked to this ill-conditioned patch through smoothness constraints are marked with black.*

Table 7.1 shows that there are no patches of a square condition number over 2000, only 4 patches between 1000 - 2000, 9 between 500-1000, 21 between 200-500, and 109 under 200, among the total 143 patches. The weights computed using equation (7.23) were under 0.01 for about 75% of the grid points, and only 14 points that were adjacent to the patches of square condition number (ie. $\lambda_{max}/\lambda_{min}$) over 1000 were given a weight over 0.25. The intention of giving such small weights to the constraints is to ensure that the estimation is dominanted by the similarity of the SST features, and to minimise the interference of the constraints, if the patch is not really of ill-condition. Generally, the constraints are based on certain models or assumptions, thus, the reduction in the weight

of the constraints can reduce the effect of imperfection of the model or assumptions the constraints are based on, and also, the minimising the modification due to the constraints, will reduce the complexity in the interpretation of the resultant field for oceanographers. The oceanographers would normally prefer the measurements of the real ocean compared the estimation under certain assumption or via a model.

Due to the use of the joined patch, the displacement of each inner grid point is estimated based on the information in the 4 adjacent patches. However, the grid point located along the edges of the grid and the point at the corners of the grid has only 2 and 1 adjacent patches respectively, and relative less information is available for the estimation at these points. Therefore, in test 3, the smoothness constraints related to the corner points are given a weight of 0.5, and a weight of 0.25 to the grid points on the edges of the grid.

The weight for the incompressibility constraint is also determined based on the normal equation condition number (see section 7.3.4) of each patch and using equation (7.23), and the patches along the edges of the grid and at the corners are also given the weights 0.25 and 0.5 respectively.

The computations take about 18 iterations to converge. The resultant fields of three tests are shown in Figures 7.9, 7.10, and 7.11. The resultant displacement fields are compared with the control field used for the generation of the synthetic image. The control field (the displacements field of 18 hours separation) is shown in Figure 6.15.

The comparison is measured by the improvement in in correlation coefficient, the *rms* difference between the control field and the resultant field in magnitude *dm* and orientation *da*, and the significant erroneous estimates as for the cases in Chapters 5 and 6. However, since the input approximate displacement field was estimated using the relaxation labelling method, the number of significant erroneous estimates of the resultant field was significantly reduced compared with the resultant field using the MCC method. The refinement process based on the joined-patch least square matching proposed in this chapter further increases the consistency and accuracy of the resultant

field. Therefore, two levels of measure are used to determine the significant erroneous estimates. The low level measure is the same as that used in Chapter 5, ie. if the difference between estimated vector and corresponding vector in control field is greater than 7 pixels in magnitude, or 30^0 in orientation, the estimated vector is counted as an erroneous estimate. The higher level measure is 5 pixel in magnitude, or 20^0 in orientation. These two levels of measure are determined based on the *rms dm* and *rms da* values. In Chapter 5, the resultant field estimated using the MCC method with rotational search and 18 hours separated high-pass filtered synthetic image pair, had a *rms* difference of 6.6 pixels in magnitude, and 31^0 in orientation, thus, the 7 pixels in magnitude and 30^0 were used as the measures of significant erroneous estimate. The relaxation labelling method improves the *rms* differences to 4.7 pixels in magnitude and 19^0 in orientation, and the JPLSM refining process further improves the accuracy of the resultant field, thus, 5 pixels or 20^0 are used in this chapter as the higher level measure for the significant erroneous estimate. The results of the three tests are listed in Table 7.2. The corresponding measures of the resultant fields from the relaxation labelling method and the rotational MCC method are also listed in Table 7.2, for comparison. In the table 7.2, n_1 is the number of vectors that are different from the control field with errors greater than 7 pixels or 30^0 , n_2 is the number of the vectors that are different from the control field within 5-7 pixels or 20^0 -30^0 .

Table 7.2 *Results of tests of using joint-patch least square matching (JPLSM) refining.*

	average correlation coefficient	*rms dm*	*rms da*	n_1	n_2
JPLSM refining test 1	0.79	4.3	11^0	3	7
JPLSM refining test 2	0.87	3.2	12^0	3	1
JPLSM refining test 3	0.88	2.2	9^0	0	1
Relaxation labelling	0.66	4.7	19^0	4	10
MCC with rotation search	0.58	6.6	31^0	15	NA

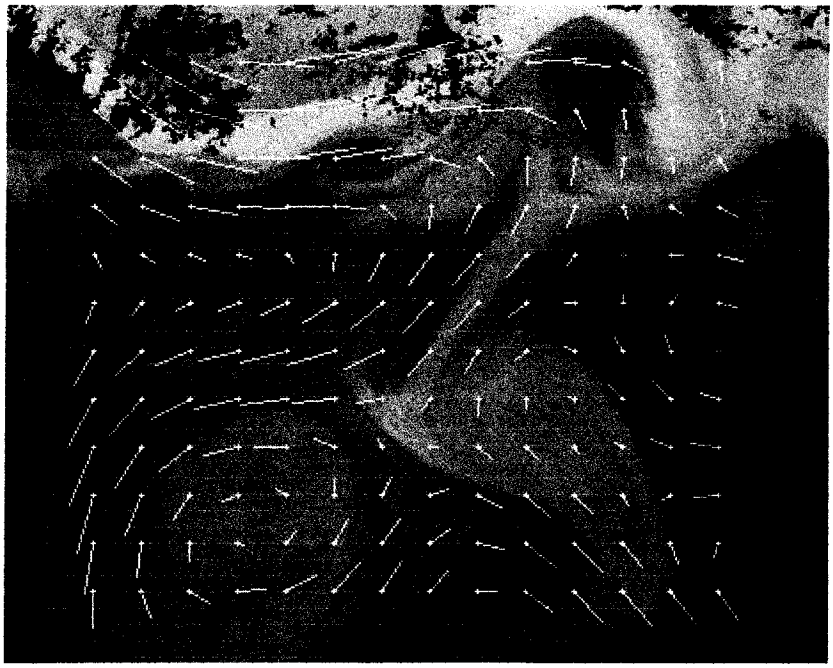

Figure 7.9 *The resultant displacement field from test* 1, *computed using JPLSM refining scheme, where all constraints were given an equal weight of* 1.

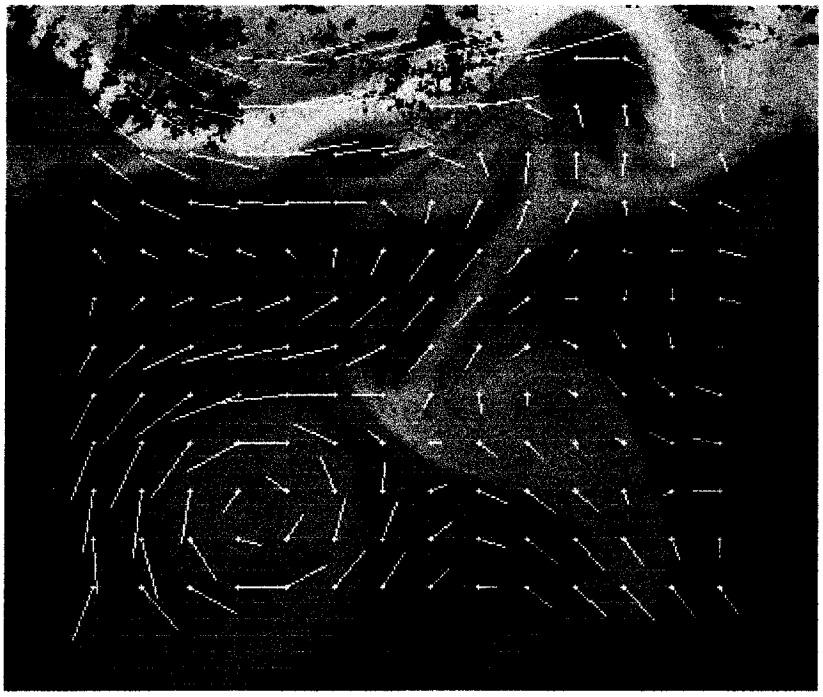

Figure 7.10 *The resultant displacement field of test* 2, *computed using JPLSM refining scheme, where all constraints were given an equal weight* of 0.001.

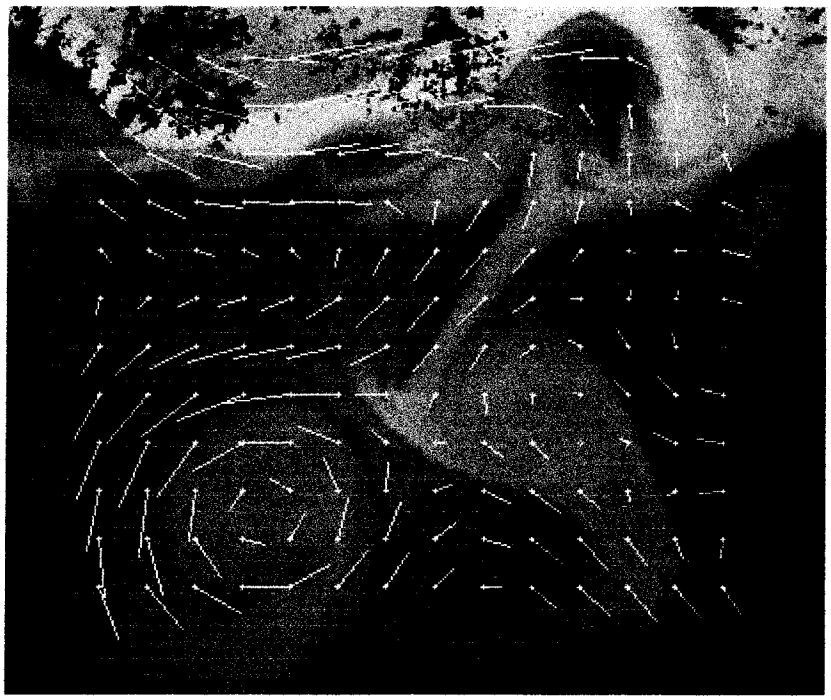

Figure 7.11 *The resultant displacement field from test 3, computed using JPLSM refining scheme, where the weight of constraints were computed based on the condition number of the normal equation of each patch using equation* (7.23).

The correlation coefficients between the templates and the corresponding patches, resampled using the initial approximate displacement field estimated using the relaxation scheme, are shown in the first array Table 7.3. The correlation coefficients after the refining process in test 3, where the weight of the constraints computed are based on the condition of normal equation of each patch as previously described, are shown in the second array. The correlation coefficient improvements are shown in the third array in Table 7.3. The correlation values and the corresponding improved values are arranged in arrays of the same order as the corresponding patches.

Table 7.3 *The correlation coefficients of each patch before and after the JPLSM refinement process and the improvements in correlation value (computed using the input and outcome displacement fields of test 3, using the synthetic image pair)*

(a) *correlation coefficients of each patch before the least squares matching refinement*

0.6	0.4	0.6	0.6	0.4	0.3	0.1	0.1	0.2	0.7	0.8	0.9	0.6
0.5	0.5	0.6	0.5	0.9	0.9	0.2	-0.1	0.2	0.6	0.8	0.9	0.8
0.5	0.6	0.5	0.8	0.7	0.9	0.3	0.7	0.9	0.6	0.6	0.9	0.8
0.2	0.5	0.7	0.6	0.7	0.7	0.9	1.0	1.0	0.9	0.9	0.9	0.6
0.7	0.7	0.5	0.6	0.8	0.7	0.6	1.0	0.9	0.8	0.6	0.5	0.7
0.7	0.6	0.7	0.7	0.6	0.7	0.8	0.9	0.9	0.8	0.7	0.4	0.7
0.7	0.9	0.7	0.8	0.7	0.5	0.9	0.8	0.4	0.9	1.0	0.8	0.7
0.8	0.6	0.8	0.9	0.7	0.6	0.8	0.5	0.5	0.3	1.0	0.8	0.4
0.5	0.7	0.6	0.6	0.2	0.5	0.7	0.9	0.5	0.7	0.6	1.0	0.1
0.5	0.7	0.8	0.7	0.3	0.8	0.4	0.8	0.8	1.0	0.8	0.9	0.5
0.2	0.6	0.6	0.6	0.7	0.8	0.6	0.6	1.0	0.8	0.7	0.9	0.5

(b) *correlation coefficients after the refinement process*

0.9	0.8	0.9	0.7	0.6	0.3	0.6	0.5	0.2	0.7	0.9	1.0	0.9
0.9	0.9	0.9	0.7	1.0	0.9	0.6	0.2	0.3	0.7	0.9	1.0	0.9
0.9	0.9	0.7	0.9	1.0	1.0	0.9	0.9	1.0	0.9	0.9	1.0	0.9
0.8	0.9	0.9	0.9	0.9	1.0	1.0	1.0	1.0	1.0	1.0	1.0	0.8
0.9	0.9	0.8	0.9	0.9	0.9	0.9	1.0	1.0	1.0	1.0	0.8	0.8
0.9	0.8	0.9	0.9	0.9	1.0	1.0	1.0	1.0	1.0	0.9	0.5	0.7
0.9	1.0	0.9	1.0	0.9	0.9	1.0	1.0	0.9	0.9	1.0	0.9	0.9
0.9	0.9	1.0	1.0	0.9	0.9	0.9	0.7	0.8	0.8	1.0	0.9	0.8
0.9	0.9	0.9	0.8	0.8	0.9	0.9	1.0	0.9	0.9	0.8	1.0	0.8
0.9	0.9	0.8	0.9	0.7	1.0	0.9	1.0	1.0	1.0	0.9	1.0	0.9
0.8	0.9	0.9	0.8	0.9	1.0	1.0	1.0	1.0	1.0	0.9	0.9	0.9

(c) *correlation value improvements after the refinement process*

0.3	0.4	0.3	0.1	0.2	0.0	0.5	0.4	0.0	0.0	0.1	0.1	0.3
0.4	0.4	0.3	0.2	0.1	0.0	0.4	0.3	0.1	0.1	0.1	0.1	0.1
0.4	0.3	0.2	0.1	0.3	0.1	0.6	0.2	0.1	0.3	0.3	0.1	0.1
0.6	0.4	0.2	0.3	0.2	0.3	0.1	0.0	0.0	0.1	0.1	0.1	0.2
0.2	0.2	0.3	0.3	0.1	0.2	0.3	0.0	0.1	0.2	0.4	0.3	0.1
0.2	0.2	0.2	0.2	0.3	0.3	0.2	0.1	0.1	0.2	0.2	0.1	0.0
0.2	0.1	0.2	0.2	0.2	0.4	0.1	0.2	0.5	0.0	0.0	0.1	0.2
0.1	0.3	0.2	0.1	0.2	0.3	0.1	0.2	0.3	0.5	0.0	0.1	0.4
0.4	0.2	0.3	0.2	0.6	0.4	0.2	0.1	0.4	0.2	0.2	0.0	0.7
0.4	0.2	0.0	0.2	0.4	0.2	0.5	0.2	0.2	0.0	0.1	0.1	0.4
0.6	0.3	0.3	0.2	0.2	0.2	0.4	0.4	0.0	0.2	0.2	0.0	0.4

The tests results listed in Tables 7.2 and 7.3, and the resultant fields shown in Figures 7.9, 7.10, and 7.11 show the following:

The accuracy of the estimated displacement fields from all three tests is improved by the use of the JPLSM refinement process. The *rms* difference in magnitude and orientation of the resultant displacement field from test 3 (i.e. the test generating the best results) are reduced from 4.7 pixels and 19^0, determined using relaxation labelling method, to 2.2 pixels and 9^0. The accuracy of the vectors were especially improved in the areas of strong velocity gradient variation. The vector field in the areas of strong velocity gradient variation were over-smoothed due to the use of the large template in the correlation value computation, and the imperfection of the compatibility function in the relaxation process. The use of the smaller, flexible and jointed patches resolves the bi-linear deformation of the SST patterns of a spatial scale corresponding to the size of patch, and therefore, significantly reduces the over-smoothness in these areas. The improvement can be clearly seen by comparing the field estimated using the relaxation labelling process shown in Figure 6.14 (the over-smoothed vector are marked with squares and circles), with the control field shown in Figure 6.15, and the resultant field using JPLSM (test 3) algorithm shown in Figure 7.11.

The improvement , by resolving the deformation with flexible and joined patches, is also evident from the increase of the correlation coefficient between the template and the corresponding resampled patch. The average correlation coefficient increased from 0.66, for the input approximate displacement field computed using relaxation labelling method, to 0.88 for the resultant field from test 3.

In the proposed algorithm, the patches of the entire grid are integrated as a single flexible template (i.e. like a rubber sheet). Therefore, the contextual information can be conveyed among the neighbouring patches, and the strength of the inter-patch structure (the smoothness and joint-patch constraints) and the intra-patch structure (the incompressible constraint) can be controlled by varying the weight of the corresponding constraint equations based on the condition of the features contained in the patch.

The resultant field from test 2, in which all constraints were equally given a very small weight of 0.001, shows that all vectors at inner grid points were well estimated, except 4 mis-estimates which locate along the edge or at the corners of the grid. They are the vectors at row 1 column 10, row 1 column 14, row 2 column 9, and row 12 column 1. This indicates that under the condition of the images used for the test, normal equation of all patches are not ill-conditioned. For the non-ill-conditioned inner grid points, constraints can be given a very small weight. However, due to the weak inter-patch structure of the along-edge or at-corner grid points, the patches with relatively flat gradients or with features in a dominated direction, may generate mis-estimates. Thus, the structure of edge and corner points should be enhanced by the constraints as is the case in test 3.

The resultant field from test 1, in which all constraint equations were equally given a weight of 1, is relatively too smooth around the eddy in the lower-left image domain compared with the control field. This is due to the imperfection of the model used for the smoothness constraint. As discussed in section 7.3.2, the smoothness constraint based on the second order difference of neighbouring vectors, implies the velocity field varies linearly and the non-linear variation is controlled by the corresponding weight of this constraint. When this linear constraint is over-weighted in the areas where the

velocity field has strong non-linear variation, it may reduce the accuracy of the estimation.

7.5.2 The Experiment Using Real Image Pair

The proposed scheme was also tested using a pair of real thermal infrared images, shown in Figure 5.1 and Figure 5.2. These two images are separated by 12 hours. The detailed descriptions about the images have been given in Chapter 5.

As was the case for the test using the synthetic image pair, the images was preprocessed using the running average filter of 25×25 window, then smoothed using 3×3 window low pass filter to reduce the effect of noise. The initial approximate displacement field was determined using the relaxation scheme. The input approximate displacement field is shown in Figure 6.18. The elementary subset sizes and the scaling factors used in this test are the same as those used in the test using the synthetic image pair. Except for the grid point adjacent to the cloud contaminated patches, the weight of the constraints were determined, as was the case in test 3 using synthetic image pair, based on both the condition number of the normal equation of each independent patch, and the inter-structure of neighbouring grid points (ie. if the point is a inner, edge or corner point). The computed condition measure, $\lambda_{max}/\lambda_{min}$ are shown in the Table 7.4.

***Table** 7.4 The ratio of the maximum and the minimum eigenvalues of the normal equation of each patch (computed using real images). The value corresponding to cloudy patches are set to zero in the table.*

0.	0.	0.	0.	23.	608.	32.	0.	0.	172.	182.	65.	318.	83.	114.
0.	0.	0.	0.	94.	147.	0.	0.	0.	788.	28.	31.	101.	405.	80.
104.	0.	0.	0.	84.	76.	268.	429.	439.	24.	49.	53.	86.	242.	494.
53.	110.	0.	0.	663.	87.	236.	143.	43.	240.	126.	80.	72.	505.	401.
24.	45.	151.	634.	40.	51.	472.	268.	65.	172.	60.	57.	207.	69.	0.
466.	666.	40.	40.	35.	25.	51.	75.	408.	236.	15.	141.	43.	122.	0.
53.	484.	33.	74.	66.	22.	77.	156.	412.	64.	138.	112.	19.	0.	0.
365.	64.	50.	81.	63.	57.	41.	194.	285.	30.	154.	154.	171.	146.	97.
653.	24.	59.	195.	83.	208.	77.	52.	24.	26.	472.	308.	258.	95.	176.
290.	65.	756.	1571.	41.	53.	121.	122.	0.	444.	260.	31.	459.	46.	43.
0.	80.	22.	223.	23.	107.	219.	211.	123.	59.	169.	120.	631.	110.	31.
0.	0.	0.	0.	42.	134.	314.	243.	106.	86.	270.	83.	42.	59.	410.
0.	0.	0.	0.	922.	345.	53.	47.	206.	79.	212.	195.	1083.	237.	293.

In the test, the cloud contaminated pixels were detected and masked using the algorithm described in Chapter 4. When the sum of the detected cloudy pixels, within both template and the resampled sub-image from the second image, is larger than 20% of the

total number of the pixels in the template (i.e. 25×25 in our study), the patch was treated as a "no-information" patch. Their condition number is set as 0 in Table 7.4. The grid points associated with these "no-information" patches were classified as "no-information" points and "semi-effective" points —

- If all patches around a grid point are "no-information" patches, the grid point is defined as a "no-information" point.
- If at least 1 (and less than 4 patches) among the 4 adjacent patches are effective patches, the grid point is defined as a "semi-effective" point.

Figure 7.12 shows the geometry of the "no-information" patches and the "no-information" points and "semi-effective" points. In the figure, the "no-information" patches are shaded grey, the "no-information" points are marked with black dots, and the "semi-effective" points are marked with grey or white dots.

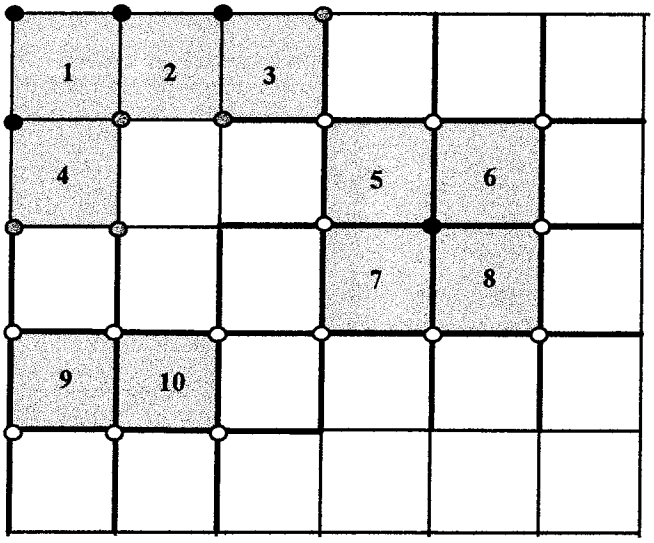

Figure 7.12 *The geometry of the "no-information" patches, the "no-information" points, and the "semi-effective" points.*

As was mentioned in section 7.3.4, the equation system of this least squares matching scheme consists of three parts, the observation equations based on equation (7.6), the smoothness constraint equations, and the equations based on the incompressible constraint, and they are denoted as $\mathbf{Ax}=\mathbf{L}_a$, $\mathbf{Bx}=\mathbf{L}_b$, and $\mathbf{Cx}=\mathbf{L}_c$ respectively. In the test, the "no-information" patches are excluded from the estimation computation and no observation equations from these patches were used in $\mathbf{Ax}=\mathbf{L}_a$. The displacements at the

"no-information" points are generally not estimated and they are exclude from the unknown vector **x**, except for the isolated "no-information" points, where all neighbouring grid points are not the "no-information" points. For example, in Figure 7.12, the point surrounded by "no-information" patches 5,6,7 and 8 is defined as an isolated no-information point. The displacements of isolated "no-information" grid points are purely determined (interpolated) through the constraints and the isolated "no-information" points were included in the unknown vector **x**. The purpose of the inclusion of such isolated "no-information" points was to keep the strength of the structure of joined-patches. Both the smoothness constraints and the incompressibility constraints over the "no-information" patches, around an isolated "no-information" point, were given a weight of 1. For the same reason, the "semi-effective" points on the two sizes of the "no-information" patches are linked using both the smoothness constraints and the incompressibility constraints, and these constraints are also given a weight of 1. The "semi-effective" point on the edges of excluded "no-information" patches such as the points marked with grey colour in Figure 7.12, are treated as if the edge points or corner points depend upon the number of effective patches adjacent to them.

The resultant displacement field estimated using real images is shown in Figure 7.13. As was mentioned previously, because simultaneous in situ data was not available, an evaluation of the absolute accuracy of the estimated field from the real image pair is impossible. The control field was used for the evaluations of the estimated field determined using the MCC method, and the relaxation labelling scheme from the real image pair in Chapters 5 and 6 is also used as the reference field for the evaluation of this test. The results are shown in Table 7.5.

The *rms dm* and *rms da* in Table 7.5 are the root squares mean difference in magnitude and orientation, n_1 is the number of erroneous vectors different from the control field bygreater than 7 pixels in magnitude or 30^0 in orientation, n_2 is the number of the erroneous vectors different from the control field by 5 to 7 pixels or 20^0 to 30^0.

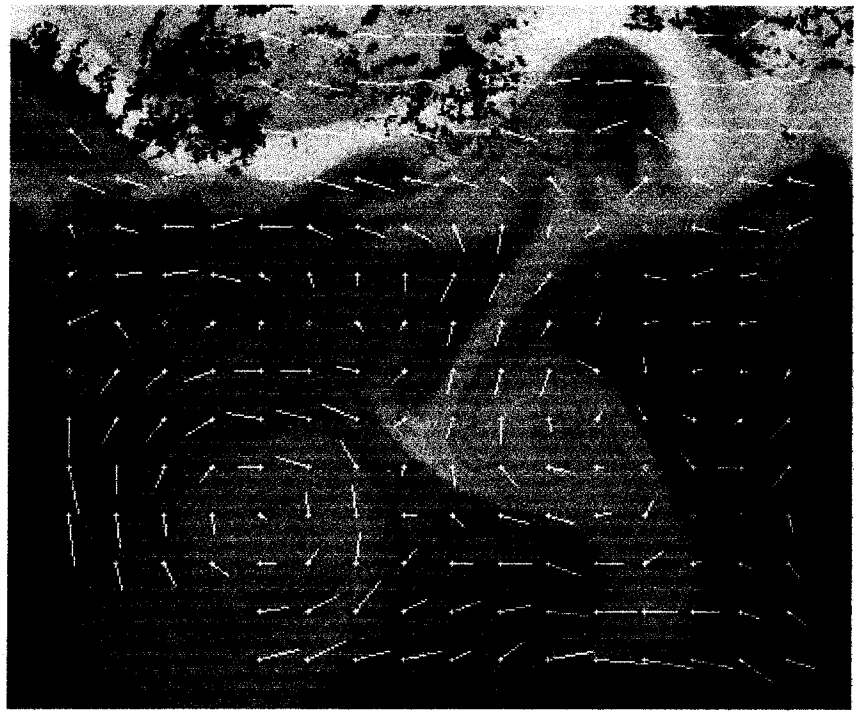

Figure 7.13 *The resultant field of JPLSM refining process using real images of 12 hours temporal separation*

Table 7.5 *Results of test of using joined-patch least square matching (JPLSM) refining (using real images), and comparison with the relaxation method and MCC method.*

	average correlation coefficient	*rms dm*	*rms da*	n_1	n_2
JPLSM refining	0.60	4.1	28^0	3	13
Relaxation labelling	0.48	4.3	27^0	5	12
MCC with rotational search	0.48	5.5	50^0	25	N/A

The difference between the comparison of the estimated velocity field using the synthetic image pair against the control field, and the field estimated using the real images against the control field, should be noted. Because the synthetic image was derived using the control field, it is an error-free reference field for the evaluation of the estimated field using synthetic images. In the case of using real images, the comparison is between two estimated fields which is a different case from the evaluation of the estimated field using synthetic images. The control field was determined by firstly subjective tracking (manually) the displacement vectors of distinguishable SST features, then interpolating the entire image domain by least squares fitting of a stream function of the Fourier series form from those subjectively determined vectors. (The detailed

method used for the determination of the control field is given in section 5.2, Chapter 5). Even though the image pair used in this test is the same pair used for the control field determination, in the subjective feature tracking method, the vectors were determined by tracking the most traceable features. Generally these vectors are not located at the positions of the grid points, and these are relatively sparse. In the control field, the displacements at grid points are actually the interpolations of these vectors. The use of the visual interpretation, and tracing most traceable features in the determination of the control field, can avoid coarse errors (i.e. the significant mis-estimates). However, the interpolation may introduce a certain degree of error. In other words, the control field is a correct but not error-free reference field for the comparison in the case of using real images.

In chapter 5, the fields estimated using the MCC method are usually inconsistent and have a large number of mis-estimates. Compared with the MCC estimates, the control field is much more consistent and accurate, therefore it was a good reference field for the evaluation, and the comparison reflected well the consistency and quality of the estimated field.

As compared to the fields estimated using MCC method in Chapter 5, the consistency of the estimated field in Chapter 6 is significantly improved by using the relaxation labelling method, and the experiments using synthetic images in section 7.5.1 of this chapter, show the accuracy of the estimation is further significantly improved by using JPLSM refining process. Figure 7.13 also shows the estimated field is almost as consistent as the control field (shown in Figure 5.3). Thus, the reference field and the estimated field may be of the same order of error, and the *rms dm*, *rms da*, n_1 and n_2 listed in Table 7.5 may not be the best measures of accuracy of estimation. Direct evaluation is impossible for this experiment.

However, some improvements and problems of the use of the JPLSM refining process can be suggested from viewing the correlation values. The correlation coefficients before and after the JPLSM refining process of each patch, and their differences are

shown in Table 7.6. As for Table 7.3, the correlation coefficients are arranged as the arrays of the same order as the grid.

Table 7.6 *The correlation coefficients of each patch before and after JPLSM refining process and the differences in correlation value using real images*

(a) *correlation coefficients of each patch before the JPLSM refinement*

0.0	0.0	0.0	0.0	-0.2	-0.3	-0.3	0.0	0.0	0.2	0.8	0.9	0.9	0.4	0.6
0.0	0.0	0.0	0.0	0.7	0.6	0.0	0.0	0.0	0.6	0.5	0.4	0.7	0.5	0.4
0.4	0.0	0.0	0.0	0.4	0.6	0.4	0.6	0.7	0.6	0.4	0.0	0.3	0.3	0.7
0.7	0.6	0.0	0.0	0.7	0.6	0.6	0.1	0.8	0.7	0.6	0.2	0.7	0.3	0.5
0.0	-0.1	0.4	0.3	0.6	0.6	0.7	0.6	0.7	0.6	0.5	0.9	0.8	0.2	0.0
0.1	0.2	0.4	0.2	0.3	0.7	0.4	0.3	0.8	0.7	0.5	0.3	0.4	-0.2	0.0
0.3	0.3	0.0	0.3	0.3	0.2	0.3	0.6	0.9	0.5	0.5	0.4	0.6	0.0	0.0
0.2	0.5	0.7	0.0	0.6	0.5	0.5	0.8	0.8	0.1	0.6	0.6	0.8	0.4	0.8
0.3	0.6	0.4	0.4	0.2	0.8	0.5	0.5	0.4	0.2	-0.1	0.9	0.9	0.2	0.4
0.6	0.5	0.8	0.0	0.2	0.2	0.7	0.3	0.0	0.7	0.6	0.4	0.9	-0.4	0.0
0.0	0.1	0.2	0.0	0.0	0.2	0.9	0.6	0.3	0.3	0.5	0.0	0.8	0.2	0.3
0.0	0.0	0.0	0.0	-0.2	0.5	0.5	0.2	0.3	0.5	-0.1	0.3	0.8	0.6	0.7
0.0	0.0	0.0	0.0	0.5	-0.1	0.3	0.3	0.4	0.4	0.3	0.5	0.3	0.5	0.5

(b) The correlation coefficient of each patch after the JPLSM refining process

0.0	0.0	0.0	0.0	0.3	0.2	-0.2	0.0	0.0	0.1	0.8	0.8	0.9	0.4	0.6
0.0	0.0	0.0	0.0	0.5	0.7	0.0	0.0	0.0	0.7	0.6	0.7	0.8	0.5	0.4
0.7	0.0	0.0	0.0	0.3	0.6	0.4	0.7	0.7	0.7	0.5	0.9	0.5	0.3	0.8
0.7	0.7	0.0	0.0	0.7	0.5	0.9	0.7	0.9	0.9	0.9	0.7	0.7	0.4	0.8
0.6	0.3	0.3	0.4	0.4	0.7	0.9	0.8	0.9	0.9	0.8	0.9	0.9	0.5	0.0
0.5	0.2	0.3	0.2	0.4	0.7	0.6	0.6	0.9	0.9	0.8	0.9	0.6	0.0	0.0
0.4	0.4	0.4	0.7	0.8	0.6	0.8	0.9	1.0	0.6	0.8	0.6	0.5	0.0	0.0
0.3	0.6	0.8	0.5	0.7	0.8	0.8	0.9	0.8	0.3	0.7	1.0	0.8	0.4	0.8
0.2	0.8	0.6	0.8	0.9	0.8	0.6	0.8	0.5	0.2	-0.1	0.9	0.9	0.5	0.5
0.7	0.7	0.8	0.3	0.1	0.3	0.7	0.8	0.0	0.8	0.5	0.4	1.0	0.3	0.1
0.0	0.3	0.2	0.0	0.3	0.4	0.9	0.6	0.6	0.6	0.9	0.8	0.9	0.6	0.6
0.0	0.0	0.0	0.0	-0.2	0.5	0.8	0.5	0.8	0.7	0.5	0.5	0.8	0.7	0.7
0.0	0.0	0.0	0.0	0.4	-0.1	0.3	0.6	0.6	0.6	0.4	0.7	0.6	0.6	0.6

(c) the correlation coefficient difference of each patch before and after the process

0.0	0.0	0.0	0.0	0.5	0.5	0.1	0.0	0.0	-0.1	0.0	-0.1	0.0	0.0	0.0
0.0	0.0	0.0	0.0	-0.2	0.1	0.0	0.0	0.0	0.1	0.1	0.3	0.1	0.0	0.0
0.3	0.0	0.0	0.0	-0.1	0.0	0.0	0.1	0.0	0.1	0.1	0.9	0.2	0.0	0.1
0.0	0.1	0.0	0.0	0.0	-0.1	0.3	0.6	0.1	0.2	0.3	0.5	0.0	0.1	0.3
0.6	0.4	-0.1	0.1	-0.2	0.1	0.2	0.2	0.2	0.3	0.3	0.0	0.1	0.3	0.0
0.4	0.0	-0.1	0.0	0.1	0.0	0.2	0.3	0.1	0.2	0.3	0.6	0.2	0.2	0.0
0.1	0.1	0.4	0.4	0.5	0.4	0.5	0.3	0.1	0.1	0.3	0.2	-0.1	0.0	0.0
0.1	0.1	0.1	0.5	0.1	0.3	0.3	0.1	0.0	0.2	0.1	0.4	0.0	0.0	0.0
-0.1	0.2	0.2	0.4	0.7	0.0	0.1	0.3	0.1	0.0	0.0	0.0	0.0	0.3	0.1
0.1	0.2	0.0	0.3	-0.1	0.1	0.0	0.5	0.0	0.1	-0.1	0.0	0.1	0.7	0.1
0.0	0.2	0.0	0.0	0.3	0.2	0.0	0.0	0.3	0.3	0.4	0.8	0.1	0.4	0.3
0.0	0.0	0.0	0.0	0.0	0.0	0.3	0.3	0.5	0.2	0.6	0.2	0.0	0.1	0.0
0.0	0.0	0.0	0.0	-0.1	0.0	0.0	0.3	0.2	0.2	0.1	0.2	0.3	0.1	0.1

As was the case using synthetic images, the use of joined, smaller and flexible patches resolved the deformation due to straining motion, and increased the average correlation coefficient from 0.48 to 0.60. It illustrates the improvement of the estimation quality.

However, the differences of the correlation coefficient (the third array in Table 7.6) shows that the improvement of the correlation after refining process is not constant over the entire image domain. The differences of some patches are negative, and most of these patches are located along the edges adjacent to the cloudy contaminated areas. The negative improvement in correlation may be due to the following reasons:

- The patches adjacent to the cloudy areas can also contain cloud contaminated pixels (include detected and undetected). The mask of the detected cloudy pixels reduces the number of effective pixels of the patch, and undetected cloud pixels add serious noise to the matching process.
- The inter-patch structure of the patches along edges or at corners is much weaker than inner patches.
- To strengthen the inter-patch structure of these along-edge or at-corner patches, large weights were used for the constraints corresponding to these patches. The use of these weights may result in over-smoothness of the estimated vectors corresponding to these patches, especially, those patches contain relative less effective pixels due to cloud contamination.

7.6 Summary

In this chapter an algorithm base on joined-patch least squares matching (JPLSM) is proposed to improve the accuracy of estimation from consecutive SST images.

In section 7.4, the relation between the proposed JPLSM algorithm and the inverse model method is illustrated. The observation equation of the least squares matching algorithm is derived based on the similarity of the intensity functions of the consecutive image pair (i.e. the geometric meaning of the observation equation). However, it is also the differential form of the energy conservation equation (i.e. physical meaning of the observation equation), in the application of estimation of the velocity field from consecutive thermal images. The algorithm traces the displacement of the SST features based on the similarity of the image intensity functions, and the iteratively determined updating values of the displacement vectors satisfy the thermal energy conservation

between the template image and the resampled second image. Therefore, the proposed algorithm unifies the method of feature tracking and the inverse model method, which is based on the thermal conservation equation.

The results of the experiments reported in the chapter show that:

1. The *rms* difference in magnitude and orientation of the resultant displacement field from test 3 using synthetic image pair of 18 hours separation (i.e. the test generated best results) are reduced from 4.7 pixels and 19^0, determined using relaxation labelling method, to 2.2 pixels and 9^0.

2. The use of the smaller, flexible and joined patches resolves the bi-linear deformation of the SST patterns of the spatial scale corresponding to the size of the patch, significantly reduces the over-smoothness in these areas.

3. The minimise the negative effect due to the approximation in smoothness and incompressibility constraints, the proposed scheme was designed to apply these constraints to only the patches which contains insufficient traceable features. The experimental results show that, under the image condition, the maximum $\lambda_{max}/\lambda_{min}$, i.e. the ratio of maximum eigenvalue and minimum eigenvalue, is less than 2,000, also under this condition, the displacement vectors at the inner grid point can be well estimated using very small weights for the constraints, while, a relatively larger weight is needed for the constraints related to along-edge and at-corner grid points, to strengthen the network structure.

7.7 Suggestion for Future Research

It is apparent that, generally, image noise and undetected cloudy pixels can affect the computed condition number of the normal equation. The noise and undetected cloud pixels can reduce the computed condition number. Since the high frequency features are more traceable then lower frequency features, and the patches dominated by high frequency features have less chance to be singular than those dominated by low

frequency features, the patches of high frequency features have smaller condition numbers than those dominated by low frequency features (smaller condition numbers corresponding to better traceability of features). Since the noise and cloud pixels of high frequency, they contribute to the condition number similar to the traceable high frequency SST features, and thus reduce the condition number. However, they are not the traceable features in this application, and thus, the small condition number due to the effect of noise and cloud pixels are not reflect the real tracebility of the SST features. The under-weighting for the constraints at ill-conditioned patches due to these small condition numbers resulting from noise and undetected cloud, can result in mis-estimate when the patch does not really contain sufficient traceable SST features. This effect has been tested by comparing the $\lambda_{max}/\lambda_{min}$ computed using the image processed with a running average high-pass filter of 25×25 pixels window, with the image filtered using firstly a 25×25 window high-pass filter then a running average low-pass filter of 3×3 pixels window (which is shown in Table 7.1 and used in the tests discussed in section 7.5.1). The comparison found that the maximum variation of computed $\lambda_{max}/\lambda_{min}$ is 875, however, both computed the vector fields using the smoothed and un-smoothed images are the same. Although the effect of noise and cloud affected condition numbers did not occur in the experiment under the image condition, this comparison shows that the noise and undetected cloud pixels can reduce the condition number. Therefore, the removal of noise using a 3×3 low-pass filter (as was applied in the tests), and the use of a consistent check after each iteration are suggested to prevent the inconsistent estimates due to the effect of small condition numbers resulting from noise and undetected cloud.

The other aspect suggested for further studies is computational efficiency. As the computation of the inversion of the large normal equation in the JPLSM scheme is time consuming, the computational efficiency needs to be improved. The computational effeciency may be significantly improved by using array algebra [see *Rauhala* 1980 for example], or nested dissection [*George* 1973].

Chapter 8

Conclusion

8.1 Summary of the Thesis and Contributions of the Research

To gain accurate information of sea surface velocity field from consecutive AVHRR thermal images, two aspects require investigation, these are:

- Improving reliability and accuracy in tracing the displacement of the SST patterns in consecutive images (i.e. optimisation of the determination of displacement of SST patterns)
- Understanding the relation between the movement of surface temperature patterns, determined from the consecutive AVHRR thermal images or ocean colour images, and the movements of ocean currents (i.e. the interpretation of the determined displacements).

The work described in this thesis focuses on the investigation of the strategies needed to improve reliability and accuracy of the determination of the SST pattern displacements.

Due to the complexity of the advective and non-advective physical processes of ocean currents, air-sea inter-effects, and gradient distribution SST or ocean surface colour patterns, the previous techniques used are, in some cases, relatively too simple for this application. As well the reliability and accuracy of the determination of the displacement of the SST features or ocean surface colour features can be affected by a number of factors as have been discussed in introduction, Chapter 1, and section 2.3.5 of Chapter 2.

The studies described in this thesis focus on:

- The general format of the cross-correlation function distribution of SST features and its variation due to different pre-filtering and correlation computation methods, and the effects of the correlation distribution format on the displacement determinations.

- Reducing the uncertainty due to the multi-peak and/or longish distributed correlation functions, through integrating the correlation value of SST features and contextual information of displacement fields by using the relaxation labelling technique.
- Further improving estimation accuracy by using jointed bi-linearly flexible templates to resolve the deformation due to the straining motion, and solve the over-smooth problem, due to the use of large fixed-shape templates, as used in the MCC method and relaxation labelling method, by using a joined-patch least squares matching method. The research further studied the inherent relation between the least squares matching scheme and the inverse model method, based on the differential form of the thermal energy conservation equation, in the application of displacement determination from consecutive AVHRR thermal images, and the necessity of using an iterative process with large to small elementary units.

Besides these, to reduce the effect of the cloud contamination, a partially cloud contaminated pixels detection algorithm, based on the Förstner operator, was developed.

The key contributions of this research and the test results of developed algorithms are summarised in following subsections.

8.1.1 Partial Cloud Contaminated Pixels Detection

Massive bulky clouds are generally much colder than the underlying sea surface. Therefore, these cloudy pixels can be detected and masked from AVHRR thermal infrared images with simple temperature thresholding methods. However, sub-pixel clouds and the cloud pixels on the edges of bulky clouds usually remain undetected with such simple thresholding methods. Because these pixels may only be partially covered by clouds, broken clouds and edges of bulky clouds are often characterised by a temperature lower than the underlying sea water, but may be higher than some portions of the sea surface water within the section. Thus, it is hard to distinguish them from SST features by the simple temperature threshold alone. However, three characteristics

of these undetected clouds can be noted. First, these scattered cloud pixels may be warmer than some parts of the water not far from them, but colder than the directly underlying sea surface. Second, they are often characterised by a high gradient magnitude. Third, after temperature thresholding, most of the undetected clouds are small broken-clouds and are characterised as point-type features which are associated with incoherent gradient directions over a small neighbourhood. The difficulty in detecting these part cloud pixels, is that the edge features and corner point features of SST patterns may also have a high gradient magnitude, the same as the scattered cloud pixels. Therefore, multiple criteria testing is necessary to separate these pixels from the SST features. The algorithm was developed based on the Förstner operator which has the advantage that it is able to classify the underlying feature by measuring gradient strength and coherency of gradient direction within a small window. In the algorithm, the local gradient magnitude, coherency of gradient direction and intensity structure of individual pixels are measured with the Förstner operator, and tested against three criteria. The experimental results show that the gradient strength, roundness of error ellipse and the difference of the intensity value between the candidate pixel and its neighbouring pixels are efficient measures for the point type cloud pixels detection, and with regional temperature thresholding and multi-criteria broken cloud screening, a majority of point-type cloud contaminated pixels can be detected.

8.1.2 The Correlation Function Distribution of SST Features and Its Variation Due to Different Pre-filtering and Correlation Computation Methods

The distribution structure of the correlation function is crucial to the reliability and accuracy of the estimation. However, it has not been well studied in previous research. In Chapter 5, the way that different pre-filtering and matching schemes vary the correlation function structures, and consequently, affect the velocity estimation reliability and accuracy was investigated. The investigation shows that:

1. The rotational search is essential in high dynamic areas, such as the areas which have strong eddies and rings. Especially when the temporal separation increases to 12 hours and more, the unresolved displacement and deformation due to rotation and straining may significantly degrade the estimation. The tests in Chapter 5 also show

that the effectiveness of using the rotational MCC method increases as the frequency of the SST features increase.

2. The SST field is usually dominated by the large scale patterns. The gradients of small scale features inside the patterns are usually very weak, but are important for the determination of the velocity component in the along-isotherm direction, such as the motion along jets, and the rotation of rings. The use of a high-pass filter of 25×25 to 35×35 window, can enhance the traceability of small features, and consequently, improve the estimation quality. The study also shows that the use of the high-pass filter, or gradient computation operator yield abruptly distributed correlation functions, This increases the sensitivity to the displacement of the corresponding features. The increase of sensitivity to the displacement can improve the matching accuracy. However, it also reduces the tolerance to unresolved displacement and deformation. Therefore, when the high-pass filter or gradient operator is used, the rotational search is even more desirable.

3. Due to the high auto-correlation of the SST patterns, the corresponding cross-correlation function frequently has a multi-peak or longish distribution. This distribution form of the correlation function introduces a high uncertainty into the estimation, and consequently, results in erroneous estimates. The rotational search and high-pass filtering partially addresses the problem, but both techniques cannot change the basic (the multi-peak or longish) distribution structure. A correlation function of such distribution alone cannot provide reliable measure for the displacement determination, and additional information is essential to resolve the uncertainty.

8.1.3 Improvement of Estimation Reliability with Relaxation Labelling

To reduce the inconsistency of the estimated field and the uncertainty in estimation due to the multiple-peak or longish distribution of the correlation function, an estimation scheme based on the relaxation labelling technique was proposed and tested. The proposed scheme estimates the displacement of SST features in consecutive images by integrating two sources of information — the correlation between the features in

consecutive images and the compatibility among the neighbouring candidate displacements. The compatibility is measured with the second order difference of neighbouring displacements.

In this study, the following capabilities of the proposed scheme were tested:

1. The reliability and robustness in handling the candidate set, containing candidates of erroneous high correlation value.
2. The feasibility of using the candidate set from coarsely determined correlation matrices, to improve computational efficiency.

The experimental results showed the following:

- The relaxation scheme is capable of identifying and eliminating the candidates of erroneous high correlation which are randomly distributed in the image domain. However, the proposed relaxation scheme is unable to eliminate the systematically biased candidates of high correlation values, when the systematically biased neighbourhood is not entirely incompatible with its surroundings.
- The use of the contextual information increases estimation robustness. Therefore, this allows the relaxation process to use a relative large leap-frog search step in correlation distribution computation and significantly reduces the computation time. The selection of the distance of the leap-frog steps is inherently an issue of sampling rate. The principle of this selection is maximising the reduction of the computation time with a minimum bias in the computed correlation distribution.

The experimental results also show that the resultant field from the proposed scheme was slightly over-smoothed in the areas of strong velocity shear gradients due to the following effects:

1. The use of a large and fixed-shape template in the correlation computation to gain sufficient information. Also, because the shape of the template is fixed, the deformation due to the velocity shear is not resolved, and the estimated

displacements, with such a template, are the average value of the displacement of features contained in the template.

2. The compatibility equation based on the assumption of the smoothness in the second order differences among the neighbouring candidates. The accuracy of the assumption is subject to the balance between the density of the grid points and the magnitude of the velocity shear gradients.

The results of the experiments show that the refining process (the process based on the relaxation method described in Chapter 6) can effectively reduce the over-smoothing effect, resulting from the inaccuracy of the compatibility equation used in the approximate relaxation. While, the effect due to the use of the large template is an inherent problem in the correlation computation using fixed-shape templates, this effect can be reduced by using flexible templates, and resolved by using joined-patch least squares matching (JPLSM), as discussed in Chapter 7. It is suggested that, when the JPLSM is used for the resultant field refining, the refining process based on the relaxation labelling can be omitted, and the computation can directly go to JPLSM refining after the approximated relaxation process.

8.1.4 Improving Accuracy Using JPLSM

To further improve the accuracy of estimation from consecutive SST images, a refining process base on jointed-patch least squares matching (JPLSM) was proposed.

The results of the experiments using synthetic image pairs showed that, using the proposed JPLSM scheme, the *rms* difference in magnitude and orientation of the resultant displacement field was reduced from 4.7 pixels and 19^0 (determined using relaxation labelling method) to 2.2 pixels and 9^0. Especially the accuracy of the vectors in the areas of strong velocity gradient variation were improved. In the MCC method and the relaxation labelling method, the vector field in the areas of strong velocity gradient variation were over-smoothed due to the use of a large template in the correlation computation. The use of the smaller, flexible and jointed patches resolves

the bi-linear deformation of the SST patterns, and significantly reduced such over-smoothness.

In the JPLSM refining process, the patches of the entire grid are integrated as a single flexible template (i.e. like a rubber sheet). Therefore, the contextual information could be conveyed among the neighbouring patches, and the strength of the inter-patch structure (the smoothness constraint) and the intra-patch structure (the incompressibility constraint) were controlled by varying the weight of the corresponding constraint equations based on the condition of the features contained in the patchs. In this study, the ratio of the maximum eigenvalue and the minimum eigenvalue of the normal equation of each independent patch, $\lambda_{max}/\lambda_{min}$, was used as the measure of the condition of features contained in the patch. The experimental results show that, under the condition of images used in the tests, the maximum $\lambda_{max}/\lambda_{min}$ is less than 2,000, that the displacement vectors at the inner grid point could be well estimated using a very small weight for the smoothness and incompressibilty constraints, while, relatively larger weight were needed for the constraints related to along-edge and at-corner grid points to strengthen the network structure. By adjusting the weights of the smoothness and incompressibility constraints according to the feature condition, the imperfection of the constraints were controlled.

The study in Chapter 7, also discussed the inherent relation between the least squares matching and the inverse model method in the application of displacement determination from consecutive AVHRR thermal images. It was illustrated that the observation equation of the least squares matching (which were derived based on the similarity of the intensity functions of the consecutive image pair) had the same form as the differential energy conservation equation (which is a physical law), in the application of estimation of the velocity field from consecutive thermal images. Therefore, the proposed least squares matching scheme is an iteratively refining inversion process. The study further analysed the error due to the use of the differential form of energy conservation equation over large elementary computational units, and showed the necessity of using an iterative process with large to small elementary units.

8.2 Suggestions for Future Study

8.2.1 Suggestions for Detection of Partially Cloud Contaminated Pixels

The algorithm was designed for the detection of point type cloud contaminated pixels. Although tests showed that the majority of cloud pixels on the border of the bulky cloud clusters can be detected as point type contaminated pixels with the proposed algorithm, when the proportion of the cloud contamination of these pixels varies widely, a complete detection for both point type and edge type partial cloud contamination still needs further study.

The thresholds used in the proposed algorithm were determined empirically based on test results. The automated optimisation of the thresholding requires further study. The empirically determined thresholds resulting from this research may be used to initialise an automated optimisation process, for example, in a heuristic refining process.

The contextual information remains unused in the proposed algorithm, and this source of information can be used to improve the detection accuracy in future studies. Especially, for the detection of the point type clouds located around the edge of bulk cloud, the contextual relation between the candidate pixel and the detected bulky cloud cluster can be a valuable source of information.

8.2.2 Suggestions Related to the JPLSM Method

In the proposed JPLSM method, the condition numbers were used to control the weights of the constraints. However, since noise and undetected cloud pixels are of high frequency, and contribute to the condition number similar to the high frequency SST features which are the most traceable features, they can reduce the computed condition number. The under-weighting for the constraints at ill-condition patch due to these fake small condition numbers can result in mis-estimate, when the patch does not really contain sufficient traceable features. Although this case did not occur in the experiment

under the conditions used, the removal of noise using a 3×3 low-pass filter (as was applied in the tests), and the use of a consistent check after each iteration are suggested to prevent the inconsistent estimates due to the effect of these fake small condition number.

The search strategy used in the proposed JPLSM method is much more efficient than the brute force search of the MCC method. However, the inversion of the large normal equation made the proposed JPLSM method still quite computational time consuming. The computational efficiency of the inversion may be significantly improved by using array algebra [see *Rauhala* 1980 for example], or nested dissection [*George* 1973].

References

Branham R. L. [1990], *Scientific Data Analysis, An Introduction to Overdetermined System*, Springer-Verlag, New York.

Caraux, O. and R. W. Austin, [1984] "Multispectral satellite remote sensing of an oceanic cyclone in the northwestern Mediterranean". *International Journal of Remote Sensing*, Vol. 5, 855-860.

Carlson, P. R. [1974] "Surface Currents along The California Coast Observed on ERTS IMAGERY". *Proceedings of the 9th International Symposium on Remote Sensing of Environment* Vol. II, 1279-1288.

Chen J. S. and Medioni G., 1992, "Adaptive smoothing: Principles and applications", *Advances in Image Analysis* p13-51, edited by Y. Mahdavieh and R. C. Gonzalez, (SPIE Optical Engineering Press).

Christou, N. T. [1990], " On the Space-Time Current Variability and its Effectives on the Length-of-Day", *Ph.D. Dissertation, Department of Surveying Engineering, Technical Report No. 148*, University of New Brunswick, Fredericton, New Brunswick, Canada, 333pp.

Collins, M. J., W. J. Emery, [1988], " A computational method for estimating sea ice motion in sequential seasat synthetic aperture radar imagery by matched filtering", *Journal of Geophysical Research*, Vol. 93, No. C8, 9241-9251

Cracknell, A. P. and W. G. Huang, [1987], "Surface Currents off the West Coast of Ireland Studied from Satellite Images", *International Journal of Remote Sensing*, Vol. 9(3), 438-446

Emery, W. J., C. Fwoler, and C. A. Clayson, [1992], "Satellite-image-derived Gulf Stream currents compared with numerical model results", *Journal of Atmospheric and Oceanic Technology*, Vol.9, 286-304

Emery, W. J., A. C. Thomas, M. J. Collins, W. R. Crawford, and D. L. Mackas, [1986], "An objective method for computing advective surface velocities from sequential infrared satellite images", *Journal of Geophysical Research*, Vol. 91, No. C11, 12,865-12,878

Essen, H. -H., [1995] "Geostrophic Surface Currents as Derived From Satellite SST Images and Measured by a Land-Based HF radar". *International Journal of Remote Sensing*, Vol. 16, 239-256.

Förstner, W., [1987], "A fast operator for detection and precise location of distinct points, corners and centres of circular features", *ISPRS Intercommission Workshop on "Fast processing of photogrammetric Data"*, Interlaken 281-305.

Förstner, W, [1982], "On the Geometric Precision of Digital Correlation", *International Archives of Photogrammetry* Vol. 24 III, Proceedings of the Symposium of the ISPRS Commission III, Helsinki, pp 176-189.

Garcia, C. A. E., and I. S. Robinson [1989], "Sea surface velocities in shallow seas extracted from sequential Coastal Zone Colour Scanner satellite data", *Journal of Geophysical Research*, Vol. 94(C9), 12,681-12,691

Gaspar, P., and C. Wunsch, [1989], "Estimates From Altimeter Data of Barotropic Rossby Waves in The Northwestern Atlantic Ocean", *Journal of Physical Oceanography*, Vol. 19, 1821-1844.

George, A., [1973], "Nested Dissection of a Regular Finite Element Mesh", *Journal of Numerical Analysis*, Vol. 10(2), 345-363

Gruen, A. and D. Stallmann, [1991] "High-Accuracy Edge-Matching with an Extension of the MPGC-Matching Algorithm", *Proceedings Industrial Vision Metrology, SPIE,* Volume 1526, pp 42-55

Gruen, A. and E. P. Baltsavias, [1988], "Geometrically Constrained Multiphoto Matching", *Photogrammetric Engineering and Remote Sensing*, Vol. 54, pp 633-641.

Holland, W. R., D. E. Harrison, and A. J. Semtner, [1983]. "Eddy-Resolving Numerical Models of the Large-Scale Ocean Circulation", in *Eddy in Marine Science*, A. R. Robinson edt., Springer-Verlag, Berlin.

Kamachi, M., [1989], "Advective surface velocities derived from sequential images for rotational flow field: limitations and applications of maximum cross-correlation method with rotational registration", *Journal of Geophysical Research*, Vol. 94, No. C12, 18227-18233

Kelly, A. K. and P. T. Strub [1992] "Comparison of velocity estimates from Advanced Very High Resolution Radiometer in the coastal transition zone", *Journal of Geophysical Research,* Vol 97(C6) , 9653-9668

Kelly, K. A. [1989] "An inverse model for near-surface velocity from infrared images", *Journal of Physical Oceanography*, Vol. 19, 1845-1864

Kelly, K. A., [1983], *Swirls and Plumes or Application of Statistical Method to Satellite-Derived Sea Surface Temperature*, Ph.D. Thesis, University of California, San Diego.

Kittler, J and, J. Illingworth, [1985], " Relaxation Labelling Algorithm — a Review", *Image and Vision Computing,* Vol. 3(4) 206-215

Koblinsky, C. J., J. J. Simpson and T. D. Dickey, [1984], "An Offshore Eddy in The California Current System, II, Surface Manifestation", *Progress in Oceanography*, Vol. 13, 51-69.

Kreyszing, E. [1970], *Introductory Mathematical Statistics: Principles and Methods*, New York: John Wiley

La Violette, P. E., [1984], "The Advection of Submesoscale Thermal Features in The Alboran Sea Gyre", *Journal of Physical Oceanography*, Vol. 14, 550-565.

Lee, H. and W. Lei, [1990], "Regional Matching and Depth Finding for 3D Objects in Stereo Aerial Photographs", *Pattern Recognition*, Vol. 23, 81-94

Leese, J. A., C. S. Novak and B. B. Clarke, [1971], "An Automated Technique for Obtaining Cloud Motion From Geosynchronous Satellite Data Using Cross Correlation", *Journal of Applied Meteorology*, Vol. 10, 110-132.

Levy, M., [1988], "A New Theoretical Approach to Relaxation, Application to Edge Detection", *IEEE proceedings of 9th International Conference on Pattern Recognition*, Vol. 1, 208-212

Lin. Z. J. [1988] Multi-information and Multi-criterion Adaptive Image Matching, *Doctoral Dissertation Wuhan Technology University of Surveying and Mapping*, Wuhan, China

Maul, G. A., A. G. Mourad, P. Wlison, O. H. Shemdin, R. H. Estes and G. Weiffenbach, [1980], "Report on the international symposium on interaction of marine geodesy and ocean dynamics", *Marine Geodesy*, Vol. 3, 3-24

Mesias, J. M., and P. T. Strub, [1995], "An Inversion Method to Determine Ocean Surface Currents Using Irregularly Sampled Satellite Altimetry Data", *Journal of Atmospheric and Oceanic Technology*, Vol. 12, 830-849.

Mulhearn, P. J., [1987] "The Tasman Front: A Study Using Satellite Infrared Imagery". *Journal of Physical Oceanography*, Vol. 17, 1148-1155.

Ninnis, R. M., W. J. Emery, and M. J. Collins, [1986], "Automated Extraction of Pack Ice Motion from Advanced Very High Resolution Radiometer Imagery", *Journal of Geophysical Research*, Vol. 91(C9), 10,725-10,734

Okubo, A., and R. V. Ozmidov [1970] " Empirical dependence of the coefficient of horizontal turbulent diffusion in the ocean on the scale of the phenomenon in question", *Izvestiya Academy of Sciences, USSR, Atmospheric and Oceanic Physics* Engl. Transl. Vol. 6(5), 308-309.

Peleg, S., [1980], " A New Probabilistic Relaxation Scheme", *IEEE Transaction on Pattern Analysis and Machine Intelligence*, Vol. PAMI-2,362-368

Rauhala, U. A., [1980], " Introduction to Array Algebra", Photogrammetric Engineering and Remote Sensing, Vol. 46(2), 177-192

Robinson, A. R., [1983]. "Overview and Summary of Eddy Science", in *Eddies in Marine Science*, Robinson edited., Springer-Verlag, Berlin.

Robinson, I. S. [1994] *Satellite Oceanography: A Introduction for Oceanographers and Remote Sensing Scientists*, Wiley-Praxis, Chichester

Rosenfeld, A., R. A. Hummel, and S. W. Zucker, [1976], "Scene Labelling by Relaxation Operations", *IEEE Transaction on System, Man, and Cybernetics*, Vol. SMC-6, 420-433

Rosenholm D, [1985] "Multi-point Matching Using the Least-Squares Technique for Evaluation of Three-Dimensional Model", *Photogrammetric Engineering and Remote Sensing*, Vol. 51, pp 621-626.

Saunders R. W., 1986, "An automated scheme for the removal of cloud contamination from AVHRR" radiances over western Europe, *International Journal of Remote Sensing*, Vol. 7, 867-886.

Sheres D. and K. E. Kenyon, [1990], "An Eddy, Coastal Jets and Incoming Swell All Interacting Near Pt Conception, California", *International Journal of Remote Sensing*, Vol. 11, No.1, 5-25.

Simpson J. J. and Humphrey C., 1990, "An automated cloud screening algorithm for daytime Advanced Very High Resolution radiometer imagery". *Journal of Geophysical Research.* 95(C8) 13,459-13,481.

Stewart R. H., 1985, *Methods of Satellite Oceanography*, (University of California Press, Berkeley).

Stow, D. A., [1988], "Remote Sensing and Image Processing Requirements for Eulerian Flow Field Estimations". *International Journal of Remote Sensing*, Vol 9, 351-364.

Svejkosky, S. [1988], "Sea surface flow estimation from Advanced Very High Resolution Radiometer and Coastal Zone Colour Scanner satellite imagery: a verification study", *Journal of Geophysical Research*, Vol 93(C6), 6735-6743

Tokmakian, R., P. T. Strub and J. McClean-Padman. [1990], "Evaluation of the maximum cross-correlation method of estimating sea surface velocities from sequential satellite images", *Journal of Atmospheric and Oceanic Technology*, Vol. 7, 852-865

TOPEX , [1981], "Satellite Altimetric Measurements of the ocean", Report to the TOPEX Science Working Group, NASA JPL, California, Institute of Technology, California.

Trinder J. C. and Huang Y., 1993, "Edge detection with sub-pixel accuracy for a flexible manufacturing system". *Videometrics II* SPIE, Vol. 2067, 151-161, Boston, Mass.

Van Woert, M, [1982], " The Subtropical Front: Satellite Observations During FRONTS 80", *Journal of Geophysical Research*, Vol 87, 9523-9536

Vastano, A. C. and R. O. Reid, [1985], " Sea Surface Topography Estimation with Infrared Satellite Imagery", *Journal of Atmospheric and Oceanic Technology*, Vol. 2, 393-400.

Vastano, A. C. and S. E. Borders, [1984], "Sea Surface Motion over An Anticyclonic Eddy on The Oyashio Front", *Remote Sensing of Environment*, Vol. 16, 87-90.

Vesecky, J. F., R. Samadani, J. M. Daida, M. P. Smith and R. N. Bracewell, [1987] "Observing rotational and deformation of sea ice with synthetic aperture radar", *Proceedings of the International Geoscience and Remote Sensing Symposium*, IGARSS, Ann Arbor, 1137-1145.

Wahl, D. D. and J. J. Simpson [1990], "Physical processes affecting the objective determination of near-surface velocity from satellite data", *Journal of Geophysical Research*, Vol. 95 (C8), 13,511-13,528.

Wu Q. X., D. Pairman, S. J. McNeill and E. J. Barnes [1992] "Computing advective velocities from satellite images of sea surface temperature", *IEEE Transactions on Geoscience and Remote Sensing*, Vol. 30, No.1, 166-176

Wunsch, C., [1978], " The North Atlantic General Circulation West of 50W Determined by Inverse Method", *Reviews of Geophysics and Space Physics*, Vol. 16, No. 4, 583-620.

Wunsch, C.[1993], "Physics of Ocean Circulation", in *Satellite Altimetry in Geodesy and Oceanography*, edited by R. Rummel and F. Sansò, Springer-Verlag, Berlin, 1993.

Zucker, S. W., E. V. Krishnamurthy, and R. L. Haar, [1978] "Relaxation For Scene Labelling: Convergence, Speed and Stability", *IEEE Transaction on System, Man, and Cybernetics*, Vol. SMC-8, No.1, 41-48

Publications from the

SCHOOL OF GEOMATIC ENGINEERING

THE UNIVERSITY OF NEW SOUTH WALES
ABN 57 195 873 179

To order, write to:
Publications Officer, School of Geomatic Engineering
The University of New South Wales, UNSW SYDNEY NSW 2052, AUSTRALIA

NOTE: ALL ORDERS MUST BE PREPAID. CREDIT CARDS ARE ACCEPTED.
SEE BACKPAGE FOR OUR CREDIT CARD ORDER FORM.

UNISURV REPORTS - S SERIES

(Prices effective November 2000)

Australian Prices *:	S8 - S20		$11.00
	S29 onwards	Individuals	$27.50
		Institutions	$33.00
Overseas Prices **:	S8 - S20		$10.00
	S29 onwards	Individuals	$25.00
		Institutions	$30.00

* Australian prices include postage by surface mail and GST.
** Overseas prices include delivery by UNSW's air-lifted mail service (~2-4 weeks to Europe and North America). Rates for air mail through Australia Post on application.

S8. A. Stolz, "Three-D Cartesian Co-ordinates of Part of the Australian Geodetic Network by the Use of Local Astronomic Vector Systems", Unisurv Rep. S8, 182 pp, 1972.

S10. A. J. Robinson, "Study of Zero Error and Ground Swing of the Model MRA101 Tellurometer", Unisurv Rep. S10, 200 pp, 1973.

S12. G. J. F. Holden, "An Evaluation of Orthophotography in an Integrated Mapping System", Unisurv Rep. S12, 232 pp, 1974.

S14. E. G. Anderson, "The Effect of Topography on Solutions of Stokes` Problem", Unisurv Rep. S14, 252 pp, 1976.

S16. K. Bretreger, "Earth Tide Effects on Geodetic Observations", Unisurv S16, 173 pp, 1978.

S17. C. Rizos, "The Role of the Gravity Field in Sea Surface Topography Studies", Unisurv S17, 299 pp, 1980.

S18. B. C. Forster, "Some Measures of Urban Residential Quality from LANDSAT Multi-Spectral Data", Unisurv S18, 223 pp, 1981.

S19. R. Coleman, "A Geodetic Basis for Recovering Ocean Dynamic Information from Satellite Altimetry", Unisurv S19, 332 pp, 1981.

S29. G. S. Chisholm, "Integration of GPS into Hydrographic Survey Operations", Unisurv S29, 190 pp, 1987.

S30. G. A. Jeffress, "An Investigation of Doppler Satellite Positioning Multi-Station Software", Unisurv S30, 118 pp, 1987.

S31. J. Soetandi, "A Model for a Cadastral Land Information System for Indonesia", Unisurv S31, 168 pp, 1988.

S33. R. D. Holloway, "The Integration of GPS Heights into the Australian Height Datum", Unisurv S33, 151 pp, 1988.

S34. R. C. Mullin, "Data Update in a Land Information Network", Unisurv S34, 168 pp, 1988.

S35. B. Merminod, "The Use of Kalman Filters in GPS Navigation", Unisurv S35, 203 pp, 1989.

S36. A. R. Marshall, "Network Design and Optimisation in Close Range Photogrammetry", Unisurv S36, 249 pp, 1989.

S37. W. Jaroondhampinij, "A model of Computerised Parcel-Based Land Information System for the Department of Lands, Thailand," Unisurv S37, 281 pp, 1989.

S38. C. Rizos (Ed.), D. B. Grant, A. Stolz, B. Merminod, C. C. Mazur "Contributions to GPS Studies", Unisurv S38, 204 pp, 1990.

S39. C. Bosloper, "Multipath and GPS Short Periodic Components of the Time Variation of the Differential Dispersive Delay", Unisurv S39, 214 pp, 1990.

S40. J. M. Nolan, "Development of a Navigational System Utilizing the Global Positioning System in a Real Time, Differential Mode", Unisurv S40, 163 pp, 1990.

S41. R. T. Macleod, "The Resolution of Mean Sea Level Anomalies along the NSW Coastline Using the Global Positioning System", 278 pp, 1990.

S42. D. A. Kinlyside, "Densification Surveys in New South Wales - Coping with Distortions", 209 pp, 1992.

S43. A. H. W. Kearsley (Ed.), Z. Ahmad, B. R. Harvey and A. Kasenda, "Contributions to Geoid Evaluations and GPS Heighting", 209 pp, 1993.

S44. P. Tregoning, "GPS Measurements in the Australian and Indonesian Regions (1989-1993)", 134 + xiii pp, 1996.

S45. W.-X. Fu, "A Study of GPS and Other Navigation Systems for High Precision Navigation and Attitude Determinations", 332 pp, 1996.

S46. P. Morgan et al, "A Zero Order GPS Network for the Australia Region", 187 + xii pp, 1996.

S47. Y. Huang, "A Digital Photogrammetry System for Industrial Monitoring", 145 + xiv pp, 1997.

S48. K. Mobbs, "Tectonic Interpretation of the Papua New Guinea Region from Repeat Satellite Measurements", 256 + xc pp, 1997.

S49. S. Han, "Carrier Phase-Based Long-Range GPS Kinematic Positioning", 185 + xi pp, 1997.

S50. M. D. Subari, "Low-cost GPS Systems for Intermediate Surveying and Mapping Accuracy Applications", 179 + xiii pp, 1997.

S51. L.-S. Lin, "Real-Time Estimation of Ionospheric Delay Using GPS Measurements", 199 + xix pp, 1997.

S52. M. B. Pearse, "A Modern Geodetic Reference System for New Zealand", 324 + xviii pp, 1997.

S53. D. B. Lemon, "The Nature and Management of Positional Relationships within a Local Government Geographic Information System", 273 + xvi pp, 1997.

S54. C. Ticehurst, "Development of Models for Monitoring the Urban Environment Using Radar Remote Sensing", 282 + xix pp, 1998.

S55. S. S. Boey, "A Model for Establishing the Legal Traceability of GPS Measurements for Cadastral Surveying in Australia", 186 + xi pp, 1999.

S56. P. Morgan and M. Pearse, "A First-Order Network for New Zealand", 134 + x pp, 1999.

S57. P. N. Tiangco, "A Multi-Parameter Radar Approach to Stand Structure and Forest Biomass Estimation", 319 + xxii pp, 2000.

S58. M. A. Syafi'i, "Object–Relational Database Management Systems (ORDBMS) for Managing Marine Spatial Data: ADCP Data Case Study", 123 + ix pp, 2000.

S59. X.-Q. Lu, "Strategies for Improving the Determination of Displacements of Sea Surface Temperature Patterns Using Consecutive AVHRR Thermal Images", 209 + xiii pp, 2000.

Credit Card Orders / Payment

from / to

School of Geomatic Engineering

The University of New South Wales

Name and postal address of ordering person/organisation:

_____

_____

_____

_____

_____

Date : _____

Day time phone number : _____

Credit Card debit for:

_____ $ _____

_____ $ _____

_____ $ _____

_____ $ _____

Total $ _____

Please debit my credit card: ☐ Mastercard ☐ Visa ☐ Bankcard

Card Name: _____ Signature: _____

Card No: | | | | | | | | | | | | | | | | |

Expiry Date : _____

Note: UNSW requires that you attach a photocopy of your credit card to this order.